A Computational Study of human Islet Amyloid Polypeptide Aggregation and its Inhibition

A Thesis Submitted

in Partial Fulfillment of the Requirements

for the Degree of

DOCTOR OF PHILOSOPHY

by

Rituparna Roy

to the

Department of Chemistry

Indian Institute of Technology Guwahati, India

2023

Dedicated to
Ma and Baba

Declaration

I hereby declare that the matter manifested in this thesis entitled "*A Computational Study of human Islet Amyloid Polypeptide Aggregation and its Inhibition*" is the result of research carried out by me in the Department of Chemistry, Indian Institute of Technology Guwahati, India under the supervision of Prof. Sandip Paul.

In keeping with the general practice of reporting scientific observations, due acknowledgement has been made wherever the work described is based on the findings of other investigators.

Rituparna Roy
IIT Guwahati

Certificate

It is certified that the work contained in this thesis entitled, "*A Computational Study of human Islet Amyloid Polypeptide Aggregation and its Inhibition*" has been carried out by Ms. Rituparna Roy for the Degree of Doctor of Philosophy under my supervision and the same has not been submitted elsewhere for a degree.

Prof. Sandip Paul
Thesis Supervisor
Department of Chemistry
Indian Institute of Technology Guwahati
Guwahati-781039, India

Preface

This thesis would not have been complete without the support of several people who in some way or the other extended their invaluable support and adoration during the years leading up to this day, especially for the last few years of my doctoral studies.

First and foremost, I would like to express my sincere gratitude to my supervisor, Prof. Sandip Paul. for his excellent guidance, constant support and immense encouragement over the period of years. His willingness to always impart illuminating advice and conduct valuable discussions made my journey much easier. I am also very grateful to him for providing me the opportunity and the privilege to pursue my research ideas without reserve. He also motivated me to pay attention to minute details in my research and provided valuable feedback on every step of the journey.

Besides my supervisor, I am also indebted to the doctoral committee members, Prof. Aditya Narayan Panda, Prof. Bhubaneswar Mandal and Prof. Aiyagiri Ramesh for their valuable suggestions and assessment through the preceding years. Besides, I would also like to thank Prof. Gopal Das for his wonderful suggestions. I extend my gratitude to all the other faculties, staffs and students of the Department of Chemistry, IIT Guwahati at various stages of my doctoral work. I gratefully acknowledge the Ministry of Human Resource and Development (MHRD), India for financial support and IIT Guwahati for providing the facilities to carry out my research work. Further, I would also like to acknowledge DST-SERB, Government of India, for providing the financial support to carry out this project. I would like to appreciate the IIT Guwahati super-computing facilities, PARAM-ISHAN and PARAM-KAMRUPA, without which the completion of my dissertation would not have been possible.

No words will be sufficient to express my deepest regards towards my fellow lab mates Aritra, Madhusmita, Rimjhim, Sanjib, Mira, Anandita, Vanneikima and Balaram for their unstinting support, helpful discussions, and creating a pleasant environment to

work peacefully in the lab. A heartfelt thanks to my seniors Dr. Shubhadip Das, Dr. Srijita Paul, Dr. Saikat Pal, Dr. Krishna Gopal Chattaraj and Dr. Rabindranath Paul for sharing their valuable suggestions and experiences during my Ph.D. days.

I take this opportunity to express my sincere thanks to all my teachers in school, college, and university days for helping and encouraging me in various aspects of my life and academics. All the learning from them will be an asset in every walk of my life.

I extend my sincere thanks and bundles of love to my friends Dr. Bushra, Dr. Santa, Dr. Tania, Dr. Nilanjana, Dr. Rabindranath, Retwik, Arya, Sammo, Ankur, Komal, Avijit, Dr. Prama, Dr. Soumyadip, Dr. Dipanjan, Dr. Sounak Da for providing the mental and physical support throughout the years. I would to like to especially mention Sayantani, who has been by my side, supporting, guiding and helping me for the past fourteen years. I would also like to thank Dr. Prasenjit Sarkar, who, like a brother, was always present to guide and support me, whenever required. And last but not least, I am extremely grateful to Saikat for his constant guidance, support and adoration through every step of this arduous journey, which would have been very difficult to conclude without him.

Finally, this journey would not have been possible without the endless love, support, and blessings of my family. I would like to extend my sincere gratitude to my mother for always being my best friend, philosopher, and guide. I am genuinely grateful to my parents for their great sacrifices and compassion. I would also like to thank my brother for his support and sacrifices in helping me to be achieve this goal, and allowing me to fly high. I also extend my gratitude towards my sister-in-law for her love and support. I want to acknowledge my late grandmother, who always dreamt of me obtaining a doctorate since childhood but, unfortunately, is not present today to witness it. As I stand at the terminus, I realize how extremely privileged I am to be able to reach this point and, therefore, grateful to each and every person who has contributed to this journey.

Rituparna Roy

2023

"But science and everyday life cannot and should not be separated. Science, for me, gives a partial explanation of life."

– Rosalind Franklin

Table of Contents

Chapter 1

Introduction

"Life is a relationship between molecules not a property of any one molecule. So is therefore disease which endangers life. While there are molecular diseases, there are no diseased molecules....."

– Emile Zuckerkandl and Linus Pauling

1.1 Intrinsically Disordered Proteins

Intrinsically disordered proteins and peptides (IDPs) are a class of proteins which lack a rigid three-dimensional structure[1]. Although the classical structure-function paradigm (where the biological activity of a protein is determined by its particular structured state) dominated the protein universe for than a century, these IDPs do not require unique structures to perform their functions, thereby challenging the traditional perspective[1, 2]. IDPs can often be found in nature, and thus, are involved in several crucial biological processes[1, 2]. However, due to their intrinsic disordered nature, IDPs undergo extensive conformational fluctuations, often leading to misfolding[2]. Some of these IDPs misfold and aggregate into thread-like, elongated insoluble intra- and extra-cellular accumulations known as amyloid fibrils[3]. These amyloid fibrils are linked to the pathology of many human degenerative diseases, such as Alzheimer's Disease (AD), Parkinson's Disease (PD), Hungtinton Disease (HD), amyotrophic lateral sclerosis (ALS), Type II Diabetes (T2D) and prion diseases. Thus, investigating the conformational activity of these IDPs has currently received great attention in the scientific world[2].

The amyloidogenic peptides differ in their sequences, structures and physiological functions. Nonetheless, they all aggregate into amyloid fibrils[3], which have a common cross-β structure and intermolecular hydrogen bond network parallel to the fibril axis (Fig 1.1)[4].

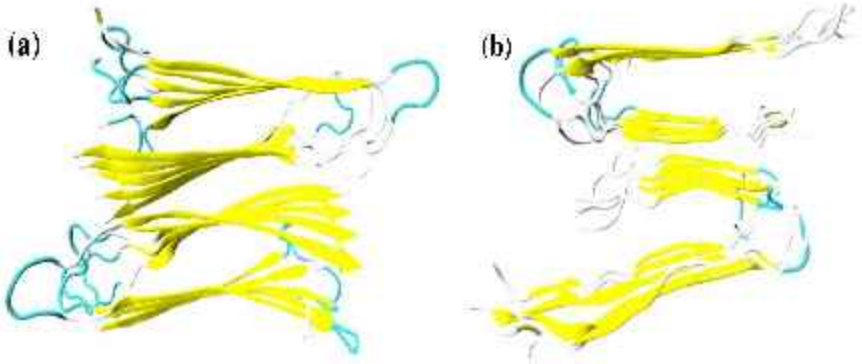

Figure 1.1: *Fibrillar structure of (a) human islet amyloid polypeptide and (b) amyloid-β peptide, which are linked to T2D and AD respectively.*

The aggregation kinetics of these peptides (Fig 1.2) involves a nucleation-elongation sig-

moidal profile, where the unstructured peptide monomers, in the lag phase, misfold into small soluble oligomers, which act as a nucleation site for the association of either monomers or oligomers, ultimately leading to fibril growth in the elongation or growth phase. This is followed by the plateau where the monomers and fibrils are in equilibrium in the saturation phase[4, 5].

Figure 1.2: *Schematic diagram of the kinetics of aggregation of amyloid peptides. This figure is adapted from Ref [6].*

The amyloid aggregation depends on a variety of factors, such as, solution pH, temperature, addition of cosolvents or osmolytes, and presence of membranes[3]. Accumulation of these amyloidogenic proteins leads to cellular apoptosis and tissue damage, inducing inflammation, oxidative stress, and cell death[7]. Previously, it was reported that the presence of insoluble plaques of amyloid fibrils results in cell loss[8]. However, the current hypothesis believes that the soluble oligomers is the pathogenic species in amyloid oligomers[9]. In this thesis, we are focused on the aggregation of one such amyloidogenic peptide, i.e., human islet amyloid polypeptide, which is associated with Type II Diabetes.

1.2 Type II Diabetes

Type II Diabetes (T2D) is a metabolic disease which is primarily designated by high blood glucose levels. It involves insulin resistance, increased glucagon secretion and liver glucose production, caused due to β-cell failure and reduced sensitivity to release insulin[10]. It is

the most common form of diabetes and is related to obesity and aging. The recent sedentary lifestyle with insufficient exercise and irregular eating habits has led to an immense increase in the prevalence of T2D[10]. Currently the number of people suffering from diabetes (90% with T2D) is estimated to be 463 million, which is predicted to increase to 700 million by 2045. Diabetes, further, gives rise to complications in the cardiovascular system, kidney, vision and also the nerves, even leading to death[10]. The treatment for T2D involves reducing insulin resistance, by primarily increasing the production and release of insulin, and also promoting insulin sensitivity[10]. Nonetheless, a complete cure for T2D is yet to be discovered. The presence of abundant amyloid plaques has been ascertained in about 90% of the people suffering from T2D. These amyloid deposits mostly consisted of a hormone, known as human islet amyloid polypeptide or amylin[10]. Due to the prevalence of amylin deposits in T2D patients, the association of hIAPP with the pathogenesis of T2D has been inferred. Hence, another approach has been proposed to cure T2D, which deals with research on drugs to prevent the amyloid aggregation of this polypeptide[10].

1.3 Human Islet Amyloid Polypeptide

Human Islet Amyloid Polypeptide (hIAPP) is a 37 amino acid neuroendocrine hormone (Fig 1.3). It is co-expressed and co-secreted from the β-cells in the pancreas alongwith insulin in the ratio of 1:10 to 1:100 (hIAPP:insulin)[11]. An 89 amino acid residue preproIAPP cleaves at the N-terminal to produce proIAPP, which consists of 67 amino acid residues. This proIAPP is, thereafter, postransitionally processed by prohormone convertase 2 (PC2) to give rise to mature hIAPP[11]. hIAPP also belongs to the calcitonin family, since the sequences of hIAPP and calcitonin gene-related peptide (CGRP) are similar[12]. hIAPP is involved in delaying of gastric emptying, inhibiting insulin secretion, controlling satiety, and regulating glucose metabolism by suppressing glucagon release[11, 12].

hIAPP consists of the amino acid sequence, KCNTATCATQ^{10}RLANFLVHSS^{20}NNFGAILSST^{30}NVGSNTY (Fig 1.3). It has an intrinsic disulphide bond linking Cys2 and Cys7 and an amidated C-terminal end. There are three positively charged residues, Lys1, Arg11 and His18, which makes hIAPP cationic at or below physiological pH. However, hIAPP is relatively hydrophobic in nature[13]. The N-terminal domain exists in α-helix conformation (which is stabilized by the presence

of disulphide bond)[10], and is involved in membrane binding. The C-terminal region is mostly amyloid prone and contributes to the aggregation of hIAPP[13]. The presence of disulphide bond constrain the peptide structure and prohibit the formation of β-strand, thus, preventing amyloid aggregation[10].

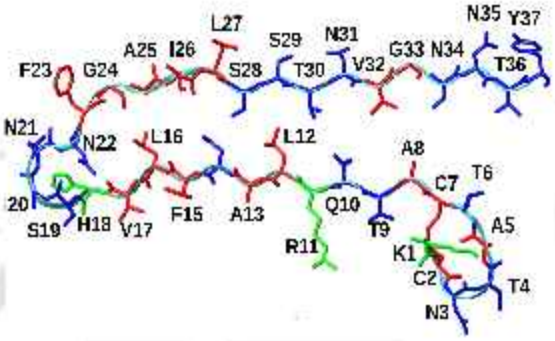

Figure 1.3: *Sequence of human Islet Amyloid Polypeptide (hIAPP). The polar, non-polar and basic residues in hIAPP monomer are represented in blue, red and green respectively.*

hIAPP monomers is unstructured in its native form, which aggregate into small soluble oligomers. The oligomers are more compact than the unfolded monomers, but their structural characterization has proved to be difficult due to their transient nature (especially in low concentrations)[8]. Reports suggest that they consists of random coil structures to β-sheet conformers and transition into ordered protofibrils and fibrils[13]. Solid-state NMR[14] (Fig 1.4a) and X-ray crystallography[15] (Fig 1.4b) studies depict that the structure of fibrils involves stacking of parallel β-sheets which are perpendicular to the fibril axis, generating "steric zipper" interface. A recent cryo-EM study displayed the S-shaped structure of synthetic hIAPP polymorph which consisted of residues, Ala13-Tyr37[16] (Fig 1.4c).

The soluble oligomers are more cytotoxic to the membranes than the subsequent fibrils. In addition, the formation of these oligomers and fibrils result in the production of reactive oxygen stress (ROS), which compromised membrane integrity[10]. The presence of membranes also influence the kinetics of hIAPP assembly. The membranes act as a platform for nucleation sites for further fibrillation. The cytotoxic hIAPP aggregates permeabilize cell membranes, leading to cell apoptosis. Reports suggest that β-sheet rich hIAPP oligomers insert into the hydrophobic region of the bilayer and results in mem-

brane disruption[10]. The perturbation activity of small soluble oligomers is indicated to be higher than fibrils[10]. Also, the in situ oligomer assembly at the membrane or their insertion into the bilayer may lead to non-specific pores or ion-channel assemblies within the bilayer[10]. A detergent-like mechanism is also observed, where fibrils attract lipid molecules to disrupt the membrane integrity[17]. Different mechanisms have been proposed for the disruption of membranes by hIAPP intermediate states, but physiological relevant information is required to develop inhibitors to prevent this phenomenon[10].

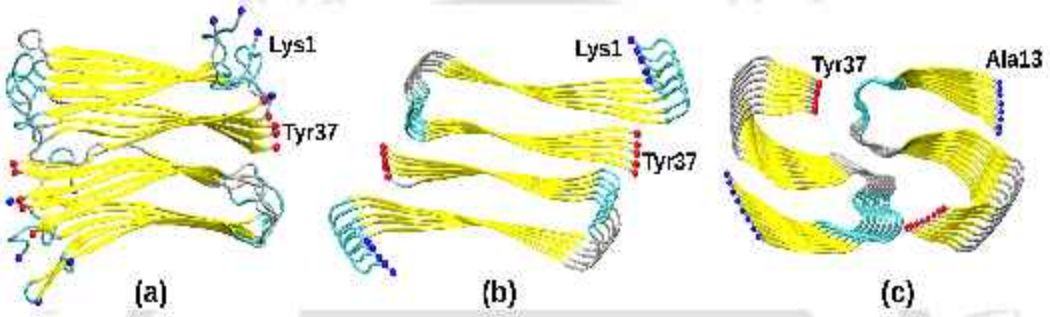

Figure 1.4: *Structure of hIAPP fibrils obtained by (a) Solid-state NMR[14], (b) X-ray[15] and (c) cryo-EM[16] methods. The blue and red balls indicate the N- and C-terminal ends respectively.*

The amyloidogenic nature of peptides depends on the presence of specific amino acid residues and their arrangement. These sequences can promote aggregation and the formation of cross-β structures[18]. For example, unlike hIAPP, rat IAPP (rIAPP) is not amyloidogenic in nature, even though, their sequences are 83% identical[19]. The differences lie in the region spanning residues 20–29. Consequently, Ser20-Ser29 of hIAPP is found to enhance the aggregation of hIAPP[20]. Also, this segment can form amyloid fibrils in isolation *in vivo* and is related to the onset of T2D. The pentapeptide fragment $F_{23}GAIL_{27}$ is the shortest sequence to form amyloid fibrils individually[21]. Apart from this, $F_{15}LVHS_{19}$ and $N_{14}FLVH_{18}$ on the N-terminal are also amyloid prone[10]. The aggregation of this peptide is, hence, not governed by any single sequence chain, but is much more complex. However, the charge, hydrophilicity and aromaticity of the amino acids are crucial for the aggregation property of hIAPP[10]. Out of the three positively charged residues, the protonation state of His18 is important for hIAPP fibrillation[22]. Also, on mutating His18 with amino acids of varying polarity, charge and size, the resulting fragments are less

amyloidogenic[22]. In addition, substituting the aromatic residue Phe23 with Ala abolishes amyloid formation[10]. The stacking interactions between aromatic residues stabilize the aggregation of amyloid peptides. Further, Phe15 and Phe23 are involved in forming early intermolecular interactions at the onset of aggregation pathway. Together, these studies shed light on the contribution of the various types of amino acid residues on the aggregation of hIAPP[10].

1.4 Inhibitors of hIAPP Aggregation

To control the expansion of T2D, the search for novel drugs is ongoing. One of the therapeutic approaches to treat T2D is focused on the aggregation of hIAPP[23]. A variety of inhibitors has been reported to affect the aggregation of amyloid peptides and, in general, can broadly be classified into three categories: small molecules, peptides and peptidomimetics, and lastly nanoparticles[23]. Since the mechanism of misfolding of hIAPP into toxic aggregates is still unclear, it is important to discover various classes of inhibitors which can hinder the abnormal folding of hIAPP.

1.4.1 Small Molecules Based Inhibitors of hIAPP Aggregation

The most common type of anti-amyloid inhibitors explored are small molecules. These small molecules often contain aromatic rings and polar groups, due to which they can effectively interact with the aromatic residues, and as well as the hydrophilic residues. This suppresses the interactions between the peptide residues and hence interrupts its aggregation[23]. Several polyphenols, which are biosynthesized in plants and also found in foods, have gained particular attention for their anti-amyloid properties, due to their stability, easy availability and low side effects. The polyphenols possess anti-oxidant and anti-inflammatory properties that help them to capture free radicals and suppress reactive oxygen species (ROS), which promotes their utilization as amyloid drugs[23]. Further, they can bind to metal ions, which significantly affects amyloid aggregation[7]. Among the polyphenols, flavonoids are the largest and the most well-studied group of compounds to have been tested for therapeutic applications to treat amyloid diseases[24]. Among the wide range of flavonoids, one of the most well-known flavonols, epigallocatechin-3-gallate (EGCG), inhibits the fibrillogenesis of various amyloid proteins, including hIAPP[23, 25].

This green tea extract has the intrinsic ability to diminish the aggregation and cytotoxicity of amyloid peptides due to the presence of non-specific hydrophobic and hydrogen-bonding interactions. EGCG can pass through the blood-brain barrier (BBB), which makes it a good drug candidate to treat T2D[26]. EGCG preferentially interacts with the C-terminal region of hIAPP with the help of aromatic interactions between the gallate ester moiety of EGCG and the aromatic residues of hIAPP (F15, F23, and Y37)[27–29]. Other green tea extracts, such as catechin, epicatechin, gallocatechin gallate (GCG), epicatechin gallate (ECG), and epigallocatechin (EGC), also display anti-amyloidogenic properties by directly binding with the steric zipper of the fibrillar segments to freeze fibrillation[30]. The inhibitory capacity of green tea extracts on hIAPP aggregation and destabilization of preformed aggregates follows the order EGCG > GCG > EGC > ECG > epicatechin in an equimolar ratio. The gallic acid ester moiety of EGCG is instrumental in its anti-amyloid activity against hIAPP. However, gallic acid is a poor inhibitor of hIAPP aggregation[31].

Other natural flavonoids such as genistein, isorhamnetin, kaemferol, morin, myricetin, quercetin, rhamnazin, and tamarixetin share a similar scaffold but differ in the number and position of -OH and -OCH_3 groups[23, 32]. Morin demonstrated the best results among all the above-listed compounds. The ortho-hydroxyl group of morin plays an important role in its interaction with hIAPP oligomers (preferentially binding with L16, H18, F23, G24, and I26)[33]. Quercetin, whose structure differs from that of morin by the position of one –OH group, reduces hIAPP fibrillation by almost 70% and increased RIN-m5F cells by 8%[23]. A derivative of quercetin combining with disaccharide rutinose, rutin (25 μm) completely inhibited hIAPP (25 μm) aggregation[34]. Additionally, quercetin protects amyloid-induced cells *in vitro* and *in vivo*, confirming the importance of this compound for drug development[32]. Myricetin interacts with the amyloidogenic core of hIAPP and disrupts its fibrils and reduced amyloid formation by 22-25%[23]. The structure of genistein differs from those of the previous three compounds in the position of the phenolic moiety. Thioflavin-T data showed that genistein induced stronger inhibitory ability toward hIAPP (C-terminal) fibrillation than that of Aβ (N-terminal)[35]. Silibinin binds to S28 of hIAPP and prohibits hIAPP monomers from transitioning from random coil to α-helix configuration[36]. It alleviates hIAPP-induced cytotoxic effects and does not show a negative effect on cell viability[23]. On comparing the inhibitory efficacy of five flavonoids (EGCG, genistein, quercetin, rutin, and silibinin) on hIAPP aggregation, it was

revealed that these flavonoids favorably interacted with the L12-N14 and N31-N35 regions of hIAPP. The order of inhibition is as follows: genistein > rutin > quercetin > EGCG > silibinin[23]. A recent study on two diastereoisomers of silibinin, Silybin A and Silybin B, showed that the potency of Silybin B toward inhibition of hIAPP aggregation and protection of INS-1 cells from hIAPP-induced toxicity is more than that of Silybin A[37]. This is ascribed to the fact that Silybin B stereospecifically binds to the amyloidogenic core of hIAPP, $hIAPP_{20-29}$[37]. Due to steric hindrance by the OH group connected to ring D in Silybin B, ring E is unable to rotate freely, in contrast to that in Silybin A. Hence, interactions between the OH group (ring D) and the OCH3 group (ring E) of Silybin B and hIAPP are crucial.

Curcumin targets the α-helix conformation of hIAPP to prevent the formation of on-pathway oligomers[38]. Curcumin is widely used for therapeutic purposes due to its low cost, easy availability, anti-inflammatory and antioxidant properties, and potential to cross the BBB (due to its lipophilic character)[39]. While curcumin is not toxic at low doses, its low solubility limits its clinical trials. However, to account for the instability of curcumin in aqueous solution (which makes it difficult to study the curcumin-peptide interactions), a derivative of curcumin, curcumin diacetate, is formed which not only halts fibril formation and destabilizes preformed fibrils but also protects lipid membranes[40]. Caffeine delays the α-helix to β-sheet transition, leading to inhibition of formation of hIAPP aggregates[41]. Clusters of caffeine form a hydrophobic environment around the hydrophobic residues of hIAPP, interrupting the inter-peptide interactions, thus blocking the oligomerization of these peptides. The three coffee compounds are most effective against hIAPP aggregation, compared to other peptides. Also, cell viability assays proved that the protection effect on pancreatic INS-1 cells imposed by these compounds in T2D patients follows the order caffeic acid > chlorogenic acid > caffeine[23]. Cichoric acid, a derivative of caffeic acid, also targets the residues of hIAPP via electrostatic and π-π stacking[30]. Brazilin has also displayed amyloid inhibition, delay of conformational transition, and fibril disruption of hIAPP[32]. It also protects cultured cells from hIAPP-induced cytotoxicity. Its inhibition property against hIAPP aggregation arises due to its preferential interactions with the N-terminus and turn region of hIAPP[23]. Based on pharmacokinetic studies *in vivo*, brazilin, due to its high stability, long half-life, and ability to cross the BBB, might prove to be a good therapeutic candidate[32]. Oleuropein, a polyphenol found in olive plants, displays

dual anti-diabetic functions: i.e., it promotes the secretion of insulin from β-cells and also protects them from hIAPP-induced cytotoxicity[23]. However, its inability to penetrate cell monolayers hampers its potential as a drug candidate. Oleuropein aglycone, an oleuropein derivative found in extra-virgin olive oil, is more lipophilic, making it more suitable for bioavailability. It inhibits hIAPP fibrillization more efficiently than oleuropein, also reducing the size of the fibrils[32]. It is more effective in protecting hIAPP-induced membrane damage than EGCG[42, 43]. Resveratrol, the phytoalexin stilbenoid polyphenol found in grapes and red wine, suppresses the aggregation of hIAPP by interrupting the lateral extension of a single-layered β-sheet oligomer. It prevents hIAPP from interacting with the membrane surface by locking the peptide conformation into a helix conformation[44]. The small size of resveratrol enables it to occupy the groove of hIAPP's protofibrillar surface near the N-terminal end, blocking the lateral association of β-sheets and thus destabilizing the ordered structure[44]. EGCG, on the other hand, occupies the C-terminal amyloidogenic region on the surface of the β-sheet layer. Since the N-terminal region of hIAPP is responsible for its binding to the cell membrane, which is associated with amyloid toxicity, the preferential interaction of resveratrol with N-terminal hIAPP protects β-cells[44]. Resveratrol also degrade hIAPP deposits and restore the insulin secretion ability in hIAPP-INS1 cells. To combat the poor solubility of resveratrol, it was functionalized with a phosphoryl moiety that also improves its pharmacological properties and inhibits amyloid growth. Another resveratrol derivative is synthesized which has a lipid tail and, therefore, can anchor the resveratrol functional group on the membrane surface and intercept membrane disruption. A mixture of both of these derivatives resulted in preventing hIAPP amyloid growth and amyloid-mediated POPC/POPS membrane damage *in vitro*. This novel strategy can thus be employed to prevent amyloid growth and membrane damage[45]. Orcein, which is extracted from lichens, binds to the amyloid core of hIAPP, N22-I26, converting the ordered protofibrillar structure into a less ordered arrangement via aromatic and hydrophobic interactions[46]. hIAPP forms amorphous off-pathway assemblies in the presence of orcein which inhibits the formation of mature hIAPP fibrils.

Dopamine, which is a common neurotransmitter, decreases the β-sheet propensity of hIAPP and interacts with the amyloid-prone regions (especially with R11, L12, F15, H18, F23, I26, L27, and Y37 residues) primarily by hydrophobic and π-π interactions[47]. It interacts with the N-terminal and turn regions of hIAPP protofibrils to disrupt them.

Tanshinones are extracted from the roots of Salvia miltiorrhiza Bge and have been used as neuroprotectors and also to treat diabetes[23]. They consist of two major compounds, tanshinone I and tanshinone IIA. They interrupt hIAPP aggregation and simultaneously protect cultured cells from induced toxicity by binding to N14-F15 and the amyloid-prone F23-L27 residues of hIAPP[39]. Tanshinone I displays better disaggregation potency toward preformed hIAPP fibrils than tanshinone IIA[48]. The association between the amyloidogenic region of hIAPP, $hIAPP_{20-29}$, and melatonin is dominated by hydrogen-bonding interactions, followed by aromatic stacking and CH-π interactions, which prevent the β-sheet formation of hIAPP[49]. Choline-O-sulfate (COS), which has a tertiary amino group and a sulfate group, is a naturally occurring osmolyte which inhibits the oligomerization of hIAPP[50, 51]. MD simulations of COS with hIAPP monomers disclosed that the sulfate oxygen of COS binds with the hIAPP backbone and causes disruption of the β-sheet formed between the amyloidogenic regions of hIAPP (R11-S20 and F23-T36)[51]. Various hypoglycemic drugs, such as, troglitazone, repaglinide, reduces β-sheet formation and amyloid fibrils, and hence has potential to treat T2D. However, the poor solubility of small molecules posses a problem for their use as drugs, therefore, their bioaccessibility has to be improved[23].

1.4.2 Peptide Based Inhibitors of hIAPP Aggregation

This class of inhibitors consists of small peptides or peptide mimetics, most of which are derived from the original sequence of hIAPP or de novo design. They are then modified by substituting with different amino acid residues or organic moieties. The peptide-based hIAPP inhibitors possess intrinsic merits, such as, high biocompatibility, low immunogenicity, ease of synthesis and modification, high binding affinity to targets and controllable folding structures[23]. The N-methylation at Gly24 and Ile26 of the $hIAPP_{22-27}$ fragment helps in the inhibition of hIAPP fibrillogenesis by 68% and reduction in the hIAPP mediated apoptotic β-cell death by 20%[52]. Similar N-methylation of $hIAPP_{20-29}$[53] and the full length hIAPP[54] showed inhibitory effect against hIAPP aggregation at nanomolar level, with a high binding affinity. The mutation of residues by β-sheet breaker units, such as proline (Pro) or α-aminoisobutyric acid (Aib)[55] also prevents the folding of hIAPP into β-structure. In addition, the non-amyloidogenic H18R/I26P or H18R/G24P/I26P or H18R/A25P/S28P/S29P mutants displayed improved inhibitory

ability with higher solubility[56]. Furthermore, the two β-sheet forming regions of hIAPP, $hIAPP_{8-18}$ and $hIAPP_{22-28}$, joined by a series of linkers, effectively inhibits both hIAPP and Aβ aggregation[57]. The lag time of hIAPP fibrils is prolonged by rIAPP and pramlintide, which are used as peptide drugs for diabetes, and their mutants in a dose-dependant manner[58]. Further insulin B-chain derived peptides slowed down hIAPP aggregation at equimolar ratio[59]. Moreover, decrease in the Thioflavin T (ThT) fluorescence intensity of hIAPP was observed in presence of ten fold excess of β-sheet breaker hybrid peptidomimetics, thus displaying potent inhibitory ability[60]. A peptide extracted from the extra-membrane C-terminal tail of the SARS corona virus, TVYVYSRVK, modifies the kinetics of hIAPP aggregation and inhibits the formation of hIAPP fibril[61]. Another strategy implemented to design peptide inhibitors is to replace the natural L-amino acid residues with their stereochemical mirror images (i.e. D-amino acids).

Due to the sequence resemblance of small peptide inhibitors derived from hIAPP with the parent peptide, they often self-aggregate at low concentrations to form amyloid-like aggregates, several of which are toxic to the cells[62]. Consequently, various β-breaker elements have been incorporated in the parent sequence, which prevent the misfolding of hIAPP into β-sheet rich structure. The replacement of Ile26 by α,β-dehydrophenylalanine (ΔF) in the small peptide derived from hIAPP amyloidogenic core resulted in two peptide inhibitors, FGAΔFL and NFGAΔFL, which delay the conformational change of hIAPP and suppress hIAPP fibrillation[63]. The ThT assay indicated that FGAΔFL is a better inhibitor against hIAPP aggregation than NFGAΔFL at a molar ratio of 5:1 for inhibitor:hIAPP. Further I26P point mutant of hIAPP is also a potent inhibitor of amyloid formation at an equimolar ratio and it lengthens the lag phase of amyloid formation by almost 20 fold[64]. Eight analogues of HW-155 designed by Bolarinwa et al. by truncating or substituting HW-155 side chains proved to be effective inhibitors of hIAPP aggregation[65]. 10-fold excess of peptide 1 not only reduced hIAPP aggregation to 26.1%, but also disrupted the preformed hIAPP fibrils[65]. γ-peptide foldamers, with structures homologous to 3_{10}-helix, are designed to trap the α-helix conformation of Aβ and hIAPP to prevent their transition into β-sheet amyloids[66]. Further, using α-aminoisobutyric acid (Aib) residues, Gilead and Gazit designed three peptide inhibitors by replacing Ala and Leu residues in $hIAPP_{13-20}$, $hIAPP_{13-18}$ and $hIAPP_{13-17}$ sequences. Here also, the presence of 10-fold excess of Aib-containing peptides lowers the extent of hIAPP fibril formation[55]. These

studies highlight the advantage of insertion of conformational restriction in the designed breaker peptides that serve as potent inhibitors of amyloid aggregation. The peptide inhibitors may undergo rapid proteolytic degradation *in vivo*, inherit toxicity from their parent proteins and have low membrane permeability[23], due to which they are least explored among all the categories of inhibitors.

1.4.3 Nanomaterial Based Inhibitors of hIAPP Aggregation

Recently, due to the ease of blood-brain barrier penetration, application of surface-functionalized ligands, and body clearance, utilization of nanoparticles in anti-aggregation research has received great attention in recent years[23]. The nanoparticles have a large surface-to-volume ratio, which enables them to provide strong adsorption sites to trap amyloid peptides, both *in vitro* and *in vivo*, thus controlling self-aggregation possibility[67]. The efficiency of these inhibitors depends on the shape, size, surface charge and ligands, and lattice facets of the nanoparticles[23].

Among numerous types of nanoparticles, the influence of carbon nanoparticles on protein aggregation has attracted particular interests[68–75]. A variety of carbon nanoparticles, such as carbon nanotubes (CNT), fullerenes (C_{60}), graphene or graphene oxide, carbon quantum dots has been recognized as an inhibitor of amyloid aggregation, due to their unique physicochemical properties and structure. The amyloidogenic core of hIAPP, $IAPP_{22-28}$ are strongly adsorbed onto graphene, single walled CNT and C_{60}, which inhibits its aggregation[74]. Further, the hydrophilicity and solubility of fullerenes coated with hydroxyl groups, $C_{60}(OH)_n$, enhances their inhibitory effect on hIAPP aggregation and the cell apoptosis caused by it[70]. Graphene oxide (GO) nanosheets inhibit hIAPP[71] aggregation by providing rich binding sites for hydrogen bonding and aromatic stacking interactions, which is possible due to the amphiphilic structure of GO and it also reduces cell toxicity from 60% to 12%. Carbon dots, including carbon nanodots (CNDs), carbon quantum dots (CQDs), graphene quantum dots (GQDs) and polyethyleneimine polymer dots (PDs) display great inhibitory efficacy against both hIAPP and Aβ aggregation, in the following order, GQDs>PDs>CQDs>CNDs[75]. The fluorine atoms in fluorinated GQDs (F-GQDs) induces hIAPP to form α-helical structures at the expense of β-sheet conformation, enabling F-GQDs to demonstrate stronger inhibitory ability than GQDs and N,N'-Dimethylformamide modified GQDs[23]. Furthermore, polymer

nanoparticles provide chemical and spatially rich binding sites for interacting with amyloid aggregates[23]. Equimolar polyamidoamine nanoparticles terminated with hydroxyl groups suppresses hIAPP fibrillization and hIAPP induced cell death[76]. PEG-PE micelles inhibits the oligomerization and fibrillization of hIAPP and rescued hIAPP-mediated β-cell death[77]. Although much effort has been devoted to the application of carbon nanoparticles in the field of amyloid aggregation, the cytotoxicity of these nanomaterials, along with their effect on cell damage, swelling of endoplasmic reticulum and nervous system toxicity proves to be a disadvantage[78]. In this respect, boron nitride nanotube (BNNT), which is structurally similar and isoelectronic to CNT, serves as a superior alternative.

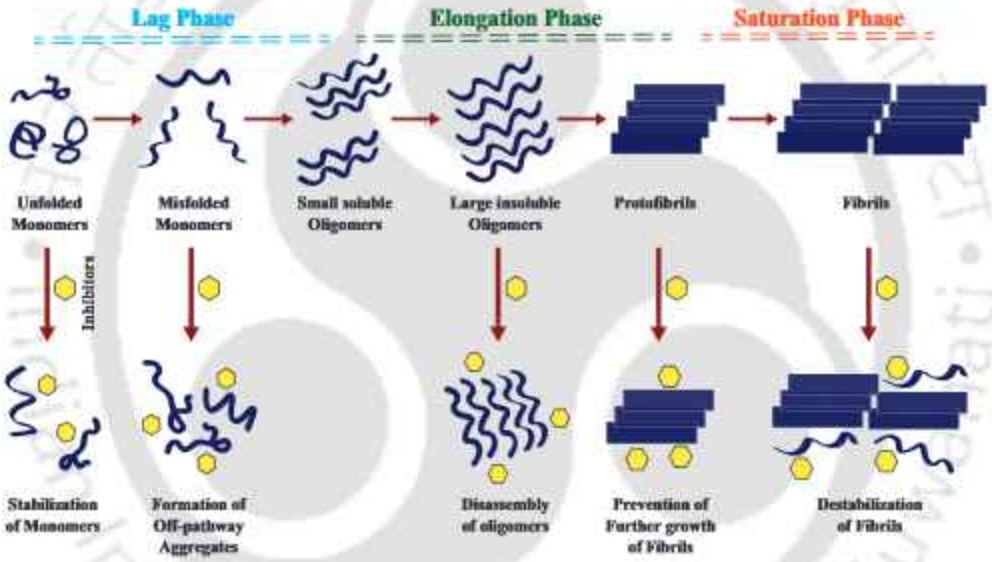

Figure 1.5: *Schematic diagram of the aggregation mechanism of hIAPP and its inhibition.*

These different categories of inhibitors modulate structures, assembly pathways, and membrane interactions of hIAPP, *in vitro*, *in vivo*, and *in silico*. These inhibitors achieve their anti-amyloidogenic functions by one or more of the following pathways (Fig 1.5)[7] (i) they interact with the extended monomeric peptides and impede the conformational transition to α-helix or β-sheet-rich structure; (ii) they convert toxic oligomers into non-toxic, off-pathway oligomers; (iii) they alter the aggregation kinetics such that the non-toxic fibril generation is accelerated by slowing the formation of toxic oligomers; (iv) they can disaggregate preformed fibrils; (v) they protect cell membranes from amyloid-induced poration; (vi) they may chelate metal ions to interject the aberrant interactions between

the peptides and metal; and finally, (vii) they can target the secondary processes, such as inflammation, oxidative stress, and protein homeostasis, which are caused by the formation of misfolded proteins[7].

1.5 Methodology

1.5.1 Molecular Dynamics Theory

In this thesis, we have used classical MD simulation technique. It has been widely used to investigate the structure and dynamics of biomolecular systems, such as proteins, nucleic acids, and small molecules like amino acids, sugars and drugs[2–6]. In MD simulation, the potential energy function (U) is described by all interactions between the atoms that are covalently bonded as well as non-bonded interactions between atoms and molecules in the condensed phase. The interactions between particles are governed by the so-called force field parameterization[79].

The potential energy function is written as a sum of bonded and non-bonded interaction terms

$$U = U_{bond} + U_{angle} + U_{dihedral} + U_{vdw} + U_{Coulomb} \tag{1.1}$$

The first three terms (U_{bond}, U_{angle}, $U_{dihedral}$) are the bonded terms, which describe the bond stretching, angle bending, and torsion rotation, and the last two terms are for the non-bonded potential. In bonded terms, the bond and angle contributions are described by harmonic potentials and all of the interactions between directly bonded atoms (1-2 interactions), angles (1-3 interactions, where two atoms bonded to a common atom), and torsion (interactions between pairs of 1-4 atoms) are defined as;

$$U_{bond} = \sum_{bonds} K_b(b_{ac} - b_{eq})^2 \tag{1.2}$$

$$U_{angle} = \sum_{angles} K_\theta(\theta_{ac} - \theta_{eq})^2 \tag{1.3}$$

$$U_{dihedral} = \sum_{dihedrals} \frac{V_n}{2}(1 + cos(n\phi - \delta)) \tag{1.4}$$

The letters b, θ, ϕ, and δ represent the bond length, bond angle, dihedral angle, and phase angle, respectively. The subscripts ac stands for actual and eq stands for equilibrium. The

parameters K_b, K_θ, and V_n are the force constants for bond, bond angle, and dihedral angle, respectively.

The non-bonded potentials are calculated using two terms, the first one is the Lennard-Jones term (U_{vdw})[80] describing the van der Waals interaction[81], and the second one is the Coulomb term ($U_{coulomb}$)[82] that deals with the electrostatic interactions between particles having partial charges on them. The non-bonding interaction terms are defined as:

$$U_{vdw} = \sum_{i} \sum_{i<j} 4\epsilon_{ij} \left[\left(\frac{\sigma_{ij}}{r_{ij}} \right)^{12} - \left(\frac{\sigma_{ij}}{r_{ij}} \right)^{6} \right] \tag{1.5}$$

$$U_{coulomb} = \sum_{i} \sum_{i<j} [\frac{q_i q_j}{4\pi\epsilon_o r_{ij}}] \tag{1.6}$$

where the overall sum is over all the atom pairs i and j. Lennard-Jones parameters σ and ϵ are the diameter of atomic sites and well depth energy, respectively. r_{ij} is the inter-atomic distance. q_i and q_j are the partial charges on interaction sites i and j and ϵ_o is the electrical permittivity.

The aim of the MD simulation is to observe the evolution of atomic coordinates in time. We consider an N-particle system characterized by the following Hamiltonian

$$H = \sum_{i=1}^{N} \frac{p_i^2}{2m} + U(\mathbf{r}^N) \tag{1.7}$$

where m is the mass of each particle, p_i is the momentum of the i-th particle and $U(\mathbf{r}^N)$ is the total potential energy of the system which includes the all particle-particle interactions. The coordinates of the particles are denoted by $\mathbf{r}^N = \{\mathbf{r}_1, \cdots, \mathbf{r}_N\}$. The position and velocity of i-th particle is represented by $\mathbf{r}_i$ and $\mathbf{v_i}$, respectively. The method of molecular dynamics consists of solving the equation

$$a_i = \frac{\mathbf{F_i}}{m_i} \tag{1.8}$$

where $i = 1, 2, ...N$, m_i is the mass of i-th particle and $\mathbf{F}_i$ is the force acting on particle i. This equation is obtained easily from the Lagrangian

$$L = \frac{1}{2} \sum_{i=1}^{N} m_i \mathbf{v_i}.\mathbf{v_i} - \frac{1}{2} \sum_{i=1}^{N} \sum_{j \neq i}^{N} u(r_{ij}) \tag{1.9}$$

where the potential U has been assumed to be the sum of pair potentials u_{ij}. The Lagrangian equation of motion is

$$\frac{d}{dt}(\frac{\partial L}{\partial \dot{q}_i}) - \frac{\partial L}{\partial \dot{q}_i} = 0 \tag{1.10}$$

It is clear from equation 1.10 that the dynamics of particles is described by 3N number of second order differential equations.

It is also possible to write down the Hamiltonian (H) for the system and solve the the Hamiltonian equations of motion

$$\dot{\mathbf{q}}_k = \frac{\partial H}{\partial p_k} \tag{1.11}$$

$$\dot{\mathbf{p}}_k = -\frac{\partial H}{\partial q_k} \tag{1.12}$$

where $\mathbf{q}_k$ and $\mathbf{p}_k$ represent generalized coordinates and momenta. For a system with pairwise interaction potential, the Hamiltonian is

$$H = \frac{1}{2}\sum_{i=1}^{N} m_i \mathbf{v_i}.\mathbf{v_i} + \frac{1}{2}\sum_{i=1}^{N}\sum_{j\neq i}^{N} u(r_{ij}) \tag{1.13}$$

and equations 1.11 and 1.12 yield

$$\frac{dr_i}{dt} = \frac{\mathbf{p_i}}{m_i} \tag{1.14}$$

$$-\dot{\mathbf{p}}_i = -\nabla \mathbf{u} = \mathbf{F_i} \tag{1.15}$$

where i=1,2,....N. There are now $6N$ first order differential equations to be solved.

The equation of motion is solved numerically to yield particle velocities and positions as a function of time. It is usually integrated by using finite difference approach. The Verlet algorithm is one of the most commonly used algorithm for this purpose[83]. The advantage of the use of Verlet algorithm is that its implementation is straightforward and storage requirements are modest. Although, it has the disadvantage of moderate precision during the calculation and velocity does not appear explicitly in the Verlet integration. As an improvement to the Verlet algorithm, the leap-frog algorithm[84] has been developed. But, it has a disadvantage that the positions and velocities are not synchronized. As an alternative of Verlet or the leapfrog algorithm, Velocity Verlet algorithm has been developed and the following relations are used to calculate new position and velocity at the same time:

$$r(t+dt) = r(t) + v(t)dt + \frac{1}{2}a(t)dt^2 \tag{1.16}$$

$$v(t+dt) = v(t) + \frac{1}{2}[a(t) + a(t+dt)]dt \tag{1.17}$$

To calculate the velocities at time t+dt, this method requires acceleration at time t and t+dt. In the present work, we have employed Velocity Verlet algorithm[85].

1.5.2 Simulation Setup

The initial coordinates of $hIAPP_{1-37}$ monomeric structure was extracted from the solid-state NMR-based model of decameric hIAPP, provided by the Tycko lab[14], in most of our work. Similarly the protofibrillar unit was generated by extracting the coordinates of five hIAPP chains, which exhibits a fibrillar network of parallel β-sheets. Each of the five $hIAPP_{1-37}$ chains was folded into a β-hairpin comprised of two β-strands (Ala8-Val17 and Ser28-Tyr37), which was joined together by a loop (His16-Leu27). Another hIAPP protofibril was obtained by cryo-EM methods (PDB ID 6Y1A)[16]. In this model, $hIAPP_{13-37}$ was arranged in S-shape, consisting of β-strand (Asn14-Ser20)–loop (Asn21-Ala25)– β-strand (Ile26-Val32)–loop (Gly33-Ser34)–β-strand (Asn35-Tyr37). In each hIAPP chain, a disulphide bridge interconnected the Cys2 and Cys7 residues and the C-terminal was amidated. The positively charged hIAPP peptides were neutralized by adding Cl^-[86] ions and was solvated with TIP3P water. All the systems were prepared using PACKMOL[87] and the TLEAP module of the AMBER package[88] was used to create the initial parameters. The peptides were modelled using AMBER14SB force field[89].

Initially, each system was energy minimized for 5000 steps, each with steepest descent method and then conjugate gradient method, to remove bad contacts between the solute and solvent. The system was then gradually heated from 0 K to 300 K over a period of 180 ps in canonical (NVT) ensemble. Afterwards, an equilibration step of 5 ns was performed first in NVT ensemble, and then in isothermal-isobaric (NPT) ensemble at a pressure of 1 atm for 500 ps. This was followed by a production run of in NPT ensemble at 300 K and a pressure of 1 atm. The temperature was regulated, throughout the simulation, using Langevin dynamics[90] with a collision frequency of 1 ps^{-1}. To control the physical pressure, Berendsen barostat[91] with a pressure relaxation time of 2 ps was used. SHAKE algorithm[92] with a tolerance of 10^{-5} Å was used to constrain the bond lengths involving

hydrogen atoms. The particle mesh Ewald (PME)[93] method was applied to treat the long-ranged non-bonding electrostatic interactions and 10 Å cut off radius was employed for short-ranged non-bonding Lennard-Jones interactions. For each system, in all three directions, periodic boundary condition was used. All the molecular dynamics simulations were performed using AMBER18 or AMBER20[88] package.

1.5.3 Analysis Methods

In order to analyze the MD trajectories, we have used the CPPTRAJ program of the AMBER toolkit[94] and VMD[95], which was also used for visualization purposes. The secondary structure of the peptides was recognized using the Dictionary of Secondary Structure Prediction (DSSP)[96] method. The solvent accessible surface area (SASA) was calculated by Linear Combinations of Pairwise Overlaps (LCPO)[97] algorithm with 1.4 Å of probe radius. A hydrogen bond is considered to form if the distance between the donor (D) and acceptor (A) is within 3.5 Å and simultaneously the D-A-H angle is within 45°[98]. The cluster structure analysis was carried out using the Density-Based Spatial Clustering of Applications with Noise (DBSCAN) clustering algorithm[99]. The preference of hIAPP to interact with itself over solvent was determined by the parameter, Γ_{pw}, which was calculated by the following equation[100],

$$\Gamma_{pw} = \rho_p(G_{pp} - G_{pw}) \tag{1.18}$$

where p and w indicates hIAPP and water respectively, and ρ_p corresponds to the number density of hIAPP. The Kirkwood-Buff (KB) integrals, G_{pp} and G_{pw}, were calculated from the radial distribution functions of the center of mass of the peptides with itself and water respectively. The two-dimensional free energy landscapes (FELs) were computed using two reaction coordinates, following the equation,

$$\Delta G_i = -k_B T \left[\ln P_i - \ln P_{\max}\right] \tag{1.19}$$

where k_B is the Boltzmann constant and T indicates the absolute temperature, ΔG_i is the free energy of coordinate i at a probability distribution of P_i and the maximum probability is represented by P_{max}. Two aromatic rings were considered to be involved in π-π stacking when the distance between the center of mass of each ring (r) was within 6 Å and

the angle formed by the normals of these rings (θ) determined the orientation of stacking (Fig 1.6a). A θ lying in the range of 0°-30° or 150°-180° indicated parallel stacking, 30°-60° or 120°-150° symbolized herringbone, while 60°-120° was for perpendicular or T-shaped stacking[47] (Fig 1.6a). The distance cut-off for NH-π stacking interaction was taken to be 5 Å[27] (Fig 1.6b).

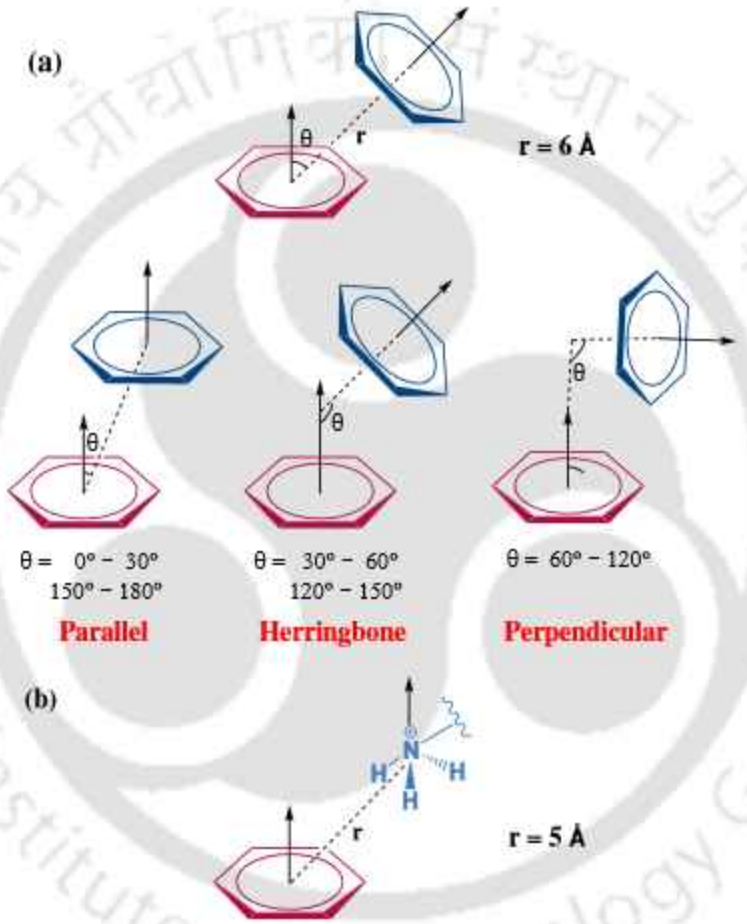

Figure 1.6: *Schematic representation showing (a) π-π and (b) NH-π stacking orientation.*

The binding free energy of hIAPP with the inhibitors was calculated using Molecular Mechanics/ Generalized Born Surface Area (MM/GBSA)[101], using the Python script, MMPBSA.py[102]. The binding energy (ΔG_{bind})between a receptor and a ligand was calculated as:

$$\Delta G^{0}_{bind} = \Delta E_{vac} + \Delta G_{solv} \tag{1.20}$$

$$\Delta E_{vac} = \Delta E_{ele} + \Delta E_{vdw} \tag{1.21}$$

$$\Delta G_{solv} = \Delta G_{GB} + \Delta G_{NP} \tag{1.22}$$

$$\Delta G_{NP} = \gamma(SASA) + \beta \tag{1.23}$$

The energy in vacuum (gas phase), ΔE_{vac}, consists of the electrostatic energy (ΔE_{ele}) and the van der Waals energy (ΔE_{vdw}). The solvation free energy (ΔG_{solv}) is the summation of polar solvation energy (ΔG_{GB}) and non-polar solvation energy (ΔG_{NP})[103]. The GB model was implemented to assess ΔG_{GB} and ΔG_{NP} was obtained from the solvent accessible surface area (SASA), which was calculated from MSMS program[104]. The surface tension of the solvent γ and fitting parameter β were 0.0072 kcal $Å^{-2}$ and 0.0 respectively.

1.6 Present Work

Within this thesis, we embark on a comprehensive exploration on the intricate journey of hIAPP aggregation, coupled with the myriad classes of compounds harboring the potential to impede this process.

In **Chapter 1**, a foundation is laid through the introduction of hIAPP. It is followed by an in-depth foray into the manifold conformational states, pivotal in engendering the aggregation phenomenon. Furthermore, we dissect an array of different categories of inhibitors, each contributing to the modulation of hIAPP aggregation pathways. A brief discussion of the molecular dynamics simulation methodology, which is a vital framework underpinning our study is followed. Thereafter, **Chapter 2** takes the helm into venturing the different conformational states of an amyloid prone fragment of hIAPP, $hIAPP_{20-29}$, via Markov State Modelling. Here, the transition pathway between the metastable states of $hIAPP_{20-29}$ dimer is analyzed and an in-depth investigation into the metamorphosis between the different conformations, which are crucial for the misfolding of hIAPP is also carried out. **Chapter 3** explores the influence of two small biological molecules on hIAPP aggregation, via all-atom molecular dynamics. In the first part, **Chapter 3.1**, we have

explored the effect of norepinephrine, which is a common neurotransmitter, on the amyloidogenesis of hIAPP. In **Chapter 3.2**, a new aspect of adenosine triphosphate (ATP), other than being the energy source for biochemical processes, is inquired. Here, the tendency of ATP to prevent the oligomerization of hIAPP is discerned. Norepinephrine and ATP, not only prevent the aggregation of hIAPP, but also disassemble previously formed aggregates. This chapter, thus, enlighten us about the diversity of the molecular structures that can modulate the aggregation of hIAPP and the effect of these structures on the activity of the inhibitors. **Chapter 4** turns the discourse towards peptides and peptidomimetics, probing their roles in shaping the aggregation narrative. Two such inhibitors are investigated, both of which are extracted from the amyloid core region of hIAPP, i.e., $N^{22}FGAIL^{27}$. In **Chapter 4.1**, this hIAPP fragment is replaced with all D-amino acids, and is used to prohibit the self-assembly of full-length hIAPP. In **Chapter 4.2**, a conformationally restricted element, aminobenzoic acid is incorporated into NFGAIL sequence, by replacing Ile26 and/or Gly24 residues. Here, three different isomers of aminobenzoic acid is used, i.e., (β, γ, δ), where contrasting behaviour of the isomers is observed. Hence, in this chapter, we have conveyed the effect of stereochemistry of the amino acid residues or modified organic moieties on the inhibitory potential of peptides or peptidomimetics. A novel dimension unfurls in **Chapter 5**, where the alliance between boron nitride nanomaterials and hIAPP aggregation is explored. These biocompatible nanomaterials not only inhibit the dimerization of hIAPP, but also disaggregate pre-formed fibrils. Finally, **Chapter 6** unfurls a tapestry of conclusions, weaving together the diverse threads from our journey. In unity, this thesis parades as an extensive survey, deciphering the aggregation pathway of hIAPP and unveiling an assembly of agents suspected to intervene.

References

[1] Uversky, V. N. Intrinsically Disordered Proteins and Their "Mysterious" (Meta)Physics. *Front. Phys.* **2019**, *7*.

[2] Khatua, P.; Mondal, S.; Gupta, M.; Bandyopadhyay, S. In Silico Studies to Predict the Role of Solvent in Guiding the Conformations of Intrinsically Disordered Peptides and Their Aggregated Protofilaments. *ACS Omega* **2022**, *7*, 43337–43345.

[3] Ilie, I. M.; Caflisch, A. Simulation Studies of Amyloidogenic Polypeptides and Their Aggregates. *Chem. Rev.* **2019**, *119*, 6956–6993.

[4] Nguyen, P. H.; Ramamoorthy, A.; Sahoo, B. R.; Zheng, J.; Faller, P.; Straub, J. E.; Dominguez, L.; Shea, J.-E.; Dokholyan, N. V.; De Simone, A.; Ma, B.; Nussinov, R.; Najafi, S.; Ngo, S. T.; Loquet, A.; Chiricotto, M.; Ganguly, P.; McCarty, J.; Li, M. S.; Hall, C.; Wang, Y.; Miller, Y.; Melchionna, S.; Habenstein, B.; Timr, S.; Chen, J.; Hnath, B.; Strodel, B.; Kayed, R.; Lesné, S.; Wei, G.; Sterpone, F.; Doig, A. J.; Derreumaux, P. Amyloid Oligomers: A Joint Experimental/Computational Perspective on Alzheimer's Disease, Parkinson's Disease, Type II Diabetes, and Amyotrophic Lateral Sclerosis. *Chem. Rev.* **2021**, *121*, 2545–2647.

[5] Roy, R.; Paul, S. Potential of ATP toward Prevention of hIAPP Oligomerization and Destabilization of hIAPP Protofibrils: An In Silico Perspective. *J. Phys. Chem. B* **2021**, *125*, 3510–3526.

[6] Moore, S. J.; Sonar, K.; Bharadwaj, P.; Deplazes, E.; Mancera, R. L. Characterisation of the Structure and Oligomerisation of Islet Amyloid Polypeptides (IAPP): A Review of Molecular Dynamics Simulation Studies. *Molecules* **2018**, *23*.

[7] Roy, R.; Paul, S. Illustrating the Effect of Small Molecules Derived from Natural Resources on Amyloid Peptides. *J. Phys. Chem. B* **2023**, *127*, 600–615.

[8] Selkoe, D. J.; Hardy, J. The amyloid hypothesis of Alzheimer's disease at 25 years. *EMBO Mol. Med.* **2016**, *8*, 595–608.

[9] Goldberg, M. S.; Jr, P. T. L. Is there a cause-and-effect relationship between α-synuclein fibrillization and Parkinson's disease? *Nat. Cell Biol.* **2000**, *2*, E115–E119.

[10] Milardi, D.; Gazit, E.; Radford, S. E.; Xu, Y.; Gallardo, R. U.; Caflisch, A.; Westermark, G. T.; Westermark, P.; Rosa, C. L.; Ramamoorthy, A. Proteostasis of Islet Amyloid Polypeptide: A Molecular Perspective of Risk Factors and Protective Strategies for Type II Diabetes. *Chem. Rev.* **2021**, *121*, 1845–1893.

[11] Press, M.; Jung, T.; König, J.; Grune, T.; Höhn, A. Protein aggregates and proteostasis in aging: Amylin and β-cell function. *Mech. Ageing Dev.* **2019**, *177*, 46–54, Molecular aspects of aging and longevity.

[12] Pillay, K.; Govender, P. Amylin uncovered: a review on the polypeptide responsible for type II diabetes. *Biomed Res. Int.* **2013**, *2013*, 826706.

[13] Saghir, A. E.; Farrugia, G.; Vassallo, N. The human islet amyloid polypeptide in protein misfolding disorders: Mechanisms of aggregation and interaction with biomembranes. *Chem. Phys. Lipids* **2021**, *234*, 105010.

[14] Luca, S.; Yau, W. M.; Leapman, R.; Tycko, R. Peptide Conformation and Supramolecular Organization in Amylin Fibrils: Constraints from Solid-State NMR. *Biochemistry* **2007**, *46*, 13505–13522.

[15] Wiltzius, J. J. W.; Sievers, S. A.; Sawaya, M. R.; Eisenberg, D. Atomic structures of IAPP (amylin) fusions suggest a mechanism for fibrillation and the role of insulin in the process. *Protein Science* **2009**, *18*, 1521–1530.

[16] Röder, C.; Kupreichyk, T.; Gremer, L.; Schäfer, L. U.; Pothula, K. R.; Ravelli, R. B. G.; Willbold, D.; Hoyer, W.; Schröder, G. F. Cryo-EM structure of islet amyloid polypeptide fibrils reveals similarities with amyloid-β fibrils. *Nat. Struct. Mol. Biol.* **2020**, *27*, 660–667.

[17] Brender, J. R.; Salamekh, S.; Ramamoorthy, A. Membrane Disruption and Early Events in the Aggregation of the Diabetes Related Peptide IAPP from a Molecular Perspective. *Acc. Chem. Res.* **2012**, *45*, 454–462, PMID: 21942864.

[18] de la Paz, M. L.; Serrano, L. Sequence determinants of amyloid fibril formation. *Proc. Natl. Acad. Sci. U.S.A.* **2004**, *101*, 87–92.

[19] Young, L. M.; Cao, P.; Raleigh, D. P.; Ashcroft, A. E.; Radford, S. E. Ion Mobility Spectrometry–Mass Spectrometry Defines the Oligomeric Intermediates in Amylin Amyloid Formation and the Mode of Action of Inhibitors. *J. Am. Chem. Soc.* **2014**, *136*, 660–670, PMID: 24372466.

[20] Betsholtz, C.; Christmanson, L.; Engström, U.; Rorsman, F.; Jordan, K.; O'Brien, T. D.; Murtaugh, M.; Johnson, K. H.; Westermark, P. Structure of Cat Islet Amyloid Polypeptide and Identification of Amino Acid Residues of Potential Significance for Islet Amyloid Formation. *Diabetes* **1990**, *39*, 118–122.

[21] Tenidis, K.; Waldner, M.; Bernhagen, J.; Fischle, W.; Bergmann, M.; Weber, M.; Merkle, M.-L.; Voelter, W.; Brunner, H.; Kapurniotu, A. Identification of a penta- and hexapeptide of islet amyloid polypeptide (IAPP) with amyloidogenic and cytotoxic properties. *J. Mol. Biol.* **2000**, *295*, 1055–1071.

[22] Khemtemourian, L.; Guillemain, G.; Foufelle, F.; Killian, J. A. Residue specific effects of human islet polypeptide amyloid on self-assembly and on cell toxicity. *Biochimie* **2017**, *142*, 22–30.

[23] Tang, Y.; Zhang, D.; Zhang, Y.; Liu, Y.; Gong, X.; Chang, Y.; Ren, B.; Zheng, J. Introduction and Fundamentals of Human Islet Amyloid Polypeptide Inhibitors. *ACS Appl. Bio Mater.* **2020**, *3*, 8286–8308.

[24] Patel, P.; Parmar, K.; Vyas, V. K.; Patel, D.; Das, M. Combined In Silico Approaches for the Identification of Novel Inhibitors of Human Islet Amyloid Polypeptide (hIAPP) Fibrillation. *J. Mol. Graph. Model.* **2017**, *77*, 295–310.

[25] Yao, Y.; Tang, Y.; Wei, G. Epigallocatechin Gallate Destabilizes α-Synuclein Fibril by Disrupting the E46–K80 Salt-Bridge and Inter-protofibril Interface. *ACS Chem. Neurosci.* **2020**, *11*, 4351–4361.

[26] Jokar, S.; Khazaei, S.; Behnammanesh, H.; Shamloo, A.; Erfani, M.; Beiki, D.; Bavi, O. Recent Advances in the Design and Applications of Amyloid-β Peptide Aggregation Inhibitors for Alzheimer's Disease Therapy. *Biophys. Rev.* **2019**, *11*, 901–925.

[27] Mo, Y.; Lei, J.; Sun, Y.; Zhang, Q.; Wei, G. Conformational Ensemble of hIAPP Dimer: Insight into the Molecular Mechanism by which a Green Tea Extract Inhibits hIAPP Aggregation. *Sci. Rep.* **2016**, *6*, 1–11.

[28] Xu, Z.-X.; Ma, G.-L.; Zhang, Q.; Chen, C.-H.; He, Y.-M.; Xu, L.-H.; Zhou, G.-R.; Li, Z.-H.; Yang, H.-J.; Zhou, P. Inhibitory Mechanism of Epigallocatechin Gallate on Fibrillation and Aggregation of Amidated Human Islet Amyloid Polypeptide. *ChemPhysChem* **2017**, *18*, 1611–1619.

[29] Wang, Q.; Guo, J.; Jiao, P.; Liu, H.; Yao, X. Exploring the Influence of EGCG on the β-Sheet-Rich Oligomers of Human Islet Amyloid Polypeptide (hIAPP1–37) and Identifying Its Possible Binding Sites from Molecular Dynamics Simulation. *PLoS One* **2014**, *9*, 1–12.

[30] Smith, A. A.; Moore, K. B. E.; Ambs, P. M.; Saraswati, A. P.; Fortin, J. S. Recent Advances in the Discovery of Therapeutics to Curtail Islet Amyloid Polypeptide Aggregation for Type 2 Diabetes Treatment. *Adv. Bio.* **2022**, *6*, 2101301.

[31] Franko, A.; Rodriguez Camargo, D. C.; Böddrich, A.; Garg, D.; Rodriguez Camargo, A.; Rathkolb, B.; Janik, D.; Aichler, M.; Feuchtinger, A.; Neff, F., et al. Epigallocatechin Gallate (EGCG) Reduces the Intensity of Pancreatic Amyloid Fibrils in Human Islet Amyloid Polypeptide (hIAPP) Transgenic Mice. *Sci. Rep.* **2018**, *8*, 1–12.

[32] Dhouafli, Z.; Cuanalo-Contreras, K.; Hayouni, E. A.; Mays, C. E.; Soto, C.; Moreno-Gonzalez, I. Inhibition of Protein Misfolding and Aggregation by Natural Phenolic Compounds. *Cell. Mol. Life Sci.* **2018**, *75*, 3521–3538.

[33] Wang, Q.; Zhou, S.; Wei, W.; Yao, X.; Liu, H.; Hu, Z. Computational Insights into the Inhibition and Destabilization of Morin on the Oligomer of Full-length Human Islet Amyloid Polypeptide. *Phys. Chem. Chem. Phys.* **2015**, *17*, 29103–29112.

[34] Aitken, J. F.; Loomes, K. M.; Riba-Garcia, I.; Unwin, R. D.; Prijic, G.; Phillips, A. S.; Phillips, A. R.; Wu, D.; Poppitt, S. D.; Ding, K., et al. Rutin Suppresses Human-Amylin/hIAPP Misfolding and Oligomer Formation *in vitro*, and Ameliorates Diabetes

and its Impacts in Human-Amylin/hIAPP Transgenic Mice. *Biochem. Biophys. Res. Commun.* **2017**, *482*, 625–631.

[35] Ren, B.; Liu, Y.; Zhang, Y.; Cai, Y.; Gong, X.; Chang, Y.; Xu, L.; Zheng, J. Genistein: A Dual Inhibitor of Both Amyloid β and Human Islet Amylin Peptides. *ACS Chem. Neurosci.* **2018**, *9*, 1215–1224.

[36] Cheng, B.; Gong, H.; Li, X.; Sun, Y.; Zhang, X.; Chen, H.; Liu, X.; Zheng, L.; Huang, K. Silibinin Inhibits the Toxic Aggregation of Human Islet Amyloid Polypeptide. *Biochem. Biophys. Res. Commun.* **2012**, *419*, 495–499.

[37] García-Viñuales, S.; Ilie, I. M.; Santoro, A. M.; Romanucci, V.; Zarrelli, A.; Di Fabio, G.; Caflisch, A.; Milardi, D. Silybins Inhibit Human IAPP Amyloid Growth and Toxicity through Stereospecific Interactions. *Biochim. Biophys. Acta - Proteins Proteom.* **2022**, *1870*, 140772.

[38] Sparks, S.; Liu, G.; Robbins, K. J.; Lazo, N. D. Curcumin Modulates the Self-Assembly of the Islet Amyloid Polypeptide by Disassembling α-Helix. *Biochem. Biophys. Res. Commun.* **2012**, *422*, 551–555.

[39] Ghosh, P.; Bera, A.; Bhadury, P.; De, P. From Small Molecules to Synthesized Polymers: Potential Role in Combating Amyloidogenic Disorders. *ACS Chem. Neurosci.* **2021**, *12*, 1737–1748.

[40] Pithadia, A. S.; Bhunia, A.; Sribalan, R.; Padmini, V.; Fierke, C. A.; Ramamoorthy, A. Influence of a Curcumin Derivative on hIAPP Aggregation in the Absence and Presence of Lipid Membranes. *Chem. Commun.* **2016**, *52*, 942–945.

[41] Ma, L.; Yang, C.; Zheng, J.; Chen, Y.; Xiao, Y.; Huang, K. Non-polyphenolic natural inhibitors of amyloid aggregation. *Eur. J. Med. Chem.* **2020**, *192*, 112197.

[42] Pithadia, A.; Brender, J. R.; Fierke, C. A.; Ramamoorthy, A. Inhibition of IAPP Aggregation and Toxicity by Natural Products and Derivatives. *J. Diabetes Res.* **2016**, *2016*, 2046327.

[43] Lolicato, F.; Raudino, A.; Milardi, D.; La Rosa, C. Resveratrol Interferes with the Aggregation of Membrane-Bound Human-IAPP: A Molecular Dynamics Study. *Eur. J. Med. Chem.* **2015**, *92*, 876–881.

[44] Wang, Q.; Ning, L.; Niu, Y.; Liu, H.; Yao, X. Molecular Mechanism of the Inhibition and Remodeling of Human Islet Amyloid Polypeptide ($hIAPP_{1-37}$) Oligomer by Resveratrol from Molecular Dynamics Simulation. *J. Phys. Chem. B* **2015**, *119*, 15–24.

[45] Sciacca, M. F.; Chillemi, R.; Sciuto, S.; Greco, V.; Messineo, C.; Kotler, S. A.; Lee, D.-K.; Brender, J. R.; Ramamoorthy, A.; La Rosa, C., et al. A Blend of Two Resveratrol Derivatives Abolishes hIAPP Amyloid Growth and Membrane Damage. *Biochim. Biophys. Acta Biomembr.* **2018**, *1860*, 1793–1802.

[46] Zou, Y.; Qian, Z.; Sun, Y.; Wei, G.; Zhang, Q. Orcein-Related Small Molecule O4 Destabilizes hIAPP Protofibrils by Interacting Mostly with the Amyloidogenic Core Region. *J. Phys. Chem. B* **2017**, *121*, 9203–9212.

[47] Lao, Z.; Chen, Y.; Tang, Y.; Wei, G. Molecular Dynamics Simulations Reveal the Inhibitory Mechanism of Dopamine against Human Islet Amyloid Polypeptide (hIAPP) Aggregation and Its Destabilization Effect on hIAPP Protofibrils. *ACS Chem. Neurosci.* **2019**, *10*, 4151–4159.

[48] Ren, B.; Liu, Y.; Zhang, Y.; Zhang, M.; Sun, Y.; Liang, G.; Xu, J.; Zheng, J. Tanshinones Inhibit hIAPP Aggregation, Disaggregate Preformed hIAPP fibrils, and Protect Cultured Cells. *J. Mater. Chem. B* **2018**, *6*, 56–67.

[49] Wang, G.; Zhu, X.; Song, X.; Zhang, Q.; Qian, Z. Melatonin Inhibits hIAPP Oligomerization by Preventing β-Sheet and Hydrogen Bond Formation of the Amyloidogenic Region Revealed by Replica-Exchange Molecular Dynamics Simulation. *International Journal of Molecular Sciences* **2022**, *23*, 10264.

[50] Hagihara, M.; Takei, A.; Ishii, T.; Hayashi, F.; Kubota, K.; Wakamatsu, K.; Nameki, N. Inhibitory Effects of Choline-O-Sulfate on Amyloid Formation of Human Islet Amyloid Polypeptide. *FEBS Open Bio* **2012**, *2*, 20–25.

[51] Paul, S.; Paul, S. Molecular Dynamics Simulation Study on the Inhibitory Effects of Choline-O-Sulfate on hIAPP Protofibrilation. *J. Comput. Chem.* **2019**, *40*, 1957–1968.

[52] Tatarek-Nossol, M.; Yan, L.-M.; Schmauder, A.; Tenidis, K.; Westermark, G.; Kapurniotu, A. Inhibition of hIAPP Amyloid-Fibril Formation and Apoptotic Cell Death by a Designed hIAPP Amyloid- Core-Containing Hexapeptide. *Chem. Biol.* **2005**, *12*, 797–809.

[53] Kapurniotu, A.; Schmauder, A.; Tenidis, K. Structure-Based Design and Study of Non-Amyloidogenic, Double N-methylated IAPP Amyloid Core Sequences as Inhibitors of IAPP Amyloid Formation and Cytotoxicity. *J. Mol. Biol.* **2002**, *315*, 339–350.

[54] Yan, L.-M.; Tatarek-Nossol, M.; Velkova, A.; Kazantzis, A.; Kapurniotu, A. Design of a mimic of nonamyloidogenic and bioactive human islet amyloid polypeptide (IAPP) as nanomolar affinity inhibitor of IAPP cytotoxic fibrillogenesis. *Proc. Natl. Acad. Sci. U.S.A.* **2006**, *103*, 2046–2051.

[55] Gilead, S.; Gazit, E. Inhibition of Amyloid Fibril Formation by Peptide Analogues Modified with α-Aminoisobutyric Acid. *Angew. Chem.* **2004**, *43*, 4041–4044.

[56] Wang, H.; Abedini, A.; Ruzsicska, B.; Raleigh, D. P. Rationally Designed, Nontoxic, Nonamyloidogenic Analogues of Human Islet Amyloid Polypeptide with Improved Solubility. *Biochemistry* **2014**, *53*, 5876–5884.

[57] Andreetto, E.; Malideli, E.; Yan, L. M.; Kracklauer, M.; Farbiarz, K.; Tatarek-Nossol, M.; Rammes, G.; Prade, E.; Neumüller, T.; Caporale, A. et al. A Hot-Segment-Based Approach for the Design of Cross-Amyloid Interaction Surface Mimics as Inhibitors of Amyloid Self-Assembly. *Angew. Chem.* **2015**, *54*, 13095–13100.

[58] Wang, H.; Ridgway, Z.; Cao, P.; Ruzsicska, B.; Raleigh, D. P. Analysis of the Ability of Pramlintide To Inhibit Amyloid Formation by Human Islet Amyloid Polypeptide Reveals a Balance between Optimal Recognition and Reduced Amyloidogenicity. *Biochemistry* **2015**, *54*, 6704–6711.

[59] Figueroa, H.; Peddi, D.; Osborne, J. M.; Wilson, B. M.; Pesaru, R. R.; Kurva, B.; Ramaraju, S.; Milletti, M. C.; Heyl, D. L. Modeling the Interface between Islet Amyloid

Polypeptide and Insulin-Based Aggregation Inhibitors: Correlation to Aggregation Kinetics and Membrane Damage. *J. Chem. Inf. Model.* **2012**, *52*, 1298–1307.

[60] Paul, A.; Kalita, S.; Kalita, S.; Sukumar, P.; Mandal, B. Disaggregation of Amylin Aggregate by Novel Conformationally Restricted Aminobenzoic Acid containing α/β and α/γ Hybrid Peptidomimetics. *Sci. Rep.* **2017**, *7*, 40095.

[61] Ghosh, A.; Pithadia, A. S.; Bhat, J.; Bera, S.; Midya, A.; Fierke, C. A.; Ramamoorthy, A.; Bhunia, A. Self-Assembly of a Nine-Residue Amyloid-Forming Peptide Fragment of SARS Corona Virus E-Protein: Mechanism of Self Aggregation and Amyloid-Inhibition of hIAPP. *Biochemistry* **2015**, *54*, 2249–2261.

[62] Saini, R. K.; Goyal, D.; Goyal, B. Targeting Human Islet Amyloid Polypeptide Aggregation and Toxicity in Type 2 Diabetes: An Overview of Peptide-Based Inhibitors. *Chem. Res. in Toxicol.* **2020**, *33*, 2719–2738.

[63] Mishra, A.; Misra, A.; Sri Vaishnavi, T.; Thota, C.; Gupta, M.; Ramakumar, S.; Chauhan, V. S. Conformationally Restricted Short Peptides Inhibit Human Islet Amyloid Polypeptide (hIAPP) Fibrillization. *Chem. Commun.* **2013**, *49*, 2688–2690.

[64] Abedini, A.; Meng, F.; Raleigh, D. P. A Single-Point Mutation Converts the Highly Amyloidogenic Human Islet Amyloid Polypeptide into a Potent Fibrillization Inhibitor. *J. Am. Chem. Soc.* **2007**, *129*, 11300–11301.

[65] Bolarinwa, O.; Li, C.; Khadka, N.; Li, Q.; Wang, Y.; Pan, J.; Cai, J. γ-AApeptides–based Small Molecule Ligands That Disaggregate Human Islet Amyloid Polypeptide. *Sci. Rep.* **2020**, *10*, 95.

[66] Kaffy, J.; Berardet, C.; Mathieu, L.; Legrand, B.; Taverna, M.; Halgand, F.; Rest, G. V. D.; Maillard, L. T.; Ongeri, S. Helical γ-Peptide Foldamers as Dual Inhibitors of Amyloid-β Peptide and Islet Amyloid Polypeptide Oligomerization and Fibrillization. *Chem. Eur. J.* **2020**, *26*, 14612–14622.

[67] Liu, Z.; Robinson, J. T.; Sun, X.; Dai, H. PEGylated Nanographene Oxide for Delivery of Water-Insoluble Cancer Drugs. *J. Am. Chem. Soc.* **2008**, *130*, 10876–10877.

[68] Mo, Y.; Brahmachari, S.; Lei, J.; Gilead, S.; Tang, Y.; Gazit, E.; Wei, G. The Inhibitory Effect of Hydroxylated Carbon Nanotubes on the Aggregation of Human Islet Amyloid Polypeptide Revealed by a Combined Computational and Experimental Study. *ACS Chem. Neurosci.* **2018**, *9*, 2741–2752.

[69] Wang, M.; Sun, Y.; Cao, X.; Peng, G.; Javed, I.; Kakinen, A.; Davis, T. P.; Lin, S.; Liu, J.; Ding, F. et al. Graphene Quantum Dots against Human IAPP Aggregation and Toxicity *in vivo*. *Nanoscale* **2018**, *10*, 19995–20006.

[70] Bai, C.; Lin, D.; Mo, Y.; Lei, J.; Sun, Y.; Xie, L.; Yang, X.; Wei, G. Influence of Fullerenol on hIAPP Aggregation: Amyloid Inhibition and Mechanistic Aspects. *Phys. Chem. Chem. Phys.* **2019**, *21*, 4022–4031.

[71] Nedumpully-Govindan, P.; Gurzov, E. N.; Chen, P.; Pilkington, E. H.; Stanley, W. J.; Litwak, S. A.; Davis, T. P.; Ke, P. C.; Ding, F. Graphene Oxide Inhibits hIAPP Amyloid Fibrillation and Toxicity in Insulin-producing NIT-1 Cells. *Phys. Chem. Chem. Phys.* **2016**, *18*, 94–100.

[72] Bai, C.; Lao, Z.; Chen, Y.; Tang, Y.; Wei, G. Pristine and Hydroxylated Fullerenes Prevent the Aggregation of Human Islet Amyloid Polypeptide and Display Different Inhibitory Mechanisms. *Front. Chem.* **2020**, *8*, 51.

[73] Szunerits, S.; Abderrahmani, A.; Boukherroub, R. Nanoparticles and Nanocolloidal Carbon: Will They Be the Next Antidiabetic Class That Targets Fibrillation and Aggregation of Human Islet Amyloid Polypeptide in Type 2 Diabetes? *Acc. Chem. Res.* **2022**, *55*, 2869–2881.

[74] Guo, J.; Li, J.; Zhang, Y.; Jin, X.; Liu, H.; Yao, X. Exploring the Influence of Carbon Nanoparticles on the Formation of β-Sheet-Rich Oligomers of $IAPP_{22-28}$ Peptide by Molecular Dynamics Simulation. *PLoS One* **2013**, *8*, 1–10.

[75] Wang, L.; Zhu, S.; Lu, T.; Zhang, G.; Xu, J.; Song, Y.; Li, Y.; Wang, L.; Yang, B.; Li, F. The Effects of a Series of Carbon Dots on Fibrillation and Cytotoxicity of Human Islet Amyloid Polypeptide. *J. Mater. Chem. B* **2016**, *4*, 4913–4921.

[76] Gurzov, E. N.; Wang, B.; Pilkington, E. H.; Chen, P.; Kakinen, A.; Stanley, W. J.; Litwak, S. A.; Hanssen, E. G.; Davis, T. P.; Ding, F. et al. Inhibition of hIAPP Amyloid Aggregation and Pancreatic β-Cell Toxicity by OH-Terminated PAMAM Dendrimer. *Small* **2016**, *12*, 1615–1626.

[77] Fang, X.; Yousaf, M.; Huang, Q.; Yang, Y.; Wang, C. Dual Effect of PEG-PE Micelle over the Oligomerization and Fibrillation of Human Islet Amyloid Polypeptide. *Sci. Rep.* **2018**, *8*, 4463.

[78] Zhou, R.; Gao, H. Cytotoxicity of Graphene: Recent Advances and Future Perspective. *Wiley Interdiscip. Rev. Nanomed. Nanobiotechnol.* **2014**, *6*, 452–474.

[79] Ponder, J. W.; Case, D. A. *Protein Simulations*; Advances in Protein Chemistry; Academic Press, 2003; Vol. 66; pp 27–85.

[80] Jones, J. E.; Chapman, S. On the determination of molecular fields. —II. From the equation of state of a gas. *Proceedings of the Royal Society of London. Series A, Containing Papers of a Mathematical and Physical Character* **1924**, *106*, 463–477.

[81] J. D. van der Waals, *Verhandelingen der Koninklijke Akademie der Wetenschappen*, 1893,**1**, 1.

[82] C. A. Coulomb, *Collection de ṁemoires relatifs à la physique*, Gauthier-Villars, 1884, 569-638.

[83] Verlet, L. Computer "Experiments" on Classical Fluids. I. Thermodynamical Properties of Lennard-Jones Molecules. *Phys. Rev.* **1967**, *159*, 98–103.

[84] Hockney, R. W. POTENTIAL CALCULATION AND SOME APPLICATIONS. *Methods Comput. Phys. 9: 135-211(1970).*

[85] Swope, W. C.; Andersen, H. C.; Berens, P. H.; Wilson, K. R. A computer simulation method for the calculation of equilibrium constants for the formation of physical clusters of molecules: Application to small water clusters. *J. Chem. Phys* **1982**, *76*, 637–649.

[86] Joung, I. S.; Cheatham III, T. E. Determination of Alkali and Halide Monovalent Ion Parameters for Use in Explicitly Solvated Biomolecular Simulations. *J. Phys. Chem. B* **2008**, *112*, 9020–9041.

[87] Martínez, L.; Andrade, R.; Birgin, E. G.; Martínez, J. M. PACKMOL: A Package for Building Initial Configurations for Molecular Dynamics Simulations. *J. Comput. Chem.* **2009**, *30*, 2157–2164.

[88] Case, D. A. Belfon, K. Ben-Shalom, I. Y. Brozell, S. R. Cerutti, D. S. Cheatham, III, T. E. Cruzeiro, V. W. D. Darden, T. A. Duke, R. E. Giambasu, G. et al. *AMBER 2020*. University of California, San Francisco, 2020.

[89] Maier, J. A.; Martinez, C.; Kasavajhala, K.; Wickstrom, L.; Hauser, K. E.; Simmerling, C. ff14SB: Improving the Accuracy of Protein Side Chain and Backbone Parameters from ff99SB. *J. Chem. Theory Comput.* **2015**, *11*, 3696–3713.

[90] Pastor, R. W.; Brooks, B. R.; Szabo, A. An Analysis of the Accuracy of Langevin and Molecular Dynamics Algorithms. *Mol. Phys.* **1988**, *65*, 1409–1419.

[91] Berendsen, H. J. C.; Postma, J. P. M.; van Gunsteren, W. F.; DiNola, A.; Haak, J. R. Molecular Dynamics with Coupling to an External Bath. *J. Chem. Phys.* **1984**, *81*, 3684–3690.

[92] Ryckaert, J-P.; Ciccotti, G.; Berendsen, H. J. C. Numerical Integration of the Cartesian Equations of Motion of a System with Constraints: Molecular Dynamics of n-Alkanes. *J. Comput. Phys* **1977**, 327–341.

[93] Essmann, U.; Perera, L.; Berkowitz, M. L.; Darden, T.; Lee, H.; Pedersen, L. G. A Smooth Particle Mesh Ewald Method. *J. Chem. Phys.* **1995**, *103*, 8577–8593.

[94] Roe, D. R.; Cheatham, T. E. PTRAJ and CPPTRAJ: Software for Processing and Analysis of Molecular Dynamics Trajectory Data. *J. Chem. Theory Comput.* **2013**, *9*, 3084–3095.

[95] Humphrey, W.; Dalke, A.; Schulten, K. VMD: Visual Molecular Dynamics. *J. Mol. Graph.* **1996**, *14*, 33–38.

[96] Kabsch, W.; Sander, C. Dictionary of Protein Secondary Structure: Pattern Recognition of Hydrogen-Bonded and Geometrical Features. *Biopolymers* **1983**, *22*, 2577–2637.

[97] Weiser, J.; Shenkin, P. S.; Still, W. C. Approximate Atomic Surfaces from Linear Combinations of Pairwise Overlaps (LCPO). *J. Comput. Chem.* **1999**, *20*, 217–230.

[98] Pal, S.; Roy, R.; Paul, S. Potential of a Natural Deep Eutectic Solvent, Glyceline, in the Thermal Stability of the Trp-Cage Mini-protein. *J. Phys. Chem. B* **2020**, *124*, 7598–7610.

[99] Ester, M.; Kriegel, H. P.; Sander, J.; Xu, X.; A Density-Based Algorithm for Discovering Clusters in Large Spatial Databases with Noise. In Proceedings of the Second International Conference on Knowledge Discovery and Data Mining, Oregon, USA, Simoudis, E., Han, J., Fayyad, U., Eds.; **1996**, 226-231.

[100] Ganguly, P.; Boserman, P.; van der Vegt, N. F. A.; Shea, J.-E. Trimethylamine N-oxide Counteracts Urea Denaturation by Inhibiting Protein–Urea Preferential Interaction. *J. Am. Chem. Soc.* **2017**, *140*, 483–492.

[101] Hou, T.; Wang, J.; Li, Y.; Wang, W. Assessing the Performance of the MM/PBSA and MM/GBSA Methods. 1. The Accuracy of Binding Free Energy Calculations Based on Molecular Dynamics Simulations. *J. Chem. Inf. Model.* **2010**, *51*, 69–82.

[102] Miller, B. R.; McGee, T. D.; Swails, J. M.; Homeyer, N.; Gohlke, H.; Roitberg, A. E. MMPBSA.py: An Efficient Program for End-State Free Energy Calculations. *J. Chem. Theory Comput.* **2012**, *8*, 3314–3321.

[103] Jayaram, B.; Sprous, D.; Beveridge, D. L. Solvation Free Energy of Biomacromolecules: Parameters for a Modified Generalized Born Model Consistent with the AMBER Force Field. *J. Phys. Chem. B* **1998**, *102*, 9571–9576.

[104] Sanner, M. F.; Olson, A. J.; Spehner, J.-C. Reduced surface: An efficient way to compute molecular surfaces. *Biopolymers* **1996**, *38*, 305–320.

Chapter 2

Disclosing the Conformational Transition of hIAPP$_{20-29}$ Dimers via Markov State Modeling

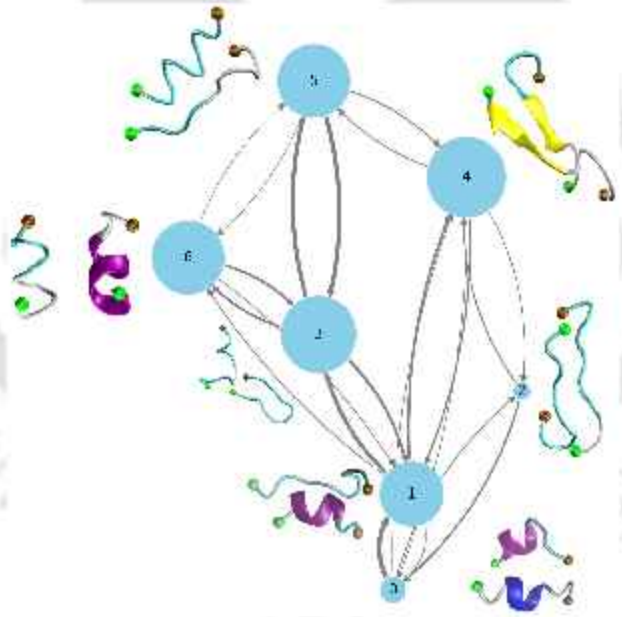

"The complexity of the protein molecule appears to furnish, when viewed in terms of atomic forces, a sufficiently intricate, detailed pattern to make understandable the precise specificity of protein reaction."

– Warren Weaver

Overview

Amyloid deposits of human islet amyloid polypeptide (hIAPP) are found in 90% of individuals suffering from Type II Diabetes (T2D). The disordered hIAPP monomers misfold into on-pathway oligomers, which finally results in amyloid fibrils. The early-stage oligomers formed during the process of hIAPP aggregation process are reportedly more cytotoxic than their mature fibril counterparts. The precise structural rearrangement that govern the initial stages of hIAPP aggregation continue to elude experimental consensus. To limit the worldwide spread of T2D, drugs targeting hIAPP aggregates are being currently developed. However, for this, adequate knowledge of the conformational change of hIAPP during its aggregation is necessary. Hence, in this chapter, the initial aggregation pathway of an amyloid core fragment of hIAPP, $hIAPP_{20-29}$ is investigated. Via Markov State Models, it is found that an assembly of conformers, ranging from random coils and turns to α-helix and β-sheet populate the structures of $hIAPP_{20-29}$ dimer. On analyzing the diverse pathways of structural reconfiguration from random coils to antiparallel β-sheets, the importance of α-helices and turn conformation is detected. Hydrophobic interactions emerge as the driving force during the transition between states. This study reveals the subtle interplay between molecular forces that orchestrate the aggregation of hIAPP and thus contribute to the attempt to decode the origins of molecular mechanism of hIAPP aggregation.

2.1 Introduction

Like most IDPs, hIAPP, under physiological conditions, lacks a stable, well-defined conformation and possesses a high propensity to misfold into soluble on-pathway oligomers, which further arranges into insoluble amyloid fibrils with a cross-β sheet structure[1]. The possible therapeutic strategies to control T2D include prevention of these early on-pathway oligomer formation[2]. Therefore, it is crucial to characterize these oligomeric intermediates and the nucleation dynamics leading to amyloid aggregates to understand the cytotoxicity mechanism, which will aid in drug design against T2D.

The hIAPP monomer is primarily, a random coil structure with a small portion of α-helical and β-hairpin conformation[1, 3–5]. Previous experimental studies of kinetics of hIAPP aggregation displayed that hIAPP monomers forms β-sheet rich oligomers via transient helical intermediates[6]. The α-helical structures are also suggested to be on-pathway intermediate during aggregation by circular dichroic spectroscopy[7]. Chiral sum frequency also showed the transitions from α-helix to β-sheet for membrane-bound hIAPP[8]. On the other hand, reports also suggest that replacing helical intermediates with non-helical analogs assisted hIAPP aggregation[9]. Prevention of helical folding amplified the cytotoxicity and membrane perturbation[10]. Hence the definitive role of helical intermediates is ambiguous. However, the β-hairpin structure is reported to be the amyloidogenic precursor[3].

Even though molecular dynamics simulations yield time-resolved trajectories, information regarding the kinetics of conformational transitions is challenging to obtain through them, unless the whole configurational space is thoroughly explored. This is again difficult for the simulation of IDPs, due to their transient nature. Markov State Models (MSMs) can be helpful, in this regard[11, 12]. Short MD simulations starting from a myriad of conformations can be assembled together and the configuration space is dicretized into states. The thermodynamics and the kinetics informations of the transition between conformation, as well as the detailed transition pathways can be obtained from the models. Hence, it is very useful to gain knowledge of the molecular mechanism involved during the conformational transitions. MSM has been used previously to study the aggregation dynamics of $A\beta_{16-22}$ dimers and tetramers[5, 13]. The helix to sheet transition of $A\beta_{42}$ is also analyzed by MSMs[14, 15]. Moreover, the aggregation of PHF6 and the conformational transition

of R3 fragment have also been studied[16, 17].

MSM of the dimerization of $hIAPP_{11-25}$ reported that hydrophobic interactions contribute to the initial collapse of the separate monomers to form anti-parallel cross-β state[18]. The amyloidogenic core of hIAPP consists of the sequence, $S^{20}NNFGAILSS^{29}$. This core region can form β-sheet aggregates in isolation *in vivo* and is related to the onset of T2D. Further, it also consists of $F^{23}GAIL^{27}$ residues, which is the shortest pentapeptide sequence to form amyloid fibrils individually[19]. Therefore, in this chapter, we investigate the conformational change of $S^{20}NNFGAILSS^{29}$ dimer via Markov State Modelling. The dimerization is the first step towards oligomerization, and therefore, it will be possible to shed light on the early oligomerization of hIAPP. $hIAPP_{20-29}$ dimers are simulated using replica-exchange molecular dynamics and the MSM is constructed to reveal that the anti-parallel extended-β conformation is the most populated state. The transition from random coils to β structure can occur via many pathways, most of which involve formation of transient helical and turn structures. The in-detail intra and inter-chain contacts are also calculated to interpret the structural transitions. This will help to elucidate the residues which are crucial for the amyloid aggregation of hIAPP.

The in-detail methods employed to carry out the simulations and MSMs are mentioned in the Simulation Methods section. The Results section reports the outcome of the analyses, while the final concluding remarks are presented in the Conclusions section.

2.2 Simulation Methods

In this study, we have investigated the different conformational states of an amyloid prone region of hIAPP, consisting of the residues $S^{20}NNFGAILSS^{29}$ and the transition between these states. At first, we performed replica exchange molecular dynamics (REMD) of $hIAPP_{20-29}$ dimer and then we analyzed the simulations using Markov State Models (MSMs) to study the kinetics of the peptide dimer.

2.2.1 REMD Simulations

The coordinates of $hIAPP_{20-29}$ were extracted from the solid state NMR model[20]. The terminal ends were capped to eliminate the influence of the terminal charges. Initially, the peptide fragment extracted from the NMR model was simulated at 500 K to remove any

bad contacts. Two chains of $hIAPP_{20-29}$ obtained above was placed in an octahedral box, at a distance of 15 Å. The minimum distance between the solute and water box wall was 10 Å. Ultimately the system was simulated at 300 K and 1 atm pressure in NPT ensemble for 50 ns. The resultant structure is finally used for REMD simulations.

305	307.57	310.16	312.77	315.4	318.04	320.7
323.37	326.06	328.77	331.5	334.25	337.01	339.77
342.57	345.39	348.22	351.08	353.95	356.85	359.76
362.69	365.63	368.6	371.59	374.59	377.62	380.67
383.73	386.82	389.92	393.11	396.25	399.42	402.64
405.85	409.08	412.33	415.6	418.89	422.21	425

Table 2.1: *List of Temperatures (K) used for REMD simulations.*

42 replicas were prepared at a temperature range of 305–425K (Table 2.1), using Ref. [21]. The exchange rate between the replicas was around 25.8%. Each of the replicas was energy minimized, which was followed by 1 ns of conventional MD with no replica exchange in order to heat each replica to the target temperature. After that, each replica was simulated for 200 ns, where exchanges were performed for every 1000 steps. The molecular dynamics simulations were carried out in AMBER20 package[22], following protocols mentioned in Chapter 1 (Section 1.5.2).

2.2.2 Construction and Validation of Markov State Models

Markov state model (MSM) is a kinetic network model which can investigate multiple short molecular dynamics simulations to predict the conformational dynamics of biomolecules, measure the dynamic pathways, and predict the kinetic and thermodynamic properties[23, 24]. MSM helps to identify relevant conformational states and also the transition rates between key conformational states. In MSM, the conformational phase space is partitioned into many discrete states, such that each metastable state consists of conformations with similar structural and dynamic properties. Thus the transition within states is fast, but between them is slow. Based on these properties, MSM has been successfully applied to investigate the conformational changes in proteins that cannot be directly accessed

by conventional MD simulations such as protein folding and aggregation[25–27]. The only requirement for securing accurate knowledge about protein dynamics is that the constructed model has to be Markovian. The transition process is considered to be Markovian if the transition probability depends only on the current state and not on the previous state (that is, it is memory-less). In MSM, the dynamics of system can be described by the following equation:

$$P(n\tau) = [T(\tau)]^n P(0) \tag{2.1}$$

where P(nτ) is the vector of state populations at time nτ, T is the transition probability matrix, and τ is the lag time of the model.

At first, selecting the proper discretization feature to capture the process of interest is necessary. The variational approach for Markov processes (VAMP)[28] is applied to compare the ability of certain features to capture slow dynamical modes in a particular molecular system. The feature with the highest VAMP-2 score was chosen among a series of features relevant to protein structure. Then, in order to project the high dimensional space to low dimensional latent space, dimensionality reduction was carried out using time-lagged independent component analysis (TICA)[29], which resulted in 2 independent components (ICs), at a lag time of 0.4 ns. After that, clustering in the TICA space was performed to identify points that are similar to each other via k-means clustering method[30]. After clustering, the trajectories are dicretized and then the approximate lag time to construct MSM was determined by calculating the implied timescales (ITs) by the following equation:

$$t_i = -\frac{\tau}{\ln \lambda_i(\tau)} \tag{2.2}$$

where λ_i ith eigenvalue of the transition probability matrix T with lag time τ. Choosing the appropriate lag time is essential to construct a proper MSM. Each IT scale represents the average transition time between two subsets of states. To this end, the implied time scale was plotted with respect to different τ values (Fig 2.7), and the lag time at which the IT values plateaus out, i.e., no change of IT is observed, is considered for MSM. This also assumes the Markovianity of the model.

Further, the Chapman-Kolmogorov (C-K) test[30] was also carried out to check the validity of the model. The C-K test measures the similarity between the transition

probability obtained by simulation trajectory (indicated by "predict" in Fig 2.8) and that generated by MSM (indicated by "estimate" in Fig 2.8), using the equation,

$$T(k\tau) = T^k(\tau) \tag{2.3}$$

where T(τ) is the transition probability matrix (obtained from MSM) at lag time τ and k is an integer larger than 1. Subsequently, coarse graining of the MSMs was done to gain meaningful insight of the models, where, the corresponding microstates were grouped into macrostates at the determined lag time. The Robust Perror-cluster cluster Analysis (PCCA+)[31] method was used for this. All the above analysis were carried out using PyEMMA package 2.5.7[32].

2.2.3 Analysis Protocols

In order to gain insight into the different transition pathways between the macrostates, transition path theory (TPT)[33] was utilized to ascertain the transition paths and fluxes. A contact between the peptide residue pair was taken into account if any heavy atom of one residue was within a distance of 4 Å from the other residue[34]. The transition pathway was calculated using PyEMMA package 2.5.7[32]. Visual Molecular Dynamics (VMD)[35], was used for visualization and hydrogen bond analysis. CPPTRAJ toolkit of AMBER20[36] package was utilized for carrying out the remaining analyses. The simulation analyses were carried out following the protocols discussed in Chapter 1 (Section 1.5.3).

2.3 Results and Discussions

2.3.1 MSM Analysis

The first step to obtain an accurate MSM is to select a suitable feature which can capture the slow dynamics of the molecular process. A number of features are selected to capture our process of interest, which are backbone (BB_torsion) and side chain (SC_torsion) torsion angles, inter- (Inter_BB_distance) and intra- (Intra_BB_distance) molecular distance between the backbone atoms and the positions of backbone (BB_position) and Cα atoms (Ca_position) (Fig 2.1). From the VAMP2 score, we observe that, for our system, the backbone torsion contain much more kinetic variance (highest VAMP2 score) compared to

the other features. Hence, we have considered this as our feature for further analysis.

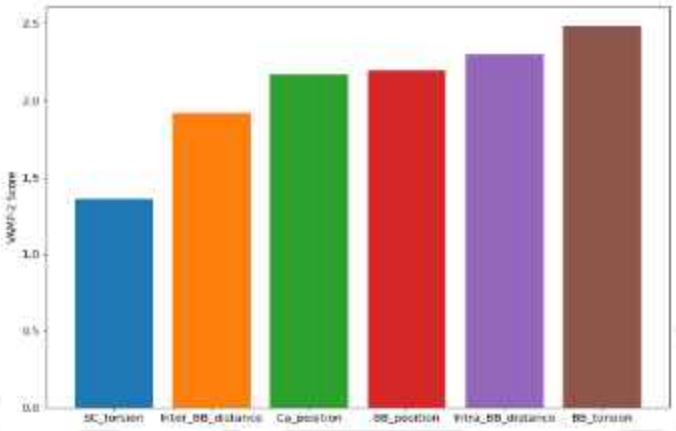

Figure 2.1: *VAMP-2 score of the six different selection features.*

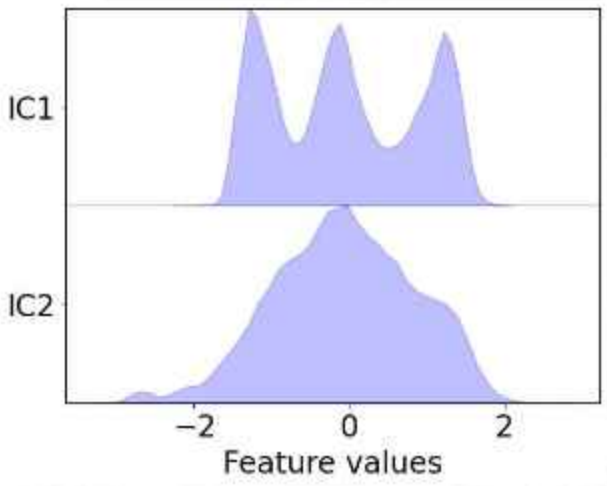

Figure 2.2: *The marginal distributions of structures on the two ICs.*

Then TICA is performed to reduce the feature space into 2 ICs at a lag time of 0.4 ns and it can be seen that IC1 is clearly able to resolve the metastable states (Fig 2.2). The sample density projected on the 2 ICs are presented in Fig 2.3, where multiple densely sampled states are observed, which indicate the presence of metastable states. The existence of multiple basins indicates that the dimer goes through a number of states in the event of aggregation. Also discrete jumps in ICs (especially in IC1) is noticed at specific time in the trajectory, which correlate to rare events or sudden transition from one state to another

(Fig 2.4).

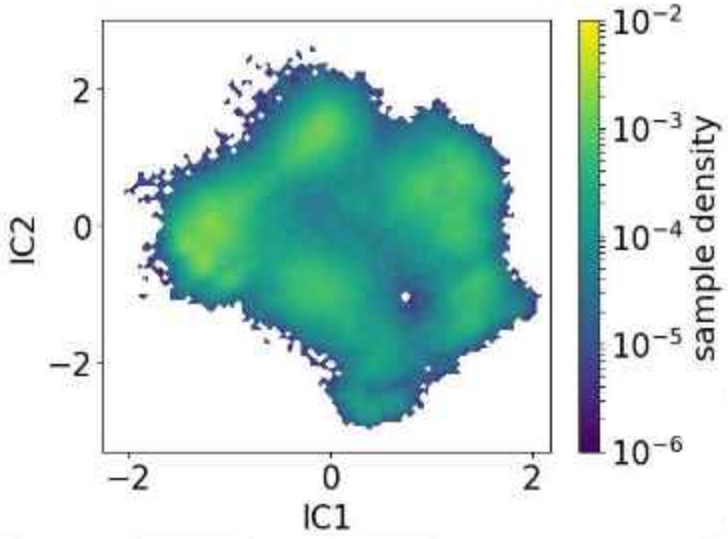

Figure 2.3: *Sample densities in the TICA space along IC1 and IC2.*

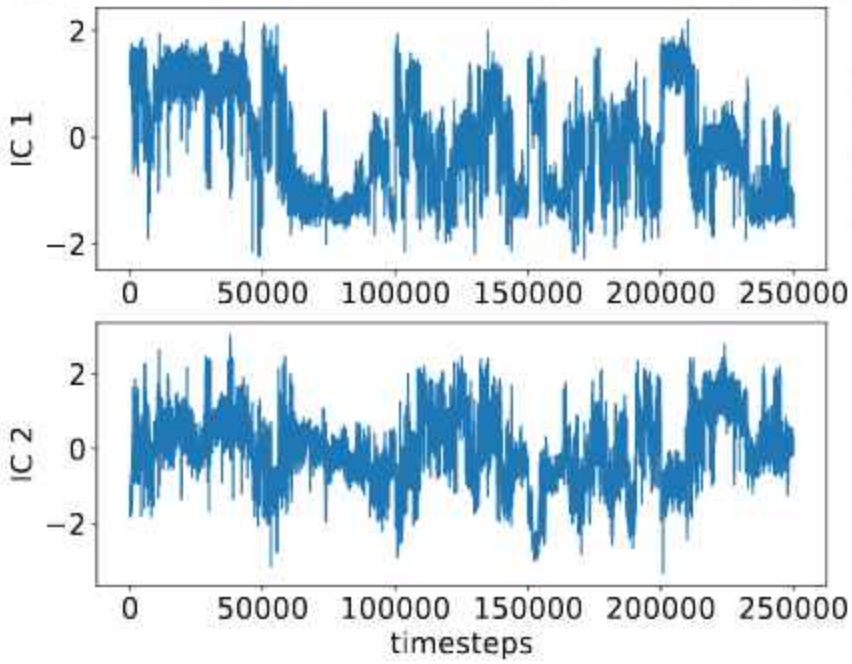

Figure 2.4: *Time evolution of IC1 and IC2.*

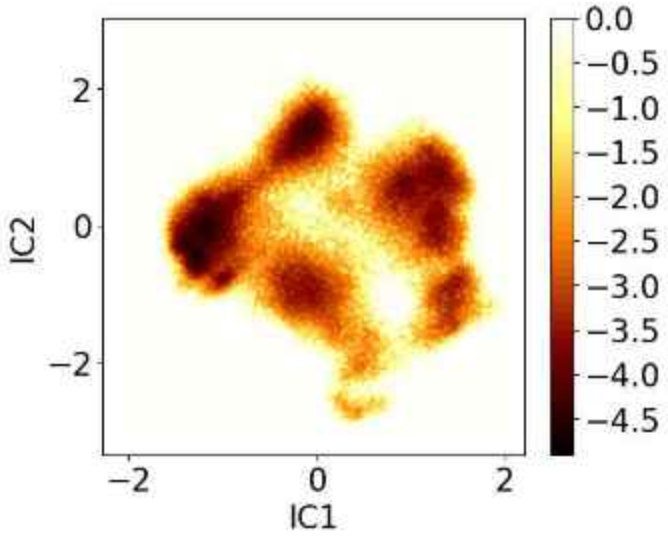

Figure 2.5: *Free energy landscape for the peptides constructed in the TICA space.*

The free energy landscape (Fig 5.6) provides an idea of the conformational phase space with respect to the 2 ICs, which is plotted following the equation,

$$\Delta G_i = -k_B T \left[\ln P_i - \ln P_{\max}\right] \tag{2.4}$$

where the number of occurrences in state 'i' corresponding to a pair of ICs is given by P_i and the maximum number of occurrences is P_{max}. Comparing with Fig 2.3, it is observed that the densely sampled states correspond to the lower energy basins. The energy minima are separated by barriers, which require significant amount of energy to cross.

After dimensionality reduction, k-means clustering is carried out to generate 500 cluster points (Fig 2.6). These clusters are seen to be mostly distributed in the energy basins than the low sampled regions, which indicates that each basin can be considered to be an assembly of closely related structures. The distribution of the cluster points helps in the discretization of the trajectories, which is further used to construct MSM. For this, choosing the correct lag time is important. From the plot of ITS versus τ (Fig 2.7), we observe that, after initial increase, IT becomes independent of τ at almost τ=50 time steps (i.e., 0.2 ns). Hence we calculate MSM at a lag time of 0.2 ns. In order to obtain a coarse-grained representation of the conformational dynamics, the 500 microstates, are lumped

together to 7 macrostates, which is used to generate the MSM.

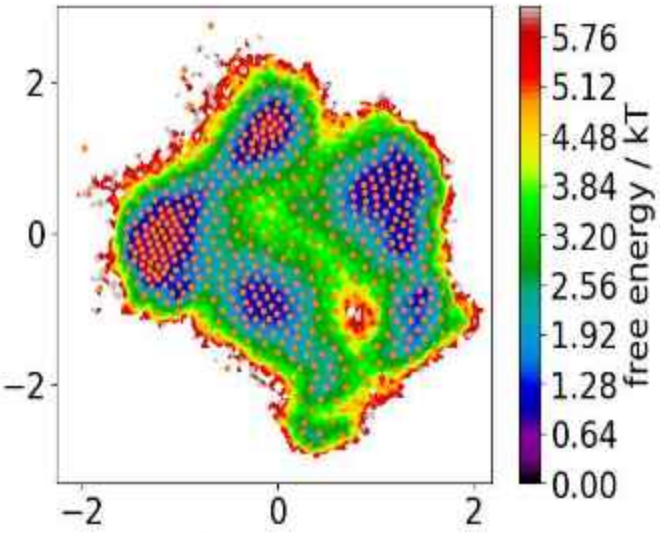

Figure 2.6: *Distribution of the cluster points on the free energy landscape.*

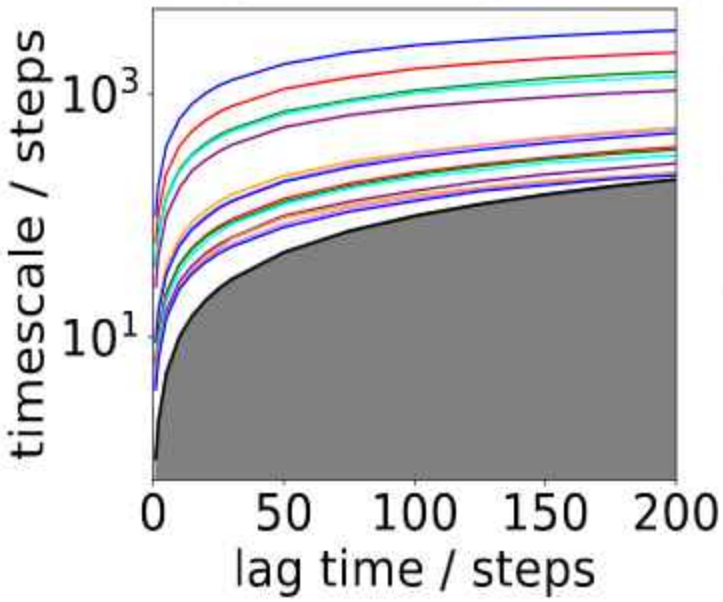

Figure 2.7: *Implied timescales as a function of lag time.*

The validity of the obtained model is confirmed by the C-K test, where it is seen that the predicted probability matches well with the estimated probability in most of the metastable

states (Fig 2.8).

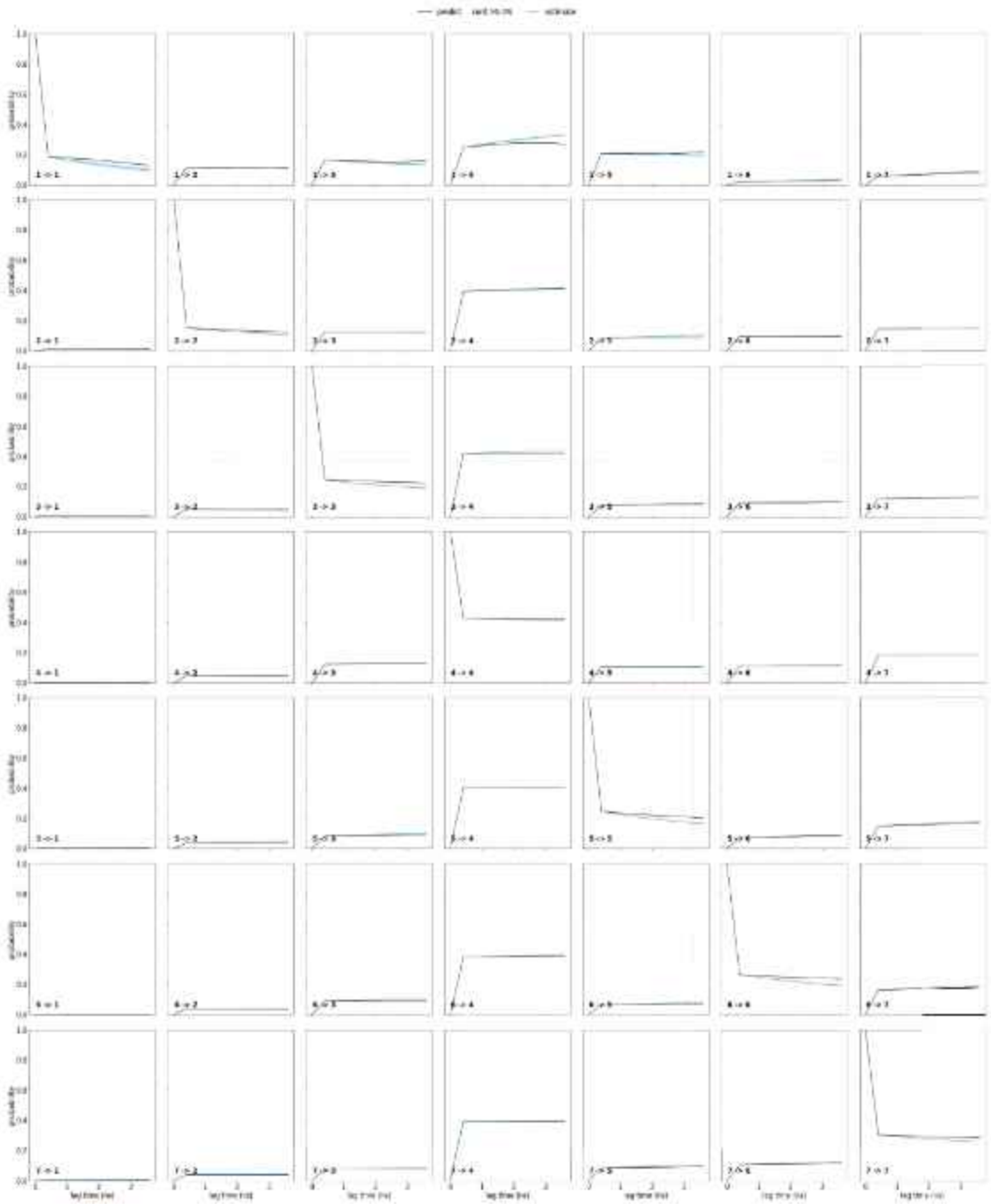

Figure 2.8: *Chapman-Kolmogorov test for model validation.*

Based on the generated MSM model, all the conformations were partitioned into 7 macrostates (Fig 2.9). To represent the conformation of each macrostate, 1000 confor-

mations are generated. The transition between each pair of macrostate can be visualized as a network diagram, as shown in Fig 2.10. The area of each node signifies their stationary probability, and the arrows indicate the transition between states, with their thickness proportional to the transition probability. The macrostates consists of folded and unfolded structures, ranging from random coils, to helices as well as β-sheet conformers. State 0 represents a 3_{10} and α-helix, States 1, 3, and 5 consists of some α-helices and mostly random coil, while State 4 consists of an extended β-sheet and State 6 has two α-helices.

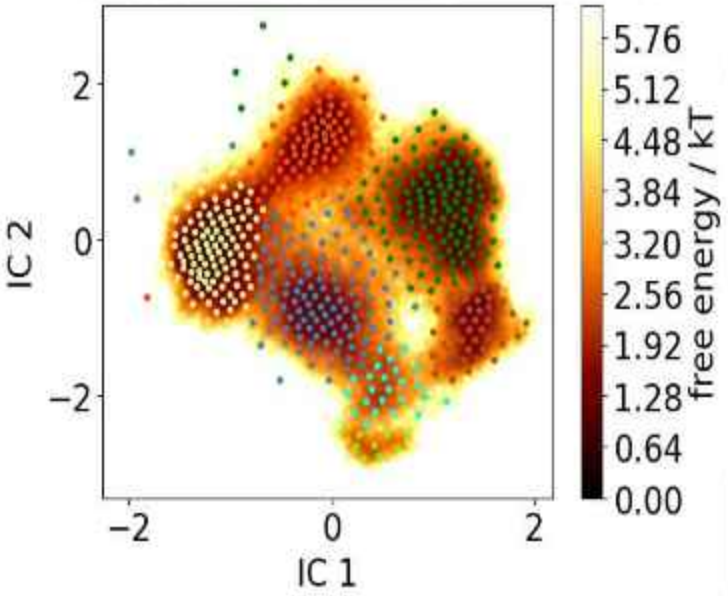

Figure 2.9: *The distribution of the 7 macrostates onto the the ICs, with each state coloured.*

State 2 consists mostly of coiled structures. State 4, which consists of the extended β-sheet conformation, has the highest stationary probability (22.9%). The α-helix structure in State 6 has a probability of 19%. States 1, 3, and 5, which primarily consists of coil and turn structures, display 14.8%, 20.8% and 19.0% probability respectively. The lowest probability is seen for States 0 (2.3%) and 2 (0.96%).

2.3.2 Secondary Structure of the Macrostates

The grouping of the microstates into macrostates is based on kinetic rates between the microstates. Hence the structures with different secondary structure conformation may

possibly belong to the same state. Therefore, it is necessary to calculate the propensity of secondary structure contents of each macrostate to determine the most probable secondary structures attained by each peptide chain (Fig 2.11). The highest probability of extended-β (above 0.08) is observed in State 4, (which is also observed in the snapshot in Fig 2.10) with a much lesser probability in State 2 (nearly 0.04). Similar observation is noticed for bridged-β conformation. High α-helix content is observed in both chains in State 6 (> 0.2), while in States 0 and 5, one of the chains exists as α-helix. In State 0, the other chain forms a 3_{10} helix, which displays the maximum percentage (0.16), among all the other states.

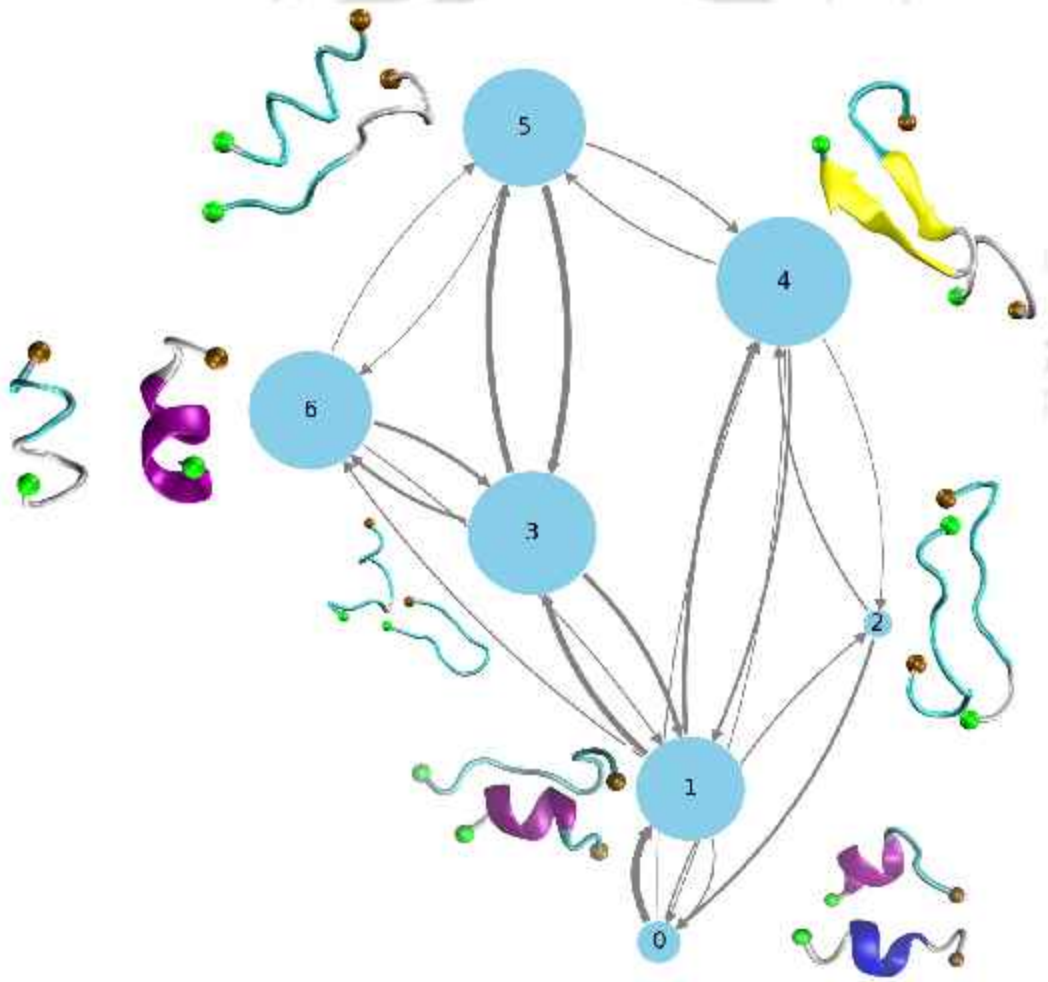

Figure 2.10: *Transition Network between the macrostates of hIAPP$_{20-29}$ dimer. β-sheet is depicted β-sheet in yellow, coil in white, turn in cyan, α-helix in purple and 3_{10}-helix in blue. The ochre and green balls at the end of the chains indicate the N- and C-terminal respectively.*

The States 1 and 3 exhibit a low propensity of α-helix (0.1), and the chains mostly exists as turns and random coils. The random coil percentage is highest among the secondary structures in all states, which justifies the disordered nature of hIAPP. The coil probability is above 0.5 in both chains in State 2, 3 and 4, while States 1, 5 and 6, at least, one of the chains have considerably high coil content. High propensity of turns are also observed in States 0, 1, 5 and 6, which can be visualized in the snapshots (Fig 2.10).

Next, the residue wise secondary structure contents in each macrostate is calculated to determine the change in the contribution of each residue towards a particular secondary structure, especially during transitions between states. The maximum β-sheet percentage, which is observed in State 4 and some in State 2, depict that residues F23-S28 forms an extended anti-parallel β-sheet (Fig 2.12).

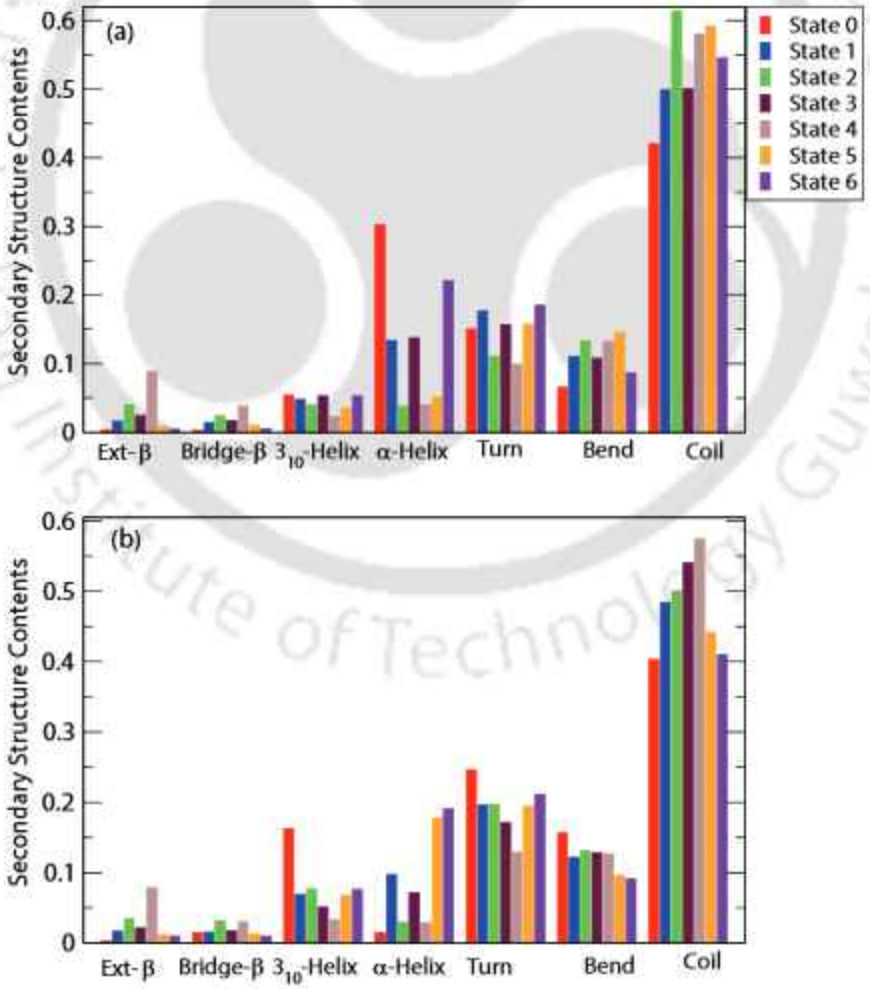

Figure 2.11: *Secondary Structure Contents of (a) chain-1 and (a) chain-2 of $hIAPP_{20-29}$.*

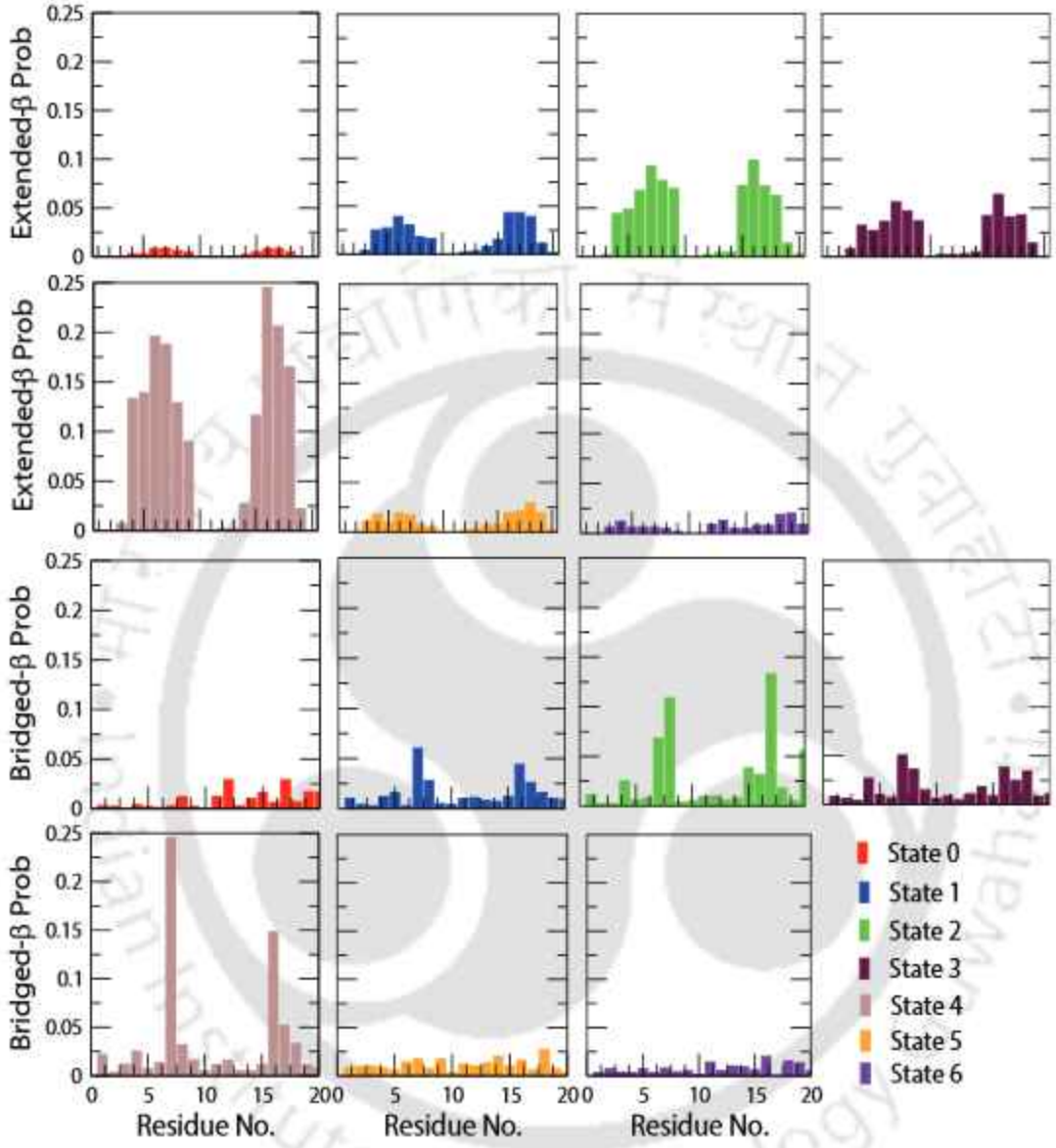

Figure 2.12: *Probability of Extended-β and Bridged-β contents of each residue of* $hIAPP_{20-29}$.

Previous reports suggests that these residues are highly β-sheet-prone and contribute to the oligomerization of hIAPP[37, 38]. The rat IAPP, which is not amyloidogenic in nature, has turn-prone prolines at positions 25 and 28, instead of Ala and Ser respectively in hIAPP. Other residues which do not match with hIAPP are F23L and I26V. Out of the 6 residues, which differ in the sequence between hIAPP and rIAPP, 4 of them exists in the positions 23-28, which consequently depicts a high β-sheet forming tendency in hIAPP. This further

rationalizes the contribution of these residues towards amyloid aggregation of hIAPP.

The helix conformation, in hIAPP, is mostly maintained by the N-terminal region. In this peptide fragment, N22-S28 adopts an α-helix conformation (Fig 2.13). The two α-helices adopted by the peptide chains are clearly seen in State 6.

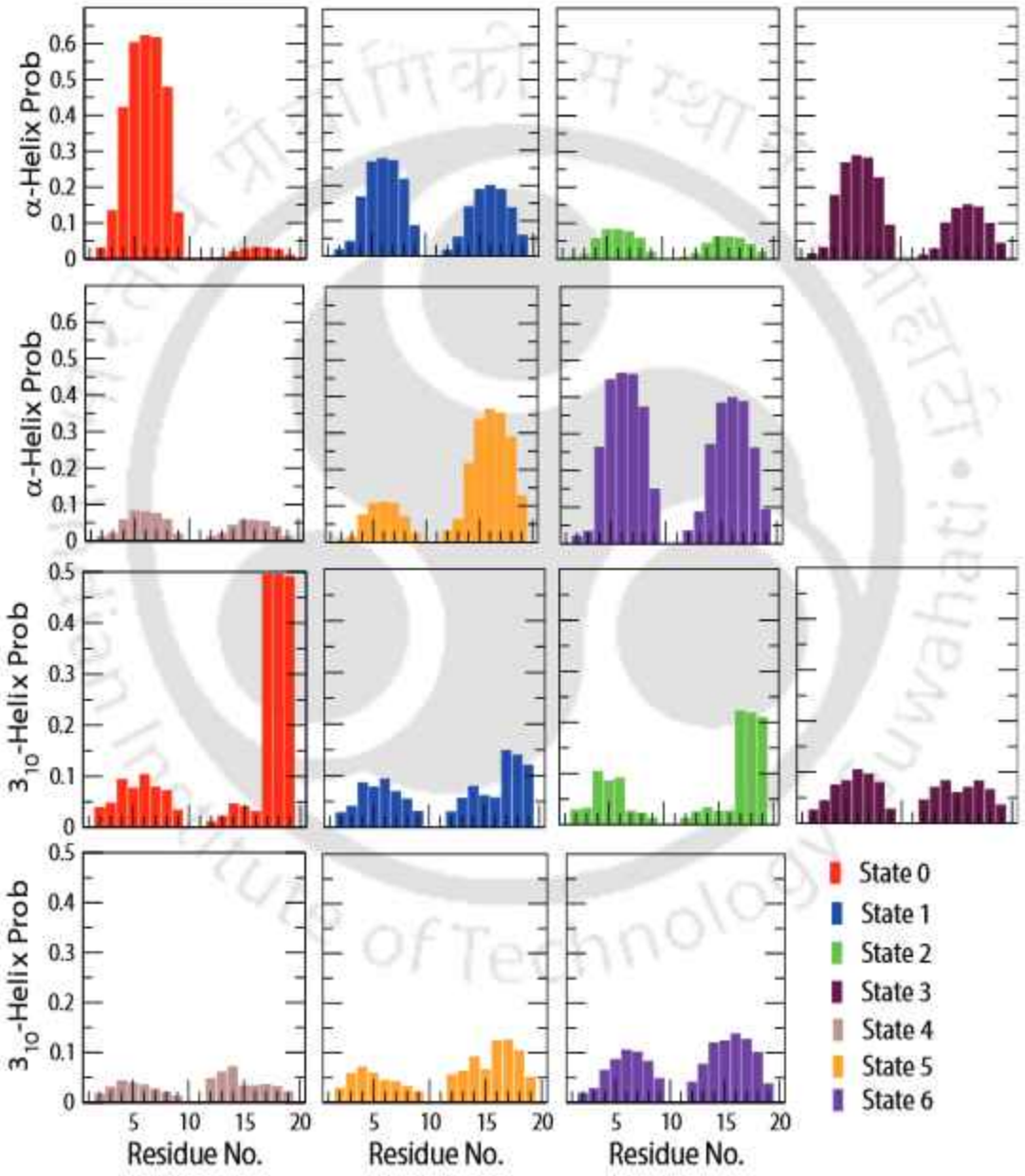

Figure 2.13: *Probability of α-helix and 3_{10}-helix contents of each residue of $hIAPP_{20-29}$.*

In State 0, the first peptide chain attains an α-helix, while the second chain exists as

3_{10} helix, formed by the residues A25-L27. State 5 also projects an α-helix in one chain, while partial helices are also observed in States 1 and 3. The terminal ends depict a high propensity to exist as random coils, while the turn propensity is mostly conserved in core residues (Fig 2.14).

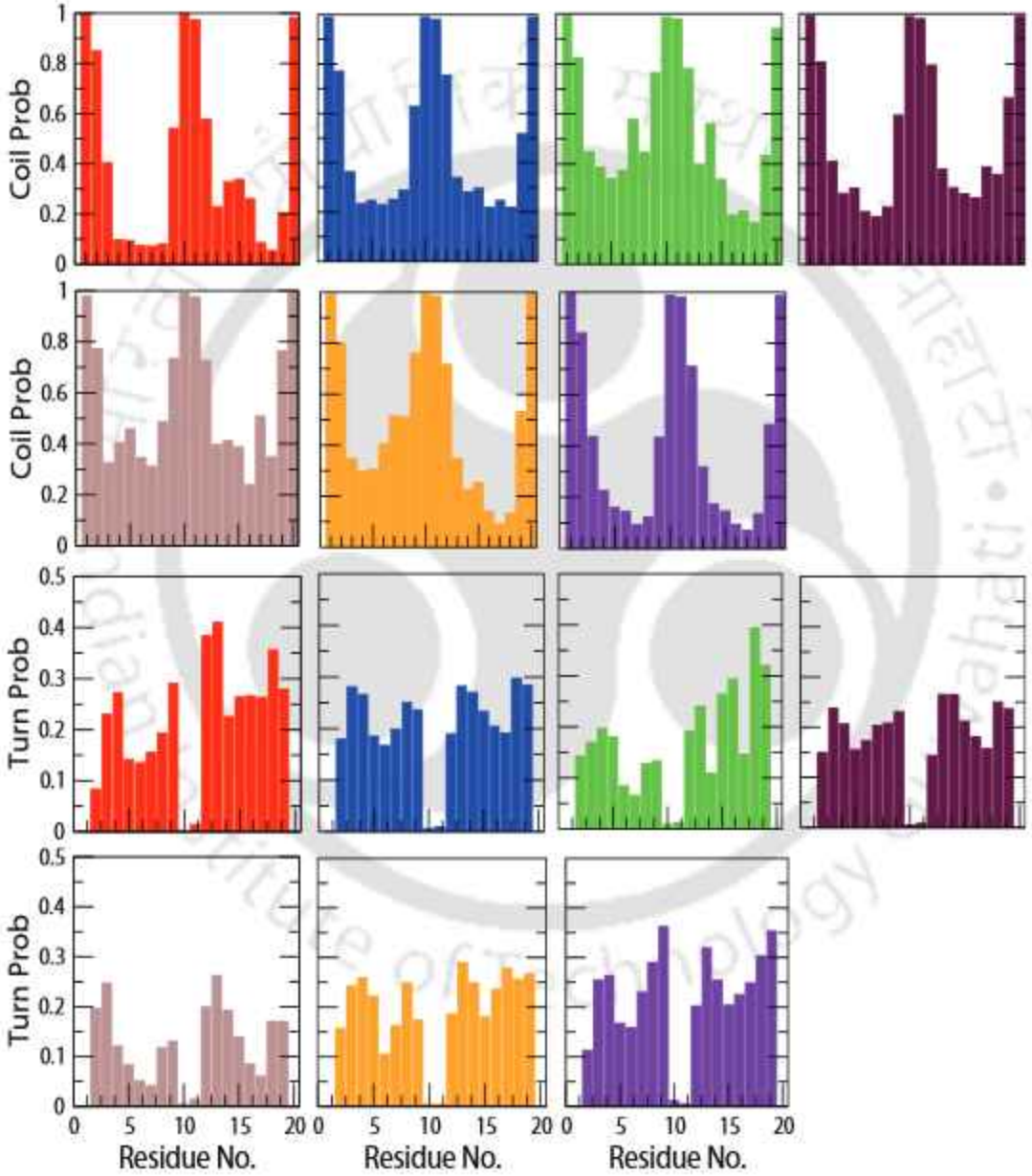

Figure 2.14: *Probability of Coil and Turn contents of each residue of* $hIAPP_{20-29}$.

The compactness of each of the peptide chains are determined by the radius of gyration (R_g) values (Fig 2.15). The extended β-sheet conformation in State 4 have the

highest R_g, followed by State 2. Chain-1 in State 5 form random coil, while Chain-2 an α-helix, hence the former have higher R_g compared to the latter. Similar R_g trend is also observed for States 1 and 3. States 0 and 6 majorly possess helix structures and hence display the lowest R_g values. This further supports the secondary structure conformations proposed in each macrostate.

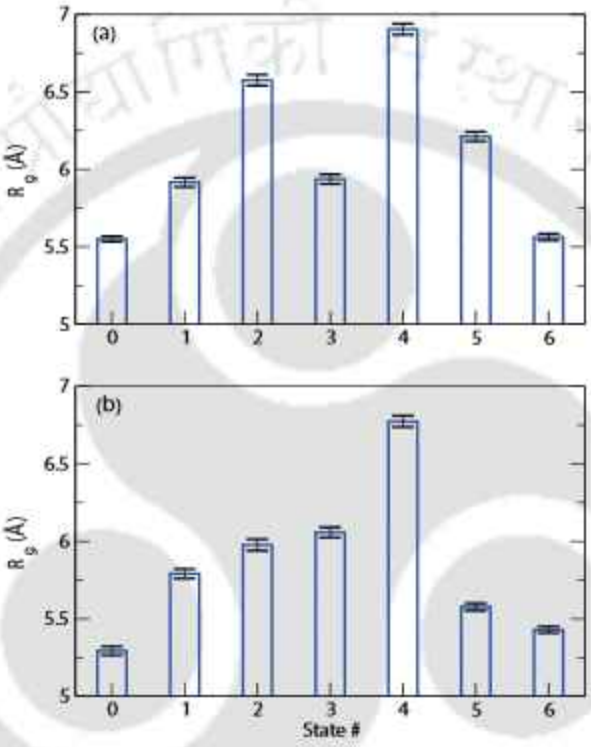

Figure 2.15: *R_g of each chain of $hIAPP_{20-29}$.*

2.3.3 Interstate Transition Analysis

The transition of random coil conformation into β-sheet rich aggregates is the main feature of the amyloid formation of hIAPP. The exact mechanism via which this transition takes place is still under study, since the soluble on-pathway oligomers are very difficult to isolate *in vivo*. Previous simulation reports proposed a variety of pathways of dimerization of hIAPP, involving disordered structures, α-helices and β-hairpins[6]. The investigation of these on-pathway metastable aggregates is crucial for the inhibition of hIAPP aggregation. Therefore, to explore this avenue, transition pathway analysis is carried out using TPT theory. For this, the initial and target states between which the pathway has to be explored

needs to be decided. States 0, 5, 6 project dominant helical conformation, while the stationary probability of State 2 is very low.

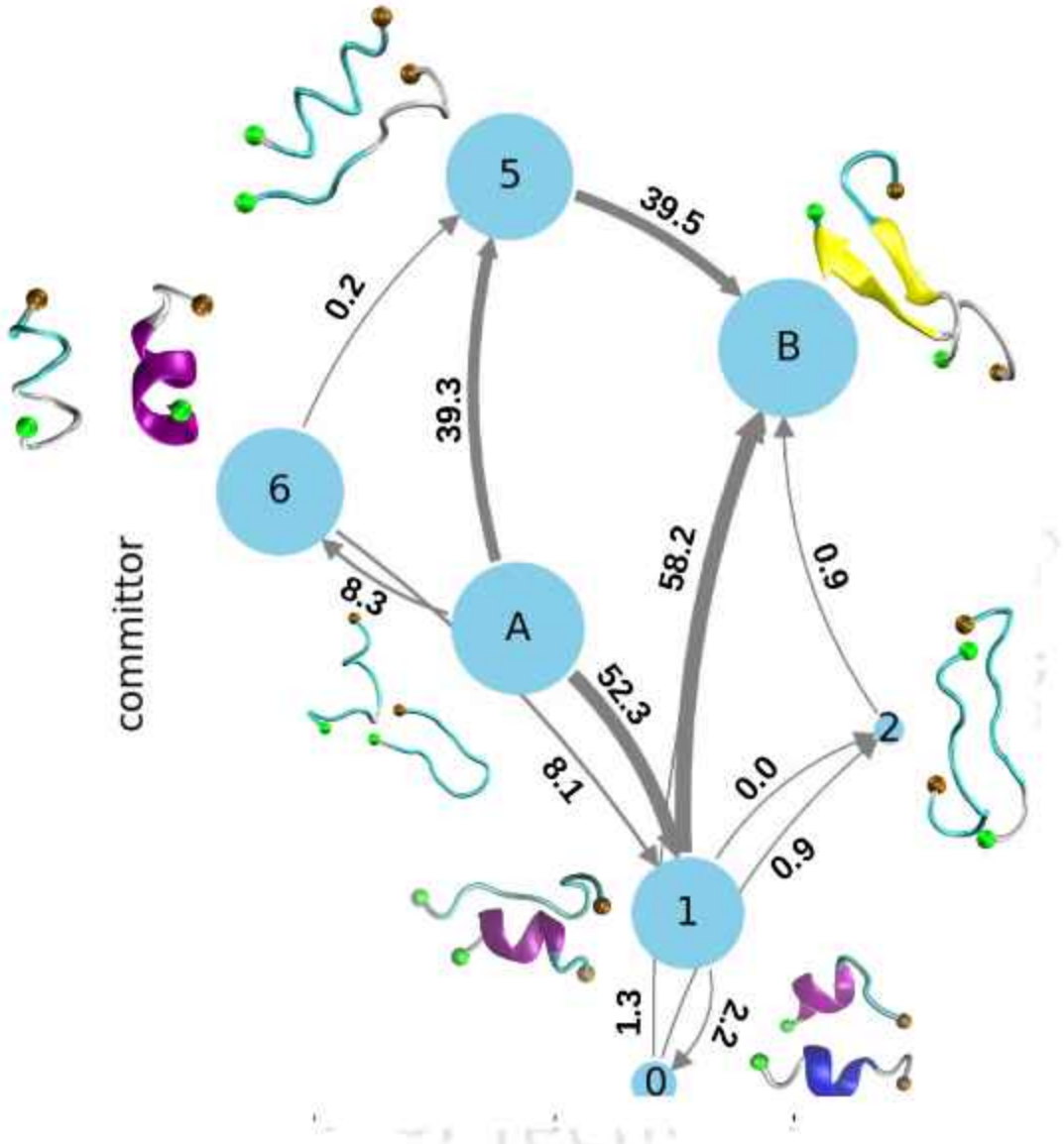

Figure 2.16: *The different pathways of transition from State 3 (A) to State 4 (B) of $hIAPP_{20-29}$ dimer. The numbers indicate the transition probability between each state.*

For this, the initial and target states between which the pathway has to be explored needs to be decided. States 0, 5, 6 project dominant helical conformation, while the stationary probability of State 2 is very low. Between States 1 and 3 (both of which consists of coils

and partial helices), the latter one has a higher coil content and lower helical contents, and also has lower stationary probability. Hence State 3 is selected as the initial state. State 4 adopts an extended-β conformation and is chosen as the target state.

The top three probable pathways are shown in Fig 2.16. In the first pathway, the disordered coils in State 3 rearranges into mostly turn conformation with short α-helices (State 1) to ultimately form a β-sheet in State 4. The next pathway involves a transition into State 5, where one chain forms an α-helix, while the other depicts a mixture of coil and turn. The helix content in State 5 is much higher than that in State 1, where mostly coil and turn content is observed. In addition, both the chains posses a small amount of helix percentage in State 1, while only one chain exists as helix in State 5. In the last pathway, the initial coils in State 3 forms two α-helices (State 6), which gets slightly destabilized to form turn conformers with two partial helix in State 1, to finally form a β-sheet in State 4. These pathways suggest that the disordered conformers passes through α-helix and turn structures to form an aggregation-prone β-sheet. Also State 1 is a hub in the network, via which most pathways undergo.

2.3.4 Contact maps and Hydrogen Bonds

To identify the structural changes during the transitions, the key interactions between the residues are investigated. A closer look into the residue wise secondary structure changes shows that the overall helicity in the hIAPP chains increases as we go from from State 3 to State 1, alongwith with an increase in turns (Fig 2.11, 2.13 and 2.14). This ultimately results in β-sheets in State 4. This change is more pronounced in chain-2, compared to that of chain-1. A previous study proposed that the formation of turn structure, prior to β-sheets, is necessary[17], corroborating with our results. The intra and inter chain contacts are calculated. From the contact probability maps (Fig 2.17, 2.18 and 2.19), we observe that in State 3, contacts between F23-I26, F23-L27, G24-I26, A25-A25, A25-I26, I26-A25, I26-I26, L27-F23 residues are present between the two chains (Fig 2.19). Hardly any intra chain contacts are noticed in this state (Fig 2.17 and 2.18). These contacts are destabilized in State 1, where inter chain contacts between F23-L27, A25-A25, A25-I26, I26-A25, I26-I26, L27-F23 residues are witnessed (Fig 2.19). These interactions assist the residues to adjust their configuration, such that they are able to attain β-sheet in the subsequent step. The contact frequency in this state is comparatively lower than that in

State 3. The contacts between N22-S28, F23-F23, F23-S28, F23-S29, I26-G24, especially, exhibit noticeable drop during this transition (Fig 2.19).

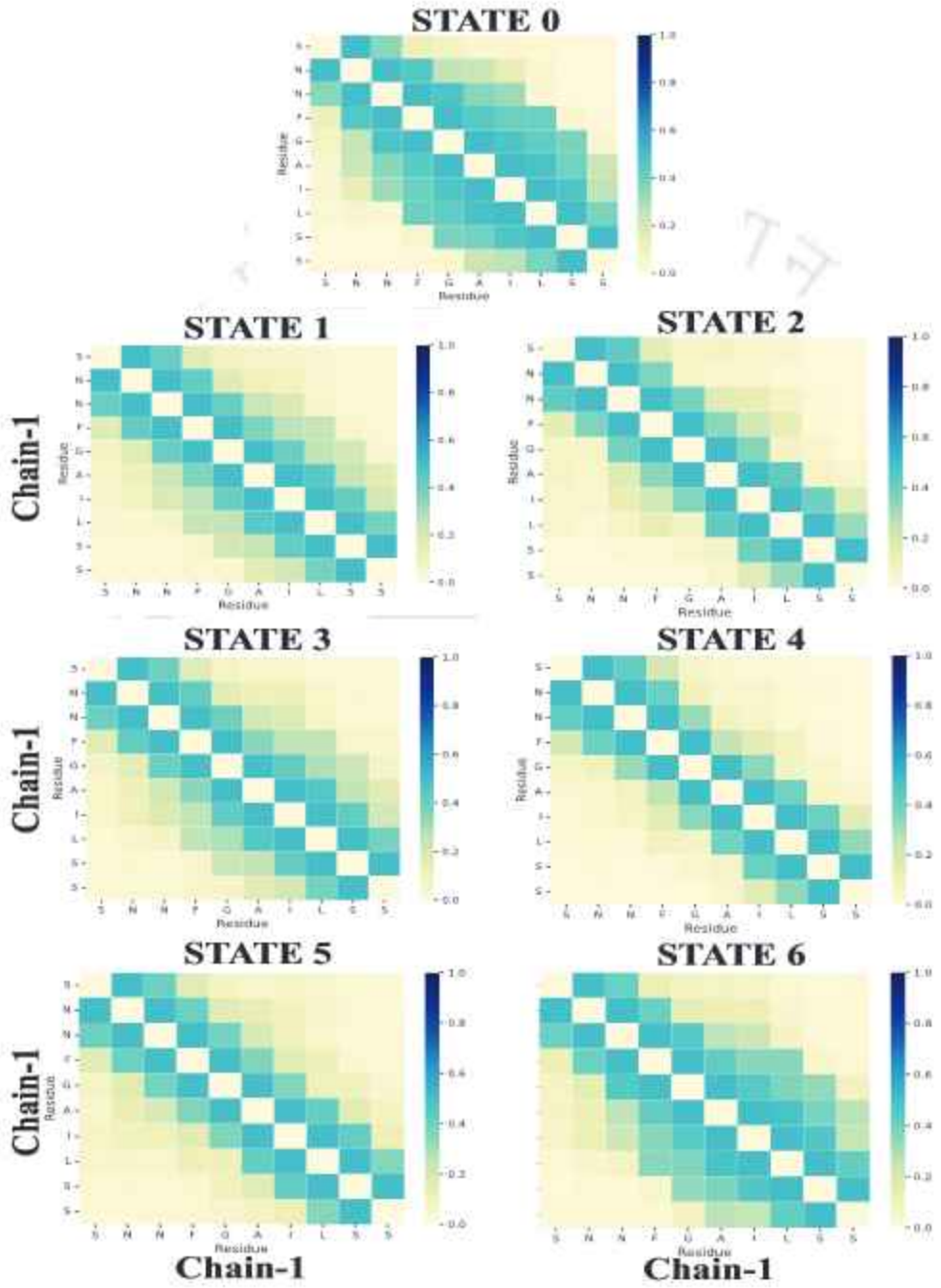

Figure 2.17: *Intra-chain contacts among chain-1 of hIAPP*$_{20-29}$.

The secondary structure contents of both the initial state (State 3) and State 1 are almost

similar, even though inter-chain contacts in them differ. State 4, which forms the anti-parallel β-sheet, depicts maximum interchain contact frequency (Fig 2.19).

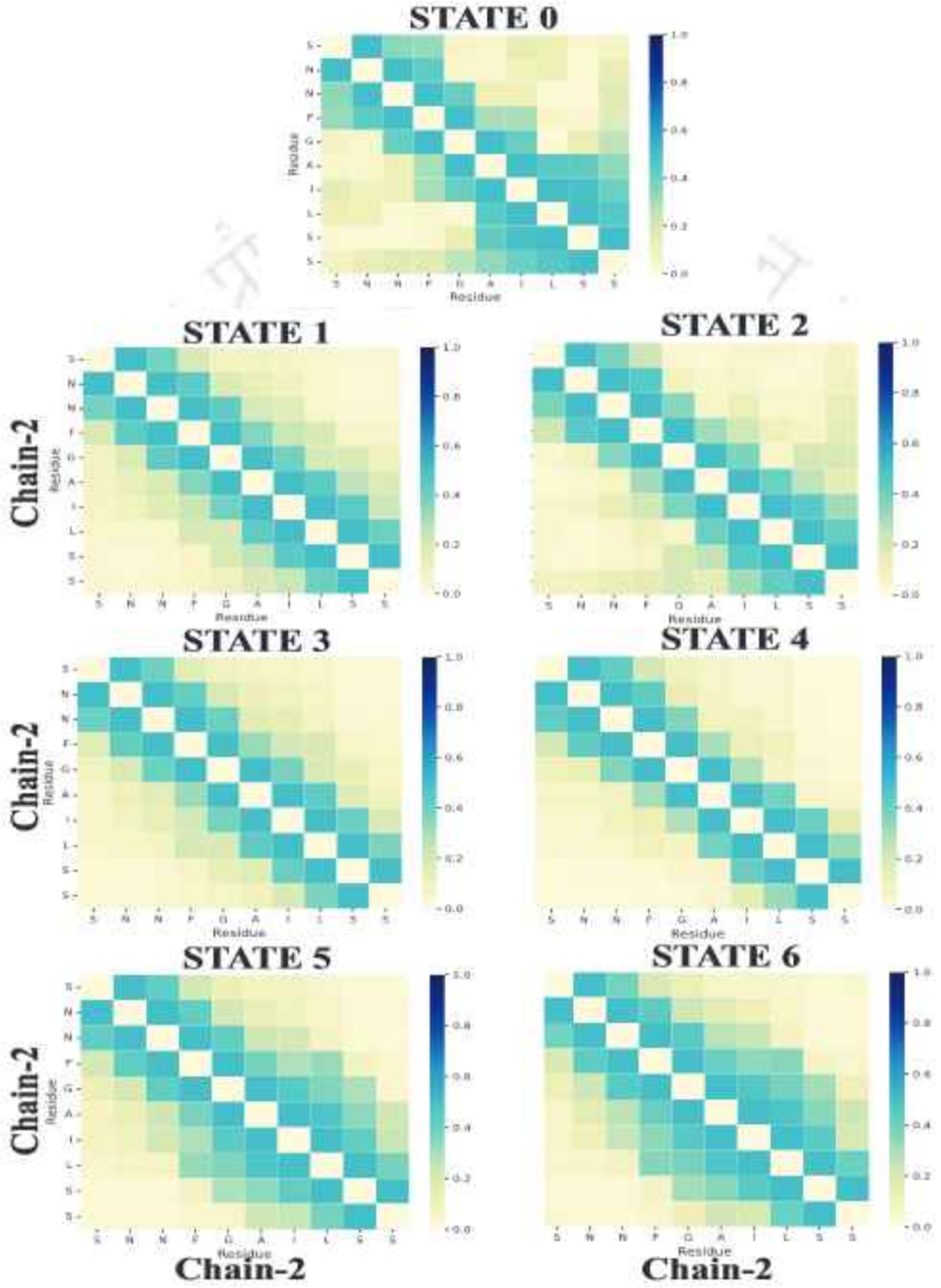

Figure 2.18: *Intra-chain contacts among chain-2 of hIAPP$_{20-29}$.*

The interactions between N22-S28, F23-I26, F23-L27, F23-S28, G24-I26, G24-L27, A25-

A25, A25-I26, I26-F23, I26-G24, I26-A25, I26-I26, L27-F23, L27-G24, S28-N22, S28-F23 stabilize the β-sheet conformation in this state. Here, the contribution of G24, A25, I26 residues towards the inter-chain contacts is dominant.

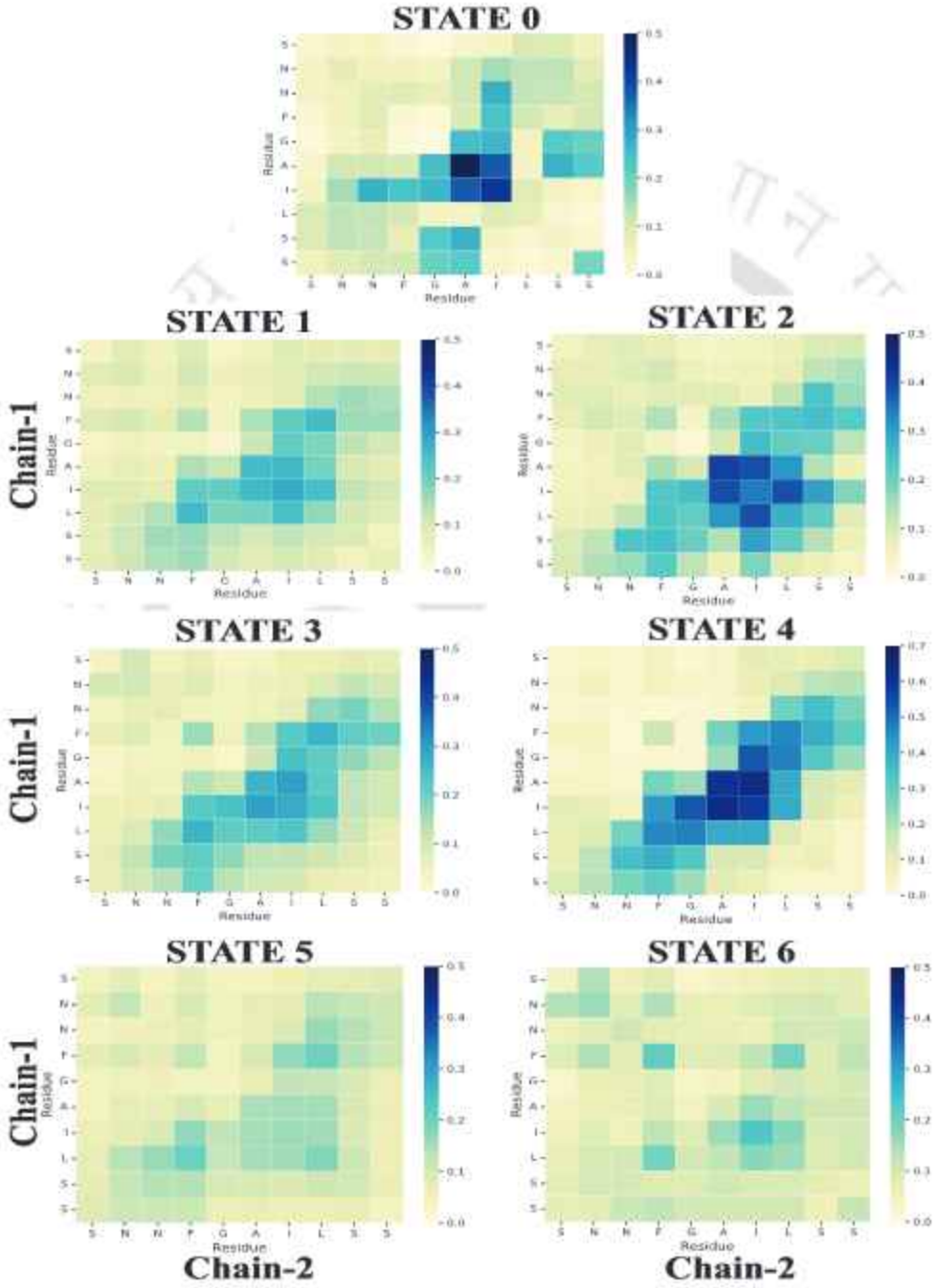

Figure 2.19: *Inter-chain contacts between the $hIAPP_{20-29}$ dimer.*

Therefore, in this pathway, the inter-chain interactions, which exist in the dimer in the initial state (State 3) collapses in the intermediate state (State 1), where a higher helical and turn content is observed compared to the earlier state. Then the residues again come together to form anti-parallel interactions to generate an extended-β conformation.

Similar secondary structure changes is also observed in the next pathway (State 3–5–4). However, the increase in the helicity and turn regions from the initial to the intermediate state in this pathway is higher compared to the previous pathway (Fig 2.11, 2.13 and 2.14). A deeper dive into the interactions shows that, the intra-chain contacts increase in chain-2, especially between F23-S28, in going from State 3 to 5 (Fig 2.19). This is due to the formation of a stable α-helix in this state. Also very few inter-chain contacts are maintained in State 5 from that in State 3. This further suggests that the interactions in State 3 are completely destabilized to form the anti-parallel β-sheet structure in State 4.

In the last pathway, it is seen that transition follows the states, 3–6–1–4. Hence the random coils in State 3 forms 2 α-helices in State 6, which then partially breaks in State 1 to ultimately form extended-β in State 4. The difference in this pathway from the first, is the involvement of the intermediate, State 6, in going from State 3 to 1. The inter-chain contacts in State 3 are completely destabilized in State 6, where only F23-F23, F23-L27, I26-I26, L27-F23 interactions are seen (Fig 2.19). These inter-chain contacts are revived in State 1, with most contacts finally appearing in State 4. Here again, chain-2 forms considerable intra-chain contact in State 6, due to the formation of α-helix (Fig 2.11 and 2.13).

State	**Inter**		**Inter**
	Chain-1	**Chain-2**	
0	4128	2964	913
1	3062	3096	803
2	1953	2728	1591
3	3132	2723	976
4	1713	1897	2488
5	2346	3667	567
6	3905	3790	542

Table 2.2: *Number of intra- and inter-chain hydrogen bonds formed between the* $hIAPP_{20-29}$ *dimer.*

The hydrophobic residues in the core, F23-L27 are primarily involved in the intra- and inter-chain contacts. Therefore the hydrophobic contribution affect the change in the interactions during transitions. The hydrophilic residues present at the terminals, S19-N22 and S28-S29, also show changes in their hydrogen bonding pattern. Due to the presence of helical content in States 1, 3, 5 and 6, intra-chain hydrogen bonds are observed (Table 2.2). Maximum inter-chain hydrogen bonds are observed in State 4, due to the formation of extended β-sheet. The contribution of hydrogen bonds towards the peptide aggregation is much lower, therefore, hydrophobic interactions are primarily responsible for the transitions between the states.

2.4 Conclusions

In this chapter, the conformational transitions involved during the dimerization of $hIAPP_{20-29}$ is studied via extensive all-atom molecular dynamics simulations. Markov State Models are constructed to analyze the trajectories, where it is displayed that the conformational space is dicretized into 7 macrostates. Among them, the most populated state represents that the dimer exists as an anti-parallel extended-β structure. This β-sheet is formed by the interactions between F23-S28 residues, which reportedly play a crucial role in the amyloid aggregation of full-length hIAPP. The anti-parallel β-sheet conformer is probably an on-pathway conformer leading to fibrillation. The other states are populated by random coils, turns and helical structures. Multiple pathways for the transition of random coils to amyloid prone β-sheet are explored, where it is revealed that,in most pathways, the intermediates form transient α-helical and turn structures. The importance of turns before the formation of β-conformers has also been declared earlier. The rearrangement of hydrophobic interactions between the core hydrophobic residues, F23-L27, influence the transitions between the states, even though substantial hydrogen bonds are also observed. This study helps to shed light on the molecular mechanisms involved during the dimerization of this peptide fragment. $hIAPP_{20-29}$ forms the amyloidogenic core of full-length hIAPP and is said to mimic its property to form amyloid aggregation. Hence, this investigation might also help to understand the aggregation dynamics of full-length hIAPP, which will assist in T2D therapy.

References

[1] Reddy, A. S.; Wang, L.; Singh, S.; Ling, Y. L.; Buchanan, L.; Zanni, M. T.; Skinner, J. L.; de Pablo, J. J. Stable and Metastable States of Human Amylin in Solution. *Biophys. J.* **2010**, *99*, 2208–2216.

[2] Berhanu, W. M.; Masunov, A. E. Full Length Amylin Oligomer Aggregation: Insights from Molecular Dynamics Simulations and Implications for Design of Aggregation Inhibitors. *J. Biomol. Struct. Dyn.* **2014**, *32*, 1651–1669.

[3] Dupuis, N. F.; Wu, C.; Shea, J.-E.; Bowers, M. T. Human Islet Amyloid Polypeptide Monomers Form Ordered β-hairpins: A Possible Direct Amyloidogenic Precursor. *J. Am. Chem. Soc.* **2009**, *131*, 18283–18292.

[4] Qiao, Q.; Bowman, G. R.; Huang, X. Dynamics of an Intrinsically Disordered Protein Reveal Metastable Conformations That Potentially Seed Aggregation. *J. Am. Chem. Soc.* **2013**, *135*, 16092–16101.

[5] Illig, A.-M.; Strodel, B. Performance of Markov State Models and Transition Networks on Characterizing Amyloid Aggregation Pathways from MD Data. *J. Chem. Theory Comput.* **2020**, *16*, 7825–7839.

[6] Milardi, D.; Gazit, E.; Radford, S. E.; Xu, Y.; Gallardo, R. U.; Caflisch, A.; Westermark, G. T.; Westermark, P.; Rosa, C. L.; Ramamoorthy, A. Proteostasis of Islet Amyloid Polypeptide: A Molecular Perspective of Risk Factors and Protective Strategies for Type II Diabetes. *Chem. Rev.* **2021**, *121*, 1845–1893.

[7] Sparks, S.; Liu, G.; Robbins, K. J.; Lazo, N. D. Curcumin modulates the self-assembly of the islet amyloid polypeptide by disassembling α-helix. *Biochem. Biophys. Res. Commun.* **2012**, *422*, 551–555.

[8] Fu, L.; Liu, J.; Yan, E. C. Y. Chiral Sum Frequency Generation Spectroscopy for Characterizing Protein Secondary Structures at Interfaces. *J. Am. Chem. Soc.* **2011**, *133*, 8094–8097.

[9] Cort, J. R.; Liu, Z.; Lee, G. M.; Huggins, K.; Janes, S.; Prickett, K.; Andersen, N. H. Solution state structures of human pancreatic amylin and pramlintide. *Protein Eng. Des. Sel.* **2009**, *22*, 497–513.

[10] Young, L. M.; Cao, P.; Raleigh, D. P.; Ashcroft, A. E.; Radford, S. E. Ion Mobility Spectrometry–Mass Spectrometry Defines the Oligomeric Intermediates in Amylin Amyloid Formation and the Mode of Action of Inhibitors. *J. Am. Chem. Soc.* **2014**, *136*, 660–670.

[11] Emperador, A.; Orozco, M. Discrete Molecular Dynamics Approach to the Study of Disordered and Aggregating Proteins. *J. Chem. Theory Comput.* **2017**, *13*, 1454–1461.

[12] Wang, Y.; Liu, Y.; Zhang, Y.; Wei, G.; Ding, F.; Sun, Y. Molecular insights into the oligomerization dynamics and conformations of amyloidogenic and non-amyloidogenic amylin from discrete molecular dynamics simulations. *Phys. Chem. Chem. Phys.* **2022**, *24*, 21773–21785.

[13] Rahman, M. U.; Song, K.; Da, L.-T.; Chen, H.-F. Early aggregation mechanism of Aβ16–22 revealed by Markov state models. *Int. J. Biol. Macromol.* **2022**, *204*, 606–616.

[14] Zhou, M.; Wen, H.; Lei, H.; Zhang, T. Molecular dynamics study of conformation transition from helix to sheet of Aβ42 peptide. *J. Mol. Graph. Model.* **2021**, *109*, 108027.

[15] Cao, Y.; Jiang, X.; Han, W. Self-Assembly Pathways of β-Sheet-Rich Amyloid-β(1–40) Dimers: Markov State Model Analysis on Millisecond Hybrid-Resolution Simulations. *J. Chem. Theory Comput.* **2017**, *13*, 5731–5744.

[16] Liu, H.; Zhong, H.; Liu, X.; Zhou, S.; Tan, S.; Liu, H.; Yao, X. Disclosing the Mechanism of Spontaneous Aggregation and Template-Induced Misfolding of the Key Hexapeptide (PHF6) of Tau Protein Based on Molecular Dynamics Simulation. *ACS Chem. Neurosci.* **2019**, *10*, 4810–4823.

[17] Liu, H.; Zhong, H.; Xu, Z.; Zhang, Q.; Shah, S. J. A.; Liu, H.; Yao, X. The misfolding mechanism of the key fragment R3 of tau protein: a combined molecular dynamics

simulation and Markov state model study. *Phys. Chem. Chem. Phys.* **2020**, *22*, 10968–10980.

[18] Qiao, Q.; Qi, R.; Wei, G.; Huang, X. Dynamics of the conformational transitions during the dimerization of an intrinsically disordered peptide: a case study on the human islet amyloid polypeptide fragment. *Phys. Chem. Chem. Phys.* **2016**, *18*, 29892–29904.

[19] Melquiond, A.; Gelly, J. C.; Mousseau, N.; Derreumaux, P. Probing Amyloid Fibril Formation of the NFGAIL peptide by Computer Simulations. *J. Chem. Phys* **2007**, *126*, 065101.

[20] Luca, S.; Yau, W. M.; Leapman, R.; Tycko, R. Peptide Conformation and Supramolecular Organization in Amylin Fibrils: Constraints from Solid-State NMR. *Biochemistry* **2007**, *46*, 13505–13522.

[21] Patriksson, A.; van der Spoel, D. A temperature predictor for parallel tempering simulations. *Phys. Chem. Chem. Phys.* **2008**, *10*, 2073–2077.

[22] Case, D. A. Belfon, K. Ben-Shalom, I. Y. Brozell, S. R. Cerutti, D. S. Cheatham, III, T. E. Cruzeiro, V. W. D. Darden, T. A. Duke, R. E. Giambasu, G. et al. *AMBER 2020*. University of California, San Francisco, 2020.

[23] Chodera, J. D.; Noé, F. Markov state models of biomolecular conformational dynamics. *Curr. Opin.* **2014**, *25*, 135–144, Theory and simulation / Macromolecular machines.

[24] Noé, F.; Schütte, C.; Vanden-Eijnden, E.; Reich, L.; Weikl, T. R. Constructing the equilibrium ensemble of folding pathways from short off-equilibrium simulations. *Proc. Indian National Sci. Acad.* **2009**, *106*, 19011–19016.

[25] Silva, D.-A.; Bowman, G. R.; Sosa-Peinado, A.; Huang, X. A Role for Both Conformational Selection and Induced Fit in Ligand Binding by the LAO Protein. *PLOS Comput. Biol.* **2011**, *7*, 1–11.

[26] Bowman, G. R.; Voelz, V. A.; Pande, V. S. Atomistic Folding Simulations of the Five-Helix Bundle Protein λ6–85. *J. Am. Chem. Soc.* **2011**, *133*, 664–667.

[27] Bowman, G. R.; Voelz, V. A.; Pande, V. S. Taming the complexity of protein folding. *Curr. Opin.* **2011**, *21*, 4–11.

[28] Mardt, A.; Pasquali, L.; Wu, H.; Noé, F. VAMPnets for deep learning of molecular kinetics. *Nat. Commun* **2018**, *9*.

[29] Pérez-Hernández, G.; Paul, F.; Giorgino, T.; De Fabritiis, G.; Noé, F. Identification of slow molecular order parameters for Markov model construction. *J. Chem. Phys* **2013**, *139*, 015102.

[30] Prinz, J.-H.; Wu, H.; Sarich, M.; Keller, B.; Senne, M.; Held, M.; Chodera, J. D.; Schütte, C.; Noé, F. Markov models of molecular kinetics: Generation and validation. *J. Chem. Phys* **2011**, *134*, 174105.

[31] Deuflhard, P.; Weber, M. Robust Perron cluster analysis in conformation dynamics. *Linear Algebra Appl* . **2005**, *398*, 161–184, Special Issue on Matrices and Mathematical Biology.

[32] Scherer, M. K.; Trendelkamp-Schroer, B.; Paul, F.; Pérez-Hernández, G.; Hoffmann, M.; Plattner, N.; Wehmeyer, C.; Prinz, J.-H.; Noé, F. PyEMMA 2: A Software Package for Estimation, Validation, and Analysis of Markov Models. *J. Chem. Theory Comput.* **2015**, *11*, 5525–5542.

[33] E, W.; Vanden-Eijnden, E. Transition-Path Theory and Path-Finding Algorithms for the Study of Rare Events. *Annu. Rev. Phys. Chem.* **2010**, *61*, 391–420.

[34] Roy, R.; Paul, S. Disparate Effect of Hybrid Peptidomimetics Containing Isomers of Aminobenzoic Acid on hIAPP Aggregation. *J. Phys. Chem. B* **2022**, *126*, 10427–10444.

[35] Humphrey, W.; Dalke, A.; Schulten, K. VMD: Visual Molecular Dynamics. *J. Mol. Graph.* **1996**, *14*, 33–38.

[36] Roe, D. R.; Cheatham, T. E. PTRAJ and CPPTRAJ: Software for Processing and Analysis of Molecular Dynamics Trajectory Data. *J. Chem. Theory Comput.* **2013**, *9*, 3084–3095.

[37] Wu, C.; Shea, J.-E. The Structure of Intrinsically Disordered Peptides Implicated in Amyloid Diseases: Insights from Fully Atomistic Simulations. Dokholyan N., Ed.; Springer: Boston, 2012, 215–227.

[38] Dupuis, N. F.; Wu, C.; Shea, J.-E.; Bowers, M. T. The Amyloid Formation Mechanism in Human IAPP: Dimers Have β-strand Monomer-Monomer Interfaces. *J. Am. Chem. Soc.* **2011**, *133*, 7240–7243.

Chapter 3

Inhibition of hIAPP Aggregation by Small Molecules

"Medicine is a science of uncertainty and an art of probability."

– William Osler

Overview

In the search for an appropriate drug to treat T2D, the pharmacological arena has witnessed the emergence of myriad small molecules which demonstrates the potential to curtail the self-assembly of hIAPP. In this thesis, the spotlight converges on the meticulous exploration of two such bioavailable molecules–each harboring the potential to influence hIAPP aggregation and destabilize preformed fibrils. One of them is a neurotransmitter, norepinephrine (NE), which orchestrates a disruption in the hIAPP self-assembly, by preferentially interacting with the amyloid prone C-terminal region. The next part introduces a fresh facet of adenosine triphosphate (ATP), known not just for its bioenergetic role but also for its potential as a regulator of amyloid aggregation. Both hydrophobic interactions and hydrogen bonding contribute towards the interactions between hIAPP and the molecules. However, the influence of adenosine moiety on hIAPP-ATP interactions outweighs the triphosphate chain, indicating the preference for hydrophobic interactions. These studies investigates the inhibitory potency of molecules with different structures against hIAPP aggregation, thus, provide valuable information about the diversity in the design for drugs against T2D.

3.1 Inhibitory Mechanism of Norepinephrine on hIAPP Amyloid Aggregation

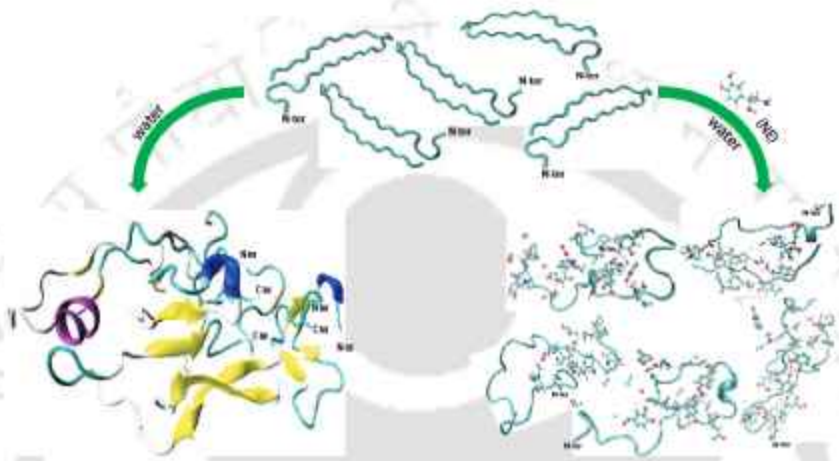

3.1.1 Introduction

Many clinical trials are being carried out in search of an appropriate cure against T2D, but the attempts have yet to provide any fruitful results[1]. To control the escalation of this disease, there is an urgent need to develop a suitable drug. Possible therapeutic strategies of T2D include prevention of β-sheet rich on-pathway oligomer formation[2]. Various natural flavonoids[3–16] as well as peptides and peptide analogues has been reported to interrupt the oligomerization of hIAPP[17–22]. Recently, nanoparticles have also received substantial attention in regulating protein aggregation[23–27]. Despite numerous studies on the design and development of inhibitors that interrupt the misfolding and aggregation of hIAPP, very few useful drugs have been identified due to high aggregation propensity and insolubility of hIAPP and also due to unclear pathologic mechanism.

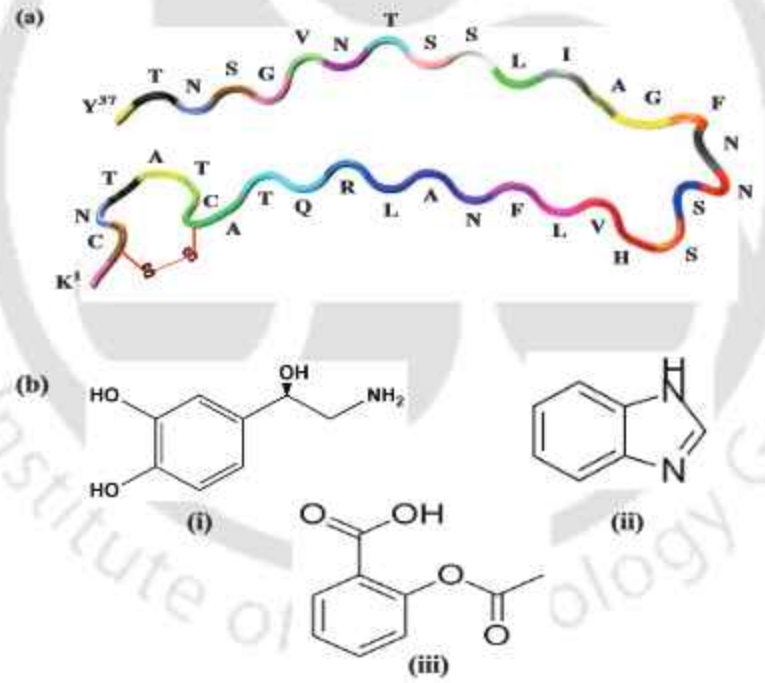

Figure 3.1: *(a) Cartoon representation of hIAPP, showing the disulphide bridge between Cys2 and Cys7. (b) Structure of (i) norepinephrine, (ii) benzimidazole and (iii) aspirin.*

The small organic molecules have been the target for amyloid inhibitors, since they are able to cross the blood-brain barrier conveniently and are stable in the biological media[28]. Previous studies report that the fibrillization and hence the cytotoxicity of hIAPP is reduced by EGCG by producing unstructured, off-pathway aggregates[29]. Brazilin

also prevents hIAPP fibrillogenesis in a dose-dependent manner as confirmed by ThT fluorescence analysis[6]. CD spectrum results showed that the transition of monomeric hIAPP peptides from random coils towards β-sheets conformation is inhibited by genistein and tanshinones, thus reducing hIAPP aggregation[4, 5]. Moreover, resveratrol inhibited the IAPP amyloid formation in solution as well as on the aggregation-fostering lipid membranes[30].

MD simulations confirm that orcein destroys the inter-peptide hydrogen-bonding network in hIAPP by binding with the amyloidogenic region[31]. Further, tanshinones preferentially interact with the β-sheet regions of hIAPP mainly via aromatic and hydrophobic interactions[4]. Moreover, the hydrophobic, aromatic stacking, cation-π and hydrogen-bonding interactions between hIAPP and EGCG harmonically influence the EGCG-induced conformational shift of hIAPP dimer[10]. The hydrophobic interactions also play crucial role in the binding process of other small molecules to hIAPP[6, 31, 32]. These small organic inhibitors contain aromatic groups, which allows selective binding to aromatic rings of amyloid peptides to interfere with their misfolding and subsequent aggregation[33].

Excerpts of hIAPP deposits have been found in the temporal lobe of gray matter of AD patients[34] and Aβ and tau aggregates have been detected in the pancreas of T2D patients[35], which leads to hypothesize that hIAPP cross-aggregate with Aβ peptides[36]. Hence, people suffering from Alzheimer's disease, have also shown a high probability of suffering from T2D[37]. Therefore, many drugs have been reported, which can inhibit both Aβ and hIAPP aggregation[5, 8–10, 31, 38–43]. A recent *in silico* study by Zou et.al revealed that norepinephrine has the ability to inhibit fibrillization of amyloid-β peptides and also disrupt pre-formed fibrils[44]. Norepinephrine (NE), also known as noradrenalin, is a catecholamine present in brain and body and it functions as a hormone and neurotransmitter (Fig 3.1b). NE leads to increased release of glucagon, increasing of production of glucose by the liver[45]. Diabetes may cause a loss of NE neurons in the sympathetic nervous system[46]. NE has been used for the treatment of Alzheimer's disease(AD) because it has shown memory retrieval power[47].

Another similar catecholamine, dopamine, was found to inhibit the aggregation of hIAPP, as well as, destabilizes the hIAPP protofibrils[32, 48]. The presence of dopamine promotes hIAPP dimer to be loosely packed, with a smaller number of hydrogen bonds, thus inhibiting the formation of long fibril-prone β-sheets in the amyloidogenic regions. Moreover, the destabilization of α-synuclein oligomers by NE and dopamine was also stud-

ied by this group[49]. Since NE is being used as an anti-amyloid agent for Aβ peptides and α-synuclein and T2D and AD have been known to cross-relate, here we have investigated the inhibitory effect of norepinephrine on the aggregation of hIAPP by all-atom molecular dynamics simulations in explicit solvent. We have also studied the effect of aspirin and benzimidazole (Fig 3.1b) on hIAPP aggregation, in order to compare the results obtained for NE, since both these molecules have been reported to have no inhibitory action on hIAPP[48, 50–52].

The obtained results provide valuable information about the molecular interaction of hIAPP with NE. Our simulations reveal that norepinephrine intercepts the production of toxic in-pathway oligomers and hence the tendency of the disordered monomers to aggregate into β-sheet conformation reduces in its presence, while aspirin and benzimidazole has no effect on hIAPP aggregation. The interactions between the peptides, which stabilize the ordered β-sheet structure is effectively reduced, due to binding between NE and the peptide residues. Moreover, NE was found to preferentially interact with the C-terminal residues of hIAPP and also destabilize the pre-formed fibrillar structures of hIAPP. This work is believed to be the first reported inhibitory effect of NE on hIAPP aggregation via molecular dynamics simulations.

The rest of the chapter is divided into Simulation Method, which consists of the simulation protocol and analyses applied for this study and Results and Discussions, which contains the in-depth outcome of each analysis, followed by the Conclusion of the study.

3.1.2 Models and Simulation Method

3.1.2.1 Simulation Setup

The coordinates of the hIAPP structure for our simulations was extracted from the solid-state NMR-based model[53]. The small molecules (Mol), i.e., norepinephrine (NE), aspirin (AS) and benzimidazole (BZ) were optimized by the Gaussian 09 software[54] at the HF/6-31G*[55] level and the partial atomic charges were obtained by the restrained electrostatic potential (RESP) [56]. The general amber force field (GAFF)[57] was used to describe these molecules. The initial system was prepared by placing five well-separated monomeric peptides in a cubic box. The dimer and protofibril systems were also arranged similarly

with two and five hIAPP peptides respectively. The hIAPP-Mol systems were similarly prepared along with random addition of the required number of NE, AS and BZ molecules in the cubic box. We performed eleven molecular dynamics simulations, in total, each starting with a different initial configuration, following simulation protocols mentioned in Chapter 1 (Section 1.5.2). Each of the system was simulated for 500 ns (200 ns for the dimer systems). The details of the systems are given in Table 3.1. Three sets of simulations for the monomeric peptide-NE system were carried out to conclude the convergence of the results.

System	N_P	N_{Mol}	N_W	Box length (Å)	C_{Mol} (M)
hIAPP	5	0	10000	68.94	0
hIAPP:10NE	5	50	10000	69.62	0.246
hIAPP:20NE	5	100	10000	70.33	0.477
hIAPP:20NE(a)	5	100	10000	70.32	0.478
hIAPP:20NE(b)	5	100	10000	70.27	0.478
hIAPP:20AS	5	100	10000	70.23	0.479
hIAPP:20BZ	5	100	10000	70.10	0.482
Protofibril	5	0	10000	83.65	0
Protofibril+NE	5	100	10000	70.35	0.478
Dimer	2	0	5000	54.49	0
Dimer+NE	2	49	5000	55.39	0.479

Table 3.1: *N_p, N_{Mol}, N_W and C_{Mol} represent the number of peptides, Mol and water molecules and the molar concentration of Mol respectively, where Mol is norepinephrine(NE)/ aspirin(AS)/ benzimidazole(BZ).*

3.1.2.2 Simulation Analysis

The simulation analyses were carried out following the protocols discussed in Chapter 1 (Section 1.5.3). For the spatial distribution functions, an isovalue of 1 is considered. An atomic contact is considered when the distance between the heavy atom pairs of NE and hIAPP is within 3.5 Å[58].

The umbrella sampling method was used to calculate the potential of mean force (PMF) between two hIAPP peptides[59]. The equilibrated dimer systems were used as the starting structure for the PMF calculations. The reaction coordinate considered for plotting PMF is the distance between the centre of mass of the two peptides. The entire

simulation was divided into 59 windows, where the distance was varied from 3.0 to 17.5 Å, with an increment of 0.25 Å. The two peptides were pulled apart at 300 K, with a spring constant of 1 kcal mol^{-1} $Å^{-2}$. Each window was first equilibrated for 10 ns, followed by a production run of 20 ns. Hence a total of 1.74 μ simulation run was performed for each system. The results were then analyzed using the Weighted Histogram Analysis Method (WHAM)[60, 61].

3.1.3 Results and Discussions

3.1.3.1 Structural changes of hIAPP in Presence of Norepinephrine

The difference in the conformation of hIAPP, in absence and presence of NE, can be investigated by the detailed analysis of the various secondary structures of the peptides. To begin with, the probability of total β-sheet of the systems is plotted versus simulation time (Fig 3.2). It is seen that the β-sheet of hIAPP almost remains constant after 400 ns and hence it can be assumed that the conformational ensembles have converged during the last 100 ns of the trajectory. The β-sheet probability of the peptides in absence of NE increases as time evolves, but is found to decrease with time for the systems containing NE and reaches a negligible amount at the end of the simulation on increasing the concentration of NE. In comparison, aspirin did not have any significant effect on the β-sheet content of the peptides, even though, it increases for the system with benzimidazole, upto 200 ns and thereafter coincides with the systems without NE. The average probability of each of the secondary structures of hIAPP is mentioned in Table 3.2. The probability of β-sheet for hIAPP is 15.088%, which is similar to the results reported elsewhere[10, 23] and is also comparable for the system containing aspirin (11.7994%) and benzimidazole (11.588%). On addition of NE, the probability is reduced to 8.288%, which is further reduced to 2.512% with increasing NE. The propensity of random coil conformation increases from 39.636% to 56.279% on addition of NE, whereas that of the helix conformation almost remains the same. Similar results are observed for all the systems with NE (Table 3.2).

The representative snapshots of hIAPP peptides (Fig 3.3) for all the systems at 250 ns time intervals enhance the above results. The presence of β-sheets is prominent at the end of simulation for all the systems without NE, but the β-sheet propensity is hardly The

change of all the secondary structural components of each residue with time is analyzed (Fig 3.4).

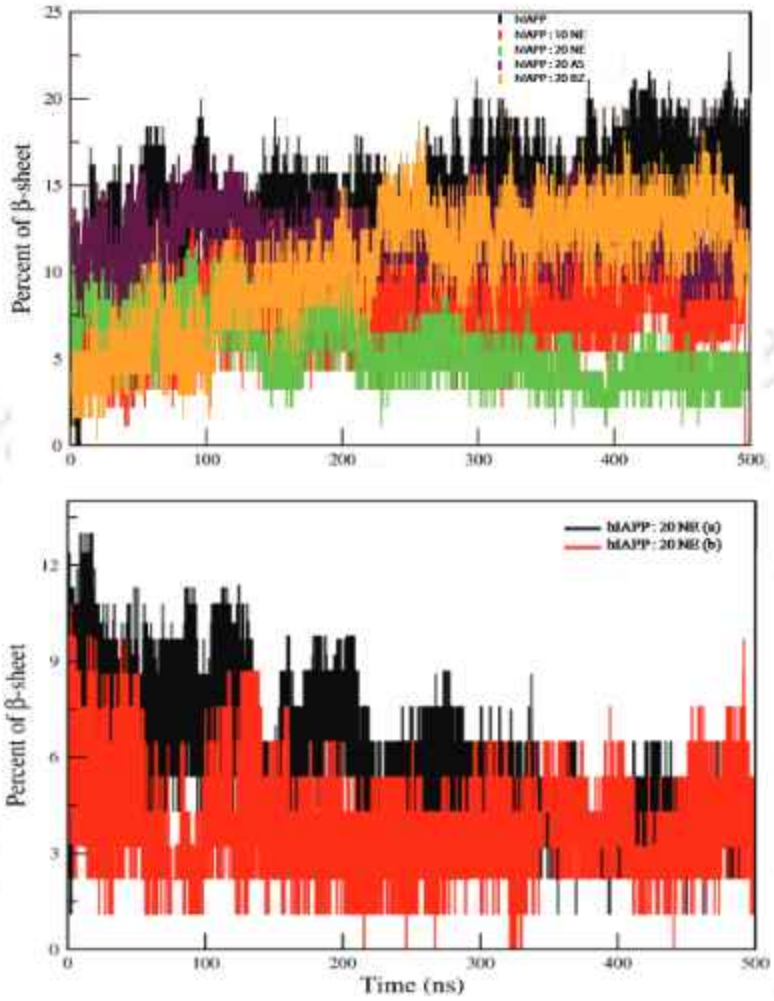

Figure 3.2: *Time evolution of β-sheet content of hIAPP peptides for different systems.*

hIAPP peptides form β-sheet almost instantly in pure water at the start of simulations and remain steady throughout the simulation, which determines the stability of the β-sheet conformation. This reduces to a negligible amount in presence of NE, while unstructured coil conformation is present in abundance. This further imposes that hIAPP, upon binding with NE, reduces its tendency to shift from disordered state conformation to β-sheet aggregates. However, in presence of aspirin and benzimidazole, the conformation the peptides remain unchanged, proving that neither of these molecules have any effect on the secondary

structures of the peptides.

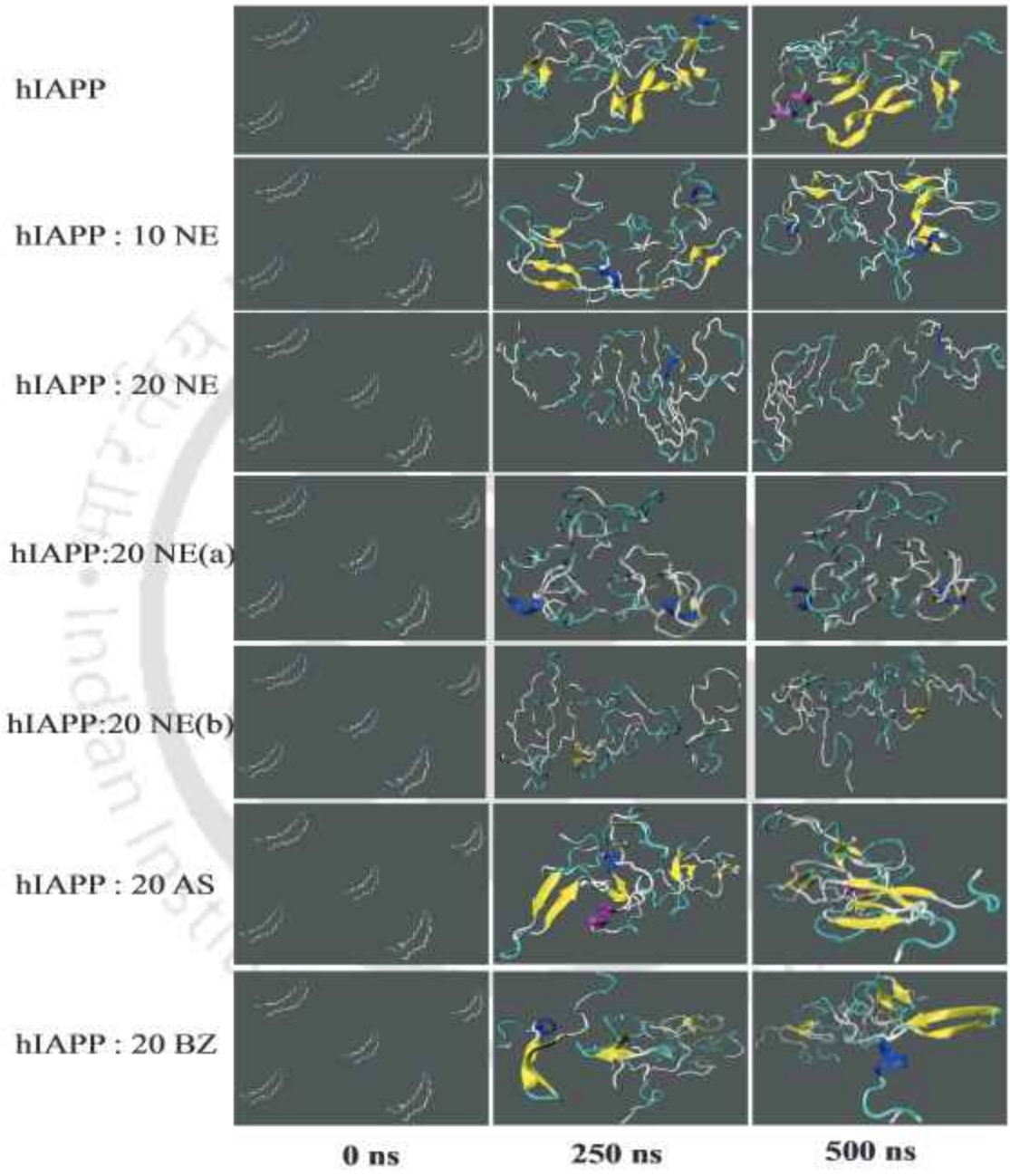

Figure 3.3: *Snapshots of five hIAPP peptides in different systems at 250 ns time interval. The peptides are represented in cartoon form, depicting β-sheet in yellow, coil in white, bend in cyan and 3_{10}-helix in blue.*

Hence the presence of NE prevents the peptides from attaining β-sheet conformation, in-

System	Parallel-β	Anti-parallel-β	3_{10}-helix	α-helix	Turn	Bend	Coil
hIAPP	8.9±0.3	6.2±0.2	1.4±0.1	2.6±0.2	14.6±0.3	26.6±0.4	39.6
hIAPP:10NE	1.0±0.1	7.3±0.2	1.7±0.1	0.1±0.0	23.6±0.3	20.7±0.3	45.6
hIAPP:20NE	1.9±0.1	0.6±0.0	4.7±0.2	0.5±0.0	10.0±0.2	26.1±0.3	56.3
hIAPP:20NE(a)	0.3±0.0	3.1±0.2	0.5±0.0	0	10.6±0.2	22.6±0.3	63
hIAPP:20NE(b)	1.6±0.1	3.4±0.2	0.1±0.0	0	14.3±0.3	20.7±0.4	50.0
hIAPP:20AS	0.2±0.0	11.6±0.3	2.9±0.1	2.8±0.2	6.8±0.2	33.4±0.4	42.3
hIAPP:20BZ	2.6±0.1	9.0±0.3	2.6±0.1	1.6±0.1	10.7±0.2	29.8±0.4	43.8

Table 3.2: *The secondary structure contents of hIAPP for different systems, along with the standard error of each value.*

clining them to a more disordered state, much like the effect of NE on Aβ peptides[44].

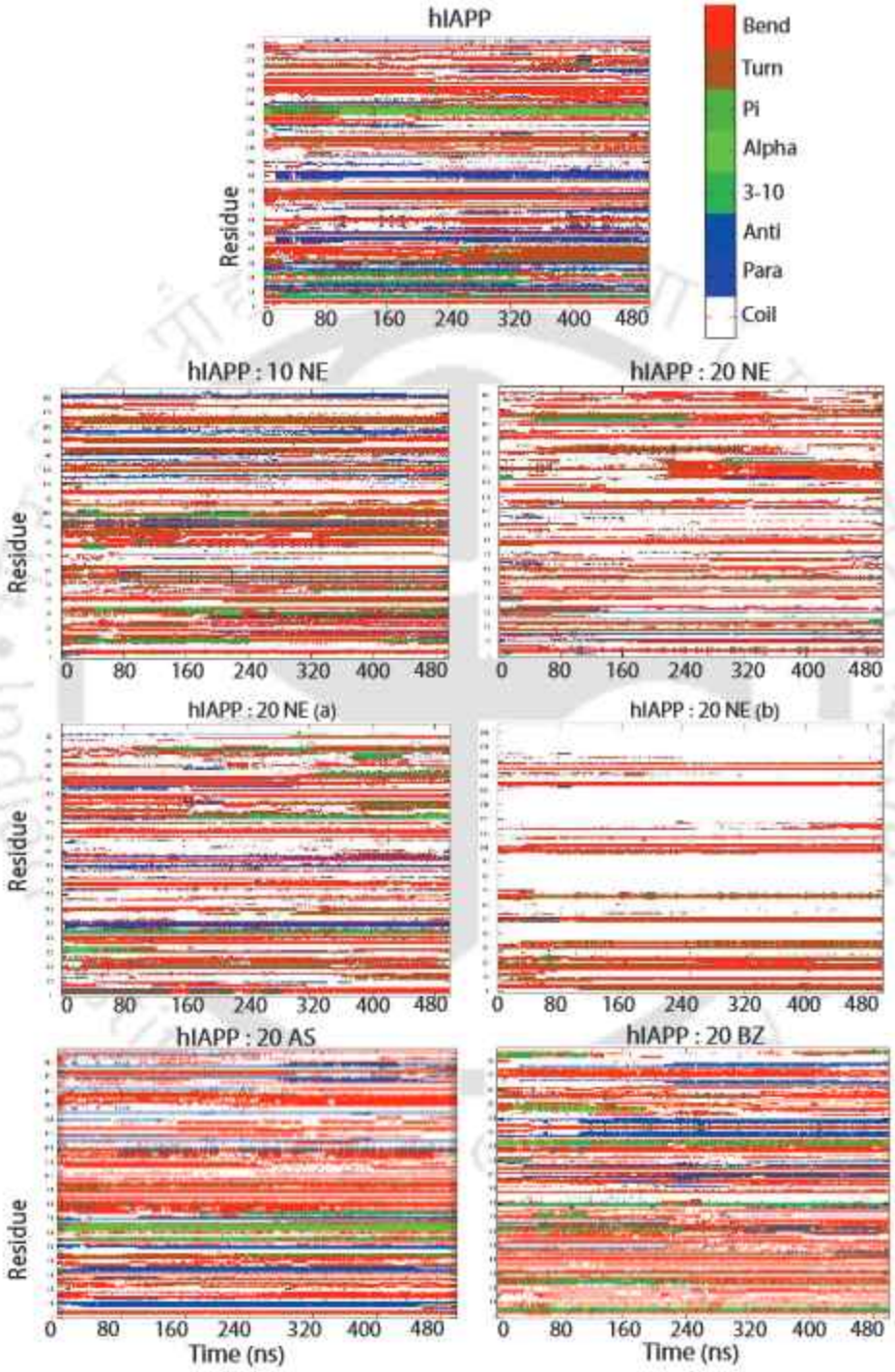

Figure 3.4: *Time evolution of change of secondary structures of each residue of hIAPP for different systems.*

3.1.3.2 Effect of Norepinephrine on the Interaction between the Peptides

The overall structural stability of hIAPP peptides, in presence of the molecules, is investigated by SASA, which determines the surface area of the peptides available for contact with the solvent molecules. Higher the probability of peptides to aggregate, lower is the SASA value, since less number of amino acid residues are being exposed to the solvent. From Table 3.3), it can be observed that SASA of the systems involving NE molecules is larger than the ones without it (peptide alone or peptide with aspirin or benzimidazole).

System	Hydrogen Bonds		SASA (Å^2)
	Pep-Pep	Pep-Mol	
hIAPP	106.8 ± 0.14		10860 ± 3.86
hIAPP:10NE	85.98 ± 0.11	49.97 ± 0.12	12220 ± 5.74
hIAPP:20NE	70.24 ± 0.09	110.2 ± 0.17	13820 ± 0.83
hIAPP:20NE(a)	68.37 ± 0.14	98.72 ± 0.17	14370 ± 2.88
hIAPP:20NE(b)	80.42 ± 0.10	86.09 ± 0.16	15340 ± 2.28
hIAPP:20AS	92.95 ± 0.02	43.32 ± 0.19	12340 ± 0.39
hIAPP:20BZ	93.0 ± 0.18	30.8 ± 0.06	12070 ± 0.23

Table 3.3: *Solvent Accessible Surface Area (SASA) of all the five hIAPP peptides and Average hydrogen bond numbers between peptide-peptide and peptide-Mol interactions, where Mol is norepinephrine(NE)/ aspirin(AS)/ benzimidazole(BZ)for different systems, along with the standard error of each value.*

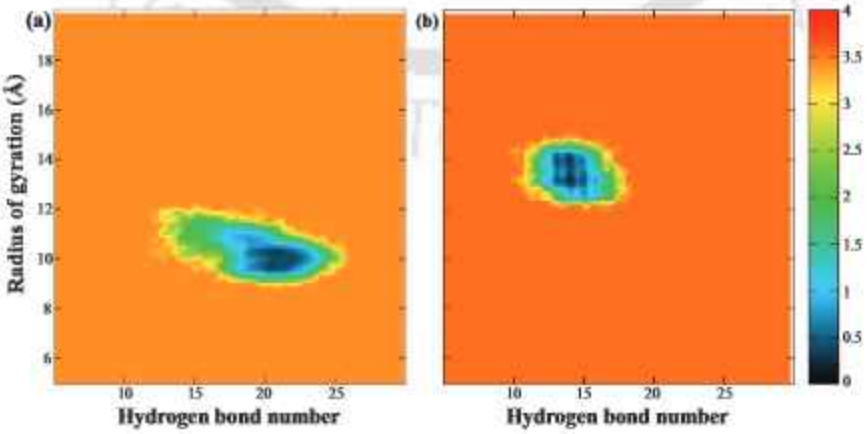

Figure 3.5: *Free energy plot (kcal/mol) as a function of R_g of hIAPP peptides and the average number of hydrogen bonds for (a) hIAPP and (b) hIAPP : 20 NE systems.*

Moreover, on increasing NE concentration, the SASA value also increases, which indicates to less aggregation propensity of the peptides. Hence we can infer that NE destabilizes peptide aggregation, causing more peptide surface solvation, but the other molecules have no effect on it.

To further probe the influence of NE on the conformational space of the peptides, the free energy surface was plotted as a function of the total number of peptide-peptide hydrogen bonds formed for each peptide and the radius of gyration (R_g) of the peptides (Fig 3.5), following the equation 1.19. The minimum free energy basin for hIAPP in absence of NE is observed where the number of hydrogen bonds range between 19.4-23 and R_g at 9.5-10.7. However, in presence of NE, the minimum free energy basin shifts to a smaller hydrogen bond number value of 13-15 and a larger R_g value of 13.1-14.3. The lower R_g value of the peptides in absence of NE portrays the compactness of the peptides, which further becomes loosely-packed (higher R_g) in presence of NE. A decrease in the peptide-peptide hydrogen bonds was observed on addition of NE, which was reasserted by the average hydrogen bond number for all the peptides (Table 3.3). The peptide-peptide hydrogen bonds hardly reduced in presence of aspirin or benzimidazole. The hydrogen-bonding interaction between the peptides have been known to play an important role in the stabilization of oligomers[31, 41, 42]. Moreover, hydrogen bonds between NE and the peptides increase with increasing concentration of NE, indicating that NE disrupts the stable hydrogen bond network of the peptides by itself involving in hydrogen bonds with them. The small hydrogen bond number of the peptides with aspirin or benzimidazole also point out that these molecules have low interaction with hIAPP.

To monitor the effect of NE on the interaction between the peptides, the contact map for all the hIAPP peptides considering C_α-C_α distances between each pair of residue was analyzed (Fig 3.6). The grayish patches scattered in the off-diagonal regions for the system without NE indicate that the peptides are much closer to each other, favouring peptide-peptide interactions. Aspirin or benzimidazole did not exhibit a considerable change in the contact map, proving their inefficiency to inhibit peptide aggregation. However, for the systems containing NE, there is a marked reduction of these patches, which proves that the peptides are present far apart from each other.

From the values of the electrostatic and the van der Waals interaction energies for

both inter-peptide as well as peptide-molecule linkages (Table 3.4), it is clear that the electrostatic energies dominate over the van der Waals energy values for both the interactions. Both the energy components become unfavourable for the inter-peptide interactions, while that for peptide-NE interactions, the energy components become more negative

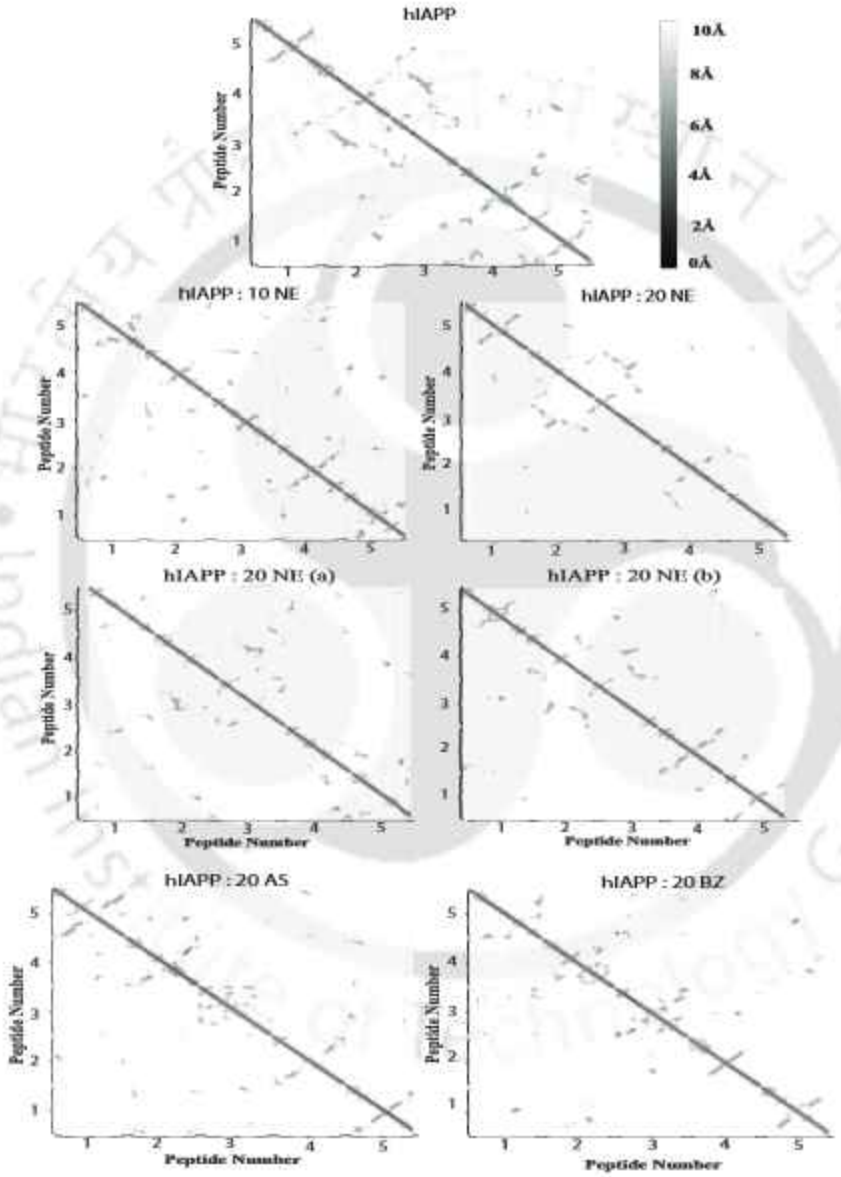

Figure 3.6: *Residue-residue contact map of the hIAPP peptides for different systems.*

(hence more favourable) with increase in the concentration of NE. These findings indicate that the peptide-peptide interactions become unfavourable with the addition of norepinephrine and the peptide-NE interactions become more and more favourable. Hence it

can be further concluded that NE hinders the aggregation of peptides by interacting with the peptides itself. However, aspirin or benzimidazole hardly have any effect on the interactions between the peptides and also exhibit low interaction affinity with hIAPP themselves, due to which they are unable to prevent peptide aggregation.

System	Electrostatic		van der Waals	
	Pep-Pep	Pep-Mol	Pep-Pep	Pep-Mol
hIAPP	-6165 ± 1.17		-401 ± 0.57	
hIAPP:10NE	-5459 ± 0.89	-474.5 ± 1.12	-385.6 ± 0.48	-281.3 ± 0.51
hIAPP:20NE	-5373 ± 1.06	-999.6 ± 1.42	-376.5 ± 0.54	-333.2 ± 0.72
hIAPP:20NE(a)	-5299 ± 1.13	-838.3 ± 1.37	-383.7 ± 0.57	-358.3 ± 0.82
hIAPP:20NE(b)	-5367 ± 1.22	-900 ± 1.58	-322.5 ± 0.56	-313.5 ± 0.78
hIAPP:20AS	-6003 ± 0.51	-386.2 ± 0.28	-650.8 ± 0.61	-224.4 ± 0.68
hIAPP:20BZ	-6072 ± 0.02	-340.7 ± 0.17	-446.7 ± 0.07	-318.7 ± 0.12

Table 3.4: *Decomposition of peptide-peptide and peptide-Mol interaction energy (kcal/mol) for different systems, along with the standard error of each value, where Mol is norepinephrine(NE)/ aspirin(AS)/ benzimidazole(BZ).*

3.1.3.3 Potential of Mean Force

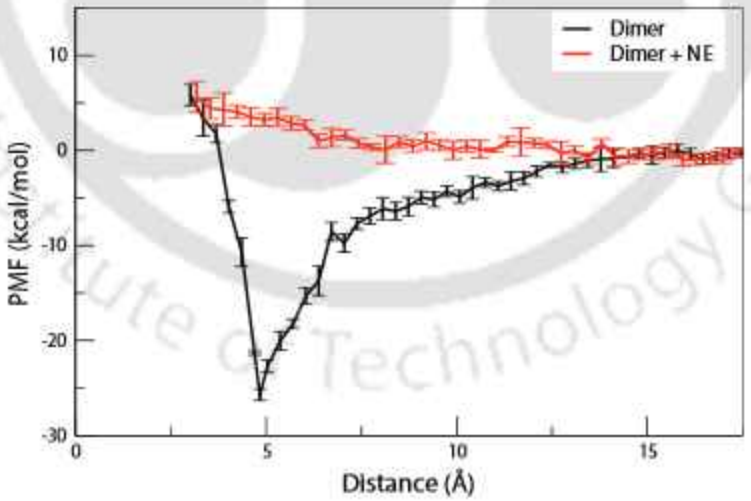

Figure 3.7: *Potential of mean force between the centre of mass of the two hIAPP peptides for the dimer and dimer+NE systems, along with the standard error bar of each value.*

The effect of NE on the stability of peptide-peptide interactions was further investigated by PMF of hIAPP dimer. The PMF was calculated as the function of the distance between

the centre of mass of the two peptides. We observe the appearance of a global minimum for the dimer at 4.835 Å, with a steep well depth (Fig 3.7). The high negative value of the free energy further suggests that the dimer is most stable in water when the two peptides are at a distance of 4.84 Å. However, in presence of NE, the minimum shifts to a larger distance with a much higher (positive) PMF value. This observation can be attributed to the fact that the two peptides are involved in stable interactions in pure water, which weakens in presence of NE.

3.1.3.4 Distribution of Norepinephrine Around the hIAPP Residues

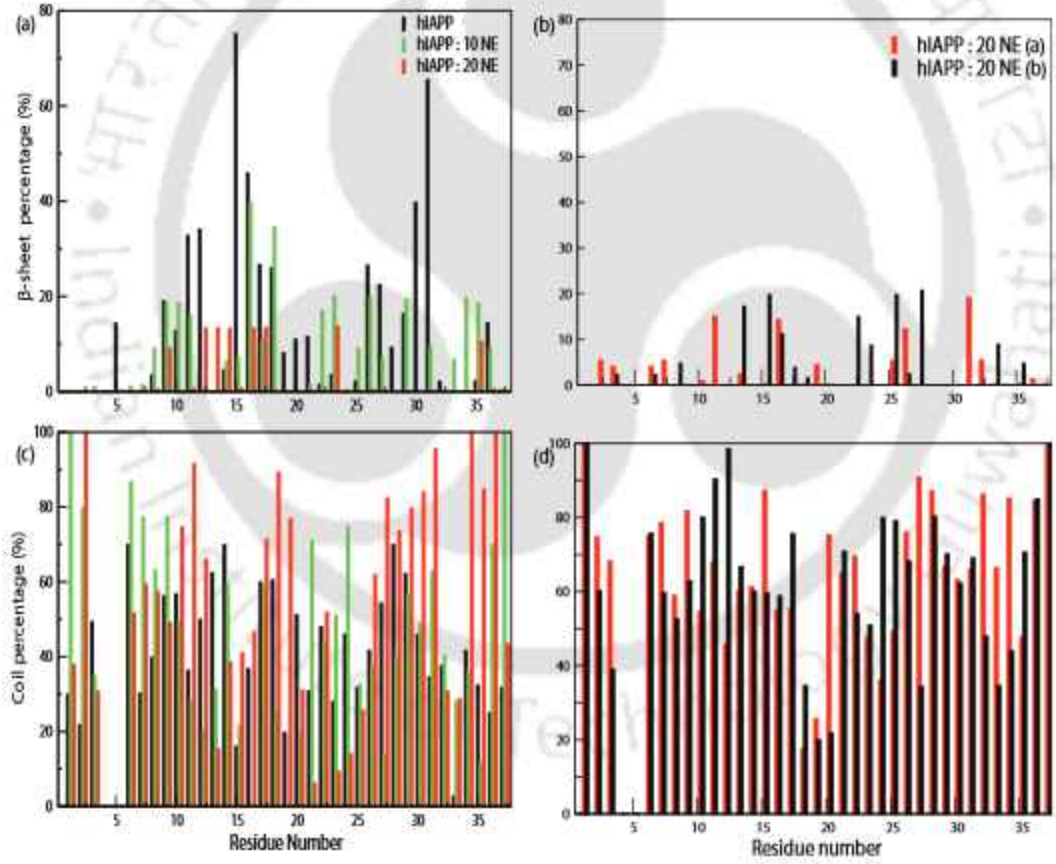

Figure 3.8: *Effect of NE on (a,b) β-sheet and (c,d) coil percentages for each residue of hIAPP for different systems.*

To monitor the residues involved in β-sheet formation, the residue-based probability of β-sheet and random coil conformation are calculated by averaging the secondary structural

components of each residue over the five peptides in absence and presence of NE (Fig 3.8). It is seen that the residues Ala5, Thr9-Leu12, Phe15-His18, Ile26-Asn31, Thr36 have a notably higher probability of β-sheet than the remaining residues. This suggests that the Thr9-His18 and Ile26-Asn31 residues participate in the β-strand regions, which resemble the β-strand regions, suggested elsewhere[23, 42, 53]. The snapshot of the monomers at the end of the simulation also reveal that peptide-2 (P2) form β-sheets with peptide-3 (P3) and peptide-5 (P5) along the similar regions (Leu12-His18 and Leu27-Gly33) (Fig 3.9). On addition of NE, the β-sheet propensity significantly reduces and the random coil conformation increases for most of these residues, especially the C-terminal region, hinting at a better interaction of NE with this region.

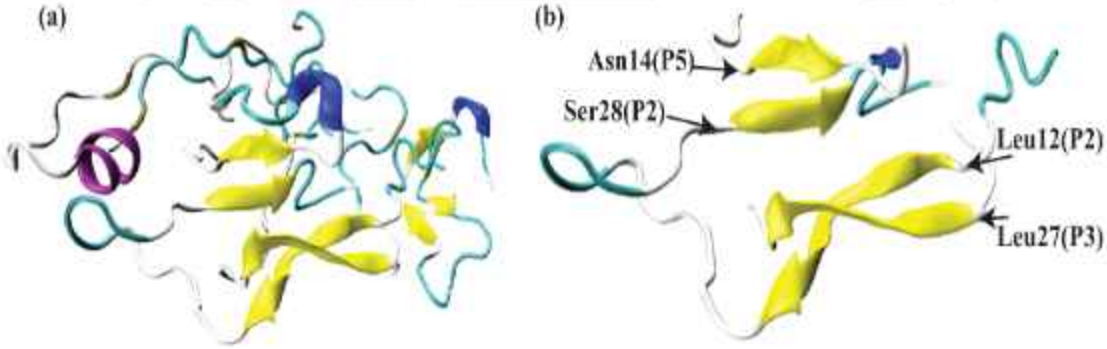

Figure 3.9: *A snapshot for hIAPP system at the end of the simulation (a) of the five hIAPP peptides and (b) highlighting the peptides involved in β-sheets.*

It is seen that the residues Ala5, Thr9-Leu12, Phe15-His18, Ile26-Asn31, Thr36 have a notably higher probability of β-sheet than the remaining residues. This suggests that the Thr9-His18 and Ile26-Asn31 residues participate in the β-strand regions, which resemble the β-strand regions, suggested elsewhere[23, 42, 53]. The snapshot of the monomers at the end of the simulation also reveal that peptide-2 (P2) form β-sheets with peptide-3 (P3) and peptide-5 (P5) along the similar regions (Leu12-His18 and Leu27-Gly33) (Fig 3.9). On addition of NE, the β-sheet propensity significantly reduces and the random coil conformation increases for most of these residues, especially the C-terminal region, hinting at a better interaction of NE with this region.

The radial distribution function (RDF) between NE and the peptides is calculated

to investigate the distribution of NE molecules around hIAPP, considering the backbone as well as the side chain atoms of the peptides. From Fig 3.10, we observe that a steep peak occurs at 1.65 Å(backbone) and 1.55 Å(side chain) for the system with NE, signifying the intense association of NE with hIAPP. The RDFs for the control systems are also provided, both of which have a much gentler peak at a higher distance, which highlight their lower affinity towards hIAPP.

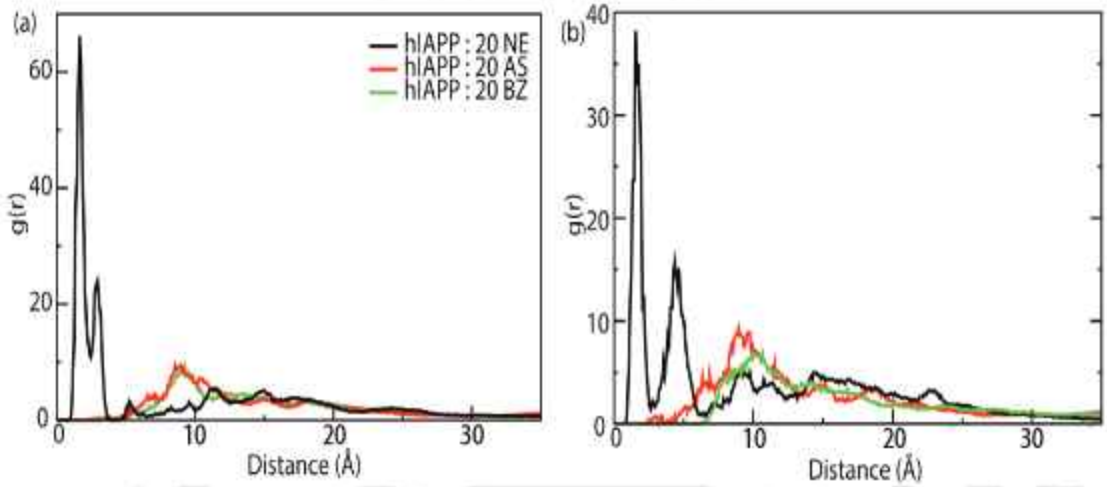

Figure 3.10: *Radial distribution functions between centre of mass of norepinephrine(NE)/ aspirin(AS)/ benzimidazole(BZ) and the (a) backbone and (b) side chain atoms of hIAPP peptides.*

The spatial distribution functions (SDF) also depict the compact arrangement of NE around hIAPP, while the AS and BZ molecules are much sparsely populated in the neighbourhood of the peptides (Fig 3.11). Hence, it is clear that, in the vicinity of the peptides, NE is densely populated, but the control molecules remain far from it.

The RDFs between the centre of mass of Leu12-His18 and Leu27-Gly33 residues, considering the backbone atoms of the peptides is plotted to investigate how NE affected the interaction between the aforementioned regions. In Fig 3.12, we observe a sharp maximum at 4.85 Å, for the peptides in absence of NE, with a very high intensity. This indicates that the residues in the first region (Leu12-His18) are strongly interacting with those in the second region (Leu27-Gly33) in water. On addition of NE, a very small peak is observed at 10.05 Å, signifying the reduction in the interaction between the peptides.

In order to probe the distribution of NE around the hIAPP residues, the average

number of NE molecules present around each residue within a radius of 3.5 Å is computed. From Fig 3.13a and b, it can be seen that NE molecules have a higher probability

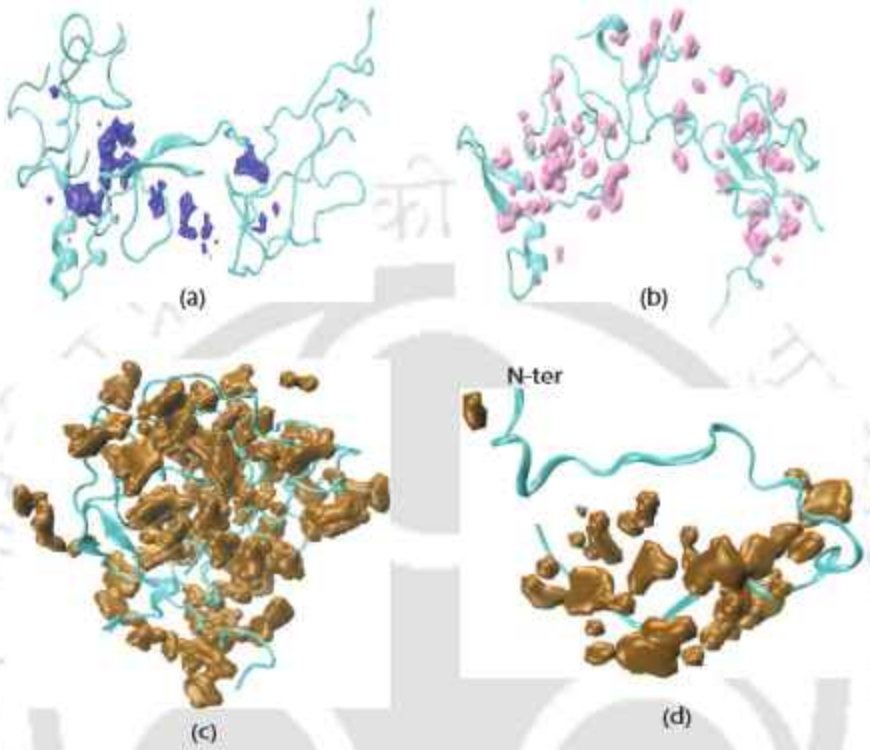

Figure 3.11: *Spatial distribution functions of (a) aspirin, (b)benzimidazole and (c) norepinephrine around hIAPP peptides. (d) SDF of a monomer depicting the distribution of norepinephrine around the C-terminal region.*

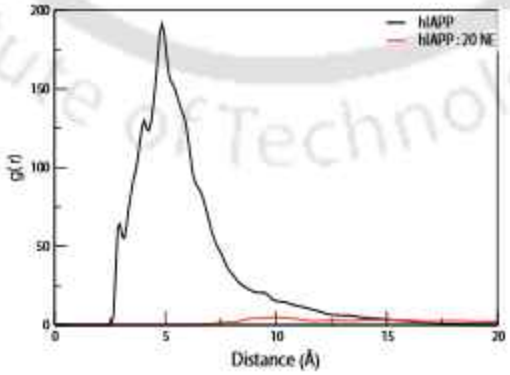

Figure 3.12: *Radial distribution functions between centre of mass of Leu12-His18 and Leu27-Gly33 residues of hIAPP peptides for the hIAPP and hIAPP : 20 NE systems.*

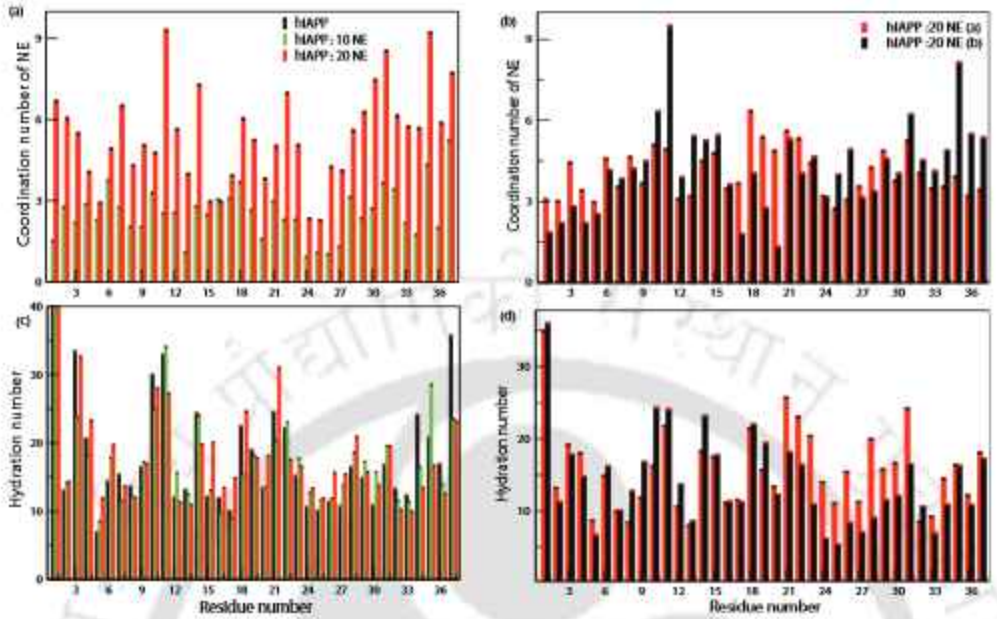

Figure 3.13: *First shell coordination number of (a,b) NE and (c,d) water around each residue of hIAPP, along with the standard error bar of each value.*

distribution around the residues Cys2, Asn3, Cys7, Arg11, Leu12, Asn14, His18-Phe23, Ser28-Thr36, much of which are involved in β-strands, suggesting preferential binding with these residues (mostly C-terminal).

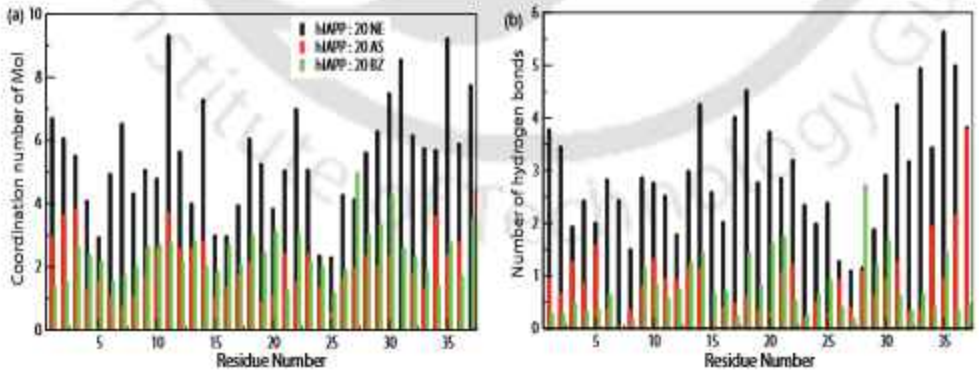

Figure 3.14: *(a) First shell coordination number and (b) Average hydrogen bond number of the Mol with each residue of hIAPP, where Mol is norepinephrine(NE)/ aspirin(AS)/ benzimidazole(BZ).*

The preferential distribution of NE around C-terminal region is also depicted in the SDF

data (Fig 3.11d). The probability of AS and BZ molecules around hIAPP residues is lower compared to that of NE (Fig 3.14a), indicating much less interaction with them. The average number of water molecules around each residue is also calculated (Fig 3.13c and d), where the first solvation shell is considered to be within 3.5 Å. It is observed that the hydration number around the residues increases for the systems containing NE, since the peptides have a lower tendency to aggregate and, hence, a better probability of getting solvated.

3.1.3.5 Potential Binding Sites of Norepinephrine with hIAPP

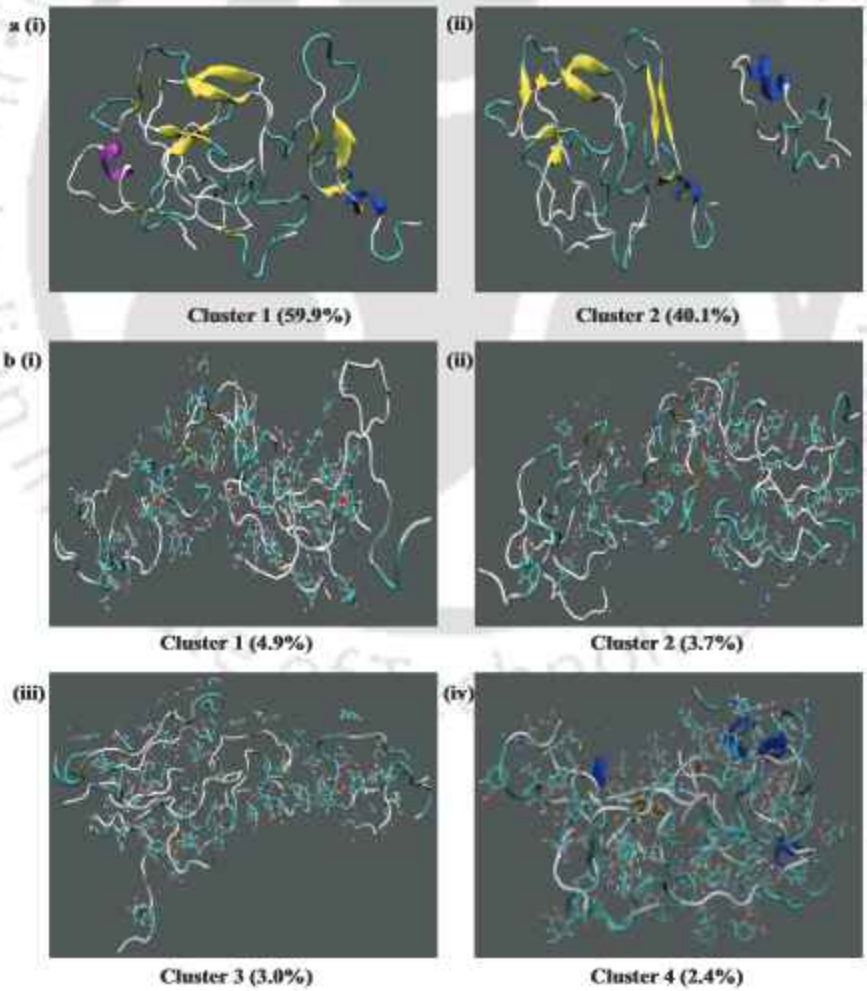

Figure 3.15: *Representative conformations of the clusters of hIAPP peptides for (a) hIAPP system and (b) the four most-populated clusters for hIAPP : 20 NE system.*

The investigation into the precise interactions between NE and hIAPP is required for the complete understanding of the molecular mechanism involved in the inhibition of aggregation of hIAPP with NE. Therefore, cluster analysis of the systems is carried out to extract the representative structures. The hIAPP and hIAPP-NE systems are separated into 2 and 11 clusters respectively. The two clusters of hIAPP and the four most-populated clusters of the hIAPP-NE system are presented in Fig 3.15, along with their respective population. The peptides form anti-parallel β-strands, with a slight hint of α-helix (Fig 3.15a). However, in presence of NE, the β-strands vanish and mostly the peptides are present in a disordered state (Fig 3.15b) and are separated from each other.

Next, we investigate the key residues and dominant binding interactions by determining the contact probability and binding free energy of NE molecules with each residue of hIAPP peptide. The negative value of the binding free energy of NE with the hIAPP monomers proves that the binding interaction is very favourable (Table 3.5).

System	hIAPP:20NE	Dimer+NE	Protofibril+NE
ΔE_{vdw}	-294.70 ± 3.13	-217.25 ± 0.53	-222.50 ± 0.64
ΔE_{ele}	-1107.67 ± 6.60	-260.33 ± 0.94	-931.33 ± 0.94
ΔG_{GB}	1352.77 ± 5.96	352.14 ± 0.89	1128.78 ± 0.91
ΔG_{NP}	-123.67 ± 0.31	-33.64 ± 0.07	-110.20 ± 0.09
ΔG_{bind}	-173.27 ± 3.32	-159.08 ± 0.62	-135.26 ± 1.02

Table 3.5: *Decomposition of binding energy (kcal/mol) of NE with hIAPP for the different hIAPP aggregates.*

From Fig 3.16a, it can be seen that the NE molecule have the maximum interaction probability with residues Cys7, Arg11, Leu12, Asn22, Ser29-Asn31, Gly33, Asn35-Tyr37 with a slightly lower probability with residues Lys1, Cys2, Thr6, His18, Phe23, Ser28, Val32. The binding free energy of NE with respect to each residue is shown in Fig 3.16b and it almost matches well with the results obtained in Fig 3.16a. The binding free energy is found to be lowest (most favourable) for the residues Cys2, Leu12, Phe23, Ile26, Leu27, Thr30, Val32, Gly33, Asn35-Tyr37, and is slightly higher (less favourable) for Asn3, Phe15, Leu16, His18, Asn22, Ser28, Ser29, Asn31, Ser34 residues. These data demonstrate that NE has a high binding probability for not only the terminal regions but also for the amyloidogenic region,

particularly favouring C-terminal region.

The polar residues forms hydrogen bonds with NE, which is calculated by the average hydrogen bond number between NE and each residue of hIAPP (Fig 3.17). Cys2, Arg11, His18, Asn22, Thr30, Asn31, Asn35, Thr36 and Tyr37 residues have shown high hydrogen bond number with NE. The hydrogen bond number for the control systems have also been provided for comparison (Fig 3.14b). The hydrophobic residues, Leu12, Ile26, Leu27, Val32, Gly33 have also shown strong binding affinity with the NE molecules.

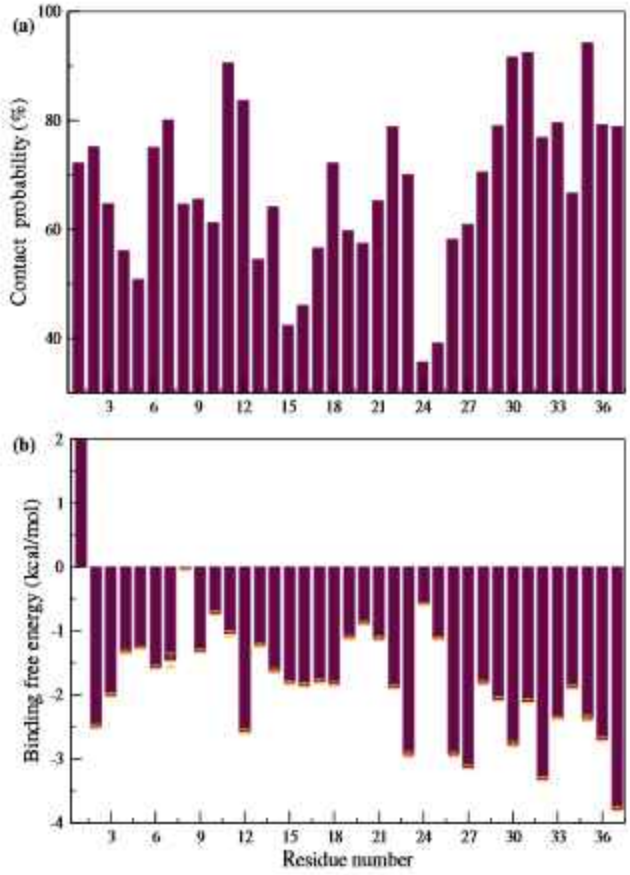

Figure 3.16: *Residue based (a) contact probability of heavy atoms of NE with hIAPP and (b) binding free energy between hIAPP and NE for hIAPP : 20 NE system, along with the standard error bar of each value.*

The stacking interactions between the aromatic rings of inhibitors and that of the peptide residues play an essential role in the binding of the drugs to amyloid peptides. To

demonstrate this, the probability distribution of the distance between the centre-of-mass of the aromatic ring of the aromatic residues (Phe15, His18, Phe23 and Tyr37) and that of the nearest NE is plotted, along with the probability distribution of the angles between the two planes formed by the corresponding aromatic rings (Fig 1.6a)[62]. From the representative snapshots of the stacking interactions (Fig 3.18), it is observed that the residues exhibit both parallel as well as perpendicular π-π stacking orientations. The two aromatic rings are considered to have a parallel stacking orientation when the centroid distance between them is 4 Å $\pm$ 1 Å and the angle is 25° $\pm$ 5° while distance and angle cutoff of 5 Å $\pm$ 1 Å and 90° $\pm$ 30° respectively depicts a perpendicular orientation[44, 63].

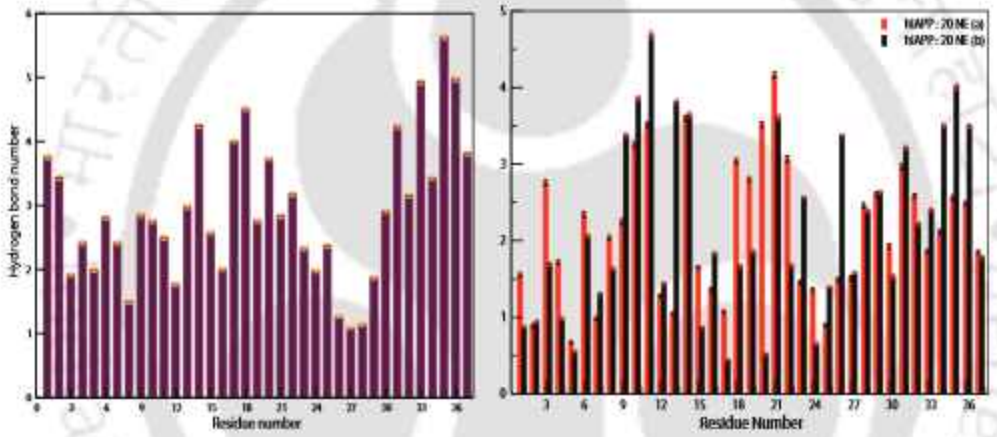

Figure 3.17: *Average hydrogen bond number of NE with each residue of hIAPP for hIAPP : 20 NE systems, along with the standard error bar of each value.*

The distance distribution portrays a sharp peak at 4.31 Å, 4.55 Å and 4.25 Å, while the angle distribution exhibits peaks at 20.6°, 26.7° and 30.11° for Phe15, His18 and Phe23 residues respectively (Fig 3.19). Therefore, it can be safely assumed that parallel π-π stacking is present for Phe15, His18 and Phe23 residues with the nearest NE molecule. Similarly, the highest probability is observed at a distance of 6.08 Å, 4.79 Å and 5.29 Å and an angle of 76.19°, 61.18° and 85.71° for residues Phe15, Phe23 and Tyr37 respectively indicating the possibility of perpendicular stacking with NE (Fig 3.20). We have also calculated the probability of stacking interactions for the control molecules (Fig 3.21). The most probable distances between Phe15, Phe23 and Tyr37 and the control molecules are around 10 Å or more, signifying the absence of stacking. The probability of stacking

between His18 and AS is negligible, considering the highest probable distance and angle between them. His18 may be involved in stacking interaction with BZ, but the probability is very low. Hence, we can conclude that, the control molecules are hardly involved in aromatic stacking interactions.

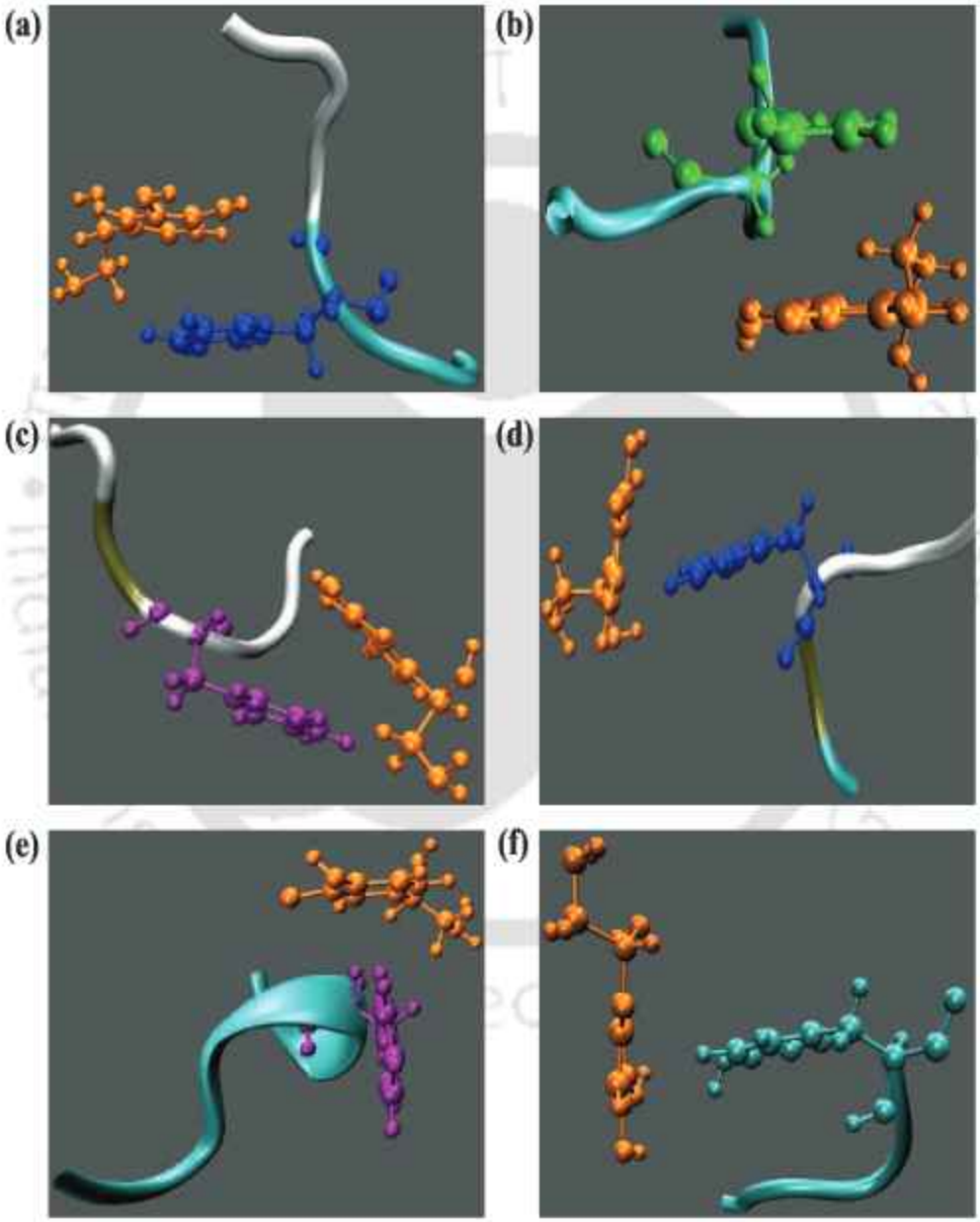

Figure 3.18: *A representative snapshot showing aromatic stacking orientation between NE (orange) and (a) Phe15 (blue), (b) His18 (green), (c) Phe23 (purple) in parallel alignment and (d) Phe15, (e) Phe23, (f) Tyr37 (cyan) in perpendicular alignment.*

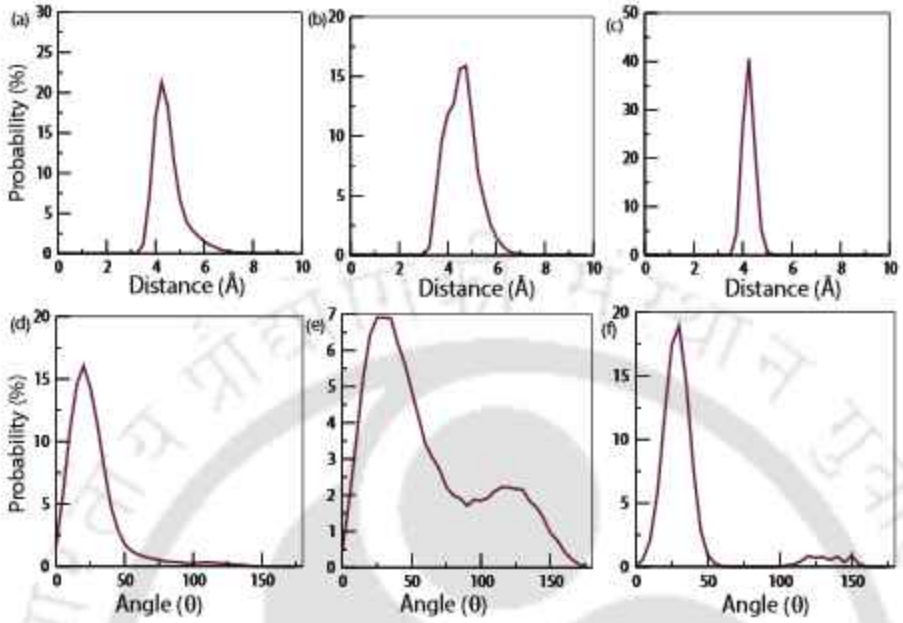

Figure 3.19: *The probability distribution of the centroid distance between the aromatic rings of (a) Phe15, (b) His18 and (c) Phe23 and NE and the angle between the aromatic planes of (d) Phe15, (e) His18 and (f) Phe23 and NE in parallel alignment.*

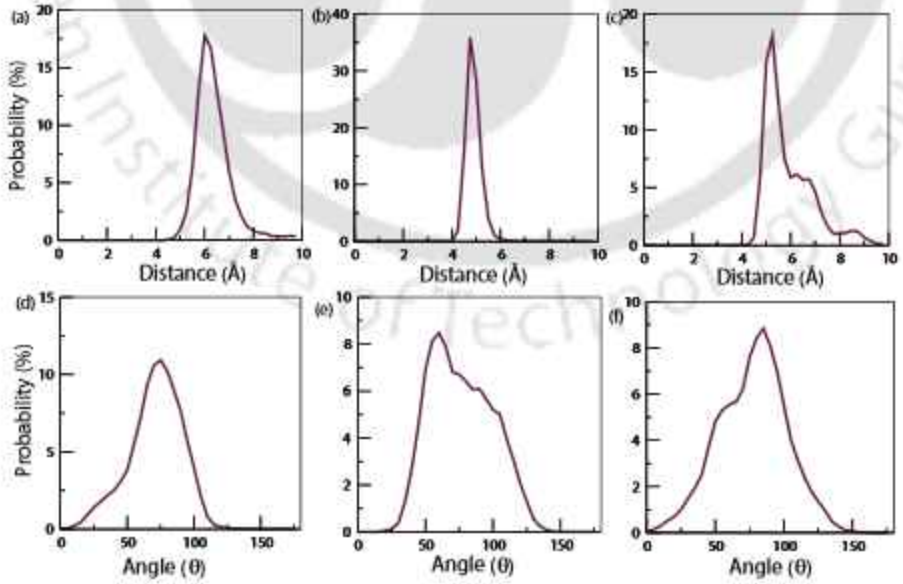

Figure 3.20: *The probability distribution of the centroid distance between the aromatic rings of (a) Phe15, (b) Phe23 and (c) Tyr37 and NE and the angle between the aromatic planes of (d) Phe15, (e) Phe23 and (f) Tyr37 and NE in perpendicular alignment.*

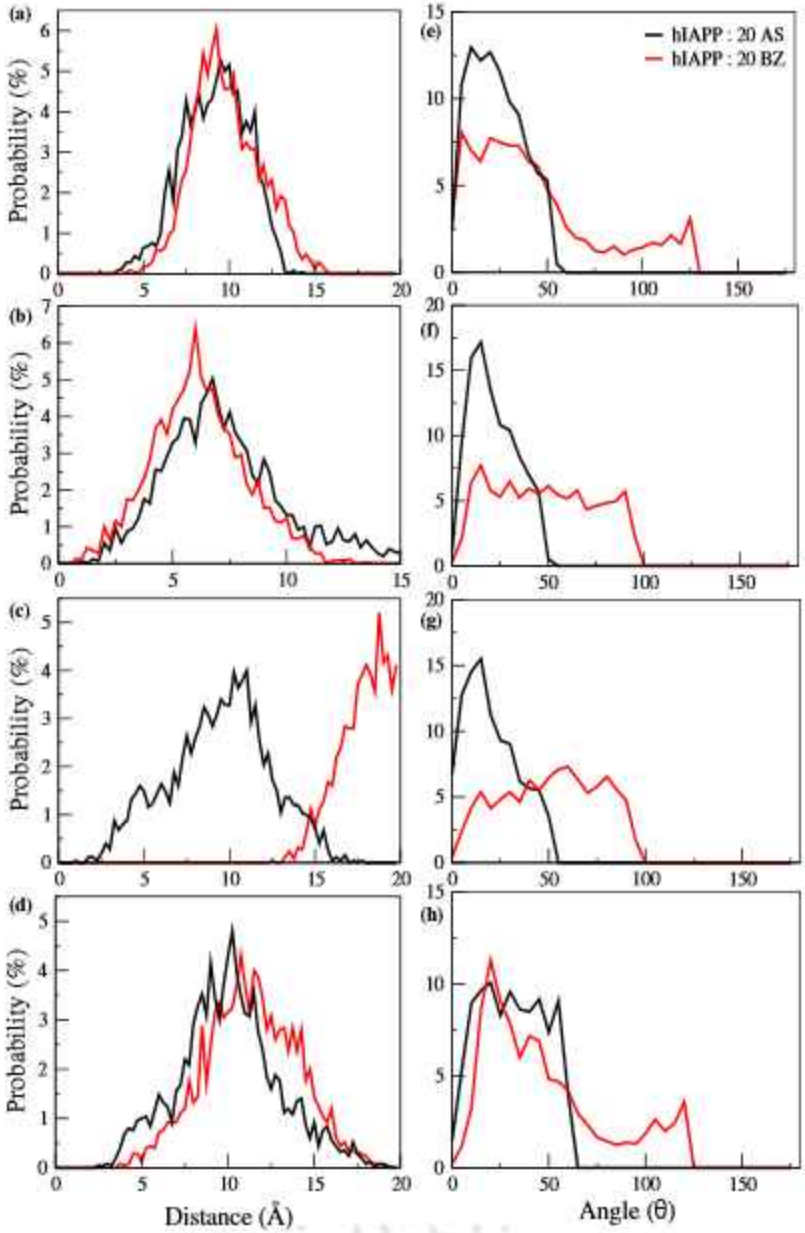

Figure 3.21: *The probability distribution of the centroid distance between the aromatic rings of (a) Phe15, (b) His18, (c) Phe23 and (d) Tyr37 and aspirin(AS)/ benzimidazole(BZ) and the angle between the aromatic planes of (e) Phe15, (f) His18, (g) Phe23 and (h) Tyr37 and the molecules.*

Arg11 also shows cation-π interaction with NE, which is analyzed by the distribution of the distance between the centre-of-mass of the aromatic ring of NE and that of NH_3^+ group of Arg11 and also of the angle formed between the corresponding planes (Fig

3.22). The cation-π interaction is considered when the centroid distance cutoff is 5 Å and the angle between them is less than 90°[44].

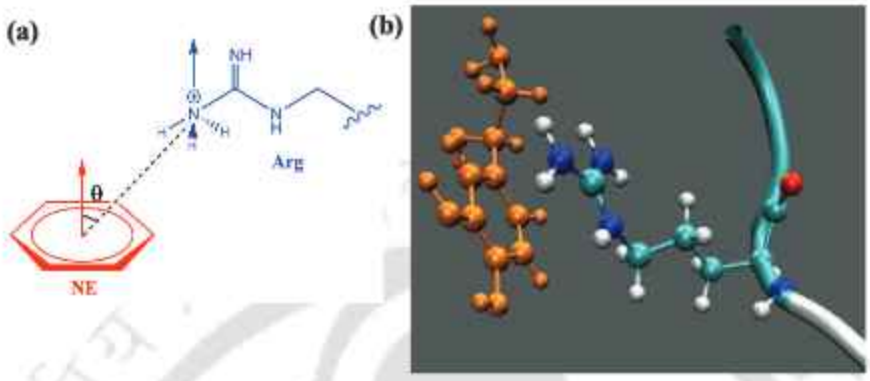

Figure 3.22: *(a) Schematic representation of stacking between the aromatic ring of NE and NH_3^+ group of Arg11 and (b) a snapshot showing the corresponding stacking orientation.*

From Fig 3.23, the maximum probability is observed at 3.76 Å and 86.56°, which clearly depicts the presence of cation-π interactions, which has been known to play an essential role in protein-protein and protein-ligand associations[64].

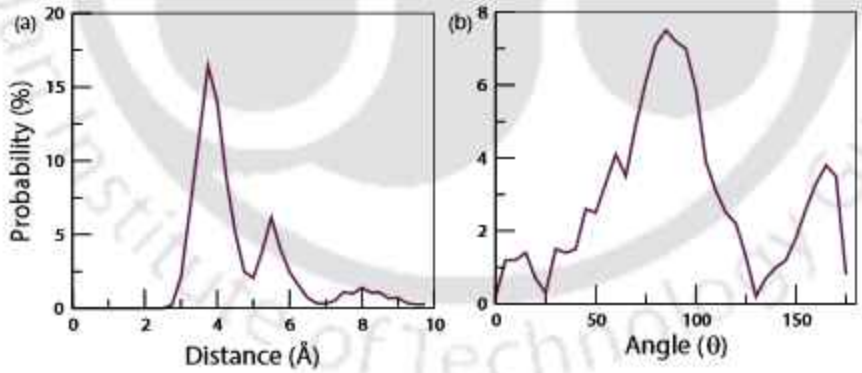

Figure 3.23: *The probability distribution of the (a) centroid distance between the aromatic ring of NE and NH_3^+ group of Arg11 and (b) the angle between them.*

Hence NE has shown to preferentially interact with the above mentioned polar, aromatic and hydrophobic residues illustrating that hydrogen bonding, aromatic stacking, cation-π and hydrophobic interactions play an important role in preventing oligomerization of hIAPP.

3.1.3.6 Disruption of hIAPP Protofibrils by Norepinephrine

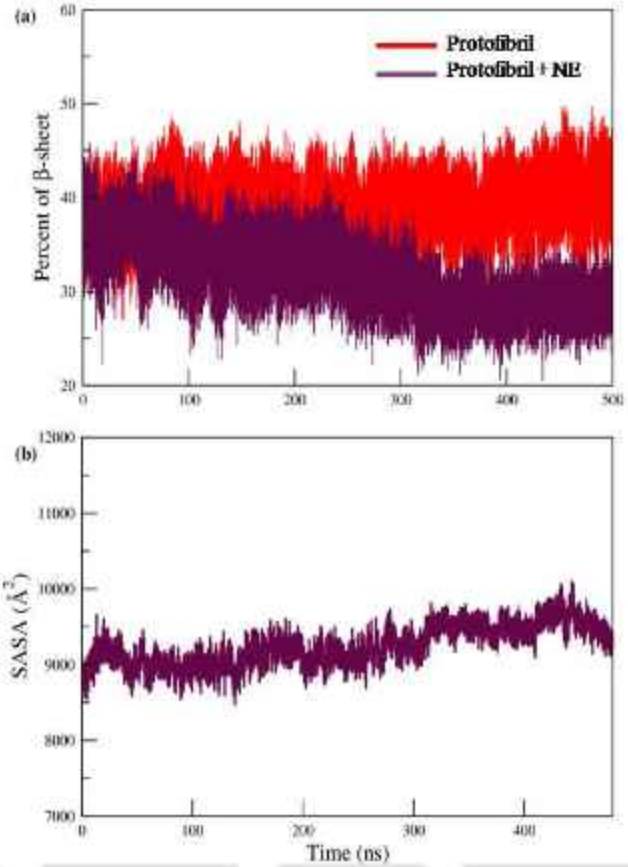

Figure 3.24: *Time evolution of (a) β-sheet content of hIAPP protofibril in different systems and (b) SASA of hIAPP protofibril in protofibril + NE system.*

From the previous analyses, we have deduced that NE has the ability to inhibit the β-sheet formation and the aggregation of hIAPP monomers. Now, we have to further investigate whether NE can disassemble the pre-formed amyloid fibrils. Hence, we have carried out all-atom MD simulations with hIAPP protofibril in the absence and the presence of NE for 500 ns. Here again, we observe that the probability of β-sheet of the peptides decreases drastically with simulation time in the presence of NE (Fig 3.24a). The ordered β-strands, especially those present at the edge chains, are disrupted (Fig 3.25), causing a decrease in the β-sheet content of the fibrils from 41.2% to 25.9%, while the coil propensity increases from 27.4% to 52.3% when NE is added to the system (Table 3.6 and Fig 3.26). The instability of the ordered structure of the peptides surrounded by NE is computed by the solvent accessible surface area (SASA) (Fig 3.24b), which is seen to increase by the end of

the simulation, depicting the disruption of peptide aggregates.

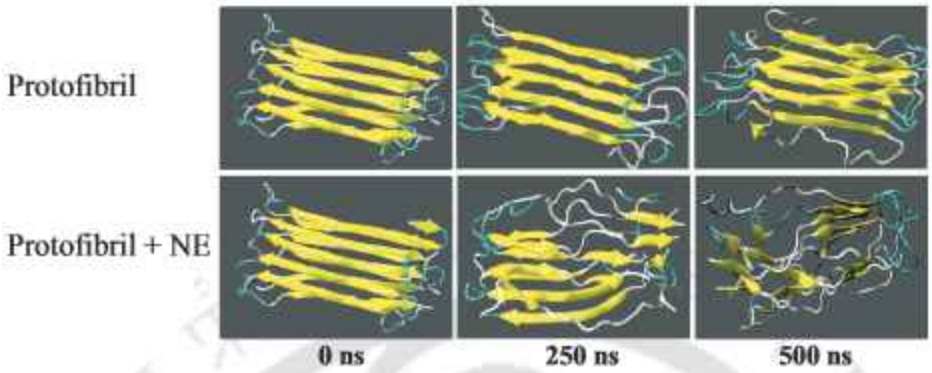

Figure 3.25: *Snapshots of hIAPP protofibril in different system at 250 ns time interval. The peptides are represented in cartoon form, depicting β-sheet in yellow, coil in white and bend in cyan.*

Representative snapshots reveal that the NE molecules gather mostly around the exterior surface of the fibrillar region, trying to break the inter-strand bonds, while some other extend into the interior surface, destabilizing the intra-strand bonds (Fig 3.27). The β-sheet propensity is the highest for residues Ala8-Val17 and Gly24-Val32 (Fig 3.28), which is analogous with the previous results[23, 42, 53].i In the presence of NE, the β-sheet content reduction is more pronounced for the C-terminal Gly24-Val32 residues, which is well in accordance with the result obtained earlier for random hIAPP peptides.

System		Protofibril	Protofibril+NE
β-sheet %	Parallel	39.16 ± 0.43	24.97 ± 0.38
	Anti-parallel	1.99 ± 0.11	0.95 ± 0.09
	Total	41.16	25.92
Helices %	3_{10}-helix	5.03 ± 0.15	0.06 ± 0.04
	α-helix	1.00 ± 0.04	0
	π-helix	0	0
	Total	6.03	0.06
Turn %		11.19 ± 0.24	7.09 ± 0.24
Bend %		14.21 ± 0.27	14.57 ± 0.30
Coil %		27.41	52.36

Table 3.6: *Different Secondary structure contents of hIAPP protofibril for different systems, along with the standard error of each value.*

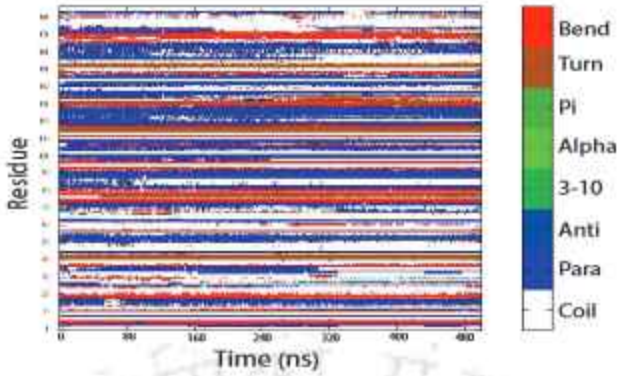

Figure 3.26: *Time series of secondary structure changes of each residue of hIAPP protofibril for protofibril + NE system .*

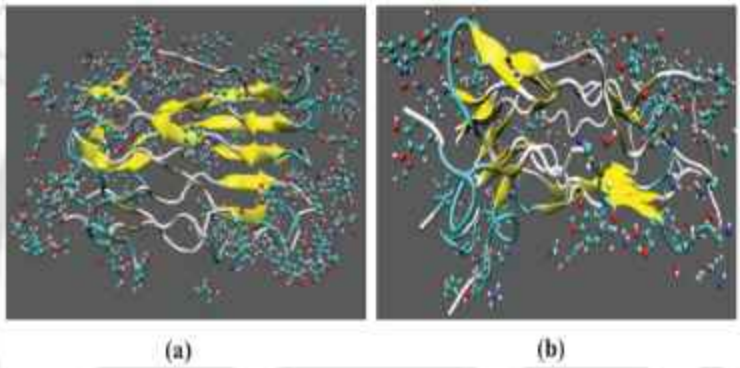

Figure 3.27: *Snapshots of the distribution of NE molecules around 5 Å of the hIAPP peptides viewing (a) perpendicular to, and (b) along the fibril axis for protofibril + NE system.*

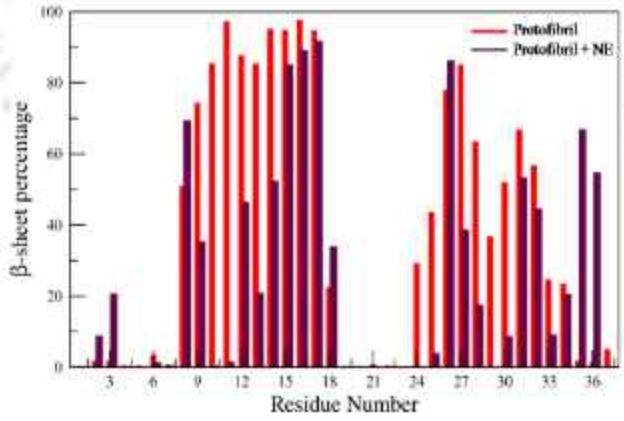

Figure 3.28: *The β-sheet content of hIAPP protofibril over each residue for different systems.*

Hence this again asserts that NE induces the peptides to remain disordered thus causing a significant decrease in the stability of the β-sheet conformation of the peptides. Moreover, the favourable interaction of NE with hIAPP protofibril is predicted from the binding free energy value (Table 3.5). Hence we can conclude that NE can partially disassemble the pre-formed fibrils.

3.1.4 Discussions

Starting with the random coil structure, we have seen that hIAPP has a tendency to aggregate into β-sheet conformation, which is inhibited when norepinephrine is added to it. The β-sheet rich peptides are destabilized, giving rise to disordered conformers. The conformational change of the peptides is established by the increased values of SASA and R_g of the peptides, suggesting that the peptide chains are unable to aggregate. The interaction between the peptides is reduced in presence of norepinephrine, which is emphasized by the contact maps, the unfavourable interaction energy values, the reduced peptide-peptide hydrogen bond number and finally the PMF results.

However, the inter-peptide interactions are hardly affected by aspirin or benzimidazole, which causes the peptides to self-aggregate, thus supporting previous reports[48, 50, 51]. The RDF and SDF analyses suggest that the control molecules are sparsely populated around the vicinity of hIAPP, which is also supported by the lower first shell coordination number. Therefore the interaction energy and the hydrogen bond number between hIAPP and the control molecules is much lower than that of NE. Further, the probability of stacking arrangement between the aromatic rings of aspirin or benzimidazole and that of hIAPP residues is also negligible. Hence, we can conclude that the control molecules have a very low interaction affinity towards hIAPP, due to which they are unable to prevent its aggregation. The low binding affinity of aspirin with hIAPP has been reported in an earlier study[52].

Further, in-depth secondary structure analyses reveal that the residues Thr9-His18 and Ile26-Asn31 of hIAPP, primarily, participate in both intra and inter-peptide β-strand formation. RDF values also confirm the strong interactions between the Leu12-His18 and Leu27-Gly33 regions, which is affected by the presence of NE. These β-strand regions resemble with that of the hIAPP fibrillar structure. The first shell coordination number of norepinephrine in the first solvation shell of the peptides highlights that the NE molecules

are concentrated around the residues, which are mostly involved in β-sheet formation.

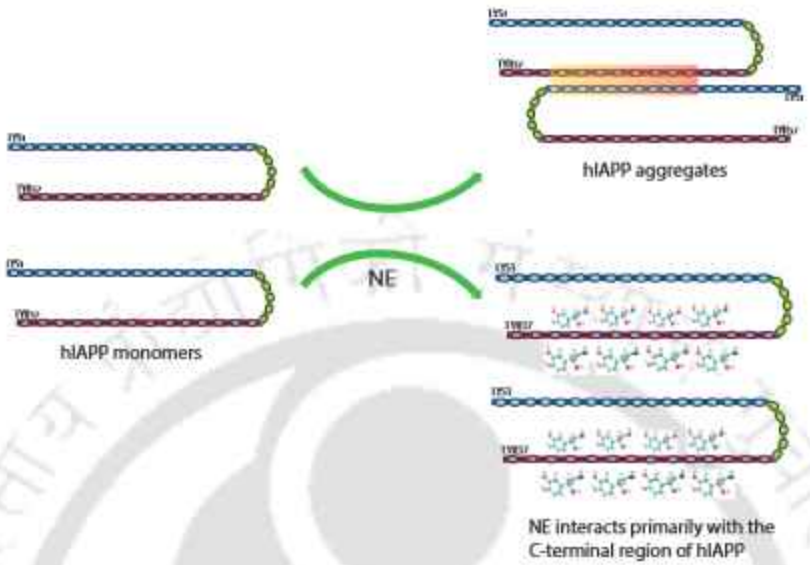

Figure 3.29: *A schematic representation depicting the effect of NE on the aggregation of hIAPP.*

The binding energy calculations reveal that NE preferentially interacts with the Cys2, Asn3, Cys7, Arg11, Leu12, Phe15, His18, Asn22, Phe23, Ile26-Gly33, Asn35-Tyr37 residues, that is, mostly with the C-terminal region. Moreover, the β-sheet probability of the C-terminal residues is primarily affected by the addition of norepinephrine. The residue-wise hydrogen bond calculations revealed the strong hydrogen bonds formed by the hydroxyl groups of NE with the polar residues. The hydrophobic residues also strongly interact with the NE molecules. The aromatic residues (Phe15, His18, Phe23, Tyr37) are also involved in stacking interactions with the aromatic ring of NE. The binding probability of Phe 15 with NE is much lower than that of Phe23, which is probably due to the position of the two Phe residues, where one (Phe23) is present at the C-terminal end (leading to better interaction with NE) while the other (Phe15) is buried within the peptide. Arg11 is also involved in cation-π interactions with NE. Hence interaction of NE with these residues hinders the formation of ordered β-sheets.

There have been numerous studies illustrating the importance of Phe residues in the aggregation of hIAPP and also other amyloid peptides[62]. His18 and Arg11 also plays an essential role in the fibril formation of hIAPP[10, 65]. Moreover, mutation of

Phe15/Phe23/Tyr37 also led to the conformational change of hIAPP, enforcing the importance of these residues[66]. Several mutational effects on His18 have shown a marked difference on the rate of fibrillation.

Hence, it can be speculated that, hIAPP aggregation is enhanced by the β-strands formed between the Leu12-His18 and Leu27-Gly33 regions. This is hampered as NE molecules preferentially interacts with one such region (C-terminal region), thus, inhibiting the aggregation (Fig 3.29). The hydrogen-bond, hydrophobic, aromatic and cation-π interactions of NE with the mentioned residues significantly contributes in preventing oligomerization of hIAPP. Moreover, the pre-formed hIAPP fibrils are also disrupted by NE.

3.1.5 Conclusion

In this study, we have investigated the effect of norepinephrine on the inhibition and destabilization of the hIAPP oligomers via all-atom molecular dynamics simulation (a total of 4.9 μs simulation run). Through a series of analyses, we observed that norepinephrine prohibits hIAPP monomers to form β-sheet rich aggregates, thus inhibiting hIAPP fibrillation and urges the peptides to remain disordered. However, the self-association of the peptides is hardly affected by aspirin or benzimidazole, due to their insufficient interaction with the peptides. Hence they are unable to prevent the aggregation of hIAPP. NE, on the other hand, disrupts the stable hydrogen-bond and hydrophobic interactions between the peptides by itself interconnecting with the peptides, via hydrogen bond, hydrophobic, π-π and cation-π interactions. The regions, which stabilize the β-sheet formed between the peptides, interact preferentially with NE molecules (especially the C-terminal residues of hIAPP), disrupting the formation of ordered aggregates. Moreover, the pre-formed hIAPP fibrils are also destabilized by NE. Hence our work features the inhibitory mechanism of hIAPP by norepinephrine with a detailed binding mode analysis. This study provides a valuable information about the inhibition mechanism of small molecules with anti-amyloid aggregation properties and can be extended to study other amyloid peptides.

3.2 Potential of ATP towards Prevention of hIAPP Oligomerization and Destabilization of hIAPP Protofibrils: an *In Silico* Perspective

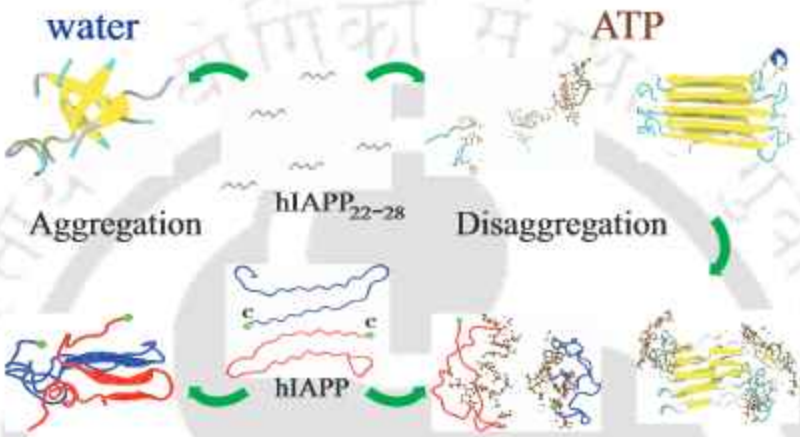

3.2.1 Introduction

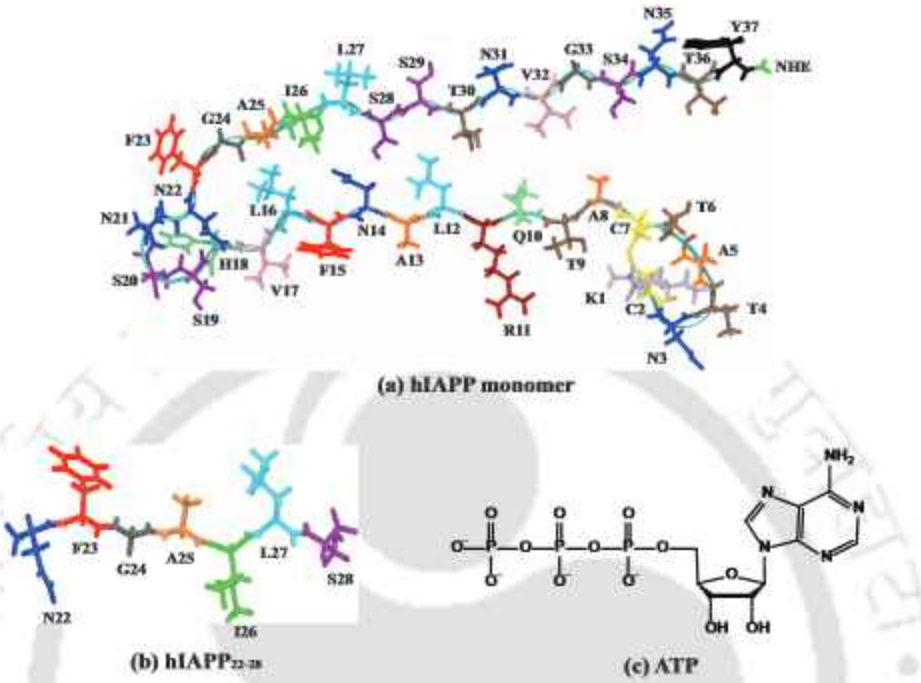

Figure 3.30: *Structures of (a) full length hIAPP monomer, (b) $hIAPP_{22-28}$ segment and (c) ATP.*

Recently, Patel et al. revealed that adenosine triphosphate (ATP) (Fig 3.30c), which is the powerhouse of energy driving the chemical reactions in biological medium, has the ability to prevent the aggregation of Aβ peptides and boiled egg white at millimolar concentration[67]. This new role of ATP is analogous to the activity of hydrotropes, which specializes in solubilizing hydrophobic compounds in aqueous media. The endogenous hydrotropic action of ATP on the protein aggregates in Xenopus oocyte nuclei has also been reported by Haynes et al[68]. The suitability of ATP as a biological hydrotrope is based on the fact that it contains both hydrophobic adenosine and charged triphosphate moieties, making it possible to interact with the hydrophobic as well as the hydrophilic amino acid residues. A recent all-atom molecular dynamics study suggested that ATP alters the thermal equilibrium of Aβ oligomers to the one favouring off-pathway species, thus dissolving previously formed Aβ fibril[62, 69]. As mentioned in the previous study (Chapter 3.1), compounds which inhibit the aggregation of both Aβ and hIAPP peptides are the new therapeutic target[7, 8, 10, 31, 38, 39, 41–44]. Hence, in this study, taking advantage of this novel role of ATP,

we investigate whether ATP can also prevent the aggregation or disassemble pre-formed aggregates of hIAPP.

Keeping that in mind, we have performed molecular dynamics simulations of hIAPP in absence and presence of ATP in explicit solvent. Initially the effect of ATP on five $hIAPP_{22-28}$ fragments, consisting of $N^{22}FGAILS^{28}$ sequence, is studied. The $N^{22}FGAIL^{27}$ segment (Fig 3.30b) is reported to be the shortest fibrillogenic sequence which induces aggregation and is often treated as the amyloid-core of the full length hIAPP[70, 71]. Structural study of $N^{22}FGAILS^{28}$ by the X-ray diffraction method revealed that this segment form out-of-register anti-parallel β-strands[72, 73]. In addition, the influence of ATP on two full-length hIAPP peptides, which are sufficiently separated, is also investigated, in order to provide a better understanding of the binding of ATP with hIAPP. The simulation results clearly point that ATP interferes with the formation of ordered β-sheet structure, due to which the peptides remain in loosely-packed, coil conformation. The hydrogen bonding, hydrophobic, π-π and N-H-π stacking interactions between ATP and hIAPP effectively reduces the interaction between the peptides. Moreover, the destabilization effect of ATP on hIAPP protofibrils is also analyzed, where we observe that ATP preferentially interacts with the N-terminal and the turn regions.

The remaining of the chapter is classified into the Simulation Method, which states the in-detail methods used for simulations and analyses and Results and Discussions sections, which clearly outlines the findings. Lastly the deduction of this work is mentioned in the Conclusion.

3.2.2 Simulation method

3.2.2.1 Simulation Setup

The effect of ATP on the amyloid formation of hIAPP was examined by a series of classical molecular dynamics simulations of $hIAPP_{22-28}$ as well as hIAPP dimer and two different protofibrils in absence and presence of ATP. The crystallographic structure of $hIAPP_{22-28}$ was taken from protein data bank (PDB id: 5E5V)[72]. The full length hIAPP monomer and one pentameric protofibril were extracted from the ssNMR structure[53]. The other protofibrillar structure was extracted from the hIAPP fibrillar polymorph constructed us-

ing cryo-EM methods (PDB: 6Y1A)[74]. The ATP molecules were modelled using the polyphosphate parameters of the AMBER force field[75, 76]. Initially five $hIAPP_{22-28}$ fragments, which were sufficiently separated, were placed in an octahedral box. Then adequate number of ATP was added depending upon the required ATP concentration. The required numbers of Mg^{2+}[77] ions were added to neutralize the ATP molecules. The dimer and protofibril systems were similarly initiated with two randomly spaced hIAPP monomers and a hIAPP protofibril respectively. Each of the simulation was conducted for 1000 ns, following simulation protocols mentioned in Chapter 1 (Section 1.5.2). The details of all the systems are presented in Table 3.7.

System	N_{frag}	N_{mono}	N_{fibril}	N_{ATP}	N_w	C_{ATP}
Frag	5			0	5000	0
Frag(a)	5			0	5000	0
Frag+20ATP	5			20	5000	0.16
Frag+25ATP	5			25	5000	0.19
Frag+30ATP	5			30	5000	0.23
Frag+30ATP(a)	5			30	5000	0.23
Dimer		2		0	5000	0
Dimer(a)		2		0	5000	0
Dimer+ATP		2		30	5000	0.23
Dimer+ATP(a)		2		30	5000	0.23
Protofibril			1	0	10000	0
Protofibril(a)			1	0	10000	0
Protofibril_cryo			1	0	10000	0
Protofibril+ATP			1	45	10000	0.21
Protofibril+ATP			1	45	10000	0.22
Protofibril_cryo+ATP			1	0	10000	0.17
Frag-PMF	2			0	4000	0
Frag-PMF+ATP	2			12	4000	0.12

Table 3.7: *Details of the simulated systems. N_{frag}, N_{mono}, N_{fibril}, N_{ATP}, N_w and C_{ATP} represent the number of $hIAPP_{22-28}$, full length hIAPP monomer, hIAPP protofibril, ATP and water molecules and the molar concentration (in M) of ATP respectively.*

One set of simulation each considering two $hIAPP_{22-28}$ segments in absence and presence of ATP was also done for potential of mean force (PMF) calculations. In total, 18 molecular dynamics simulations were performed, each starting with different initial configurations.

3.2.2.2 Simulation Analysis

The simulation analyses were carried out following the protocols discussed in Chapter 1 (Section 1.5.3). The spatial distribution functions of ATP around the peptides were estimated with an isovalue of 1. The first solvation shell coordination number of ATP was calculated by considering the number of ATP molecules that were present within 3.5 Å of the peptides[78].

The free energy landscape (FEL) representing π-π stacking interaction was constructed as a function of the distance between the centre of mass of the aromatic rings and also the angle formed between the vector normals of the respective aromatic rings, following the equation 1.19.

The potentials of mean force (PMFs) were calculated following the umbrella sampling method[59]. For this, two $hIAPP_{22-28}$ peptides were simulated, without and with ATP for 500 ns. The final trajectory was then used to estimate the PMFs between the Cα atoms of the $hIAPP_{22-28}$ peptides. The distance between the centre of mass of the backbone Cα atoms of the peptides was changed from 3 to 20 Å, with an increment of 0.25 Å, resulting in 69 windows. The peptides were pulled with a force constant of 1 kcal mol^{-1} Å^2 at 300 K. For each window, the system was subjected to 10 ns of equilibration and 20 ns of production run, leading to a total of 2.07 μs simulation for each of the two systems. The PMFs considering the centre of mass of the phenyl ring of the Phe23 residue was also calculated following the above method. Hence a total of 8.28 μs of simulation run was conducted. The PMFs were finally obtained by analyzing the results using WHAM[60, 61].

3.2.3 Results

3.2.3.1 Effect of ATP on the Secondary Structures of $hIAPP_{22-28}$

The formation of β-sheet aggregates is considered to be the principal characteristic of intrinsically disordered proteins according to the amyloid cascade hypothesis. Hence, we have calculated the evolution of β-sheet formation of $hIAPP_{22-28}$ with time progression throughout the simulation run (Fig 3.31). It is observed that the β-sheet probability increases with time, suggesting that the peptides, which are initially far apart, self aggregate within a few

nanoseconds into a β-sheet arrangement. However, in presence of ATP, the probability of β-sheet is much less and becomes almost negligible with increase in concentration of ATP. For further analysis, the change in each of the secondary structure contents is presented in Table 3.8, where we notice that, the β-sheet percentage is the highest for the system with no ATP (43.06%).

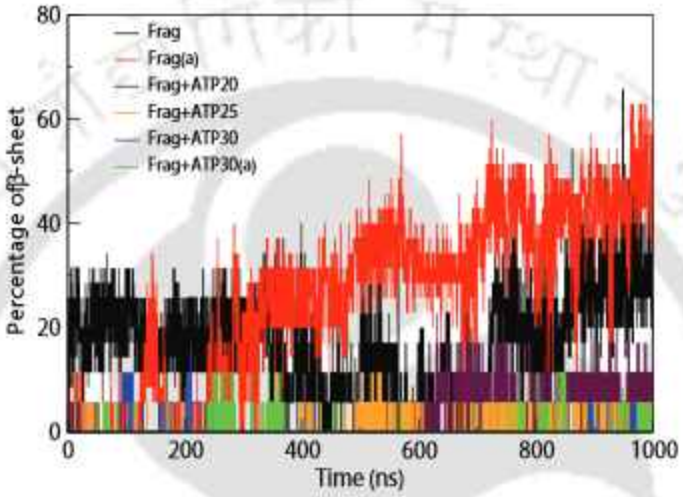

Figure 3.31: *Time evolution of β-sheet content of $hIAPP_{22-28}$ in different systems.*

System	Ext-β	Bridge-β	Helix	Turn	Bend	Coil
Frag	41.5 ± 0.4	1.6 ± 0.3	3.3 ± 0.4	2.6 ± 0.5	33.3 ± 0.6	17.8
Frag(a)	25.9 ± 0.5	10.9 ± 0.3	0.2 ± 0.0	8.5 ± 0.2	41.1 ± 0.4	13.4
Frag+ATP20	0	0.3 ± 0.0	11.4 ± 0.1	12.5 ± 0.2	39.8 ± 0.3	36
Frag+ATP25	0.1 ± 0	7 ± 0.2	0	8.5 ± 0.2	38.6 ± 0.4	45.8
Frag+ATP30	0	0	0.5 ± 0.1	1.6 ± 0.1	43.2 ± 0.7	54.7
Frag+ATP30(a)	0	0.0 ± 0	1.0 ± 0.3	4.0 ± 0.5	50.3 ± 0.7	44.7

Table 3.8: *The secondary structure contents of $hIAPP_{22-28}$ for different systems.*

However, a marked decrease is observed in this value, upon binding with ATP. With increasing concentration of ATP, the β-sheet percentage almost vanishes (0.002%) and the coil percentage increases from 17.81% to 54.72%. Hence the dominant secondary structure of $hIAPP_{22-28}$ switches from β-sheet to random coil, which concludes that ATP molecules have a major influence on the secondary structure composition of hIAPP.

In order to identify the effect of ATP on the secondary structure of particular amino acid residues, the percentage of β-sheet and coil content of each residue of hIAPP is also estimated. We observe that the residues Gly24, Ala25 and Ile26 have the highest content of β-sheet, followed by Phe23 (Fig 3.32a). Hence the hydrophobic residues are primarily responsible for the formation of ordered β-sheets. Consequently, the terminal polar residues, Asn22 and Ser28, have the maximum coil probability (Fig 3.32b). When ATP is added to the system, the β-sheet probability is negligible and the coil percentage increases for all the residues. From the snapshots of various systems (Fig 3.33), it is also perceived that the well separated peptides instantly aggregate in absence of ATP, giving rise to stable β-sheets. However, the peptides remain widely separated from each other in presence of ATP, giving rise to random coil conformation.

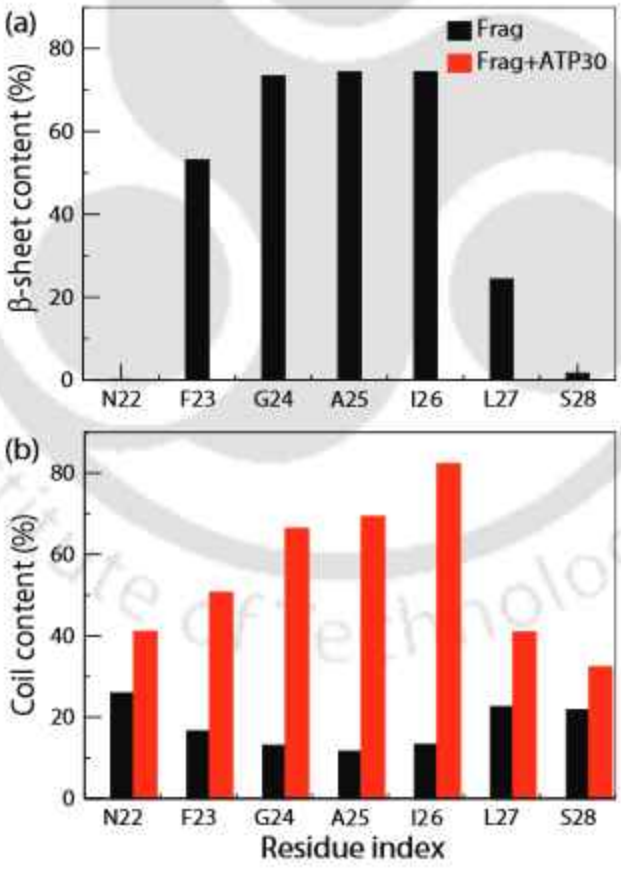

Figure 3.32: *Effect of ATP on: (a) β-sheet and (b) coil percentages for each residue of $hIAPP_{22-28}$ for different systems.*

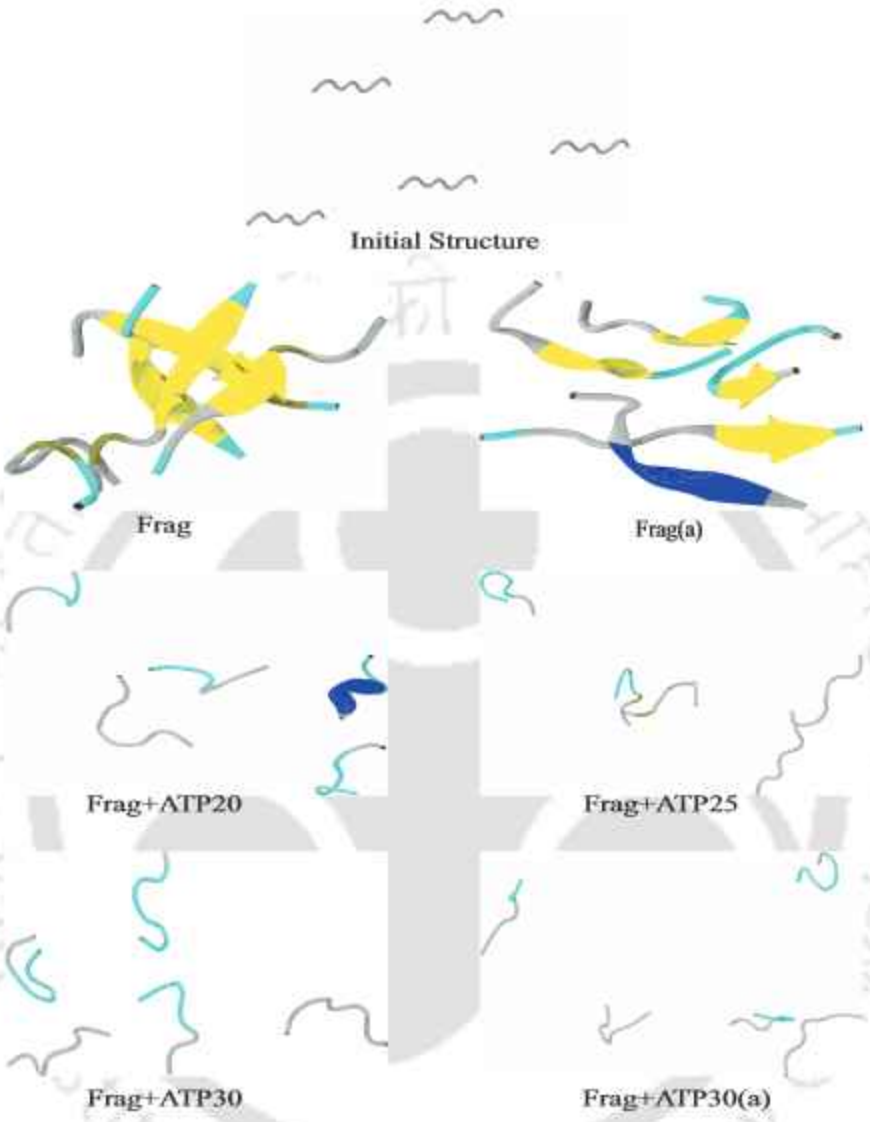

Figure 3.33: *Snapshots of five hIAPP$_{22-28}$ peptides in different systems at the end of simulation time. The peptides are represented in cartoon form, depicting β-sheet in yellow, coil in silver, bend in cyan and 3_{10}-helix in blue.*

3.2.3.2 Conformational Changes of hIAPP$_{22-28}$ in Presence of ATP

To understand the effect of ATP on the interactions between the hIAPP$_{22-28}$ peptides, the contact map considering the Cα-Cα atoms between all pairs of residues is analyzed (Fig 3.34). The Cα atoms of most of the residues are in close contact with each other for the hIAPP$_{22-28}$ fragment system. However, a marked decrease in the dark spots is observed for

the ATP systems, signifying that the distance between the Cα atoms increases, especially with increasing ATP concentration. Hence it is further confirmed that the peptides are far apart from each other in presence of ATP, thus resulting in low pairwise residue-residue inter-peptide contact.

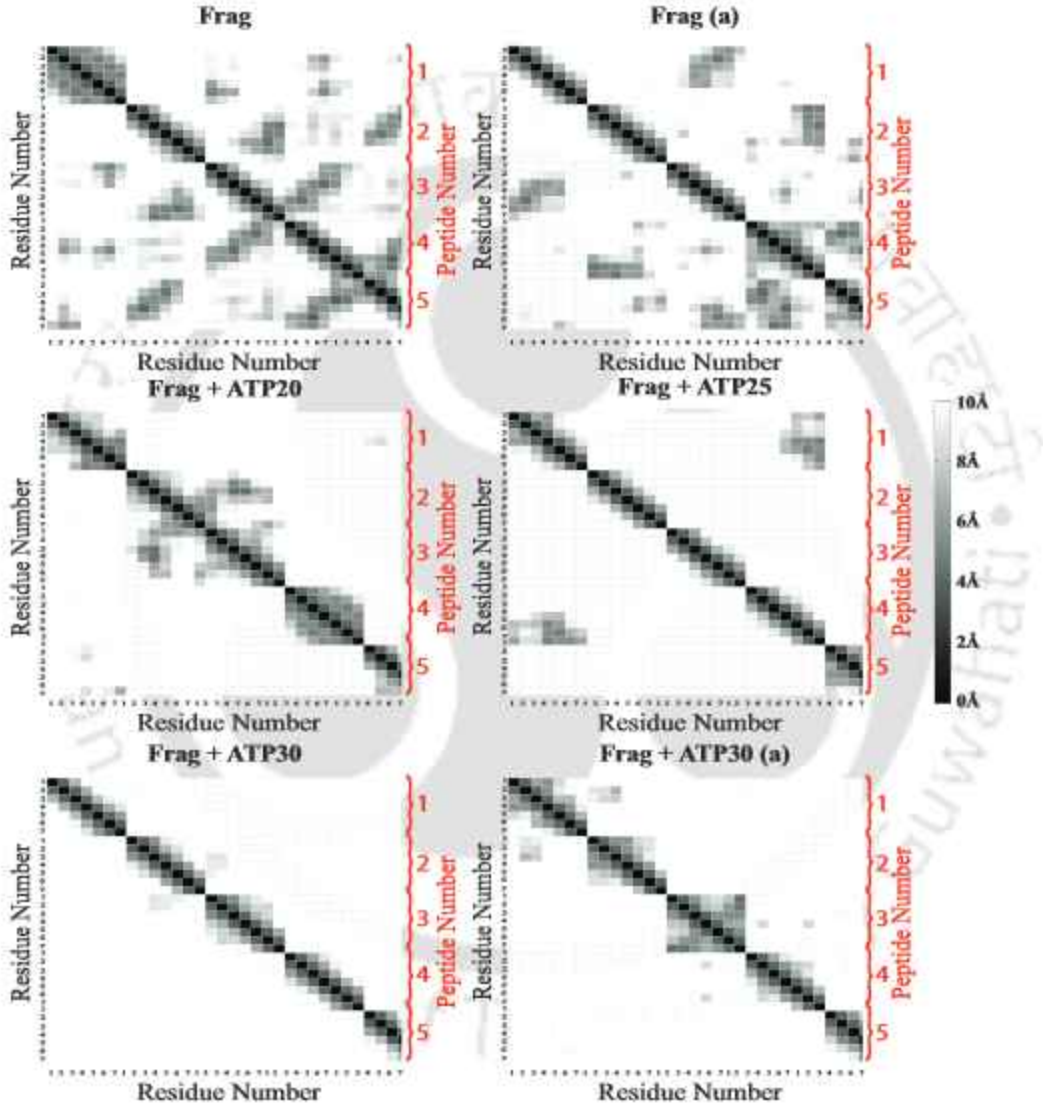

Figure 3.34: *Residue-residue contact map of the $hIAPP_{22-28}$ peptides for different systems.*

The interception of ATP on the aggregation of $hIAPP_{22-28}$ is reflected by the structural changes of the peptides in absence and presence of ATP. Hence the solvent accessible surface area (SASA) of the $hIAPP_{22-28}$ fragments is calculated, where it is seen

that, in absence of ATP, SASA is much lower than that in presence of ATP (Table 3.9). Moreover, an increase in SASA is also observed with increasing concentration of ATP. Since, SASA represents the area available for solvation by solvent molecules, lower values of SASA indicate more aggregation between the peptides and, hence, less is the available solvation area. The radius of gyration (R_g) further gives a measure of the compactness of the peptides, hence higher R_g values is indicative of a loosely packed and disordered conformer (Table 3.9).

System	SASA (Å^2)	Rg (Å)
Frag	2330 ± 41.36	9.74 ± 0.7
Frag(a)	2349 ± 45.52	9.84 ± 0.65
Frag+ATP20	3210 ± 16.32	17.61 ± 0.46
Frag+ATP25	3204 ± 20.12	16.35 ± 0.37
Frag+ATP30	3511 ± 14.13	20.93 ± 1.64
Frag+ATP30(a)	3329 ± 12.59	20.61 ± 0.59

Table 3.9: *Solvent Accessible Surface Area (SASA) and Radius of gyration (R_g) of $hIAPP_{22-28}$ for different systems.*

Together with the SASA values, it is clear that, ATP promotes the segregation of the peptides and hence inhibits hIAPP to form a compact oligomerized structure.

Interactions		**Peptide-Peptide**		**Peptide-ATP**	
Contributions		**Ele**	**vdW**	**Ele**	**vdW**
Systems	**Frag**	-281.6±10.4	-11.5±3.3	–	–
	Frag(a)	-199.5±13.2	-12.5±2.4	–	–
	Frag+ATP20	-149.4±8.7	2.3±0.2	-183±8.1	-26.1±2.2
	Frag+ATP25	-142.3±5.5	0.7±0.2	-243.2±10.9	35.7±2.6
	Frag+ATP30	-134.1±6.9	5.7±1.6	-431±20.5	-38.1±1.7
	Frag+ATP30(a)	-142.6±5.2	7.1±1.6	-358.6±17.4	-37.4±3.4

Table 3.10: *Decomposition of peptide-peptide and peptide-ATP interaction energies (in kcal/mol) of $hIAPP_{22-28}$ for different systems.*

The modification in the peptide-peptide interactions due to the ATP molecules is further analyzed by the interaction energy between the peptides (Table 3.10), where the total interaction energy is divided into electrostatic as well as van der Waals components. The electrostatic energy is more negative than the van der Waals component, indicating

that the former dominates over the latter. The interactions in-between the peptides become unfavourable with increasing ATP concentration for both the energy components. Hence it is further confirmed that ATP helps in the reduction of the interaction between the peptides. Further, hydrogen bond interactions play a very important role in the stabilization of oligomers, especially in the formation of β-sheets[62]. On considering the number of hydrogen bonds formed between the peptides for each hIAPP$_{22-28}$ fragment (Table 3.11), we observe a significant decrease in the average hydrogen bond number, with increasing ATP molecules, indicating that the peptide-peptide hydrogen bonds are broken, due to which the peptide aggregation is hindered.

System	Peptide-peptide	Peptide-ATP
Frag	3.87 ± 0.7	–
Frag(a)	3.74 ± 0.8	–
Frag+ATP20	1.52 ± 0.42	2.69 ± 0.46
Frag+ATP25	0.92 ± 0.32	3.13 ± 0.72
Frag+ATP30	0.51 ± 0.3	4.99 ± 0.5
Frag+ATP30(a)	0.98 ± 0.4	4.35 ± 0.8
Dimer	21.59 ± 1.95	–
Dimer(a)	18.89 ± 1.94	–
Dimer+ATP	11.97 ± 1.42	17.27 ± 2.75
Dimer+ATP(a)	12.48 ± 1.75	15.21 ± 1.5

Table 3.11: *Average hydrogen bond numbers of hIAPP$_{22-28}$ and hIAPP dimer between peptide-peptide and peptide-ATP interactions for different systems.*

The radial distribution functions (RDFs) between the hIAPP$_{22-28}$ fragments is calculated considering the centre of mass of the backbone (Fig 3.35a) as well as the side-chain atoms (Fig 3.35b) of the peptide fragments. For the hIAPP fragment system, a sharp peak at around 3.5 Å is observed, but with the addition of ATP, the maximum, which now has a much less intense peak, shifts to a higher distance. Moreover, on increasing the concentration of ATP, the distance at which the first maximum appears also increases. This further proves that the contact between the peptide fragments is hindered by ATP. Since π-π stacking interaction between the Phe residues enhances the stability of the ordered β-sheets[28], the RDFs between the Phe23 residues is also calculated to analyze the effect of ATP on the Phe-Phe interactions. The maximum RDF considering the centre of mass of the backbone atoms of Phe23 appears at 4.85 Å, but the peak shifts beyond 10 Å in

presence of ATP (Fig 3.35c). The RDF between the side chain aromatic ring of Phe23 appears at 5.25 Å, hinting the existence of π-π stacking arrangement between them (Fig 3.35d). However, here also, ATP interrupts the Phe-Phe stacking interactions.

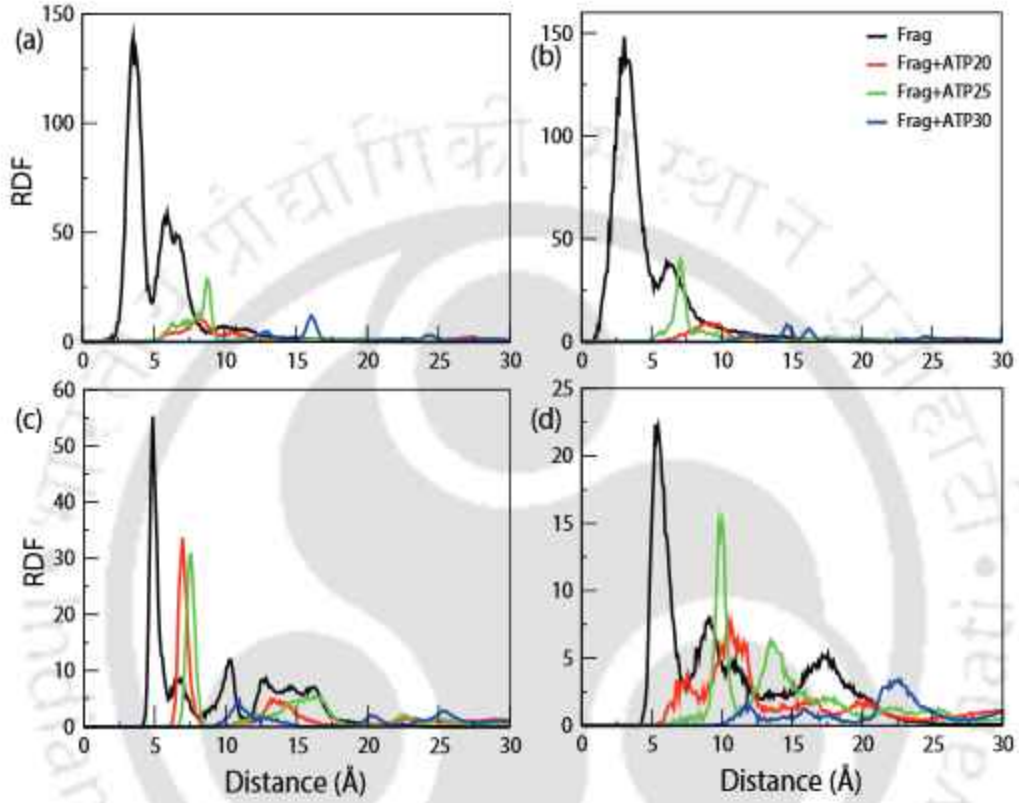

Figure 3.35: *Radial distribution functions between center of mass of (a) backbone and (b) side chain of $hIAPP_{22-28}$ and (c) backbone and (d) side chain of Phe23 for different systems.*

Since hIAPP has a high tendency to aggregate with itself, the $hIAPP_{22-28}$ fragments prefer to interact with each other rather than the solvent water molecules, which is further confirmed by the calculation of the preferential interaction parameter (Γ_{pw}). From Fig 3.36a, it can be observed that, Γ_{pw} for the hIAPP system has a high positive value, but the incorporation of ATP led to a marked decrease in Γ_{pw}, which eventually has a negative value. From equation 1.18, a positive Γ_{pw} value indicates that the peptides preferentially interact with each other, leading to its self-assembly. On the other hand, when peptides interact more with water, i.e., higher peptide solvation occurs, Γ_{pw} tends to be negative, indicating lower aggregation propensity. This further proves that, hIAPP, in the control

system, preferentially interact with itself, causing aggregation. However, in presence of ATP, this preference is reduced, and the peptides interact more with the solvent molecules, due to which they remain in random coil conformation.

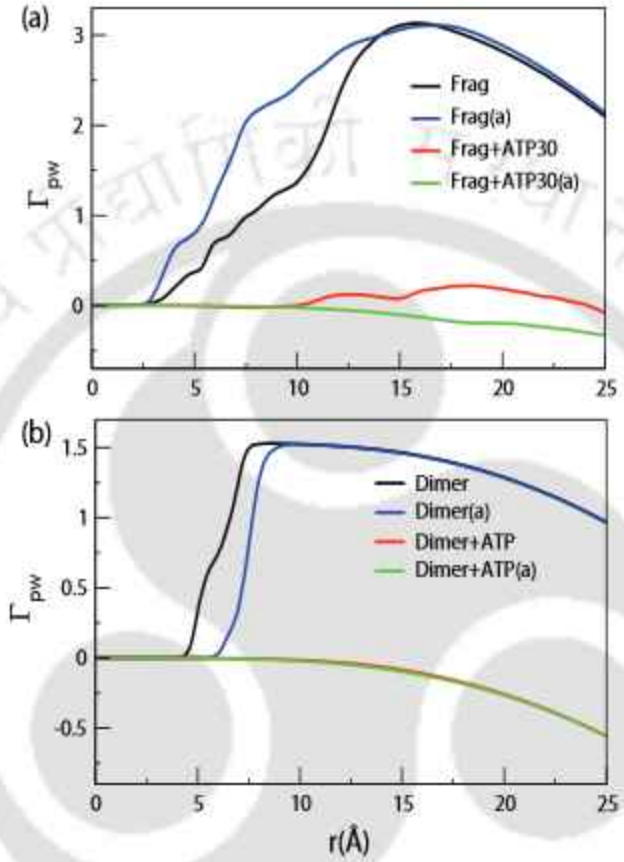

Figure 3.36: *Preferential interaction parameters of the (a) $hIAPP_{22-28}$ peptides and (b) hIAPP dimer for different systems.*

3.2.3.3 Potentials of Mean Force

To further examine the impact of ATP on the aggregation of the $hIAPP_{22-28}$ fragments, we have calculated the potentials of mean force (PMFs) of association between two $hIAPP_{22-28}$ fragments (Fig 3.37a). The PMF is calculated as a function of the distance between the centre of mass of the backbone Cα atoms of the fragments. In absence of ATP, the free energy minimum is observed at 5.09 Å, which implies that the interactions between two $hIAPP_{22-28}$ fragments is most stable when the distance between them is 5.09 Å. However, the minimum increases (PMF becomes unfavourable) on addition of ATP, pointing to the

fact that the interconnection of the two peptides is destabilized by ATP. Since π-π stacking between the two phenyl rings in Phe23 is critical for the self-association of hIAPP[79], the free energy profile considering the distance between the centre of mass of the phenyl ring of two Phe23 is also estimated (Fig 3.37b). Here also, we observe that, the stability between the two aromatic rings is maximum at 5.58 Å. With the addition of ATP, the stacking interaction between the two aromatic rings is inhibited, thus causing an increase in the free energy value. Thus, it is clear that the aggregation of $hIAPP_{22-28}$ is unfavourable in presence of ATP.

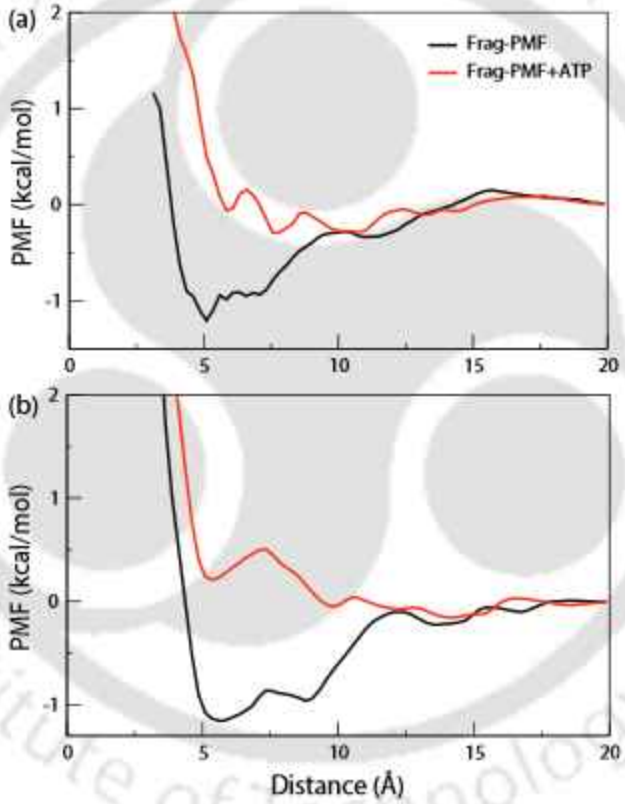

Figure 3.37: *Potential of mean force of two $hIAPP_{22-28}$ between the centre of mass of (a) the peptides and (b) the side chain of Phe23 for different systems.*

3.2.3.4 Effect of ATP on the Aggregation of Full Length hIAPP Dimer

The previous sections provide substantial evidence proving that ATP has the ability to inhibit the aggregation of $hIAPP_{22-28}$ and also certifies the concentration at which ATP can best act as an inhibitor. In this section, we focus on the effect of ATP on two full

length hIAPP to obtain a thorough understanding of the inhibition mechanism. From the snapshots (Fig 3.38), we can see that the two peptides are initially set apart and, with progression of time, arrange themselves in an ordered β-sheet conformation. However, the peptides are disassembled and randomly spaced in the system containing ATP. In order to examine the effect of ATP on the change of peptide conformation, we have calculated the change in β-sheet formation and SASA of the hIAPP dimer with time. Here also, a decrease in the β-sheet content of the dimer is observed in presence of ATP (Fig 3.39a).

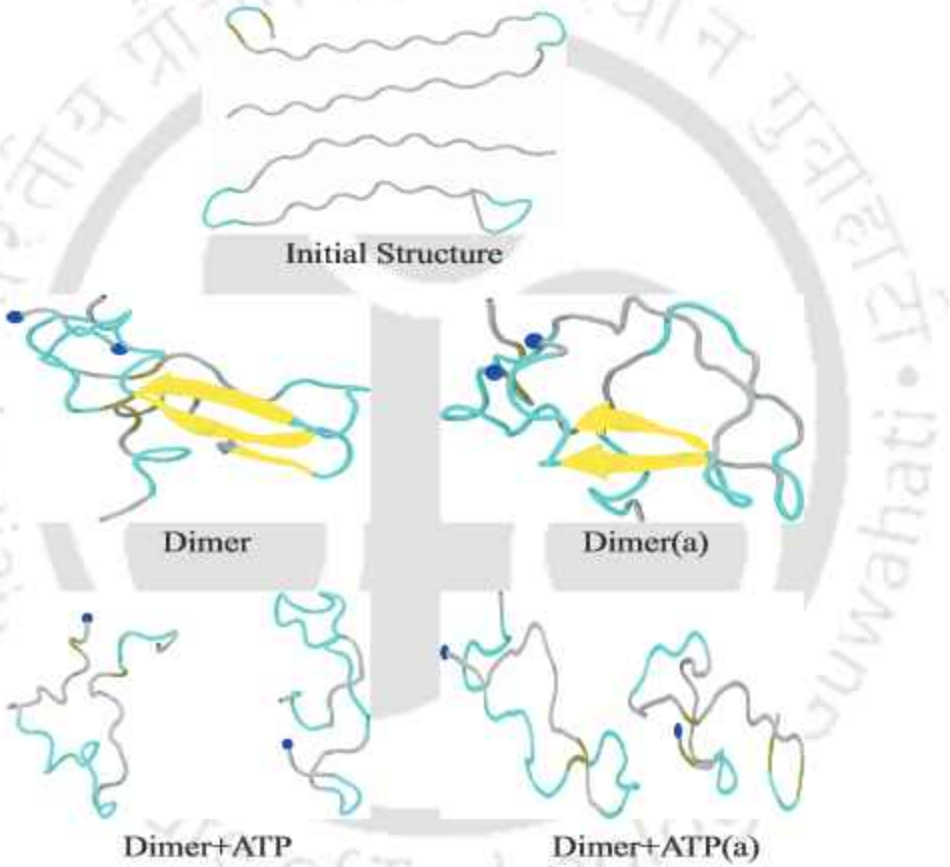

Figure 3.38: *Snapshots of hIAPP dimer in different systems at the end of simulation time. The peptides are represented in cartoon form, depicting β-sheet in yellow, coil in silver, bend in cyan and 3_{10}-helix in blue.*

The SASA value of the peptides with ATP is higher than the one without it, which demonstrates that the peptides are unable to aggregate with ATP around it (Fig 3.39b). Moreover, the above analyses also support that the conformational ensembles converge in the last 200 ns of the simulations. The R_g of the dimer also increases in presence of ATP, depicting

that the peptides are loosely packed (Fig 3.39c).

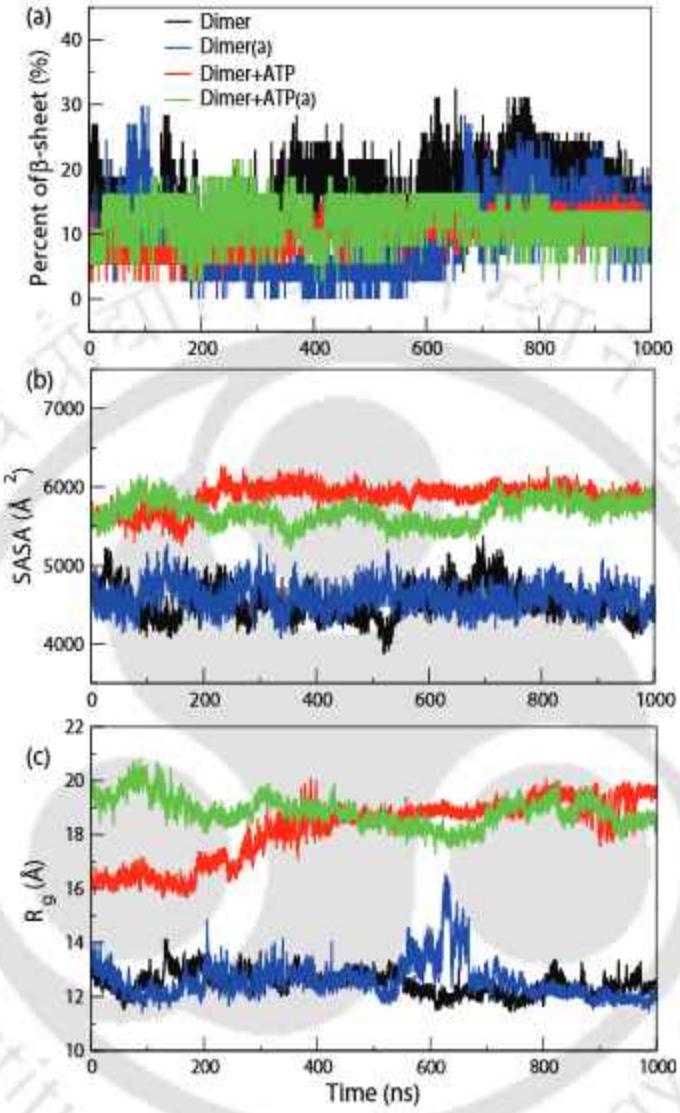

Figure 3.39: *Time evolution of (a) β-sheet content, (b) SASA and (c) R_g of hIAPP dimer in different systems.*

From the average secondary structure contents of each system (Table 3.12), it is observed that the hIAPP dimer has the highest β-sheet content of 18.43%, which reduces to only 6.31% in the presence of ATP, while the coil percentage increases from 39.37% to 53.86%. The helix content remains almost the same. Hence, it is confirmed that the ATP reduces the average β-sheet content of hIAPP dimer, by keeping the peptides away from each other, analogous to the $hIAPP_{22-28}$ fragments. Similarly, the evolution of the secondary structures of each residue over the entire simulation time (Fig 3.40) also reveals

that the hIAPP residues form stable β-sheets, but, with ATP, the peptides prefer to remain in random coil conformation.

System		Dimer	Dimer(a)	Dimer+ATP	Dimer+ATP(a)
β-sheet %	Extended β	12.7 ± 0.3	9.1 ± 0.0	2.8 ± 0.0	4.7 ± 0.3
	Bridged β	5.8 ± 0.2	4.4 ± 0.0	3.5 ± 0.2	4.7 ± 0.2
	Total	18.4	13.5	6.3	9.4
Helices %	3_{10}-helix	2.0 ± 0.0	2.6 ± 0.0	2.0 ± 0.0	1.2 ± 0.0
	α-helix	0.0 ± 0.0	6.5 ± 0.0	0.1 ± 0.0	0
	π-helix	0	0	0.0 ± 0.00	0
	Total	2.0	9.2	2.1	1.2
Turn %		18.3 ± 0.3	14.7 ± 0.0	15.3 ± 0.3	15.6 ± 0.3
Bend %		22.0 ± 0.3	22.2 ± 0.0	22.4 ± 0.4	26.1 ± 0.3
Coil %		39.4	40.6	53.9	47.8

Table 3.12: *The secondary structure contents of hIAPP dimer for different systems.*

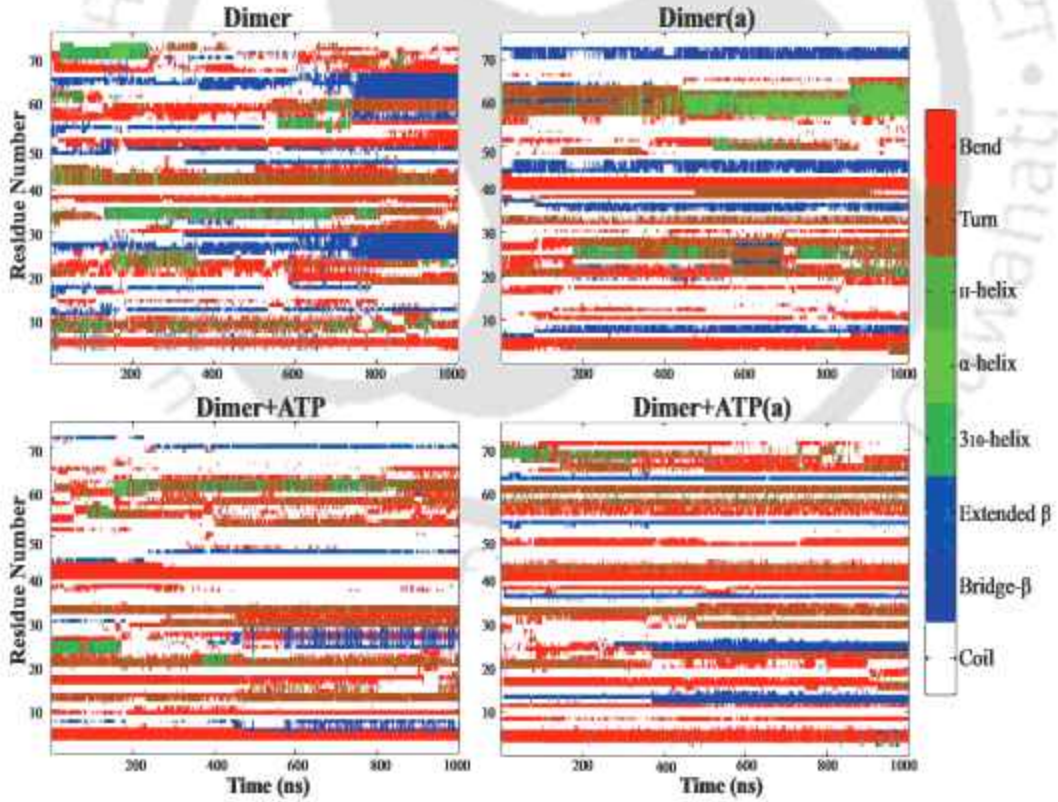

Figure 3.40: *Time evolution of change of secondary structures of each residue of hIAPP dimer for different systems.*

The β-sheet probability of each residue of hIAPP (Fig 3.41a) clearly depicts that Asn22-

Thr30 region has the highest β-sheet content, followed by Ala8-Leu12 region. The Asn22-Leu27 region is reported to be part of the amyloidogenic region of hIAPP and the effect of ATP on its aggregation is already analyzed in the previous sections.

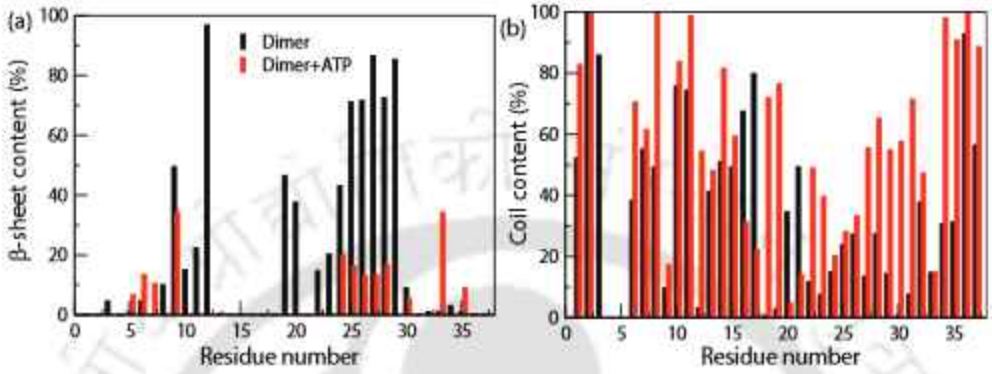

Figure 3.41: *Effect of ATP on: (a) β-sheet and (b) coil percentages for each residue of hIAPP dimer for different systems.*

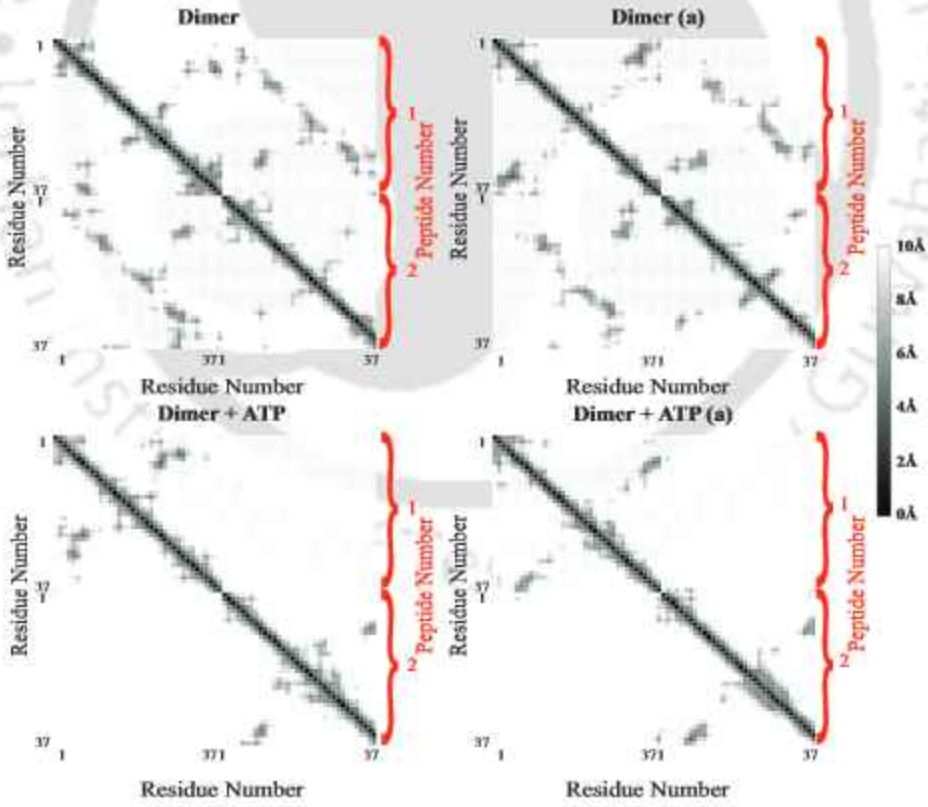

Figure 3.42: *Residue-residue contact map of the hIAPP dimer for different systems.*

In presence of ATP, the β-sheet content distinctly reduces for both the regions and the

random coil content increases (Fig 3.41b).

To probe the effect of ATP on the peptide-peptide interactions, first the residue-residue contact is calculated. The contact map analysis reveals an increase in the distance between the Cα atoms of the residues and thus a decrease in the interactions between the peptides, in presence of the inhibitor (Fig 3.42). The value of the preferential interaction parameter (Γ_{pw}) further indicates that the two peptides in the dimer preferentially interact with each other, but ATP induces the solvation of the dimer in water (Fig 3.36b). Further, from the interaction energy values between the hIAPP dimer (Table 3.13), we observe that, here again, the electrostatic energy dominates over the van der Waals energy and both the energy components, are less favourable for the systems with ATP, than the one without it.

Interactions		**Peptide-Peptide**		**Peptide-ATP**	
Contributions		**Ele**	**vdW**	**Ele**	**vdW**
Systems	**Dimer**	-1103.5±0.7	-90.8±0.3	–	–
	Dimer(a)	-1096±0.8	-87.3±0.3	–	–
	Dimer+ATP	-981.5±0.7	-27.8±0.2	-1928.5±3.3	-134.4±0.2
	Dimer+ATP(a)	-1030.5±0.6	-35.6±0.6	-1780±3.7	-118.8±0.3

Table 3.13: *Decomposition of peptide-peptide and peptide-ATP interaction energies (in kcal/mol) of hIAPP dimer for different systems.*

A notable reduction in the number of hydrogen bonds formed between the peptides is also perceived (Table 3.11), implying that the ATP molecules disrupt the hydrogen bonding interaction between hIAPP molecules. Hence it is confirmed that, the aggregation of the hIAPP dimer, similar to $hIAPP_{22-28}$, is inhibited by ATP.

3.2.3.5 Interaction of ATP with hIAPP

In order to investigate the role of ATP as an inhibitor of hIAPP aggregation, detailed analysis on the interaction of ATP with hIAPP is necessary. Hence, for the characterization of the interaction between hIAPP and ATP, the RDF between the centre of mass of the heavy atoms of the ATP molecules and that of each residue of hIAPP is calculated, which helps us to identify the specific residues interacting with the inhibitor. From Fig 3.43a, we observe that the first maxima of the hydrophobic residues in the $hIAPP_{22-28}$, i.e., Phe23, Gly24, Ile26 and Leu27, appear around 5 Å, which signifies that these residues have a

strong affinity to interact with ATP.

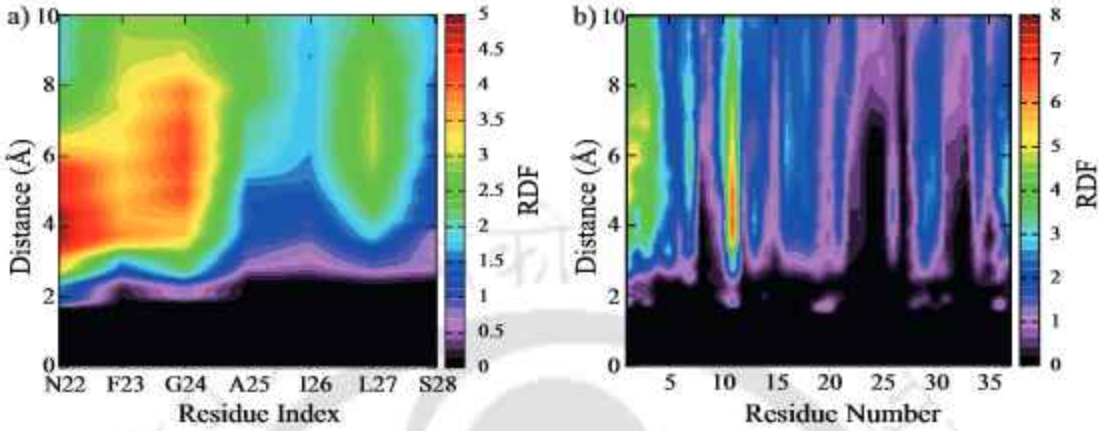

Figure 3.43: *A two dimensional heat map displaying the radial distribution functions (RDF) between centre of mass of ATP and that of each residue of (a) $hIAPP_{22-28}$ and (b) hIAPP dimer for different systems.*

On the other hand, both the hydrophilic and the hydrophobic residues in the hIAPP dimer are close in contact with ATP (Fig 3.43b). Mostly, the terminal regions of full-length hIAPP (Lys1-Cys7 and Ser28-Thr30) and the Phe15-Asn21 region are strongly interacting with ATP. Moreover, the RDF between ATP and Arg11 has a very high peak value, which appear at around 4 Å, displaying a high affinity of ATP towards Arg11.

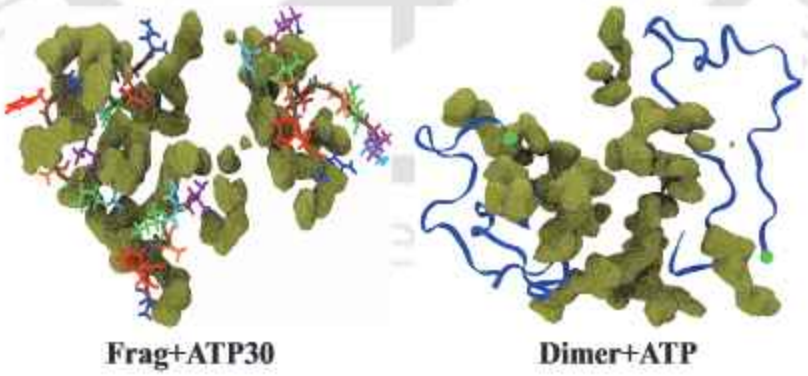

Figure 3.44: *Spatial distribution functions of ATP around $hIAPP_{22-28}$ and hIAPP dimer.*

For a detailed probabilistic three-dimensional structural view of the distribution of ATP molecules around the peptides, the spatial distribution functions of ATP around a distance of 5 Å of the peptides are estimated. We observe that the ATP molecules are densely

populated around the hydrophobic region of $hIAPP_{22-28}$ fragments (Fig 3.44). A compact arrangement of ATP molecules around the hIAPP dimer is also observed, especially around the N-terminal region.

To obtain further insight into the primary interaction sites of ATP with hIAPP, the first solvation shell coordination number of ATP is calculated. For the $hIAPP_{22-28}$ fragment (Fig 3.45a), Asn22 and Phe23 have the highest content of ATP surrounding them, followed by the residues Gly24, Leu27 and Ser28.

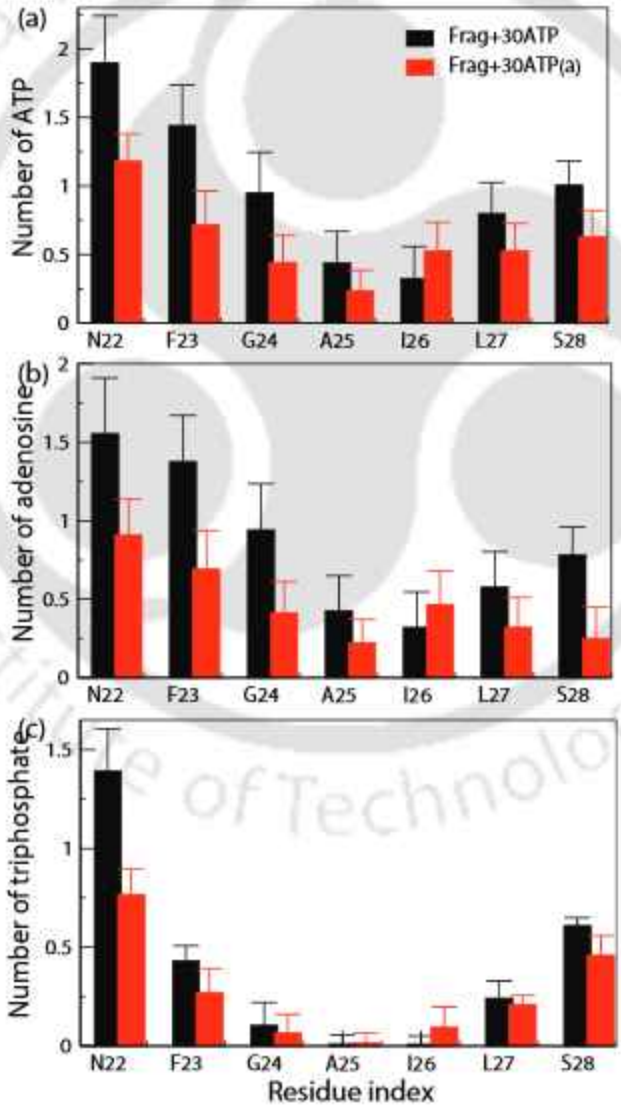

Figure 3.45: *First shell coordination number of (a) ATP, (b) adenosine and (c) triphosphate moiety around each residue of $hIAPP_{22-28}$ in different systems.*

Here again, for the hIAPP dimer, it is observed that ATP has a high propensity around the terminal regions (Lys1-Ala5 and Ser28-Thr36) and the turn region (Asn14-Asn21) (Fig 3.46a). Moreover, Gln10 and Arg11 have the highest coordination number of ATP around them.

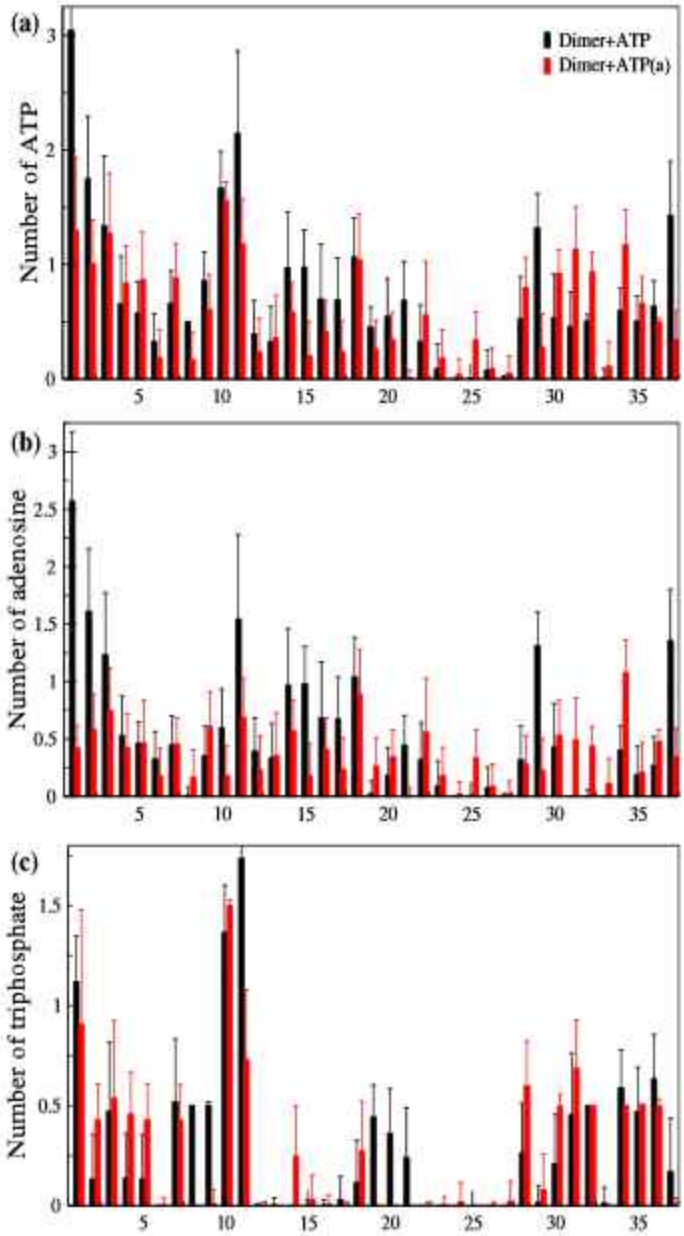

Figure 3.46: *First shell coordination number of (a) ATP, (b) adenosine and (c) triphosphate moiety around each residue of hIAPP dimer.*

The distributions of ATP around both hydrophobic and hydrophilic residues suggest that

the hydrophobic as well as the hydrogen bond interactions play an important role in the association of ATP with hIAPP. Hyman's group found that the hydrophobic adenosine ring of ATP strongly enhances the effect of the charged triphosphate moiety on the stability of proteins[67]. To identify which section of ATP has a dominant contribution in its binding with the peptides, we calculate the number of adenosine (Figs 3.45b and 3.46b) and triphosphate (Figs 3.45c and 3.46c) moieties in the first solvation shell around the peptides. The coordination number of adenosine is greater than that of the charged triphosphate moiety in both $hIAPP_{22-28}$ fragments and hIAPP dimer.

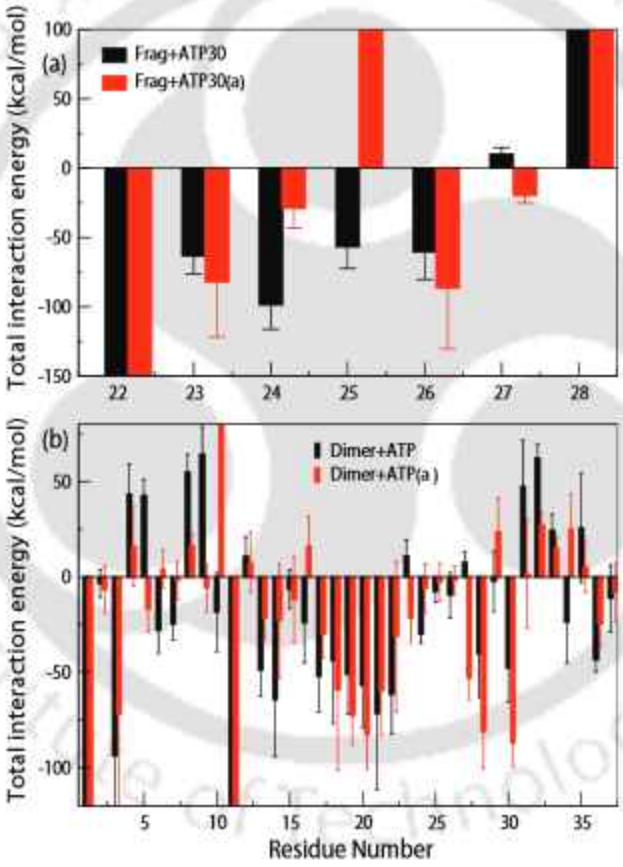

Figure 3.47: *The total interaction energy of ATP with each residue of (a) $hIAPP_{22-28}$ and (b) hIAPP dimer.*

The charged triphosphate group only interacts with the polar residues. However, the presence of hydrophobic ring and the amino group in adenine and the hydroxyl groups in ribose makes it possible for adenosine to interact with more residues. Hence we can conclude that the contact of ATP with the peptides is mostly due to hydrophobic adenosine

rather than the hydrophilic triphosphate group. Similar results are also reported for the interaction of ATP with Aβ[69].

The extent of the interaction of ATP with hIAPP$_{22-28}$ fragment and hIAPP dimer is further analyzed by estimating the interaction energy between them. From the interaction energy of hIAPP$_{22-28}$ systems (Table 3.10), we observe that the interaction with ATP increases with increasing concentration of ATP and is most favourable for the system with highest ATP concentration. Here again, the electrostatic energy dominates over its van der Waals counterpart. Favourable interaction energy values are also observed for the dimer+ATP systems (Table 3.13). To further pinpoint the residues involved in interacting with ATP, the total interaction energy of each residue with ATP is calculated (Fig 3.47). The interaction energy is most favourable for Phe23, Gly24 and Ile26 in the hIAPP$_{22-28}$ fragments. Similarly, for the dimer system, the region Phe15-Phe23 has the most favourable interaction energy, along with Arg11, Ser28 and Thr30 residues.

The cluster analysis is also performed to investigate the effect of ATP on the hIAPP structure. The hIAPP$_{22-28}$ systems are divided into 10 and 11 different conformations in absence and presence of ATP, out of which three most populated structures are presented (Fig 3.48). The hIAPP$_{22-28}$ fragments, in absence of ATP, form a β-barrel like structure, consisting of anti-parallel β-strands. However, the fragments remain separated in presence of ATP. The dimer conformations, on the other hand, are distributed into 16 and 8 clusters for the systems without and with ATP respectively. Three of the most populated structures for each system are shown in Fig 3.48. The most populated structure in hIAPP dimer consists of a three stranded cross β-sheet structure with a β-hairpin, formed by Ala8-Phe15 and Asn22-Ser29 residues of one chain and a β-strand formed by Asn24-Thr32 residues of the other chain. Similar three stranded β-sheet structure has been reported previously[10]. The other clusters consists of short β-sheets and also random coil conformations. However the dimer mostly exists in random coil in presence of ATP, indicating that ATP prevents the formation of ordered β-sheet structures in hIAPP. Moreover, it is also observed that the distribution of ATP is higher around the terminal (especially the N-terminal) residues.

The hydrogen bonding interactions play a pivotal role in the binding of ATP with hIAPP (Table 3.11). On increasing the ATP concentration, the average hydrogen bond number between ATP and hIAPP$_{22-28}$ fragment increases, displaying a stronger interaction between the peptide and inhibitor molecules. Substantial number of hydrogen bonds is also

formed between ATP and the hIAPP dimer.

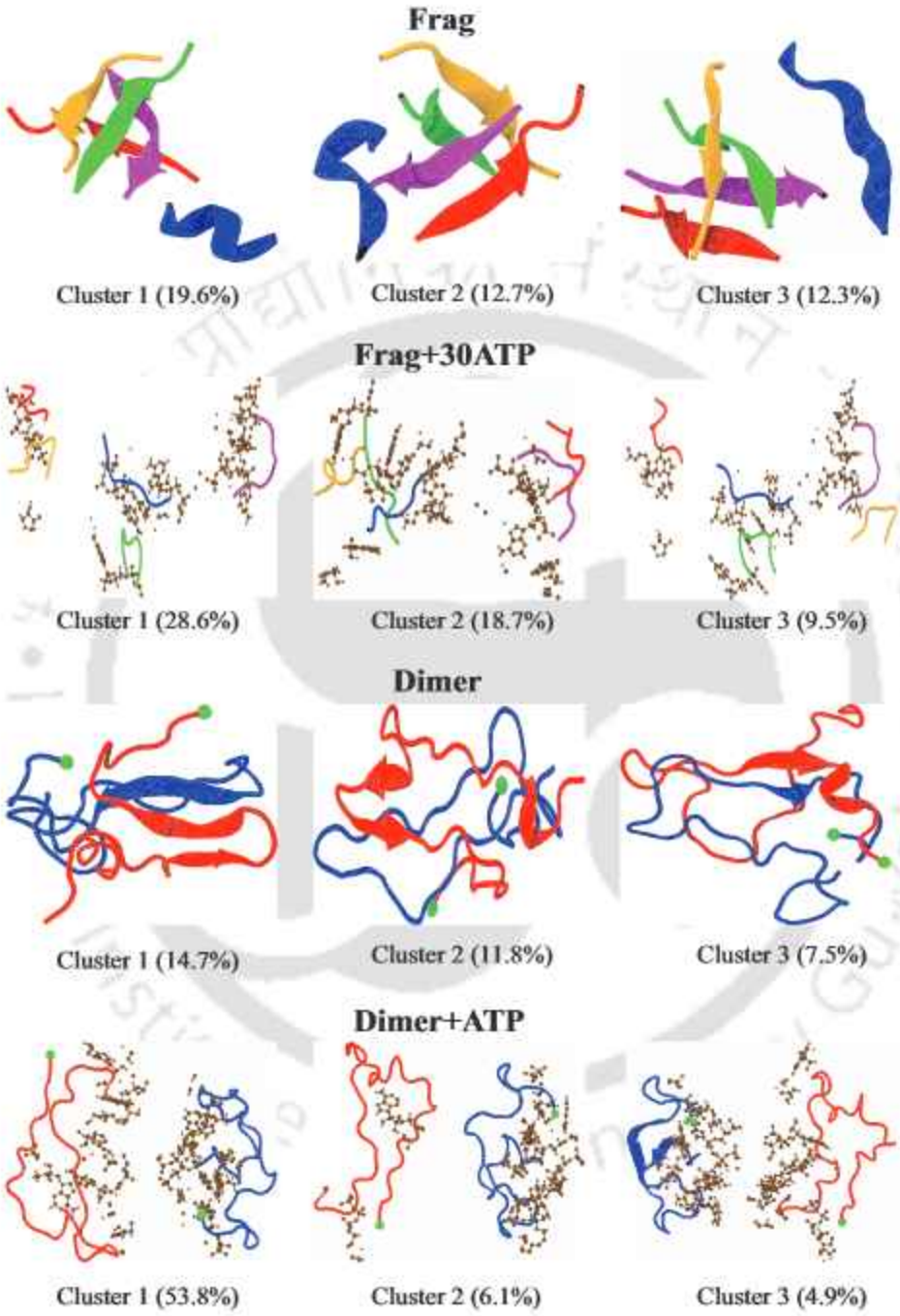

Figure 3.48: *Representative conformations of the clusters of $hIAPP_{22-28}$ and hIAPP dimer of different systems.*

Moreover, the residue wise hydrogen bond number for the peptide-peptide and also the peptide-ATP interactions help us to pinpoint the residues that mostly contribute to the

hydrogen bond disruption of the peptides. The hydrogen bond number between $hIAPP_{22-28}$ fragments is the highest for the terminal polar residues, Asn22 and Ser28, followed by Gly24, Ile26 and Leu27 (Fig 3.49a). The polar residues have the maximum hydrogen bond number with ATP as well, closely followed by Phe23 and Gly24 (Fig 3.49b).

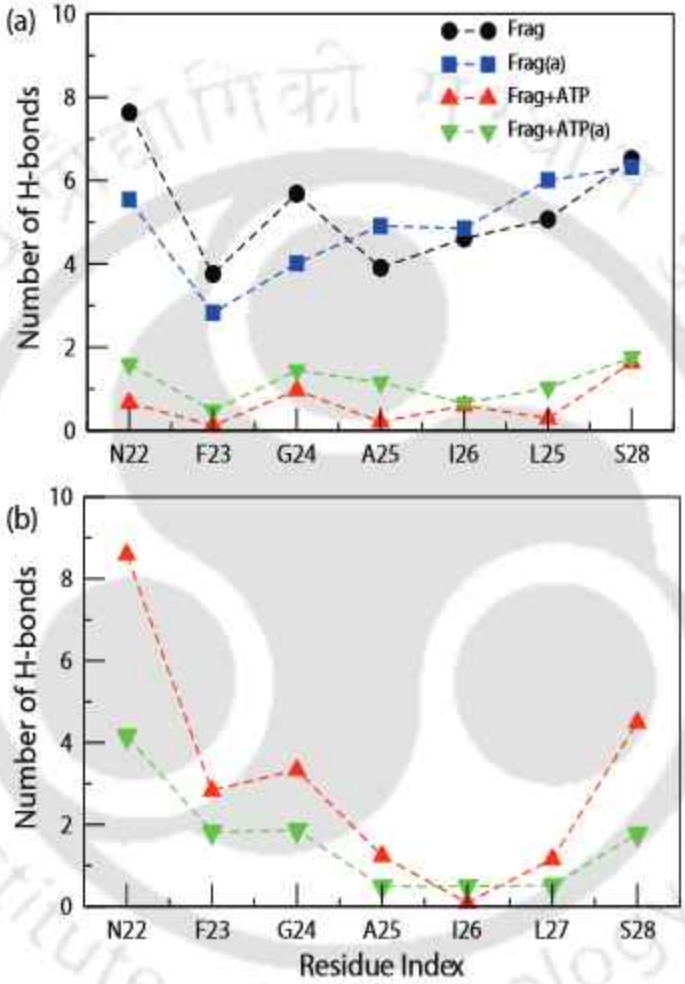

Figure 3.49: *Average hydrogen bond number of (a) peptide-peptide and (b) peptide-ATP with each residue of $hIAPP_{22-28}$.*

The small size of Gly24 makes it feasible to easily form hydrogen bonds with ATP. Consequently, in hIAPP dimer, hydrogen bonds formed in the C-terminal region, especially by Ser20, Asn22, Ser29-Asn31 residues and also by Asn10 aid in the aggregation of the peptides (Fig 3.50a). However, Arg11 has the maximum hydrogen bond number with ATP followed by Lys1-Asn3, Asn10, Asn14, His18-Asn22, Ser28-Asn31, Thr36 and Tyr37 (Fig 3.50b). As expected, the polar residues present at the terminal regions and at the turn

regions are more involved in hydrogen bonding with ATP. Hence the residues, which are responsible for hydrogen bonding between the peptides, form hydrogen bonds with ATP, thus preventing peptide aggregation.

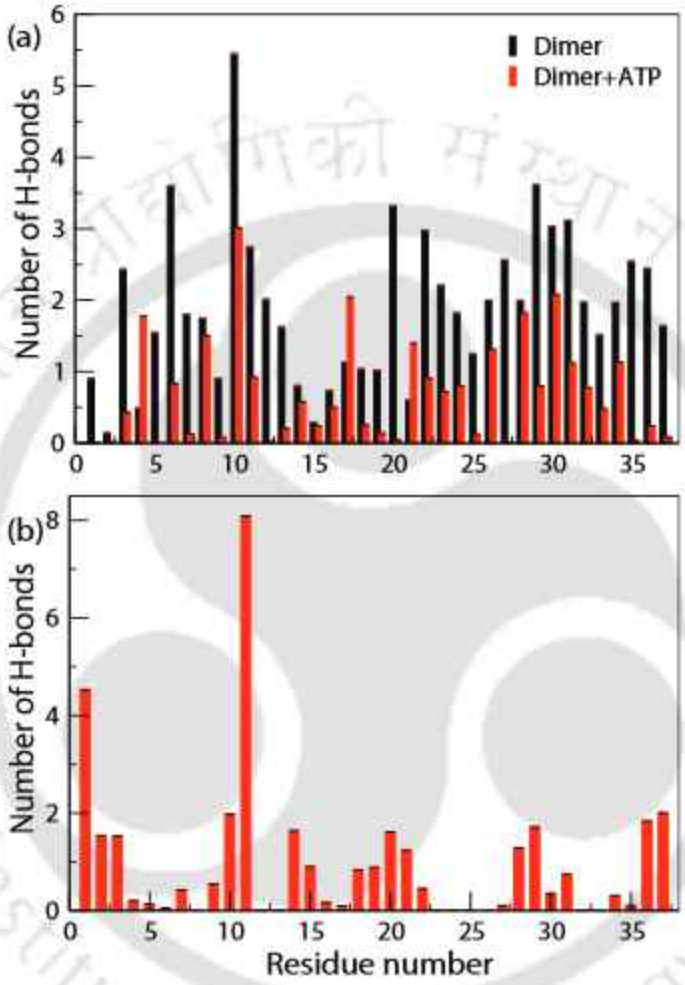

Figure 3.50: *Average hydrogen bond number of (a) peptide-peptide and (b) peptide-ATP with each residue of hIAPP dimer.*

Apart from hydrogen bonding, stacking interactions play a very important role in the drug design for amyloid inhibition[33, 66]. Hence π-π stacking interaction between the aromatic group of ATP and the aromatic residues of hIAPP is another crucial factor to the binding of ATP with hIAPP (Fig 3.51a-d). Following previous studies, the π-π stacking pattern is elucidated by the free energy plot as a function of the distance between the centre of mass of the two aromatic residues and also the angle formed between them (Fig 1.6a). The stacking patterns are categorized as parallel, herringbone and perpendicular,

depending upon the angle made by the two aromatic rings. From Fig 3.52, we can conclude that all forms of stacking are present between ATP and Phe15, His18, Phe23 and Tyr37 residues of hIAPP.

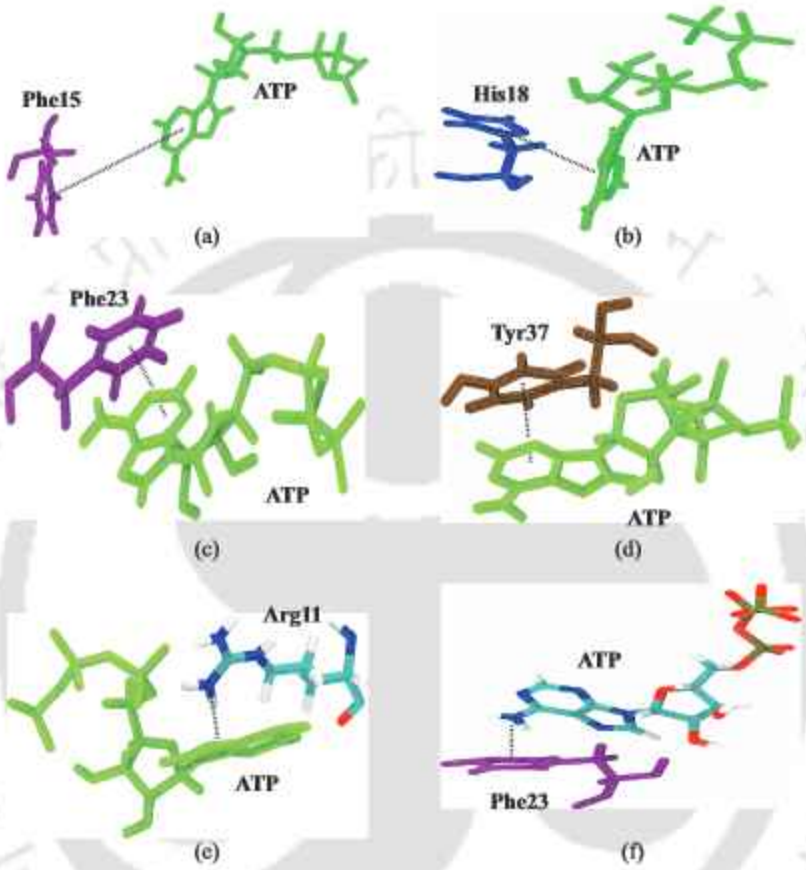

Figure 3.51: *Representative snapshots showing (a-d) π-π and (e,f) NH-π stacking orientation between ATP and the aromatic residues of hIAPP.*

However, parallel stacking is most dominant in Phe23, while herringbone stacking is mostly observed for Phe15 and Tyr37 and His18 residues is primarily involved in perpendicular arrangement with the aromatic ring of ATP.

In the above analyses, we observe that ATP has a strong affinity to interact with Arg11[64]. This may be due to the existence of N-H-π stacking interaction between them (Fig 1.6b), which is further examined (Fig 3.51e). In the plot of the distance between the centre of mass of the NH_3^+ group of Arg11 and the aromatic ring of ATP (Fig 3.53a), a sharp peak is observed at 4 Å, indicating the presence of amino-aromatic contact. Moreover, the NH_2 group of ATP is also involved in N-H-π stacking interaction with the aromatic

ring of Phe23 (Figs 3.51f and 3.53b). From all of the above analyses, it can be deduced that the hydrogen bonding, hydrophobic, π-π and N-H-π stacking interactions collaborate

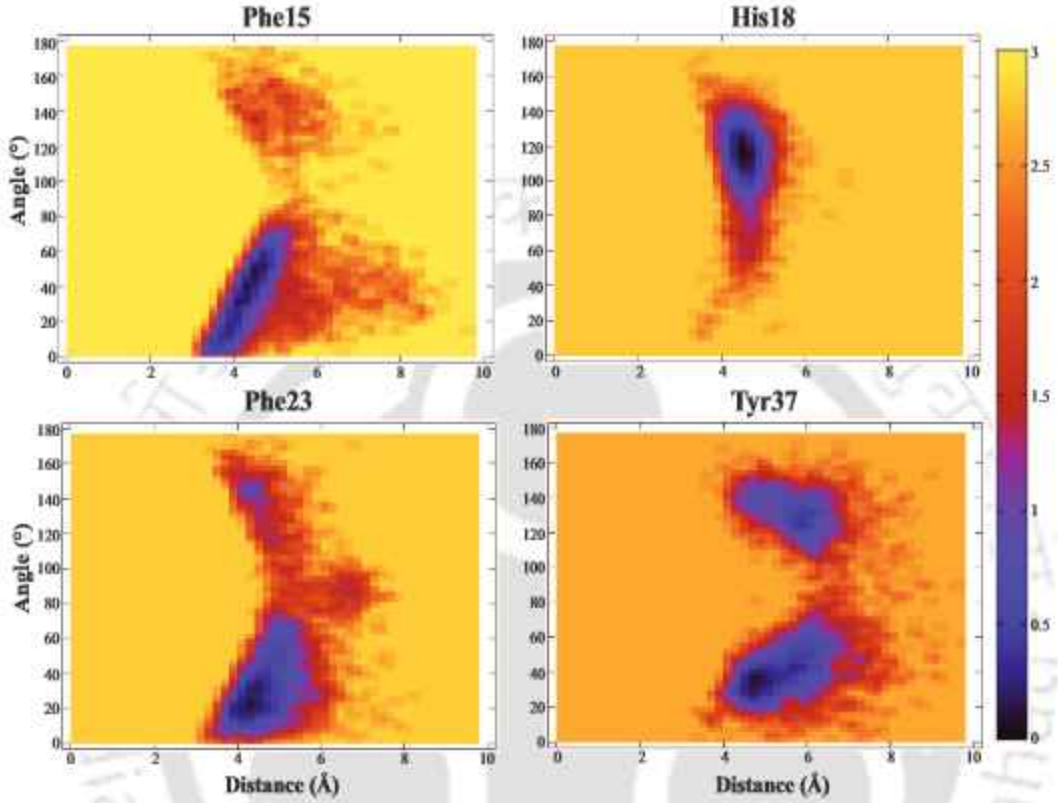

Figure 3.52: *Free energy surface (in kcal/mol) as a function of the distance and angle between the centre of mass of the aromatic rings of ATP and the aromatic residues of hIAPP.*

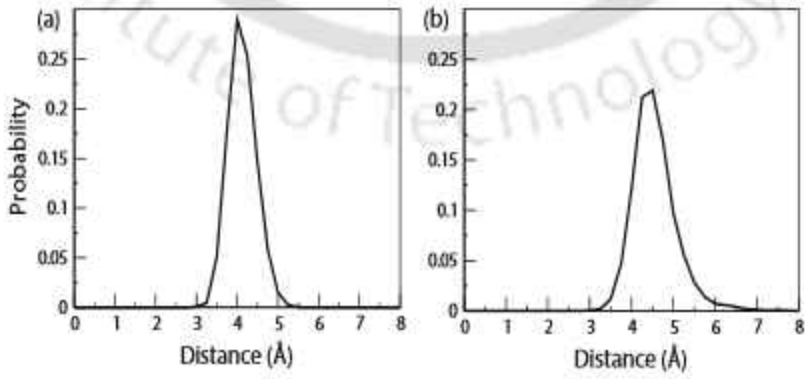

Figure 3.53: *The probability distribution of the distance between the center of mass of (a) aromatic ring of ATP and NH_3^+ group of Arg11 and (b) NH_2 group of ATP and the aromatic ring of Phe23.*

in assisting the interaction of ATP with hIAPP, thus impeding hIAPP aggregation.

3.2.3.6 Destabilization of hIAPP Protofibrils by ATP

After having concluded that ATP can, indeed, prevent hIAPP aggregation, we are now interested to learn the effect of ATP on pre-formed hIAPP fibrils. To that effect, independent 1 μs simulations on two different hIAPP protofibrillar structures in absence and presence of ATP are carried out. The ssNMR derived hIAPP protofibril consists of five $hIAPP_{1-37}$ chains, where each chain is folded into a β-hairpin made up of two β-strands (Ala8-Val17 and Ser28-Tyr37) joined together by a loop (His16-Leu27) (Fig 1.4a). The cryo-EM model of the polymorph, on the other hand, comprises of $hIAPP_{13-37}$ arranged in a S-shape,

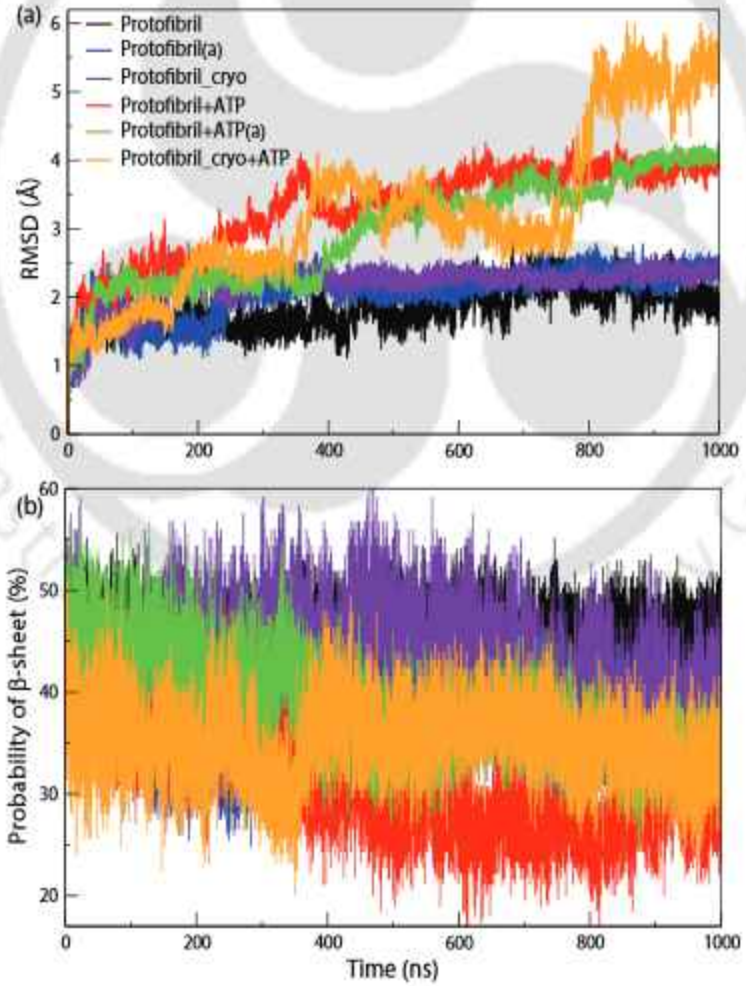

Figure 3.54: *Time series of (a) RMSD and (b) β-sheet content of hIAPP protofibril for different systems.*

involving β-strand (Asn14-Ser20)–loop (Asn21-Ala25)– β-strand (Ile26-Val32)–loop (Gly33-Ser34)–β-strand (Asn35-Tyr37) (Fig 1.4c).

The structural stability of both hIAPP protofibrils in presence of ATP is analyzed by first calculating the time evolution of the root-mean-square deviation (RMSD) of the Cα atoms of hIAPP residues, with respect to the initial structure. From Fig 3.54a, we observe that the RMSD of the both protofibril models are around 2 Å, and, in presence of ATP, it is increased to nearly 4 Å for the NMR model.

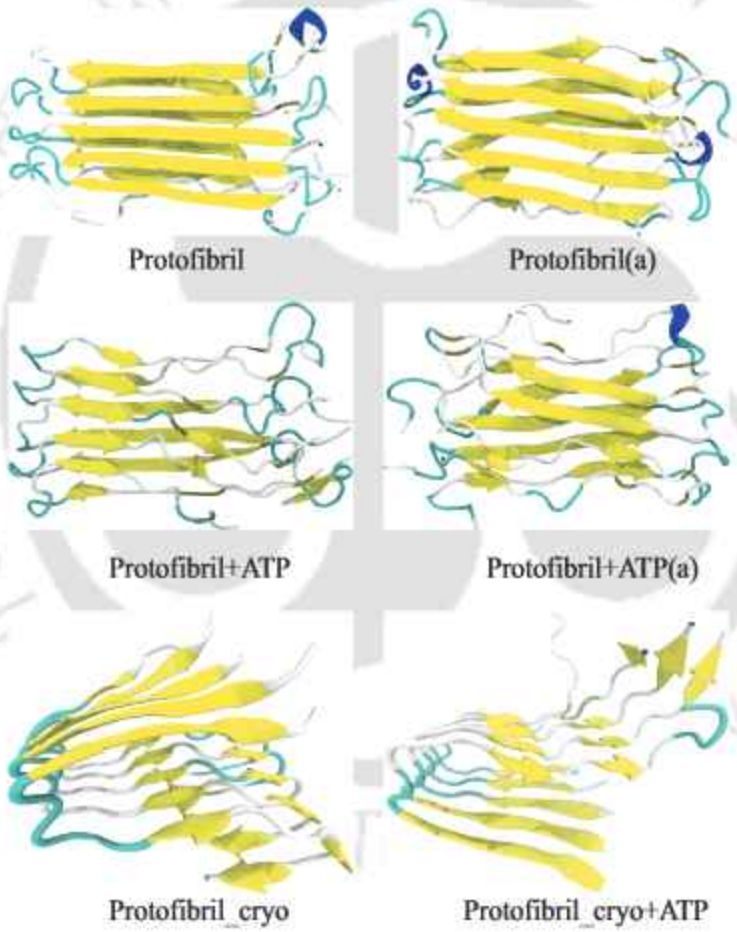

Figure 3.55: *Snapshots of hIAPP protofibril in different systems at the end of simulation time. The peptides are represented in cartoon form, depicting β-sheet in yellow, coil in silver, bend in cyan and 3_{10}-helix in blue.*

On the other hand, the RMSD values of the cryo-EM model fluctuate with time and reach as large as 6 Å. The increase in RMSD of the protofibrils on addition of ATP suggests that the

peptide chains undergo significant conformational deviations on binding with ATP, which can also be seen from the snapshots (Fig 3.55). The symmetric β-sheet conformation of the NMR model is destabilized, and the S-shaped structure of the cryo-EM model is impaired. Since the secondary structure of hIAPP protofibrils mainly consists of β-sheets, the change in β-sheet structure is associated with the stability of the pentamer. From the time evolution of the β-sheets of the hIAPP protofibril (Fig 3.54b), we observe that the β-sheet probability of hIAPP with ATP is much lower than the one without it, depicting the instability of β-sheets of the protofibrils in presence of inhibitor. Similarly, the average contents of the different secondary structures also reveal a modest decrease in the β-sheet content from 45.48/39.43 % to 29.8/31.26 %, and also an increase in the coil content from 32.66/33.83 % to 48.08/42.54 % for the NMR/cryo-EM model (Table 3.14).

System	Ext-β	Bridge-β	Helix	Turn	Bend	Coil
Protofibril	42.7±0.4	2.8±0.1	1.4±0.1	9.4±0.3	11.3±0.3	32.7
Protofibril(a)	37.5±0.4	0.8±0.0	1.6±0.1	6.0±0.2	16.4±0.3	37.7
Protofibril_cryo	33.1±0.4	6.3±0.2	0.0±0	3.9±0.2	22.9±0.4	33.8
Protofibril+ATP	26.7±0.4	3.2±0.1	0.9±0.0	9.4±0.3	11.8±0.3	48.1
Protofibril+ATP(a)	30.1±0.4	4.3±0.2	4.0±0.2	8.2±0.2	13.4±0.3	39.9
Protofibril_cryo+ATP	29.2±0.4	2.1±0.1	0.1±0.0	1.7±0.1	24.4±0.4	42.5

Table 3.14: *The secondary structure contents of hIAPP protofibril for different systems.*

Hence incorporation of ATP induces the conversion of dominant secondary structure from β-sheet to random coil composition in hIAPP protofibril as well.

The most populated structure of the protofibril with surrounding ATP is obtained from the cluster analysis, where the ATP molecules are seen to occupy mainly the edges of the protofibrils, i.e., near the turn regions, and the terminal regions (Fig 3.56). The residue-wise β-sheet content is calculated, for a precise analysis into the influence of ATP on the specific residues of the protofibrils. The regions having the highest β-sheet content, Ala8-Val17 and Gly24-Thr36 in the NMR model (Fig 3.57a), match with that reported by Luca et. al[53]. For the cryo-EM model, Asn14-Asn22, Ile26-Asn31 and Ser34-Thr36 have higher β-sheet content (Fig 3.57b)[74]. ATP drastically induces a reduction in the β-sheet probability of most of the residues, particularly the C-terminal residues. Further, the first solvation shell coordination number of ATP around each residue of the protofibril

establishes that the ATP molecules

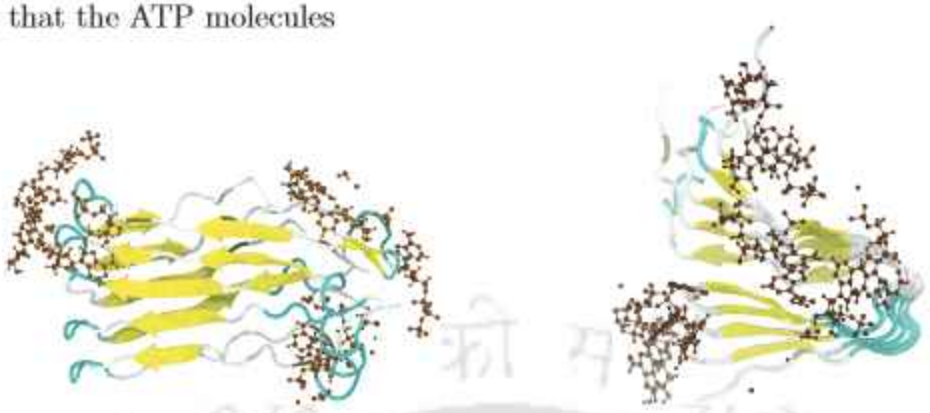

Figure 3.56: *Snapshots of the distribution of ATP molecules around 5 Å of the (a) NMR and (b) cryo-EM model of hIAPP protofibril in different systems.*

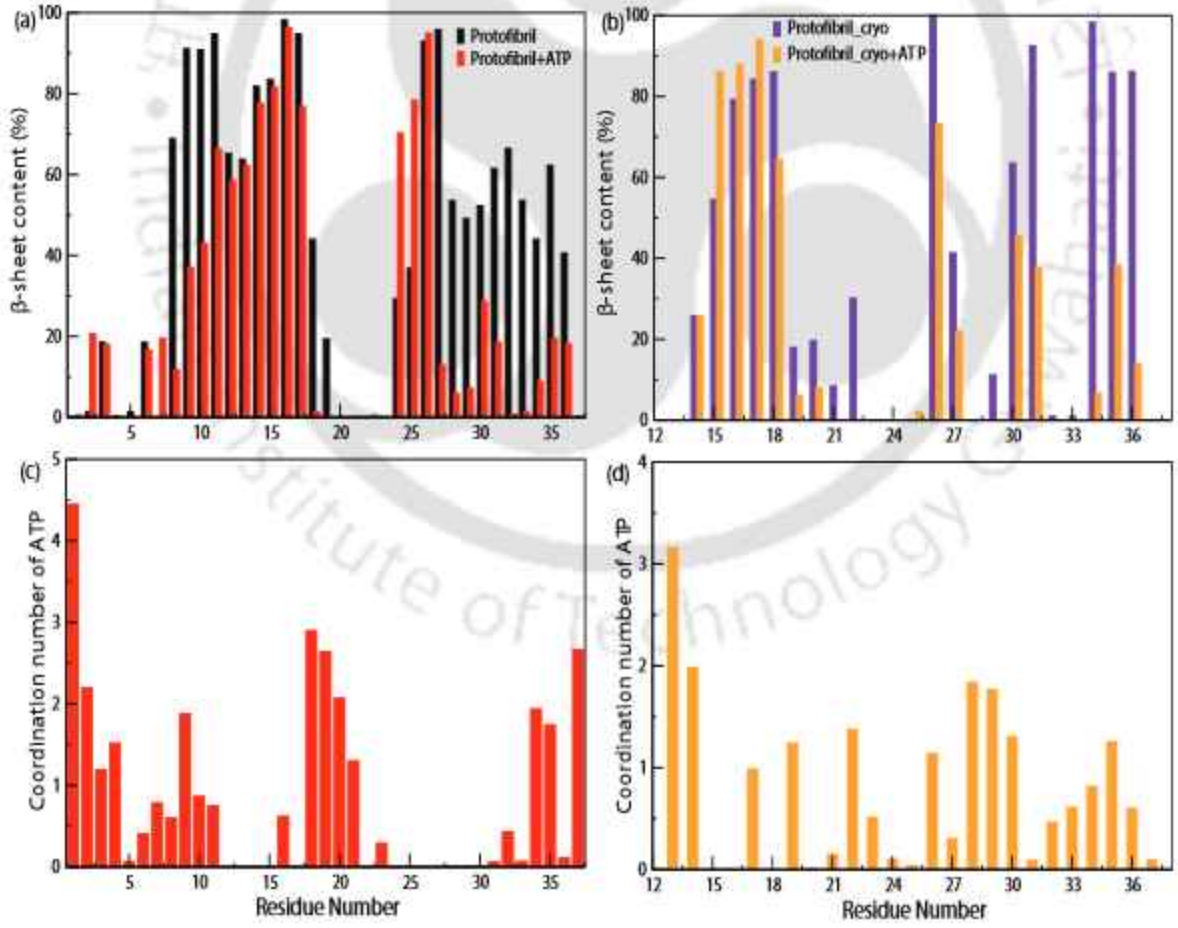

Figure 3.57: *The (a) β-sheet content and (b) first shell coordination number of ATP over each residue of NMR model of the hIAPP protofibril for different systems.*

are in contact with the turn (Leu16-Asn21) and the terminal regions (Lys1-Arg11 and Thr30-Tyr37), with higher preference towards the N-terminal region (Lys1-Arg11) in the NMR model (Fig 3.57c), equivalent to the results obtained for hIAPP dimer systems. Since the first 12 N-terminal residues is absent in the cryo-EM model of the protofibril, ATP molecules are higher in number around the C-terminal residues (Fig 3.57d). Moreover, in presence of ATP, the electrostatic as well as the van der Waals interaction energy become unfavourable (Table 3.15) and also the average hydrogen bond number decreases (Table 3.16) for the peptide-peptide interactions. The strong binding of ATP with the protofibrils, on the other hand, is also concluded from the number of hydrogen bond and interaction energy values between the protofibrils and the ATP molecules. Hence the interactions between the peptide chains are interrupted, leading to a partial destabilization of the hIAPP protofibrils.

System	Peptide-peptide		Peptide-ATP	
	Ele	vdW	Ele	vdW
Protofibril	-1139.4± 8.5	-127.6 ± 3.9		
Protofibril(a)	-1131 ± 9.8	-118.14 ± 4.2		
Protofibril_cryo	-761 ± 9.5	-102.3 ± 4.5		
Protofibril+ATP	-1127.2 ± 8.4	-119.9 ± 4.3	-351.8 ± 61.5	-32.8 ± 2.0
Protofibril+ATP (a)	-1150 ± 12.1	-123.88 ± 4.5	-261.4 ± 53.1	-30.6 ± 1.6
Protofibril_cryo+ATP	-733.4 ± 6.9	-76.28 ± 3.5	-253.4 ± 35.0	-18.4 ± 1.8

Table 3.15: *Decomposition of peptide-peptide and peptide-ATP interaction energies of hIAPP protofibril (in kcal/mol) for different systems.*

System	Peptide-peptide	Peptide-ATP
Protofibril	26.0 ± 1.2	–
Protofibril(a)	25.6 ± 1.2	–
Protofibril_cryo	20.8 ± 1.3	–
Protofibril+ATP	23.7 ± 1.2	5.3 ± 0.7
Protofibril+ATP(a)	21.8 ± 1.4	4.3 ± 0.6
Protofibril_cryo+ATP	17.8 ± 0.9	3.5 ± 0.6

Table 3.16: *Average hydrogen bond numbers of hIAPP protofibril between peptide-peptide and peptide-ATP interactions for different systems.*

3.2.4 Discussions

$hIAPP_{22-28}$ is part of the amyloidogenic core of hIAPP, consisting of a hydrophobic core (Phe23-Leu27) with terminal hydrophilic residues (Asn22 and Ser28). The aggregation of $hIAPP_{22-28}$ under the influence of ATP is, therefore, investigated. In pure water, the $hIAPP_{22-28}$ fragments instantly self-assemble into anti-parallel β-sheets. The formation of antiparallel β-sheets by $hIAPP_{22-28}$ is also observed in the crystallographic structure,[72] from where the initial structure for this study is extracted. However, in presence of ATP, the interaction between the peptides decreases, hindering the self-aggregation of the peptides (Fig 3.58). A compact arrangement of ATP around the peptides is observed, with ATP preferentially interacting with the hydrophobic core (Phe23-Leu27). A compact arrangement of ATP around the peptides is observed, with ATP preferentially interacting with the hydrophobic core (Phe23-Leu27). Since dimerization is the initial step of hIAPP aggregation, the conformational change of hIAPP dimer in presence of ATP is also investigated. The initial extended coil states of the dimer adopts a three-stranded β-sheet conformation. The β-strand regions consist of N-terminal residues, Ala8-Leu12 and the C-terminal residues, Asn22-Thr30, which resemble with a REMD simulation study on hIAPP dimer[10].

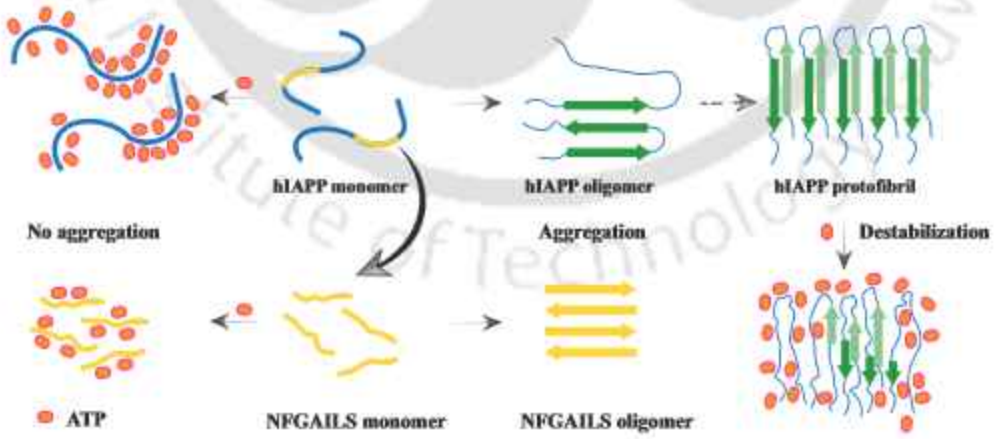

Figure 3.58: *A schematic representation of the effect of ATP on the aggregation of hIAPP.*

However, the hIAPP dimer maintains its random coil conformation on addition of ATP, disfavouring dimerization (Fig 3.58). The hydrogen bonds and hydrophobic interactions

between the peptide residues, which stabilize the oligomerization of hIAPP, are disrupted by ATP, thus, reducing the probability of amyloid aggregation. Further, in-depth analyses revealed that ATP preferentially interacts with the terminal residues (Lys1-Cys7 and Ser28-Thr30) and Phe15-Asn21 region in hIAPP dimer. Both the hydrophilic and hydrophobic residues are involved in the hIAPP-ATP interactions. The aromatic residues (Phe15, His18, Phe23 and Tyr37) are also involved in stacking interactions with ATP. The significance of Phe residues in amyloid aggregation is widely known[28, 79], due to which π-π stacking between Phe and inhibitor molecules is very crucial for drug design. Further, disparate hIAPP aggregation pathways are noticed on mutation of His18[65]. A high contact number is observed between hIAPP and Arg11, which plays an essential role in hIAPP-ATP association, by forming hydrogen bonds and N-H-π stacking interactions. The propensity of small organic polyphenols towards the aromatic and hydrophobic residues of hIAPP is recognized in numerous studies[6, 10, 32]. Moreover, a recent study of destabilization of $A\beta_{1-42}$ oligomer by ATP reported a higher interaction of the hydrophobic adenosine with the backbone of the peptide resulted in forming off-pathway species[69]. Similarly, in our study, the hydrophilic triphosphate moiety has a much lower contribution towards protein-ligand association than the hydrophobic adenosine group. The presence of both polar and aromatic groups in adenosine ensures a higher contact number with the peptides. Hence hydrogen bonds, hydrophobic interactions, π-π and N-H-π stacking interactions between ATP and hIAPP prevent the oligomerization of the peptides. Further, the destabilization of pre-formed hIAPP aggregates by ATP is also analyzed. ATP disrupts, albeit, modestly the stable β-sheet rich structure of the protofibrils by interacting with the terminal and turn regions of the protofibrils. Due to the escalating growth of T2D, the necessity to discover a drug, especially one which is easily bioavailable, is of utmost importance. Hence ATP can be utilized in this regard, so that it can not only prevent hIAPP monomers to aggregate, but also disassemble preformed fibrils. However, experimental evidence is required to support our findings.

3.2.5 Conclusion

In this work, we have studied the oligomerization of a small amyloid fragment and the full length sequence of hIAPP, along-with the influence of ATP on their aggregation property using all atom molecular dynamics simulations. To begin with, we observe that the

randomly placed $hIAPP_{22-28}$ peptides instantly aggregate to form β-sheet rich oligomers, including a β-barrel like structure in pure water. From the secondary structure analysis, we notice that these β-sheet aggregates are stable throughout the entire simulation run. However, on addition of a biological molecule, ATP, the $hIAPP_{22-28}$ fragments are unable to aggregate and remain in random, loosely-packed conformation, as inferred from SASA, R_g and preferential interaction parameter values. The contact map, interaction energy as well as hydrogen bond number of the $hIAPP_{22-28}$ peptides further conclude that the interception in the interactions among the peptides due to the binding of ATP. $hIAPP_{22-28}$ is located in the amyloidogenic segment of hIAPP and consist of the smallest fragment of hIAPP which leads to aggregation. Having deduced the ideal concentration at which ATP inhibits $hIAPP_{22-28}$ aggregation, we venture out to examine the effect of ATP on the full length peptide to acquire a complete understanding of the interaction mechanism of ATP with hIAPP. In pure water, the two randomly placed hIAPP monomers aggregate to form a three stranded β-sheet structure, which is eventually prevented in presence of ATP. Focusing on the interaction site of ATP with hIAPP, we observe that, ATP preferentially interacts with the hydrophobic residues in $hIAPP_{22-28}$ fragment, i.e., Phe23-Leu27. However, in case of the full length hIAPP dimer, ATP has a greater affinity towards the terminal residues and also the turn region. Moreover, the contribution of hydrophobic adenosine towards ATP contact with hIAPP exceeds that of the hydrophilic triphosphate group. Hence the hydrogen bonding, hydrophobic interactions, π-π and N-H-π stacking interactions collectively stabilize the binding of ATP with hIAPP. The structural stability of hIAPP protofibrils is also disturbed by ATP. Hence, we can finally conclude that ATP not only inhibits the aggregation of hIAPP monomers, but also disassembles pre-formed fibrils. This study imparts a concise information about the inhibition of ATP on hIAPP aggregation and can be used for other amyloid diseases.

References

[1] Roy, R.; Paul, S. Illustrating the Effect of Small Molecules Derived from Natural Resources on Amyloid Peptides. *J. Phys. Chem. B* **2023**, *127*, 600–615.

[2] Berhanu, W. M.; Masunov, A. E. Full Length Amylin Oligomer Aggregation: Insights from Molecular Dynamics Simulations and Implications for Design of Aggregation Inhibitors. *J. Biomol. Struct. Dyn.* **2014**, *32*, 1651–1669.

[3] Pithadia, A.; Brender, J. R.; Fierke, C. A.; Ramamoorthy, A. Inhibition of IAPP Aggregation and Toxicity by Natural Products and Derivatives. *J. Diabetes Res.* **2016**, *2016*, 2046327.

[4] Ren, B.; Liu, Y.; Zhang, Y.; Zhang, M.; Sun, Y.; Liang, G.; Xu, J.; Zheng, J. Tanshinones Inhibit hIAPP Aggregation, Disaggregate Preformed hIAPP Fibrils, and Protect Cultured Cells. *J. Mater. Chem. B* **2018**, *6*, 56–67.

[5] Ren, B.; Liu, Y.; Zhang, Y.; Cai, Y.; Gong, X.; Chang, Y.; Xu, L.; Zheng, J. Genistein: A Dual Inhibitor of Both Amyloid β and Human Islet Amylin Peptides. *ACS Chem. Neurosci.* **2018**, *9*, 1215–1224.

[6] Guo, J.; Sun, W.; Li, L.; Liu, F.; Lu, W. Brazilin Inhibits Fibrillogenesis of Human Islet Amyloid Polypeptide, Disassembles Mature Fibrils, and Alleviates Cytotoxicity. *RSC Adv.* **2017**, *7*, 43491–43501.

[7] Wang, Q.; Ning, L.; Niu, Y.; Liu, H.; Yao, X. Molecular Mechanism of the Inhibition and Remodeling of Human Islet Amyloid Polypeptide ($hIAPP_{1-37}$) Oligomer by Resveratrol from Molecular Dynamics Simulation. *J. Phys. Chem. B* **2015**, *119*, 15–24.

[8] Wang, Q.; Zhou, S.; Wei, W.; Yao, X.; Liu, H.; Hu, Z. Computational Insights into the Inhibition and Destabilization of Morin on the Oligomer of Full-length Human Islet Amyloid Polypeptide. *Phys. Chem. Chem. Phys.* **2015**, *17*, 29103–29112.

[9] Jiang, P.; Li, W.; Shea, J.-E.; Mu, Y. Resveratrol Inhibits the Formation of Multiple-layered β-sheet Oligomers of the Human Islet Amyloid Polypeptide Segment 22–27. *Biophys. J.* **2011**, *100*, 1550–1558.

[10] Mo, Y.; Lei, J.; Sun, Y.; Zhang, Q.; Wei, G. Conformational Ensemble of hIAPP Dimer: Insight into the Molecular Mechanism by Which a Green Tea Extract Inhibits hIAPP Aggregation. *Sci. Rep.* **2016**, *6*, 33076.

[11] Xu, Z.-X.; Ma, G.-L.; Zhang, Q.; Chen, C.-H.; He, Y.-M.; Xu, L.-H.; Zhou, G.-R.; Li, Z.-H.; Yang, H.-J.; Zhou, P. Inhibitory Mechanism of Epigallocatechin Gallate on Fibrillation and Aggregation of Amidated Human Islet Amyloid Polypeptide. *ChemPhysChem* **2017**, *18*, 1611–1619.

[12] Wu, L.; Velander, P.; Liu, D.; Xu, B. Olive Component Oleuropein Promotes β-Cell Insulin Secretion and Protects β-Cells from Amylin Amyloid-Induced Cytotoxicity. *Biochemistry* **2017**, *56*, 5035–5039.

[13] Cheng, B.; Gong, H.; Li, X.; Sun, Y.; Zhang, X.; Chen, H.; Liu, X.; Zheng, L.; Huang, K. Silibinin Inhibits the Toxic Aggregation of Human Islet Amyloid Polypeptide. *Biochem. Biophys. Res. Commun.* **2012**, *419*, 495 – 499.

[14] Lolicato, F.; Raudino, A.; Milardi, D.; La Rosa, C. Resveratrol Interferes with the Aggregation of Membrane-Bound Human-IAPP: A Molecular Dynamics Study. *Eur. J. Med. Chem.* **2015**, *92*, 876 – 881.

[15] Mishra, R.; Sellin, D.; Radovan, D.; Gohlke, A.; Winter, R. Inhibiting Islet Amyloid Polypeptide Fibril Formation by the Red Wine Compound Resveratrol. *ChemBioChem* **2009**, *10*, 445–449.

[16] Sciacca, M. F.; Chillemi, R.; Sciuto, S.; Greco, V.; Messineo, C.; Kotler, S. A.; Lee, D.-K.; Brender, J. R.; Ramamoorthy, A.; La Rosa, C. et al. A Blend of Two Resveratrol Derivatives Abolishes hIAPP Amyloid Growth and Membrane Damage. *Biochim. Biophys. Acta - Biomembranes* **2018**, *1860*, 1793 – 1802.

[17] Gilead, S.; Gazit, E. Inhibition of Amyloid Fibril Formation by Peptide Analogues Modified with α-Aminoisobutyric Acid. *Angew. Chem.* **2004**, *43*, 4041–4044.

[18] cheng Chiu, C.; Singh, S.; de Pablo, J. Effect of Proline Mutations on the Monomer Conformations of Amylin. *Biophys. J.* **2013**, *105*, 1227 – 1235.

[19] Kapurniotu, A.; Schmauder, A.; Tenidis, K. Structure-Based Design and Study of Non-Amyloidogenic, Double N-methylated IAPP Amyloid Core Sequences as Inhibitors of IAPP Amyloid Formation and Cytotoxicity. *J. Mol. Biol.* **2002**, *315*, 339 – 350.

[20] Sivanesam, K.; Shu, I.; Huggins, K. N. L.; Tatarek-Nossol, M.; Kapurniotu, A.; Andersen, N. H. Peptide Inhibitors of the Amyloidogenesis of IAPP: Verification of the Hairpin-Binding Geometry Hypothesis. *FEBS Lett.* **2016**, *590*, 2575–2583.

[21] Huggins, K. N. L.; Bisaglia, M.; Bubacco, L.; Tatarek-Nossol, M.; Kapurniotu, A.; Andersen, N. H. Designed Hairpin Peptides Interfere with Amyloidogenesis Pathways: Fibril Formation and Cytotoxicity Inhibition, Interception of the Preamyloid State. *Biochemistry* **2011**, *50*, 8202–8212.

[22] Tofoleanu, F.; Yuan, Y.; Pickard, F. C.; Tywoniuk, B.; Brooks, B. R.; Buchete, N.-V. Structural Modulation of Human Amylin Protofilaments by Naturally Occurring Mutations. *J. Phys. Chem. B* **2018**, *122*, 5657–5665.

[23] Mo, Y.; Brahmachari, S.; Lei, J.; Gilead, S.; Tang, Y.; Gazit, E.; Wei, G. The Inhibitory Effect of Hydroxylated Carbon Nanotubes on the Aggregation of Human Islet Amyloid Polypeptide Revealed by a Combined Computational and Experimental Study. *ACS Chem. Neurosci.* **2018**, *9*, 2741–2752.

[24] Wang, M.; Sun, Y.; Cao, X.; Peng, G.; Javed, I.; Kakinen, A.; Davis, T. P.; Lin, S.; Liu, J.; Ding, F. et al. Graphene Quantum Dots Against Human IAPP Aggregation and Toxicity *in vivo*. *Nanoscale* **2018**, *10*, 19995–20006.

[25] Nedumpully-Govindan, P.; Gurzov, E. N.; Chen, P.; Pilkington, E. H.; Stanley, W. J.; Litwak, S. A.; Davis, T. P.; Ke, P. C.; Ding, F. Graphene Oxide Inhibits hIAPP Amyloid Fibrillation and Toxicity in Insulin-Producing NIT-1 Cells. *Phys. Chem. Chem. Phys.* **2016**, *18*, 94–100.

[26] Bai, C.; Lao, Z.; Chen, Y.; Tang, Y.; Wei, G. Pristine and Hydroxylated Fullerenes Prevent the Aggregation of Human Islet Amyloid Polypeptide and Display Different Inhibitory Mechanisms. *Front. Chem.* **2020**, *8*, 51.

[27] Sorout, N.; Chandra, A. Effects of Boron Nitride Nanotube on the Secondary Structure of Aβ(1–42) Trimer: Possible Inhibitory Effect on Amyloid Formation. *J. Phys. Chem. B* **2020**, *124*, 1928–1940.

[28] Gazit, E. A Possible Role for π-Stacking in the Self-Assembly of Amyloid Fibrils. *FASEB J.* **2002**, *16*, 77–83.

[29] Meng, F.; Abedini, A.; Plesner, A.; Verchere, C. B.; Raleigh, D. P. The Flavanol (-)-Epigallocatechin 3-Gallate Inhibits Amyloid Formation by Islet Amyloid Polypeptide, Disaggregates Amyloid Fibrils, and Protects Cultured Cells against IAPP-Induced Toxicity. *Biochemistry* **2010**, *49*, 8127–8133.

[30] Evers, F.; Jeworrek, C.; Tiemeyer, S.; Weise, K.; Sellin, D.; Paulus, M.; Struth, B.; Tolan, M.; Winter, R. Elucidating the Mechanism of Lipid Membrane-Induced IAPP Fibrillogenesis and Its Inhibition by the Red Wine Compound Resveratrol: A Synchrotron X-ray Reflectivity Study. *J. Am. Chem. Soc.* **2009**, *131*, 9516–9521.

[31] Zou, Y.; Qian, Z.; Sun, Y.; Wei, G.; Zhang, Q. Orcein-Related Small Molecule O4 Destabilizes hIAPP Protofibrils by Interacting Mostly with the Amyloidogenic Core Region. *J. Phys. Chem. B* **2017**, *121*, 9203–9212.

[32] Lao, Z.; Chen, Y.; Tang, Y.; Wei, G.; Molecular Dynamics Simulations Reveal the Inhibitory Mechanism of Dopamine Against Human Islet Amyloid Polypeptide (hIAPP) Aggregation and its Destabilization Effect on hIAPP Protofibrils. *ACS Chem. Neurosci.* **2019**, *10*, 4151–4159.

[33] Porat, Y.; Mazor, Y.; Efrat, S.; Gazit, E. Inhibition of Islet Amyloid Polypeptide Fibril Formation A Potential Role for Heteroaromatic Interactions. *Biochemistry* **2004**, *43*, 14454–14462.

[34] Jackson, K.; Barisone, G. A.; Diaz, E.; Jin, L.-w.; DeCarli, C.; Despa, F. Amylin Deposition in the Brain: A Second Amyloid in Alzheimer Disease? *Ann. Neurol.* **2013**, *74*, 517–526.

[35] Miklossy, J.; Qing, H.; Radenovic, A.; Kis, A.; Vileno, B.; Làszló, F.; Miller, L.; Martins, R. N.; Waeber, G.; Mooser, V. et al. Beta Amyloid and Hyperphosphorylated

Tau Deposits in the Pancreas in Type 2 Diabetes. *Neurobiol. Aging* **2010**, *31*, 1503 – 1515.

[36] Andreetto, E.; Yan, L.-M.; Tatarek-Nossol, M.; Velkova, A.; Frank, R.; Kapurniotu, A. Identification of Hot Regions of the Aβ–IAPP Interaction Interface as High-Affinity Binding Sites in Both Cross- and Self-Association. *Angew. Chem.* **2010**, *49*, 3081–3085.

[37] Arnold, S. E.; Arvanitakis, Z.; Macauley-Rambach, S. L.; Koenig, A. M.; Wang, H.-Y.; Ahima, R. S.; Craft, S.; Gandy, S.; Buettner, C.; Stoeckel, L. E. et al. Brain Insulin Resistance in Type 2 Diabetes and Alzheimer Disease: Concepts and Conundrums. *Nat. Rev. Neurol.* **2018**, *14*, 168.

[38] Ahmed, T.; Javed, S.; Javed, S.; Tariq, A.; Šamec, D.; Tejada, S.; Nabavi, S. F.; Braidy, N.; Nabavi, S. M. Resveratrol and Alzheimer's Disease: Mechanistic Insights. *Mol. Neurobiol.* **2017**, *54*, 2622–2635.

[39] Lemkul, J. A.; Bevan, D. R. Morin Inhibits the Early Stages of Amyloid β-Peptide Aggregation by Altering Tertiary and Quaternary Interactions to Produce "Off-Pathway" Structures. *Biochemistry* **2012**, *51*, 5990–6009.

[40] Liu, F.-F.; Dong, X.-Y.; He, L.; Middelberg, A. P. J.; Sun, Y. Molecular Insight into Conformational Transition of Amyloid β-Peptide 42 Inhibited by (-)-Epigallocatechin-3-gallate Probed by Molecular Simulations. *J. Phys. Chem. B* **2011**, *115*, 11879–11887.

[41] Paul, S.; Paul, S. Inhibitory Effect of Choline-O-Sulfate on Aβ_{16-22} Peptide Aggregation: A Molecular Dynamics Simulation Study. *J. Phys. Chem. B* **2019**, *123*, 3475–3489.

[42] Paul, S.; Paul, S. Molecular Dynamics Simulation Study on the Inhibitory Effects of Choline-O-Sulfate on hIAPP Protofibrilation. *J. Comput. Chem.* **2019**, *40*, 1957–1968.

[43] Sun, Y.; Xi, W.; Wei, G. Atomic-Level Study of the Effects of O4 Molecules on the

Structural Properties of Protofibrillar Aβ Trimer: β-Sheet Stabilization, Salt Bridge Protection, and Binding Mechanism. *J. Phys. Chem. B* **2015**, *119*, 2786–2794.

[44] Zou, Y.; Qian, Z.; Chen, Y.; Qian, H.; Wei, G.; Zhang, Q. Norepinephrine Inhibits Alzheimer's Amyloid-β Peptide Aggregation and Destabilizes Amyloid-β Protofibrils: A Molecular Dynamics Simulation Study. *ACS Chem. Neurosci.* **2019**, *10*, 1585–1594.

[45] Thorp, A. A.; Schlaich, M. P. Relevance of Sympathetic Nervous System Activation in Obesity and Metabolic Syndrome. *J. Diabetes Res.* **2015**, *2015*, 341583.

[46] Neubauer, B.; Christensen, N. J. Norepinephrine, Epinephrine, and Dopamine Contents of the Cardiovascular System in Long-term Diabetics. *Diabetes* **1976**, *25*, 6–10.

[47] Liu, X.; Ye, K.; Weinshenker, D. Norepinephrine Protects Against Amyloid-β Toxicity via TrkB. *J. Alzheimers Dis.* **2015**, *44*, 251–260.

[48] Saunders, J. C.; Young, L. M.; Mahood, R. A.; Jackson, M. P.; Revill, C. H.; Foster, R. J.; Smith, D. A.; Ashcroft, A. E.; Brockwell, D. J.; Radford, S. E. An *in vivo* Platform for Identifying Inhibitors of Protein Aggregation. *Nat. Chem. Biol.* **2016**, *12*, 94–101.

[49] Zou, Y.; Qian, Z.; Gong, Y.; Tang, Y.; Wei, G.; Zhang, Q. Critical Nucleus of Greek-key-like Core of α-synuclein Protofibril and its Disruption by Dopamine and Norepinephrine. *Phys. Chem. Chem. Phys.* **2020**, *22*, 203–211.

[50] Young, L. M.; Saunders, J. C.; Mahood, R. A.; Revill, C. H.; Foster, R. J.; Tu, L.-H.; Raleigh, D. P.; Radford, S. E.; Ashcroft, A. E. Screening and Classifying Small-Molecule Inhibitors of Amyloid Formation Using Ion Mobility Spectrometry–Mass Spectrometry. *Nat. Chem.* **2015**, *7*, 73–81.

[51] Tu, L.-H.; Noor, H.; Cao, P.; Raleigh, D. P. Aspirin, Diabetes, and Amyloid: Reexamination of the Inhibition of Amyloid Formation by Aspirin and Ketoprofen. *ACS Chem. Biol.* **2014**, *9*, 1632–1637.

[52] Nedumpully-Govindan, P.; Kakinen, A.; Pilkington, E. H.; Davis, T. P.; Chun Ke, P.; Ding, F. Stabilizing Off-pathway Oligomers by Polyphenol Nanoassemblies for IAPP Aggregation Inhibition. *Sci. Rep.* **2016**, *6*, 19463.

[53] Luca, S.; Yau, W.-M.; Leapman, R.; Tycko, R. Peptide Conformation and Supramolecular Organization in Amylin Fibrils Constraints from Solid-State NMR. *Biochemistry* **2007**, *46*, 13505–13522.

[54] Frisch, M. J. et al. Gaussian˜09 Revision A.02. 2016; Gaussian Inc. Wallingford CT.

[55] Petersson, G. A.; Al-Laham, M. A. A Complete Basis Set Model Chemistry. II. Open-Shell Systems and the Total Energies of the First-Row Atoms. *J. Chem. Phys.* **1991**, *94*, 6081–6090.

[56] Bayly, C. I.; Cieplak, P.; Cornell, W.; Kollman, P. A. A Well-Behaved Electrostatic Potential Based Method Using Charge Restraints for Deriving Atomic Charges: the RESP Model. *J. Phys. Chem.* **1993**, *97*, 10269–10280.

[57] Wang, J.; Wolf, R. M.; Caldwell, J. W.; Kollman, P. A.; Case, D. A. Development and Testing of a General Amber Force Field. *J. Comput. Chem.* **2004**, *25*, 1157–1174.

[58] Paul, S.; Paul, S. Molecular Insights into the Role of Aqueous Trehalose Solution on Temperature-Induced Protein Denaturation. *J. Phys. Chem. B* **2015**, *119*, 1598–1610.

[59] Torrie, G.; Valleau, J. Nonphysical Sampling Distributions in Monte Carlo Free-Energy Estimation: Umbrella sampling. *J. Comput. Phys.* **1977**, *23*, 187 – 199.

[60] Kumar, S.; Rosenberg, J. M.; Bouzida, D.; Swendsen, R. H.; Kollman, P. A. The Weighted Histogram Analysis Method for Free-Energy Calculations on Biomolecules. I. The method. *J. Comput. Chem* **1992**, *13*, 1011–1021.

[61] Grossfield, A. WHAM: The Weighted Histogram Analysis Method. `http://membrane.urmc.rochester.edu/wordpress/?page_id=126`.

[62] Pal, S.; Paul, S. ATP Controls the Aggregation of Aβ_{16-22} Peptides. *J. Phys. Chem. B* **2020**, *124*, 210–223.

[63] Pal, S.; Paul, S. Conformational Deviation of Thrombin Binding G-quadruplex Aptamer (TBA) in Presence of Divalent Cation Sr^{2+}: A Classical Molecular Dynamics Simulation Study. *Int. J. Biol. Macromol.* **2019**, *121*, 350 – 363.

[64] Myslinski, J. M.; Clements, J. H.; Martin, S. F. Protein–ligand interactions: Probing the Energetics of a Putative Cation-π Interaction. *Bioorg. Med. Chem. Lett.* **2014**, *24*, 3164 – 3167.

[65] Abedini, A.; Raleigh, D. P. The Role of His-18 in Amyloid Formation by Human Islet Amyloid Polypeptide. *Biochemistry* **2005**, *44*, 16284–16291.

[66] Tu, L.-H.; Raleigh, D. P. Role of Aromatic Interactions in Amyloid Formation by Islet Amyloid Polypeptide. *Biochemistry* **2013**, *52*, 333–342.

[67] Patel, A.; Malinovska, L.; Saha, S.; Wang, J.; Alberti, S.; Krishnan, Y.; Hyman, A. A. ATP as a biological hydrotrope. *Science* **2017**, *356*, 753–756.

[68] Hayes, M. H.; Peuchen, E. H.; Dovichi, N. J.; Weeks, D. L. Dual roles for ATP in the Regulation of Phase Separated Protein Aggregates in Xenopus oocyte nucleoli. *eLife* **2018**, *7*.

[69] Kurisaki, I.; Tanaka, S. ATP Converts Aβ_{42} Oligomer into Off-Pathway Species by Making Contact with Its Backbone Atoms Using Hydrophobic Adenosine. *J. Phys. Chem. B* **2019**, *123*, 9922–9933.

[70] Tenidis, K.; Waldner, M.; Bernhagen, J.; Fischle, W.; Bergmann, M.; Weber, M.; Merkle, M. L.; Voelter, W.; Brunner, H.; Kapurniotu, A. Identification of a Penta- and Hexapeptide of Islet Amyloid Polypeptide (IAPP) with Amyloidogenic and Cytotoxic Properties. *J. Mol. Biol.* **2000**, *295*, 1055–1071.

[71] Melquiond, A.; Gelly, J. C.; Mousseau, N.; Derreumaux, P. Probing Amyloid Fibril Formation of the NFGAIL peptide by Computer Simulations. *J. Chem. Phys* **2007**, *126*, 065101.

[72] Soriaga, A. B.; Sangwan, S.; Macdonald, R.; Sawaya, M. R.; Eisenberg, D. Crystal Structures of IAPP Amyloidogenic Segments Reveal a Novel Packing Motif of Out-of-Register Beta Sheets. *J. Phys. Chem. B* **2016**, *120*, 5810–5816.

[73] Mo, Y.; Lu, Y.; Wei, G.; Derreumaux, P. Structural Diversity of the Soluble Trimers of the Human Amylin(20–29) Peptide revealed by Molecular Dynamics Simulations. *J. Chem. Phys* **2009**, *130*, 125101.

[74] Röder, C.; Kupreichyk, T.; Gremer, L.; Schäfer, L. U.; Pothula, K. R.; Ravelli, R. B. G.; Willbold, D.; Hoyer, W.; Schröder, G. F. Cryo-EM structure of islet amyloid polypeptide fibrils reveals similarities with amyloid-β fibrils. *Nat. Struct. Mol. Biol.* **2020**, *27*, 660–667.

[75] Ma, H.; Holub, D.; Gillet, N.; Kaeser, G.; Thoulass, K.; Elstner, M.; Krauß, N.; Lamparter, T. Two Aspartate Residues Close to the Lesion Binding Site of Agrobacterium (6-4) Photolyase are required for Mg^{2+} Stimulation of DNA Repair. *FEBS J.* **2019**, *286*, 1765–1779.

[76] Meagher, K. L.; Redman, L. T.; Carlson, H. A. Development of Polyphosphate Parameters for use with the AMBER Force Field. *J. Comput. Chem.* **2003**, *24*, 1016–1025.

[77] Li, P.; Roberts, B. P.; Chakravorty, D. K.; Merz, K. M. Rational Design of Particle Mesh Ewald Compatible Lennard-Jones Parameters for +2 Metal Cations in Explicit Solvent. *J. Chem. Theory Comput.* **2013**, *9*, 2733–2748.

[78] Pal, S.; Roy, R.; Paul, S. Potential of a Natural Deep Eutectic Solvent, Glyceline, in the Thermal Stability of the Trp-Cage Mini-protein. *J. Phys. Chem. B* **2020**, *124*, 7598–7610.

[79] Azriel, R.; Gazit, E. Analysis of the Minimal Amyloid-forming Fragment of the Islet Amyloid Polypeptide: An Experimental Support for the Key Role of the Phenylalanine Residue in Amyloid Formation. *J. Biol. Chem.* **2001**, *276*, 34156–34161.

Chapter 4

Inhibitory Effect on hIAPP Aggregation by Peptides/Peptidomimetics

"From humble beginnings as substances isolated from livestock glands, peptides have established a unique therapeutic niche and will continue to be an important element in the pharmaceutical landscape."

– Jolene Lau, *et. al.*

Overview

Very few studies have been conducted on the peptide based inhibitors against amyloid aggregation. The short peptide fragments derived from hIAPP have a high propensity to interact with hIAPP, thus interfering with hIAPP-hIAPP interactions. In this thesis, two peptide based inhibitors have been investigated against hIAPP aggregation. These peptides are derived from the amyloid core sequence of hIAPP, i.e., $hIAPP_{22-27}$, and consists of NFGAIL residues. In the first part, the L-amino acids in the peptide fragment is replaced with D-amino acid residues, which is used as an inhibitor. As a control, the effect of L-NFGAIL fragment on the oligomerization of hIAPP is also studied. While L-NFGAIL (which consists of L-amino acids) stabilizes the β-sheet-rich aggregates of full-length hIAPP, D-NFGAIL promotes the random coil conformation of hIAPP and interrupts hIAPP-hIAPP interaction. In the second part, one (Ile26) and two (Gly24 and Ile26) residues in the NFGAIL fragment is replaced with three different isomers of aminobenzoic moieties (i.e., β, γ, δ). The presence of non-proteinogenic aminobenzoic acid moiety renders the BSBHps to be more stable towards proteolytic degradation. The different isomeric BSBHps exhibit contrasting influence on the self-assembly of hIAPP. The BSBHps containing β and γ-aminobenzoic acid can sufficiently prevent hIAPP aggregation, but those with δ-aminobenzoic group stabilize the β-sheet rich aggregate of hIAPP. The difference in the angle between the amino and carboxyl groups in the isomers of the aminobenzoic moiety cause the BSBHps to attain discrete conformation and hence leads to variation in their binding preference with hIAPP, and ultimately their inhibitory potency. Hence, in this chapter, we have conveyed the effect of stereochemistry of the amino acid residues or modified organic moieties on the inhibitory potential of peptides or peptidomimetics.

4.1 A hIAPP-Amyloid-Core derived D-peptide prevents hIAPP Aggregation and destabilizes its Protofibrils

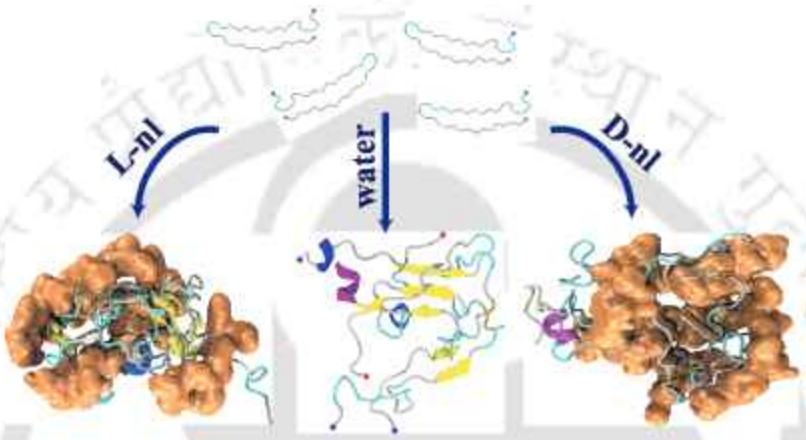

4.1.1 Introduction

A variety of inhibitors, including small organic molecules, peptides, nanoparticles, has been developed, which interfere the aggregation or eliminate existing aggregates of hIAPP[1]. Out of these, fewer studies have been conducted in the design of small peptides or peptide mimetics which can inhibit hIAPP aggregation. The merits and demerits of peptide-based hIAPP inhibitors are discussed in Chapter 1. Most of these peptides are derived from the original sequence of hIAPP and are modified by replacing with different amino acid residues or organic moieties, which favours the interaction of hIAPP with these peptides over itself[1]. Another strategy implemented to design peptide inhibitors is to replace the natural L-amino acid residues with their stereochemical mirror images (i.e. D-amino acids).

Although the biological activity of D-amino-acid containing peptides resemble with that of their L-amino acid counterparts, the D-peptides have a resistance towards proteolytic degradation and vascular clearance *in vivo*, and, hence, have longer half-life times. Due to their high selectivity, enhanced bioavailability and less immunogenics nature[2], they are suitable for therapeutics. The effectiveness of the D-peptides as a drug is reported in the treatment of tumors[3]. Furthermore, the interaction between D-amino-acid containing β-hairpin peptides and hIAPP, which is enhanced by the presence of hydrophobic sites of aromatic residues, intercepts the hIAPP-hIAPP interactions, thus preventing aggregation[4]. Ten-fold excess of WW2, a β-hairpin more potent than rIAPP, completely suppresses hIAPP cytotoxicity in rat insulinoma cells[4]. The peptides consisting of alternating L- and D-amino acid residues, designed by Daggett, inhibit both Aβ and hIAPP aggregation[5, 6]. The inhibitory potency of all D-amino acids as inhibitor against Aβ fibril formation has already been reported[7–9]. Moreover, *in silico* study of the stability of Aβ fibril in presence of full-length retro-inverso D-peptide (DRI) was also explored, where it was suggested that DRI-Aβ enhanced the fibril formation and hence decreased the ratio of toxic oligomers[10]. A similar study on hIAPP fibril disclosed that DRI-hIAPP lowers the stability of the hybrid hIAPP fibrils by separating the protofibrils and changes the elongation process, which suggested the potential inhibitory role of DRI-hIAPP on fibril formation[11].

In our study, we have investigated the inhibition of hIAPP aggregation by a novel peptide segment derived from the amyloidogenic core of hIAPP[12–14], $hIAPP_{22-27}$ or

NFGAIL, consisting of all-D-amino-acid residues (D-nl). The presence of equimolar D-nl in bulk solution of hIAPP completely suppressed the ThT fluorescence intensity and only small pieces of fibrils were observed in the TEM images[15]. Moreover, hIAPP-induced toxic cells were recovered by D-nl at a dose-dependant manner, which increased the cell viability of INS-1 cells at a hIAPP:inhibitor molar ratio of 1:20[15]. The above study also reports the inhibition of hIAPP aggregation at the phospholipid membrane by D-nl peptides[15]. However, the exact mechanism by which D-NFGAIL intercepts the aggregation at the β-sheet oligomeric intermediate state in the bulk solution is unknown. Therefore, in this work, we have investigated the possible role of D-nl as a inhibitor of hIAPP via molecular dynamics simulations. We begin our study by first observing the effect of D-nl on the stability of an aggregated structure of L-NFGAIL (L-nl). Having confirmed that D-nl peptides completely destabilizes the aggregated structure of L-nl, we explore how D-nl inhibits the aggregation of randomly packed full-length hIAPP and compare the results with the effect of L-nl peptides on hIAPP. We observe that, while L-nl enhances the stability of aggregated structure of hIAPP, D-nl interrupts the aggregation. Moreover, we also analyze the destabilization effect of D-nl on the fibrillar structure of full length hIAPP.

The simulations and the analysis methods are described in the Simulation Method section. In-detail explanation of our findings and our deductions are stated in the Results and the Discussion sections respectively, and the Conclusion section summarizes our overall observations.

4.1.2 Simulation method

4.1.2.1 Simulation Setup

All-atom molecular dynamics simulations were performed to examine the effect of D-nl peptides on the aggregation of different structures of hIAPP. In the previous chapter (Chapter 3.2), we had seen that the most populated conformation of $hIAPP_{22-28}$[16] in pure water is a β-barrel like conformation[17]. In this study, we have extracted the barrel structure, consisting of four $hIAPP_{22-27}$ (NFGAIL) strands arranged in an anti-parallel β-sheet structure, which serves as the L-nl model (Frag-L). Two alternate peptide strands in the above model were then replaced by their respective D-amino acid residues (Fig 4.1), such that the LD-hybrid models were composed of alternate L and D-amino acid containing peptide

strands[18] (Frag-LD). Another set of the above systems were simulated (Frag-L(a) and Frag-LD(a)) to conclude the convergence of the systems.

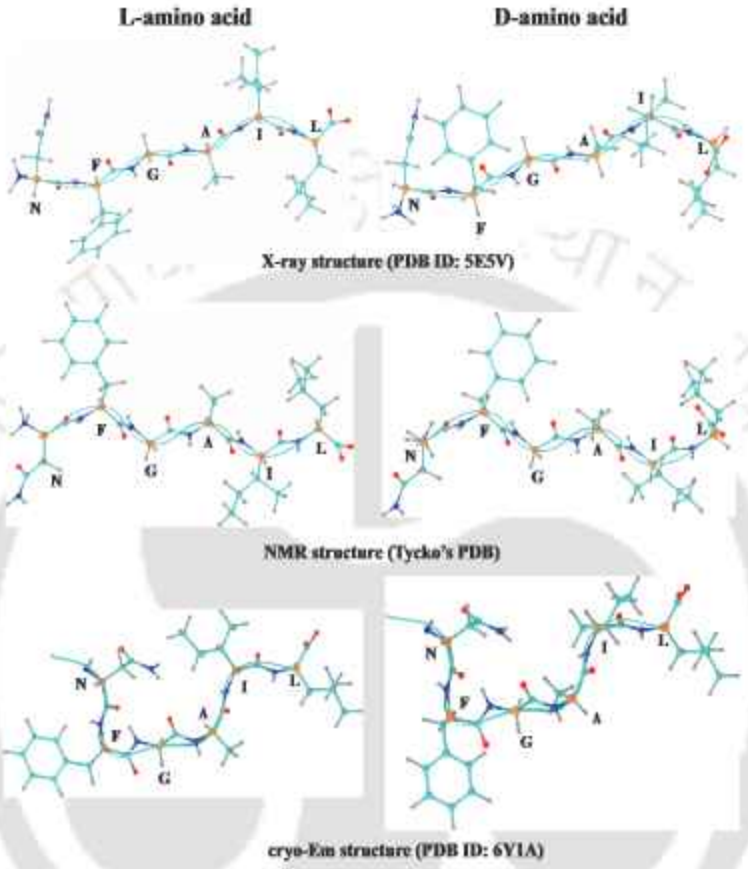

Figure 4.1: *Structures of L- and D-nl peptides used in the simulations. The Cα, N, O, H and the remaining C atoms are depicted in orange, blue, red, silver and cyan respectively*

The aggregation of four full length hIAPP in presence of L-nl and D-nl peptides were also examined. The initial structure of full length hIAPP was extracted from the solid-state NMR structure[19], while that of the L-nl peptide was obtained from PDB ID 2KIB[20]. The D-nl peptide was constructed using AMBERTools[18, 21] (Fig 4.1). The four hIAPP were sufficiently separated from each other initially and the nl peptides were randomly placed around them. Two sets of simulations each for hIAPP in water (hIAPP and hIAPP(a)), with L-nl peptides (hIAPP+L and hIAPP+L(a)) and D-nl peptides (hIAPP+L and hIAPP+L(a)) were carried out with different starting structures, such that the results do not depend on the initial configuration of the systems.

The stability of two different hIAPP protofibrils in presence of L-nl and D-nl pep-

tides were further analyzed. One of the hIAPP protofibrillar polymorph was extracted from the above mentioned ss-NMR structure[19] (Fib-N). The L-nl (Fib-N+L) and D-nl peptides (Fib-N+D) for these systems was generated from PDB ID 2KIB[20] as well (Fig 4.1). The other hIAPP protofibril was a cryo-EM model, obtained from PDB ID 6Y1A[22] (Fib-C).

System	hIAPP	L-nl	D-nl	Solvent	Box length (Å)
Frag-L		4		4000	49.97
Frag-L(a)		4		4000	49.94
Frag-LD		2	2	4000	49.94
Frag-LD(a)		2	2	4000	49.99
hIAPP	4			10000	69.71
hIAPP(a)	4			10000	69.25
hIAPP+L	4	12		10000	69.27
hIAPP+L(a)	4	12		10000	69.29
hIAPP+D	4		12	10000	69.38
hIAPP+D(a)	4		12	10000	69.36
Fib-N	5			10000	68.91
Fib-N(a)	5			10000	68.94
Fib-N+L	5	25		10000	70.32
Fib-N+D	5		25	10000	70.35
Fib-N+D(a)	5		25	10000	70.30
Fib-C	5			10000	68.08
Fib-C(a)	5			10000	68.46
Fib-C+L	5	25		10000	70.03
Fib-C+D	5		25	10000	70.13
Fib-C+D(a)	5		25	10000	69.99
Dimer	2			5000	54.41
Dimer+D	2		6	5000	54.98

Table 4.1: *Details of the simulated systems.*

The coordinates of $N_{22}FGAIL_{27}$ was extracted from this structure for the L-nl peptide (Fib-C+L) and its chirality was flipped using AMBERTools[21] to generate the D-nl peptide used with the cryo-em model of hIAPP protofibril[18] (Fib-C+D) (Fig 4.1). Each of the protofibrillar systems in pure water (Fib-N(a) and Fib-C(a)) and in presence of D-nl peptides (Fib-N+D(a) and Fib-C+D(a) was simulated twice with different initial configurations. following simulation protocols mentioned in Chapter 1 (Section 1.5.2). Overall,

for this study, a total of 20 μs of simulation time was carried out.

4.1.2.2 Simulation Analysis

The simulation analyses were carried out following the protocols discussed in Chapter 1 (Section 1.5.3). The preferential interaction parameters (Γ_{pn} and Γ_{nw}) were calculated using the following equations,

$$\Gamma_{pn} = \rho_p(G_{pp} - G_{pn}) \tag{4.1}$$

$$\Gamma_{nw} = \rho_p(G_{pn} - G_{pw}) \tag{4.2}$$

where p, w and n represent hIAPP, water and nl peptides respectively, and ρ_p corresponds to the number density of hIAPP. G_{pp}, G_{pw} and G_{pn} are the Kirkwood-Buff (KB) integrals and they are calculated from the radial distribution functions of the centre of mass of the peptides with itself, water and nl peptides respectively. The radius of gyration (R_g) and the number of inter-peptide hydrogen bonds are used to plot the free energy landscape (FEL), using the equation 1.19. The first solvation shell coordination numbers are defined by the number of water and nl peptides present within 3.5 Å of hIAPP[23]. For the spatial distribution functions of nl peptides around hIAPP, an isovalue of 0.5 was considered.

In order to estimate the effect of D-nl peptides on hIAPP dimer formation, we calculate the potentials of mean force (PMFs) of hIAPP dimer via umbrella sampling (US) method[24]. All the US simulations were renormalized using Weighted-Histogram Analysis Method (WHAM)[25, 26]. For this, two full-length hIAPP peptides, in absence (Dimer) and (Dimer+D) presence of D-nl peptides, were simulated, following above mentioned protocols, for 250 ns. The starting structures for the US simulations are taken from the final trajectory of the above simulations. For each US, the reaction coordinate applied was the distance between the centre of masses of the Cα atoms of two hIAPP monomers. The US simulations spanned through 3 to 20 Å distance, with 0.2 Å increment, thus populated by 86 windows. The peptides were sampled with a pull force of 2.5 kcal mol^{-1} Å^2 under NPT ensemble at 300 K over 30 ns per window. Hence, the two PMFs resulted in additional 5.16 μs of simulation time.

4.1.3 Results

4.1.3.1 D-nl peptides Disassemble hIAPP$_{22-27}$ Aggregates

We begin our study by first determining how D-nl affects the aggregation of its L-counterpart. The structural stability of the LD-hybrid structure is compared with that of the original L-model, which is extracted from an earlier study[17], to analyze the influence of D-nl peptides. At first, we perform the root mean square deviation (RMSD) analysis, which provides a thorough insight into the structural changes of the peptides during the simulations.

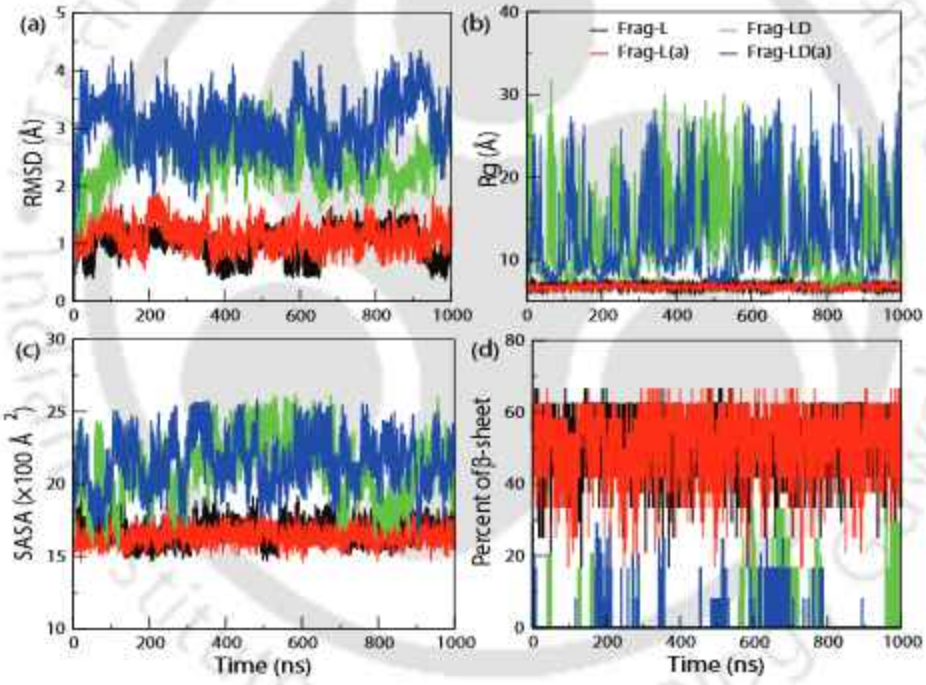

Figure 4.2: *Time evolution of (a) RMSD, (b) R_g, (c) SASA and (d) β-sheet content of hIAPP$_{22-27}$ peptides in different systems.*

From Fig 4.2a, we observe that the backbone RMSD of L-nl is stable at around 1.25 Å, while that of LD-nl is higher than its L conformation, which hints at the large structural deviations of the barrel with the incorporation of D-nl. Moreover, the RMSD of the peptides stabilize during the course of the simulation and hence makes it ideal for further analysis of the simulations.

The radius of gyration (R_g) is an important order parameter to differentiate be-

tween the structures of IDP morphologies. The compact assembly of the L-nl barrel yields a low R_g,

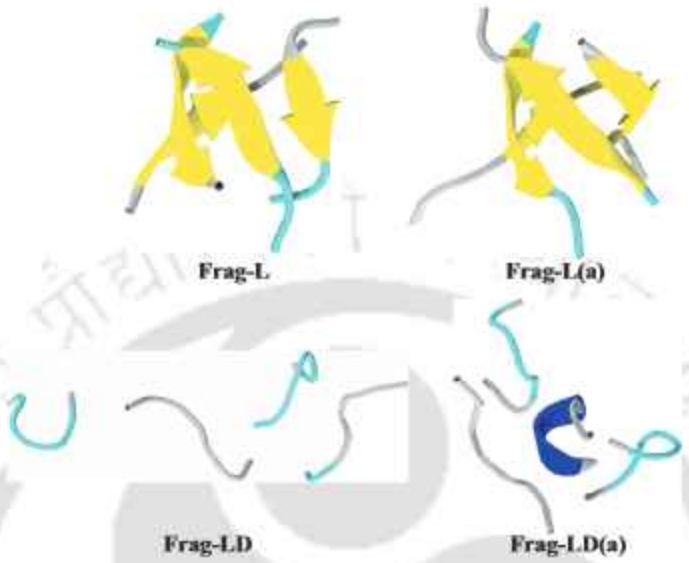

Figure 4.3: *Representative conformations of the most populated structure of $hIAPP_{22-27}$ peptides in different systems. The peptides are represented in cartoon form, depicting β-sheet in yellow, coil in silver, turn in cyan and 3_{10}-helix in blue.*

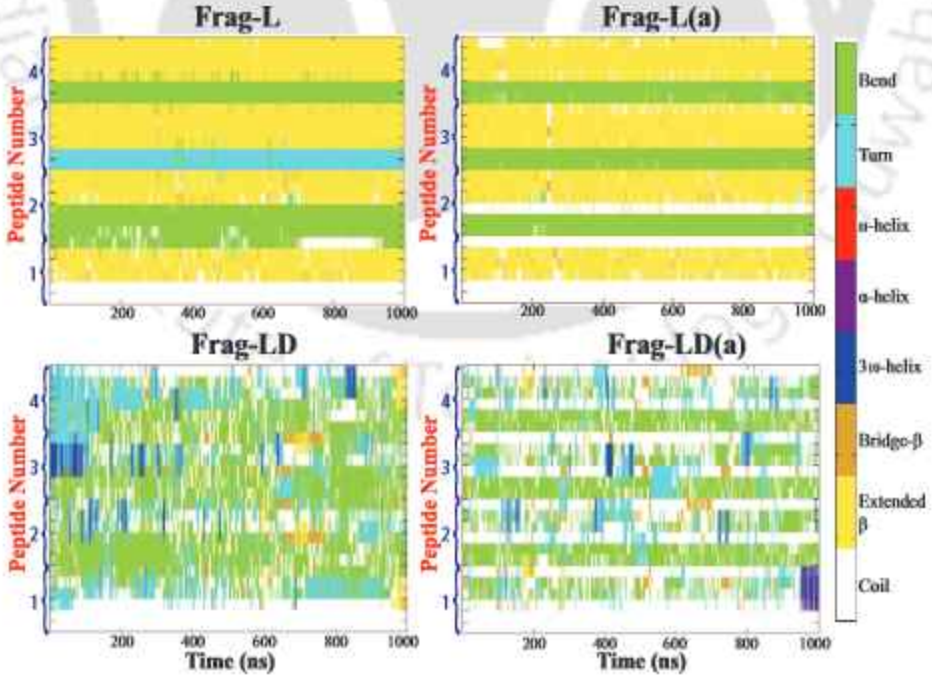

Figure 4.4: *Time evolution of change of secondary structures of each residue of $hIAPP_{22-27}$ peptides in different systems.*

System	Extended-β	Bridge-β	3_{10}-helix	α-helix	Coil
Frag-L	57.2 ± 0.5	0.3 ± 0.0	0	0	11.3
Frag-L(a)	54.8 ± 0.5	0.3 ± 0.0	0	0	20.1
Frag-LD	2.4 ± 0.0	1.6 ± 0.0	1.8 ± 0.0	0.0 ± 0.0	35.5
Frag-LD(a)	0.0 ± 0	0.5 ± 0.0	2.4 ± 0.0	2.2 ± 0.1	51.3
hIAPP	15.6 ± 0.3	2.4 ± 0.1	4.1 ± 0.2	0.0 ± 0	47.4
hIAPP(a)	19.7 ± 0.3	4.0 ± 0.1	1.7 ± 0.1	2.6 ± 0.2	40.7
hIAPP+L	12.6 ± 0.3	2.7 ± 0.1	2.2 ± 0.1	2.5 ± 0.1	45.5
hIAPP+L(a)	17.0 ± 0.3	6.7 ± 0.2	1.1 ± 0.0	2.3 ± 0.1	42.9
hIAPP+D	0.9 ± 0.0	4.7 ± 0.2	3.8 ± 0.2	3.9 ± 0.2	44.8
hIAPP+D(a)	2.5 ± 0.1	5.9 ± 0.2	1.3 ± 0.0	2.0 ± 0.1	50.4
Fib-N	40.0 ± 0.4	0.2 ± 0.0	0.0 ± 0	0	39.0
Fib-N(a)	37.3 ± 0.4	2.2 ± 0.1	0.8 ± 0.1	0.1 ± 0.0	37.0
Fib-N+L	37.0 ± 0.5	4.1 ± 0.2	0.4 ± 0.0	0	35.8
Fib-N+D	34.1 ± 0.4	4.2 ± 0.1	1.3 ± 0.1	0	52.6
Fib-N+D(a)	33.0 ± 0.4	3.9 ± 0.2	2.9 ± 0.1	0.3 ± 0.0	40.9
Fib-C	40.8 ± 0.5	0.9 ± 0.1	0	0	33.3
Fib-C(a)	43.5 ± 0.4	2.5 ± 0.1	0.2 ± 0.0	0.0 ± 0	28.8
Fib-C+L	46.0 ± 0.4	1.8 ± 0.1	0	0	25.9
Fib-C+D	30.6 ± 0.4	5.3 ± 0.2	0	0	40.0
Fib-C+D(a)	34.5 ± 0.4	2.6 ± 0.1	0	0	34.4

Table 4.2: *The primary secondary structure contents (in %) of hIAPP in different systems.*

which is consistent at around 7 Å (Fig 4.2b). However, large fluctuations are observed for the R_g of LD-nl peptides, pointing out the shift in the conformation of the peptides towards an extended unfolded state. The random loosely packed conformers interact more with the solvent molecules i and eventually result in higher solvent accessible surface area (SASA) (Fig 4.2c).

The preference of the peptides for extended structures in presence of D-nl is also revealed in the snapshots of the most populous structures (Fig 4.3). As expected, L-nl maintains its starting barrel conformation, consisting of anti-parallel β-strands. However, LD-nl adopts a scattered disordered coiled structure. A closer look into the secondary structure contents further reveal that, while the average value of β-sheet percentage is 57.19 % throughout the simulation run for L-nl peptides, it is much lower for the LD-nl peptides (Fig 4.2d and 4.4). The average value of random coil conformation, on the other

hand, increases in presence of D-nl peptides (Table 4.2, last column). The snapshots of the peptides at the beginning and the end of the simulations further justify our results (Fig 4.5).

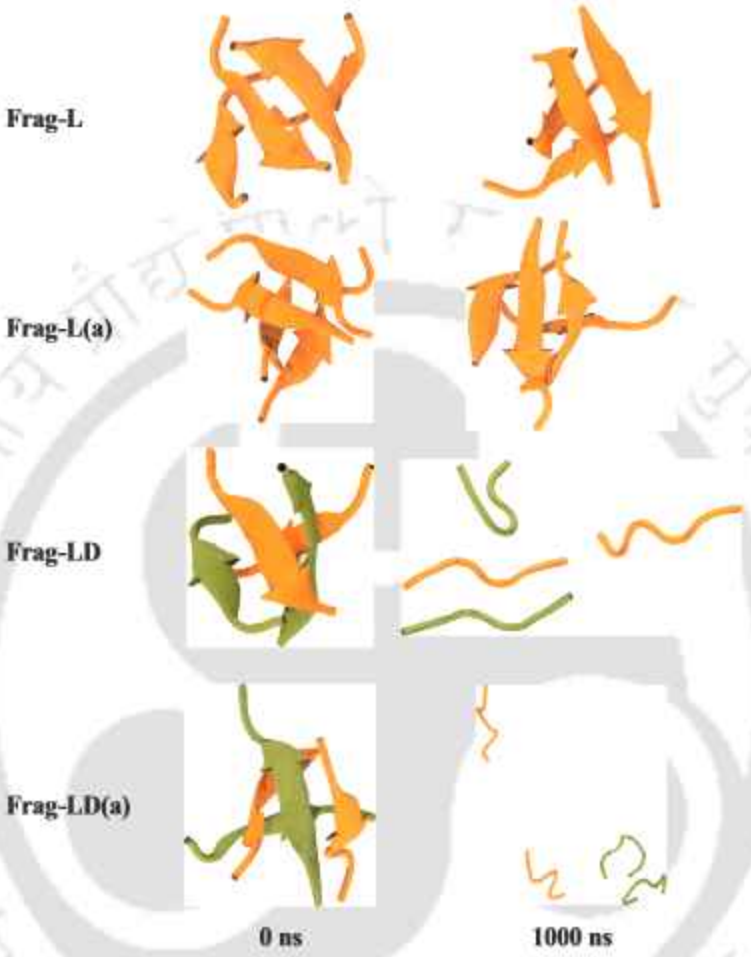

Figure 4.5: *Snapshots of the initial and the final configuration of $hIAPP_{22-27}$ peptides in different systems. L-NFGAIL is depicted in orange and D-NFGAIL is depicted in green.*

To understand the structural preferences of the different peptides by characterizing the interactions between the peptides, we first compute the residue-residue contact maps (Fig 4.6). The contact map between the backbone atoms of the L-nl peptides exhibit significant interpeptide contacts, mostly among the residues Phe23, Gly24, Ala25 and Ile26. Similarly, substantial contact between the side chain atoms is also present (Fig 4.7). However, hardly any contact is observed for the LD-nl systems. The interaction energy of the peptides also provides a quantitative idea of the intrapeptide interactions. The interaction energy is dissected into electrostatic and van der Waals (vdW) contributions, where the

first dominates over the latter one (Table 4.4).

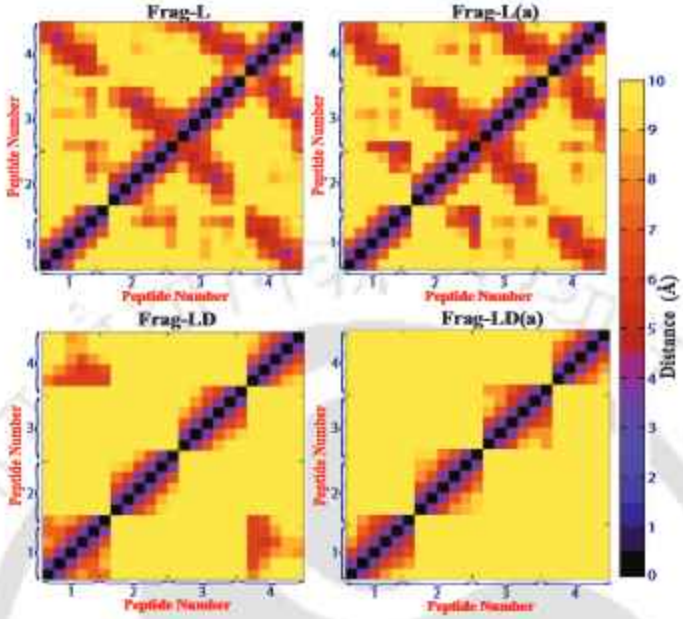

Figure 4.6: *Residue-residue contact map of the backbone atoms of $hIAPP_{22-27}$ peptides in different systems.*

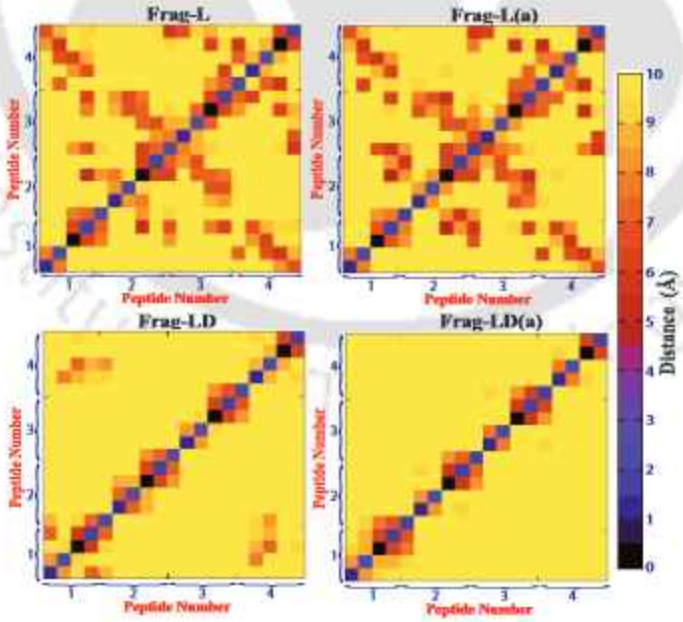

Figure 4.7: *Residue-residue contact map of the side-chain atoms of $hIAPP_{22-27}$ peptides in different systems.*

Even though the electrostatic interaction hardly changes with the incorporation of D-nl

peptides, the vdW energy becomes unfavourable. A marked decrease in the number of hydrogen bond between the peptides is also observed for the LD-nl peptides compared to that of the L-nl parent (Table 4.3). From all the above analysis, we can conclude that the barrel structure formed by L-nl peptides remains stable throughout the simulation run. However, the incorporation of D-nl into the barrel completely destabilizes the structure and the peptides attain loosely packed random conformation, following a marked decrease in the interactions between the peptides.

System	Peptide-peptide	Peptide-nl
Frag-L	14.01 ± 0.03	
Frag-L(a)	15.79 ± 0.03	
Frag-LD	8.49 ± 0.05	
Frag-LD(a)	9.47 ± 0.03	
Fib-N	131.95 ± 0.12	
Fib-N(a)	133.2 ± 0.08	
Fib-N+L	135.5 ± 0.08	40.58 ± 0.06
Fib-N+D	116 ± 0.53	47.03 ± 0.47
Fib-N+D(a)	108.4 ± 0.08	44.3 ± 0.03
Fib-C	125.6 ± 0.12	
Fib-C(a)	133 ± 0.07	
Fib-C+L	126.4 ± 0.07	36.74 ± 0.07
Fib-C+D	113.2 ± 0.32	28.09 ± 0.22
Fib-C+D(a)	94.07 ± 0.07	23.12 ± 0.04

Table 4.3: *Average hydrogen bond numbers between hIAPP-hIAPP and hIAPP-nl interactions for different systems.*

4.1.3.2 D-nl peptides Modify the Secondary Structure of Full Length hIAPP

After exploring the effect of D-nl peptides on the conformation of L-nl oligomers, we turn our attention to examine the inhibitory property of D-nl on the aggregation of full length hIAPP and compare the outcome with the effect of L-nl peptides. At first, we describe the conformation of the four full length hIAPP peptides in each of the system by performing cluster analysis. The hIAPP conformation in hIAPP, hIAPP+L and hIAPP+D systems are separated into 4, 8 and 8 clusters respectively. Three of the most populated structure in each system are represented in Fig 4.8. In absence of any nl peptides, hIAPP have a

preference to adopt an ordered three-stranded β-sheet structure, where one chain forms a β-hairpin (Arg11-His18 and Ile26-Ser29), and another chain forms the third β-strand (Arg11-His18). Disordered conformation consisting of helix and short β-sheet structures are also observed. The β-hairpin has been previously reported to be the amyloidogenic precursor of hIAPP and the position of its β-strands obtained in our study resemble with that of the NMR-derived hIAPP fibrils[19].

System	hIAPP-hIAPP		hIAPP-NL	
	Ele	vdW	Ele	vdW
Frag-L	-766.5 ± 0.78	-41.33 ± 0.11		
Frag-L(a)	-780.1 ± 0.5	-51.07 ± 0.12		
Frag-LD	-775.7 ± 1.32	-11.48 ± 0.23		
Frag-LD(a)	-766.4 ± 1.03	-10.4 ± 0.21		
hIAPP	-4409 ± 0.57	-343.6 ± 0.25		
hIAPP(a)	-4545 ± 0.71	-389.8 ± 0.27		
hIAPP+L	-4389 ± 0.74	-380.2 ± 0.29	-953.9 ± 1.7	-297.4 ± 0.21
hIAPP+L(a)	-4303 ± 0.64	-398.6 ± 0.26	-1264 ± 1.61	-249.5 ± 0.26
hIAPP+D	-4378 ± 0.64	314.5 ± 0.36	-1041 ± 1.75	-310.4 ± 0.19
hIAPP+D(a)	-4305 ± 0.69	352.2 ± 0.37	-896.6 ± 1.35	-358.4 ± 0.19
Fib-N	-5630 ± 1.01	-670.5 ± 0.39		
Fib-N(a)	-5841 ± 0.82	-621.2 ± 0.29		
Fib-N+L	-5438 ± 0.69	-685.2 ± 0.29	-1545 ± 1.99	-375.6 ± 0.27
Fib-N+D	-5304 ± 0.59	-588.1 ± 0.29	-1422 ± 1.47	-391.9 ± 0.4
Fib-N+D(a)	-5218 ± 0.7	-593.8 ± 0.32	-1386 ± 1.86	-368.9 ± 0.27
Fib-C	-3963 ± 0.67	-588.95 ± 0.32		
Fib-C(a)	-3741 ± 0.53	-434.3 ± 0.24		
Fib-C+L	-3859 ± 0.4	-439.3 ± 0.22	-895.8 ± 1.23	-410.2 ± 220.22
Fib-C+D	-3870 ± 29.64	-426.7 ± 15.45	-717.6 ± 53.14	-315.3 ± 12.87
Fib-C+D(a)	-3927 ± 0.42	-401.4 ± 0.22	-528.2 ± 0.67	-270.1 ± 0.22

Table 4.4: *Interaction energy (kcal/mol) of hIAPP-hIAPP and hIAPP-nl interactions in different systems.*

In presence of L-nl peptides, the β-sheet rich structure of hIAPP, alongwith with the three stranded β-sheet, is maintained. However, the β-hairpin vanishes when D-nl is included in the system and hIAPP mostly exists in disordered coil rich states, with much shorter helix and β-sheets.

The average secondary structure contents of hIAPP in all the systems draw a

quantitative picture on the influence of D-nl on the secondary structures of hIAPP (Table 4.2). The probability of extended β-sheet structure of hIAPP in pure water is 15.58%,

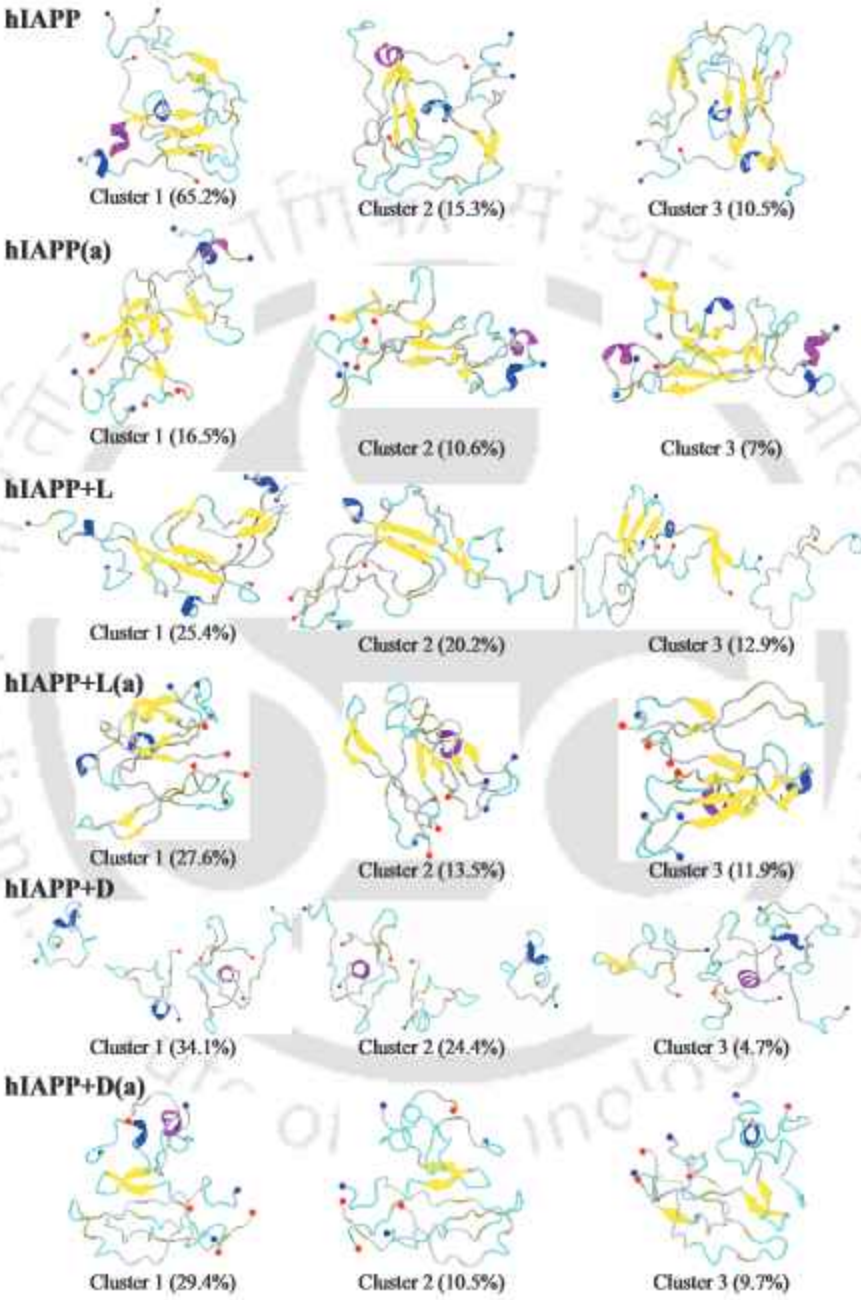

Figure 4.8: *Representative conformations of the clusters of full-length hIAPP in different systems. The peptides are represented in cartoon form, depicting β-sheet in yellow, coil in silver, turn in cyan, α-helix in purple and 3_{10}-helix in blue. The blue and red balls represent the N and C-terminal ends respectively.*

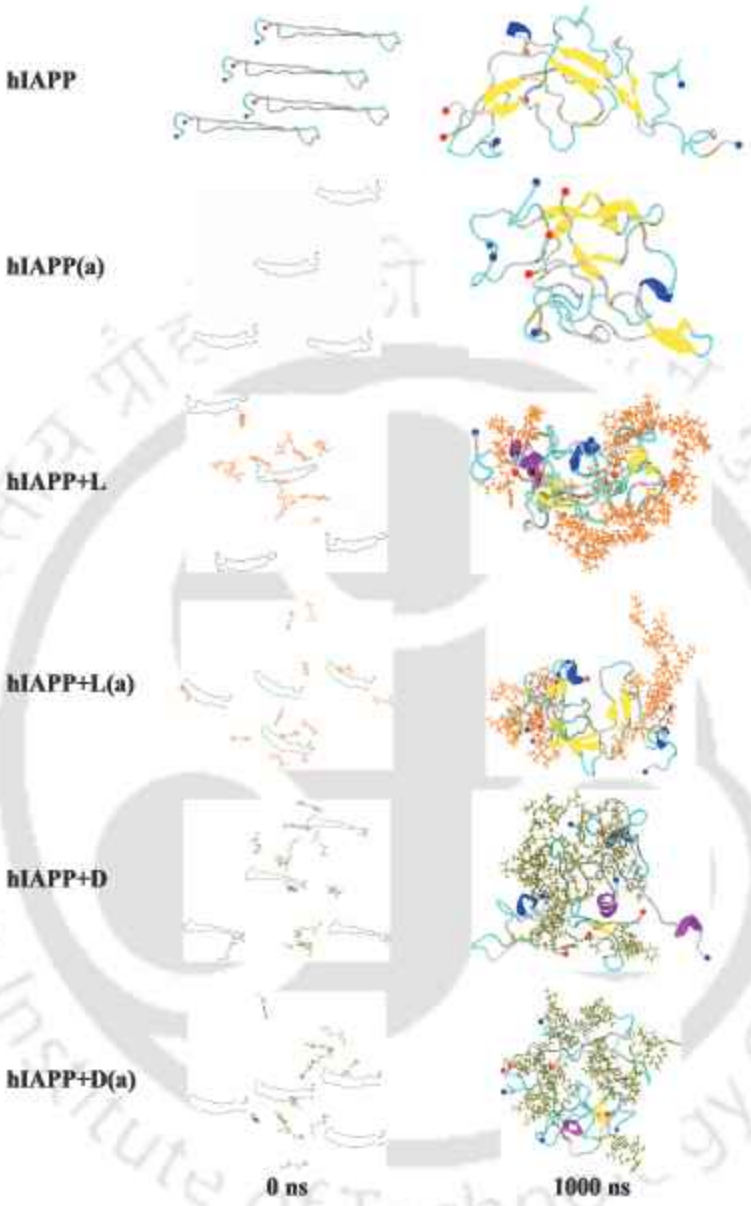

Figure 4.9: *Snapshots of the initial and the final configuration of hIAPP peptides in different systems. The full-length peptides are represented in cartoon form, depicting β-sheet in yellow, coil in white, bend in cyan and 3_{10}-helix in blue. L-NFGAIL is depicted in orange and D-NFGAIL is depicted in green, represented in CPK form.*

which remains almost same in presence of L-nl peptides, but decreases to a negligible value in presence of D-nl (Table 4.2, first column). However, hardly any change in the value of bridged β structure is observed with the incorporation of the D-nl peptides (Table 4.2,

second column).

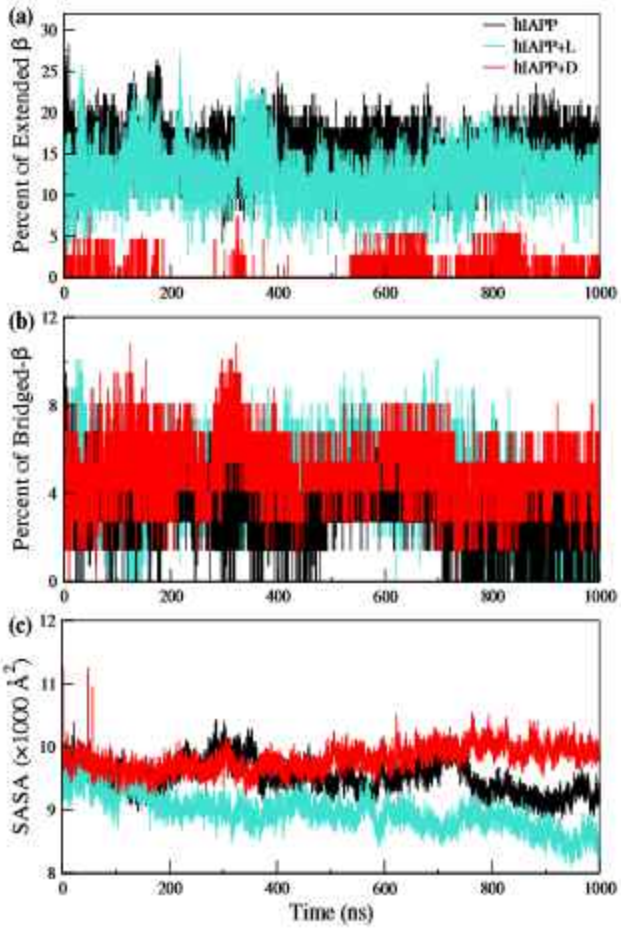

Figure 4.10: *Time evolution of (a) extended β, (b) bridged β and (c) SASA of full-length hIAPP in different systems.*

The disappearance of β-sheet in the peptides on addition of D-nl peptides is also observed in the snapshots of the initial and final configuration of the peptides (Fig 4.9). On analyzing the evolution of β structure percentage of hIAPP with time, we observe that the percentage of bridged β hardly changes (Fig 4.10b), in presence of either L- or D-nl throughout the simulation time, but the extended β-sheet conformation is much lower in presence of D-nl peptides (Fig 4.10a). The presence of bridged β in hIAPP+D system suggests that hIAPP initially starts forming β structures. However, further extension of bridged β into extended β-sheet rich aggregates is blocked by the D-nl peptides (Fig 4.11). The findings of our simulations corroborate with that of the experimental results, where

it was observed that, in bulk solution, D-nl peptides target short β-sheeted intermediates to prevent further growth of hIAPP oligomers[15]. Moreover, the random structures of hIAPP in pure water increases after D-nl peptides are added to the system. Hence, while L-nl peptides do not have any noticeable effect on the secondary structures of hIAPP, the D-nl peptides can prevent hIAPP from forming β-sheet rich prefibrillar aggregates, thus inhibiting fibrillation.

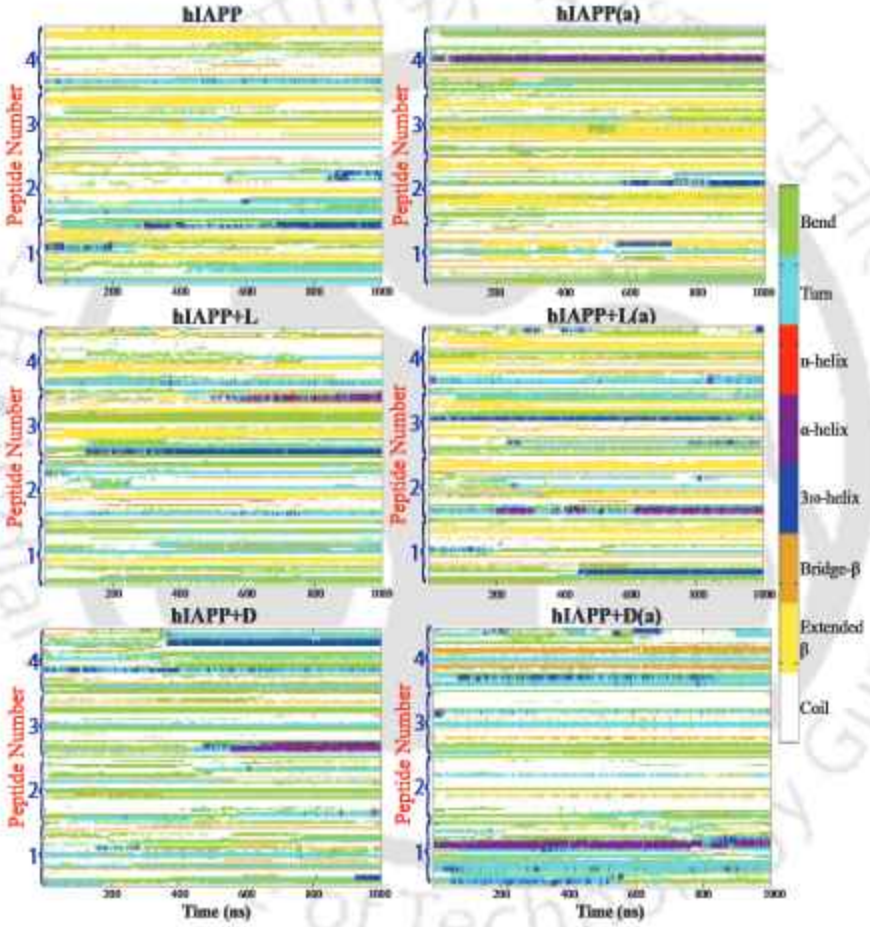

Figure 4.11: *Time evolution of change of secondary structures of each residue of full-length hIAPP in different systems.*

4.1.3.3 D-nl peptide Interrupts the Interactions between hIAPP

The conformational heterogeneity in the ensemble of peptide structure is explored by analyzing the peptide-peptide and peptide-solvent interactions. SASA helps to determine the peptide area exposed to the solvent and thus regulate the peptide conformation (Fig

4.10c). An increase in the SASA values is observed for the system containing D-nl peptides, indicating that the disordered, loosely packed conformers of hIAPP have higher interaction with water, favouring disaggregation.

The tendency of hIAPP to aggregate in pure water is further analyzed by calculating the preferential interaction parameters.

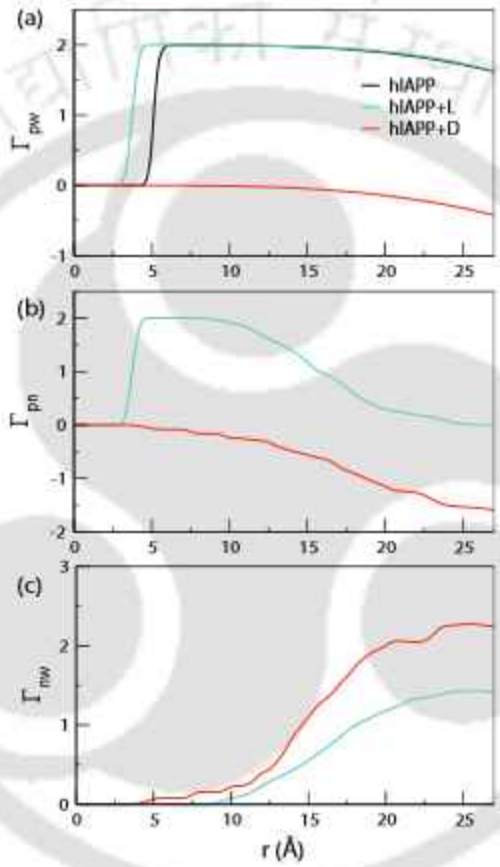

Figure 4.12: *Preferential interaction parameters of full-length hIAPP for (a) hIAPP-hIAPP over hIAPP-water, (b) hIAPP-hIAPP over hIAPP-nl and (c) hIAPP-nl over hIAPP-water interactions.*

Fig 4.12a represents the preferential interaction parameter Γ_{pw}, which calculates the preference of the peptides to interact with each other over the solvent. The positive value of Γ_{pw} (equation 1.18) indicates that hIAPP tends to self aggregate rather than be in a random coil conformation and interact more with the solvent in hIAPP and hIAPP+L systems. However, in presence of D-nl peptides, the propensity of hIAPP to aggregate decreases.

The interconversion between the different states of hIAPP is visualized by con-

structing the free energy landscapes that highlight protein ensembles as a function of radius of gyration (R_g) and the number of hydrogen bonds formed between hIAPP (Fig 4.13).

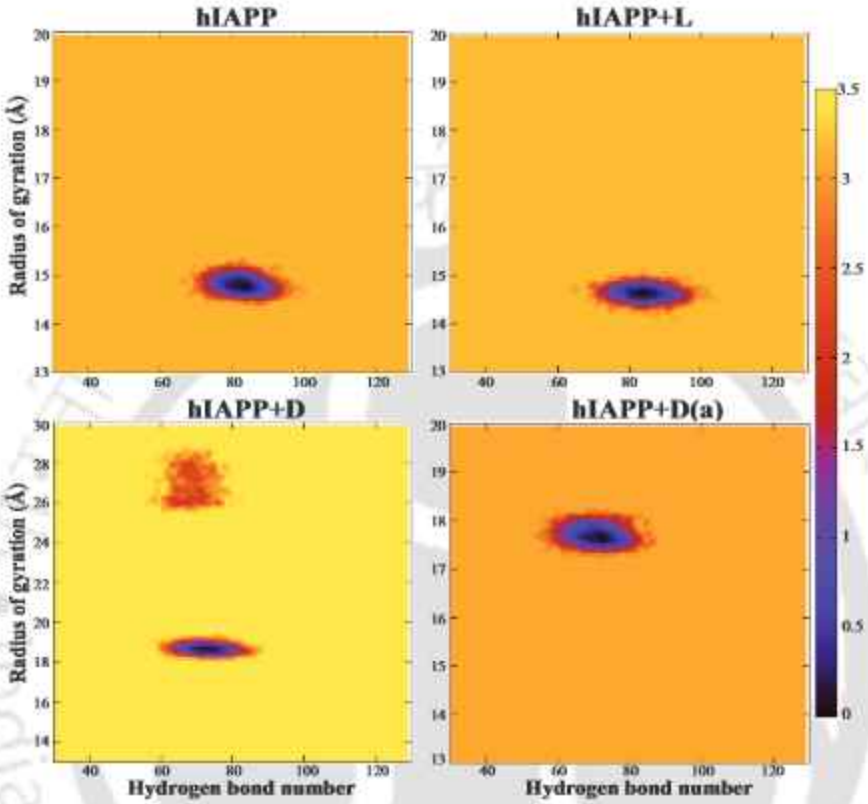

Figure 4.13: *Free energy plot (kcal/mol) as a function of R_g of full-length hIAPP and the average number of hydrogen bonds formed between them.*

The free energy basin of hIAPP without any nl peptides is positioned at R_g below 15 Å with average number of hydrogen bonds ranging between 80 to 90. Similar free energy basin is also observed for the system with L-nl peptides. However, in presence of D-nl peptides, there is an increase in R_g accompanied by a decrease in the number of hydrogen bonds formed. The aggregation of hIAPP gives rise to compact structures and consequently lower R_g values, while, in presence of D-nl peptides, the disordered hIAPP conformers result in higher R_g. Since, hydrogen bonds formed between hIAPP contribute to the structural integrity of the aggregates, an interruption in the inter-peptide hydrogen bonds promotes hIAPP to form disordered structures, hampering aggregation.

The interaction energy between hIAPP also provides information about the extent

of contacts between the peptides (Table 4.4). Here again, the contribution of the electrostatic interactions to the total interaction potentials is higher than the vdW counterpart. The electrostatic energy hardly changes while the vdW interaction becomes unfavourable in presence of D-nl peptides. Hence the total interaction potential becomes unfavourable, suggesting decrease in the interaction between hIAPP, thus intercepting hIAPP aggregation.

4.1.3.4 Potentials of Mean Force

The effect of D-nl peptides on the adhesion between two hIAPP monomers was further explicitly investigated by the potentials of mean force extracted from umbrella sampling simulations. Fig 4.14 indicates that the PMF of interaction between two hIAPP monomers is most favourable when the distance between them is 7.5 Å, in absence of D-nl peptides.

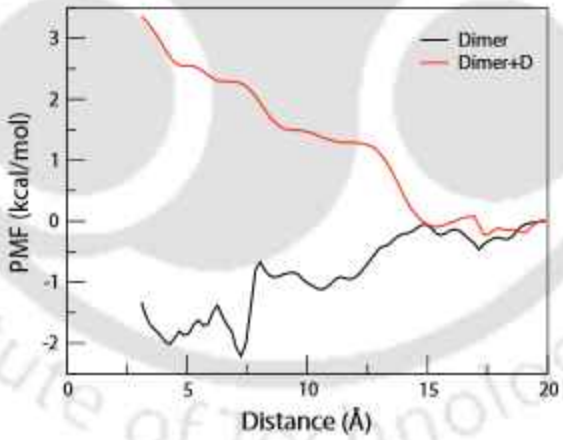

Figure 4.14: *Potential of mean force of two full-length hIAPP for different systems.*

However, the well depth decreases and the hIAPP dimer formation is completely destabilized, in presence of D-nl peptides. This indicates that, the dimer formation is most stable when the two hIAPP monomers are separated by a distance of 7.5 Å, but it becomes unfavourable with D-nl peptides surrounding them. Hence, hIAPP dimerization, which is the first step towards aggregation, is prevented.

4.1.3.5 Effect of D-nl on the Residues of Full Length hIAPP

To investigate the contribution of each residue towards the aggregation of full-length hIAPP, we first calculate the residue-residue contact map, considering both the backbone and the side-chain atoms of the hIAPP residues (Figures 4.15 and 4.16). The hIAPP peptides in pure water exhibit ample interpeptide contact between them, verifying their propensity to aggregate. The presence of inter-peptide contact among residues Ala5-Gln10, Arg11-Val17, Asn14-Gly24, Leu27-Asn35 and Ser34-Tyr37 are distinct in the backbone contact map. Some intra-peptide contacts between residues Ala8-Gln10 and Gly33-Tyr37 are also observed. Similar contacts are also visible among the side chain atoms of hIAPP with additional contact between residues Asn22-Ser28 and Ser20-Ser29. In presence of L-nl peptides, contact analogous to hIAPP in pure water is observed. However, both the inter- and intra-peptide contacts disappear for the system with D-nl peptides. Thus D-nl peptides weaken the contact between hIAPP residues, shifting the conformation of hIAPP from β-sheet rich to random coil.

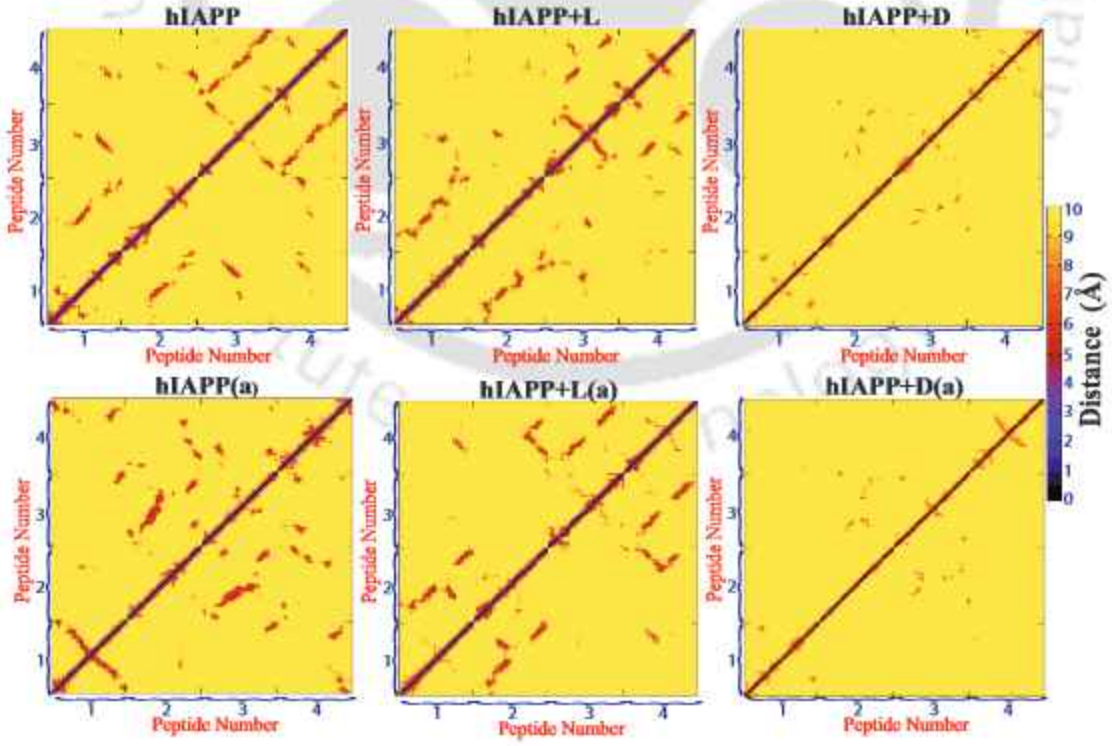

Figure 4.15: *Residue-residue contact map of the backbone atoms of full-length hIAPP in different systems.*

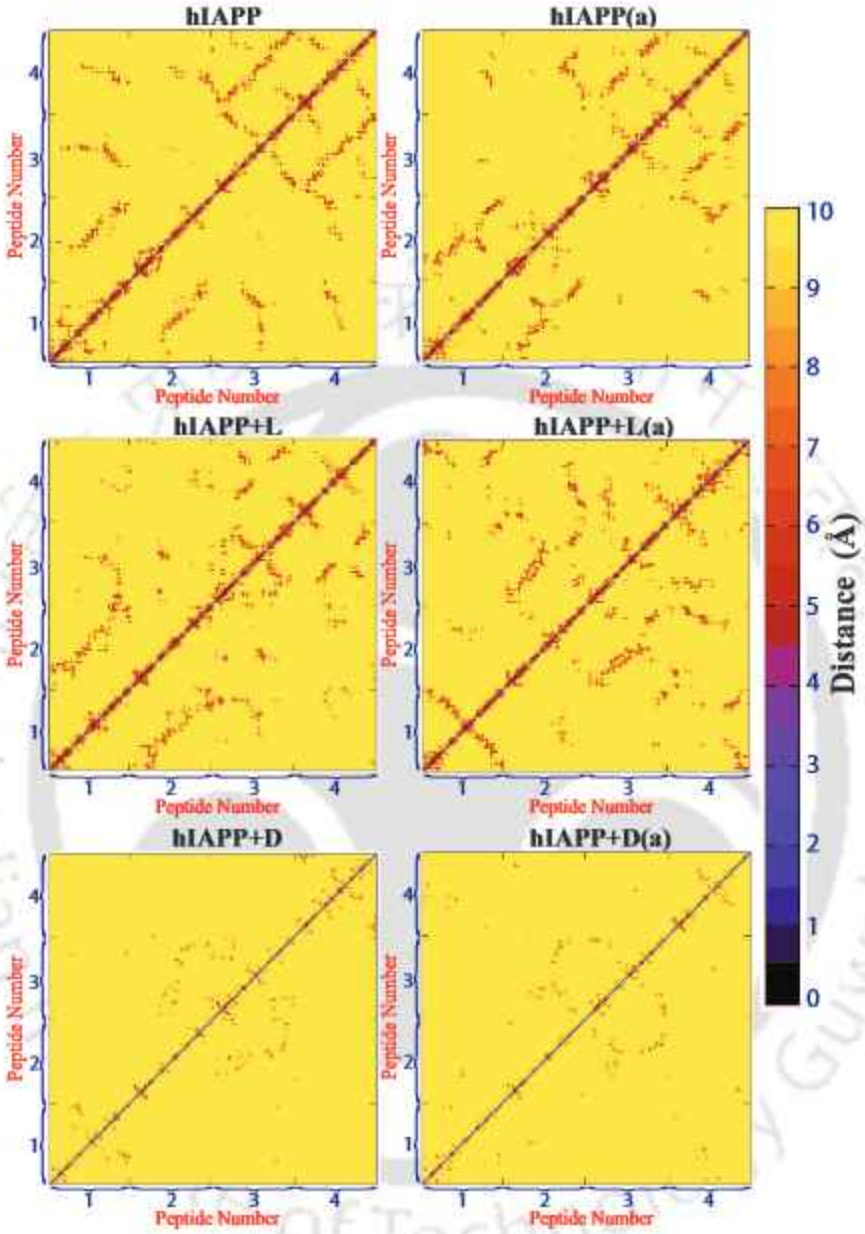

Figure 4.16: *Residue-residue contact map of the side-chain atoms of full-length hIAPP in different systems.*

This is further confirmed by calculating the residue-wise probability of β-sheet (Fig 4.17a) and random coil structure (Fig 4.17b) formation of hIAPP for all the systems. The β-sheet percentage for hIAPP in pure water is the highest for the residues Ala8-Gln10, Ala13-Val17, Asn22-Ser28, Thr30 and Asn31. The presence of L-nl peptides gives rise to high β-sheet for Thr9, Gln10, Asn14-Ser19 and Asn22-Asn35 residues. The contact

map and the residue-wise β-sheet percentage analyses validate the residues involved in the formation of the three-stranded β-sheet structure in hIAPP and hIAPP+L systems, which is observed in the most populated structure (Fig 4.8). Significant decrease in the β-sheet is observed for most of the residues with the incorporation of D-nl peptides, indicating the suppression of β-sheet rich structures. On the other hand, the coil percentage increases for most of the hIAPP residues. Overall, D-nl peptides significantly prevent β-sheet formation and induce coil conformation in hIAPP.

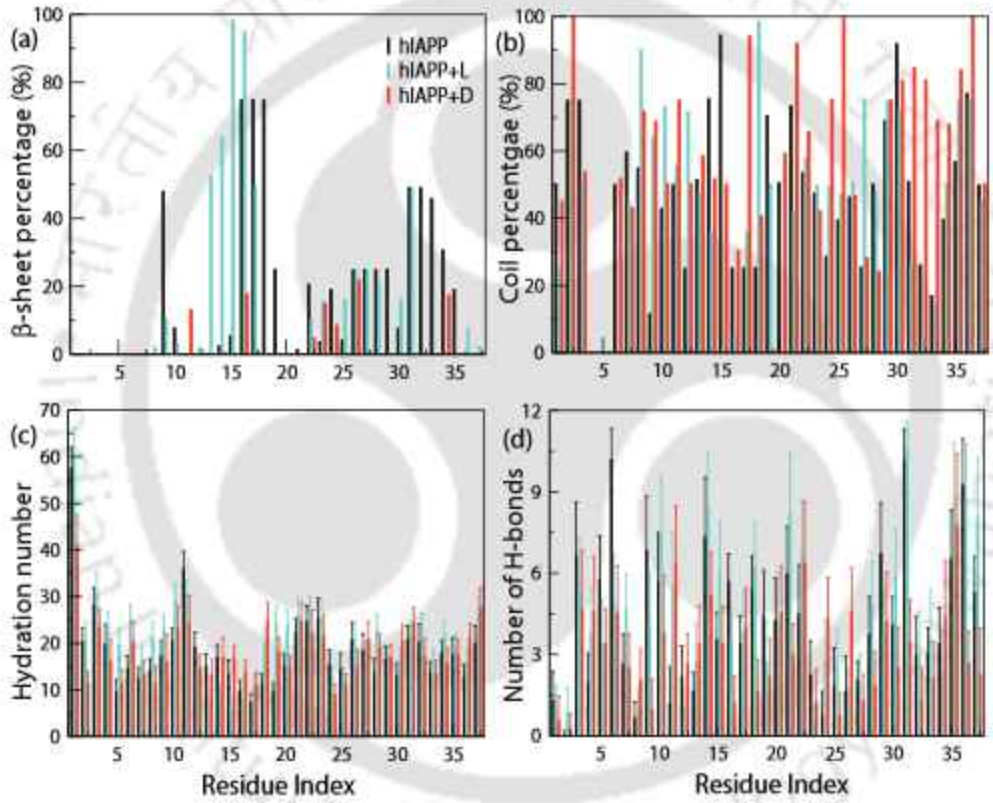

Figure 4.17: *Residue wise (a) β-sheet percentage, (b) coil percentage, (c) hydration number and (d) hIAPP-hIAPP hydrogen bond number of full-length hIAPP in different systems.*

Since the interactions between the peptide and solvent molecules play an important role in the peptide structure, we have calculated the hydration number, which defines the number of water molecules directly in contact with the hIAPP residues (Fig 4.17c). An increase in the hydration number around hIAPP indicates that hIAPP is more loosely packed due to which the hIAPP residues are interacting with higher number of solvent

molecules. For the system containing L-nl peptides, the hydration number around hIAPP either decreases or is unchanged compared to that of the pure water system, (except for some residues in the N-terminal region of hIAPP, where a slight increase is observed). However, the hydration number of hIAPP+D system is higher for most of the residues in contrast to the pure water system. Since any drastic change in the hydration number is not observed, we can infer that the number of solvent molecules do not vary much around hIAPP, possibly because hIAPP interacts more with either nl peptides or itself rather than with the solvent.

The hydrogen bonds formed among the hIAPP residues allows us to identify how they enhance the stabilization of the amyloid structure (Fig 4.17d). The polar residues, Asn3, Thr6, Thr9, Gln10, Asn14, His18, Asn21, Ser29, Asn31, Asn35, Thr36 and Tyr37 have the highest hydrogen bond number for the hIAPP system. Hydrogen bonds formed between three regions, Asn3-Gln10, Asn14-Asn22 and Ser28-Tyr37 enhance the aggregation between the amyloidogenic regions. In presence of L-nl peptides, hydrogen bonds between the hIAPP residues mostly increase. On the other hand, the hydrogen bond number decreases in all the above regions in presence of D-nl peptides. Hence we can conclude that D-nl peptides block the hydrogen bond interactions between hIAPP peptides and thus prevent aggregation.

4.1.3.6 D-nl peptides Interact with hIAPP

To understand the molecular mechanism of D-nl peptides inhibiting the aggregation of hIAPP, we first estimate the spatial distribution function of L- and D-nl peptides around hIAPP, which provides a three dimensional probability of the distribution of the nl peptides around 5 Å of hIAPP. From Fig 4.18, we observe that the β-sheet rich aggregates of hIAPP lie in the midst surrounded by a dense population of L-nl peptides in the outer surface. However, D-nl peptides are interspersed randomly in-between hIAPP, such that there is much less interaction between hIAPP itself. This observation is further supported by the calculation of the preferential interaction parameter, Γ_{pn} (Fig 4.12b). A large positive value of Γ_{pn} (equation 4.1) for the hIAPP+L system signifies that hIAPP would rather interact with itself than with L-nl peptides. However, the preference of hIAPP to interact with D-nl peptides over itself is indicated in the negative value of Γ_{pn}. Similarly, Γ_{nw} calculates the

preference of hIAPP to interact with either L- or D-nl peptides over the solvent molecules (equation 4.2). Here also the positive value of Γ_{nw} suggests that both L-nl and D-nl peptides directly interacts with hIAPP (Fig 4.12c). The similar Γ_{nw} values in both hIAPP+L and hIAPP+D systems further explain the subtle difference in the hydration number values of these systems (Fig 4.17c).

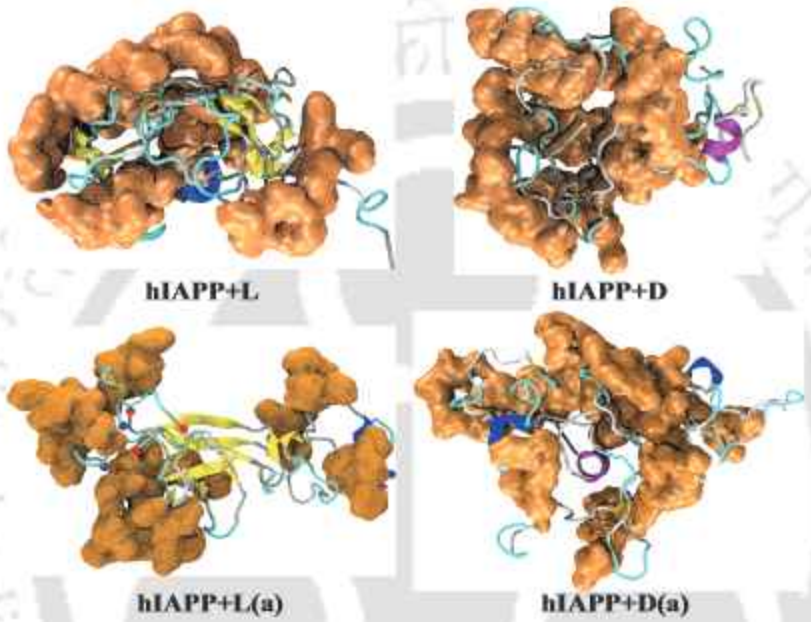

Figure 4.18: *Spatial distribution functions of nl around full-length hIAPP in different systems. The peptides are represented in cartoon form, depicting β-sheet in yellow, coil in silver, turn in cyan, α-helix in purple and 3_{10}-helix in blue. The brown surface around hIAPP represents the distribution of nl peptides around it.*

To identify the amino acid residues responsible for the association between hIAPP and D-nl peptides, the frequency of contact of D-nl with each residue of hIAPP is calculated by the first solvation shell coordination number. For comparison, the first solvation shell coordination number between the residues of hIAPP and L-nl peptides is also provided. From Fig 4.19a and b, we have observed that, while L-nl interacts mostly with the central and the C-terminal residues of hIAPP, the coordination number of D-nl peptides is homogeneously distributed throughout the hIAPP sequence. On closely monitoring how each of the residues of L- or D-nl peptides are interacting with hIAPP residues, we find that the residues of D-nl are more in contact with hIAPP than that of L-nl peptides (Fig

4.20). The hydrophobic core of L-nl, consisting of L-Phe, L-Gly and L-Ala residues have higher contact number with hIAPP than the remaining L-nl residues. On the other hand, D-Asn and D-Phe residues at the N-terminal of D-nl have higher coordination number values. Further, the heatmap representing the radial distribution function (RDF) between the centre of mass of heavy atoms of each residue of D-nl peptide is plotted as a function of hIAPP residues (Fig 4.21).

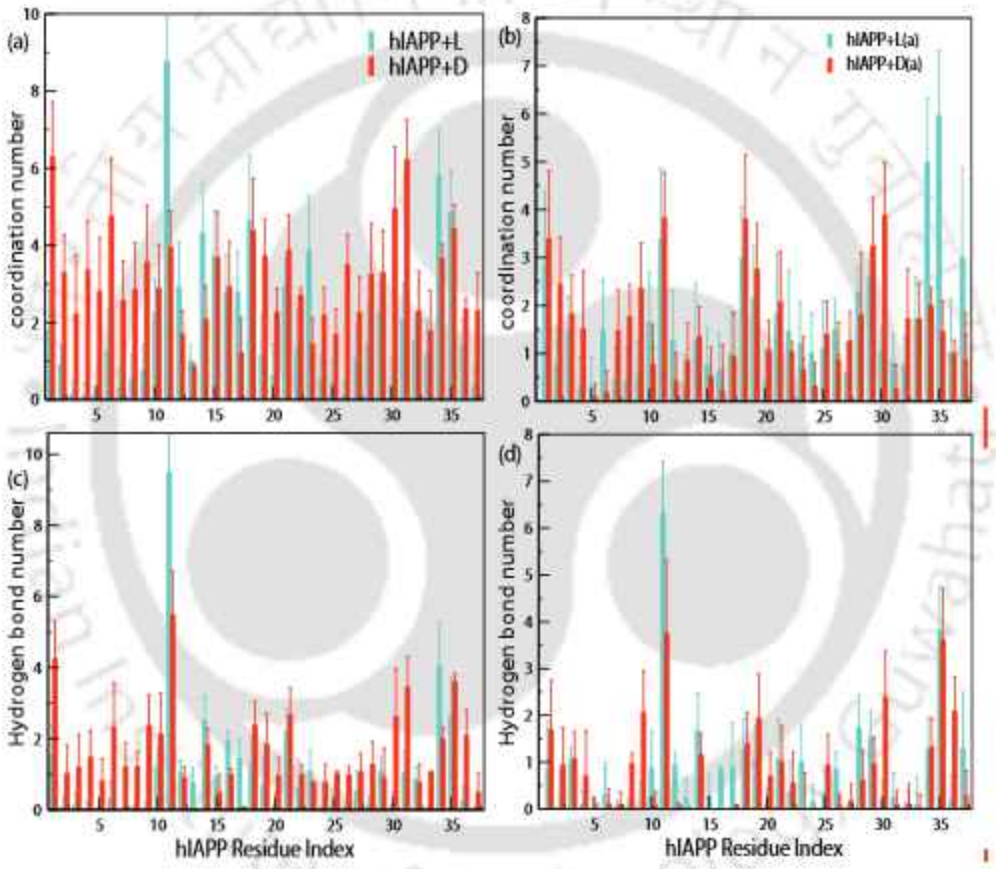

Figure 4.19: *Residue wise (a,b) coordination number and (c,d) hydrogen bond number of nl peptides with full-length hIAPP in different systems.*

The RDF of the first maxima is highest for the interaction between the C-terminal residues of hIAPP and D-Asn, D-Phe, D-Gly and D-Ala. However, D-Ile and D-Leu have higher RDF for the interactions with the N-terminal residues.

The detailed binding sites of D-nl peptides with hIAPP is identified by calculating the residue based binding free energy of the inhibitor peptide with hIAPP. Table 4.5

represents the favourable values of total binding free energy of D-nl with hIAPP. Negative values of both electrostatic and vdW interactions infer that they significantly contribute to the binding of hIAPP with D-nl. Here also, the electrostatic contribution dominates over its vdW counterpart.

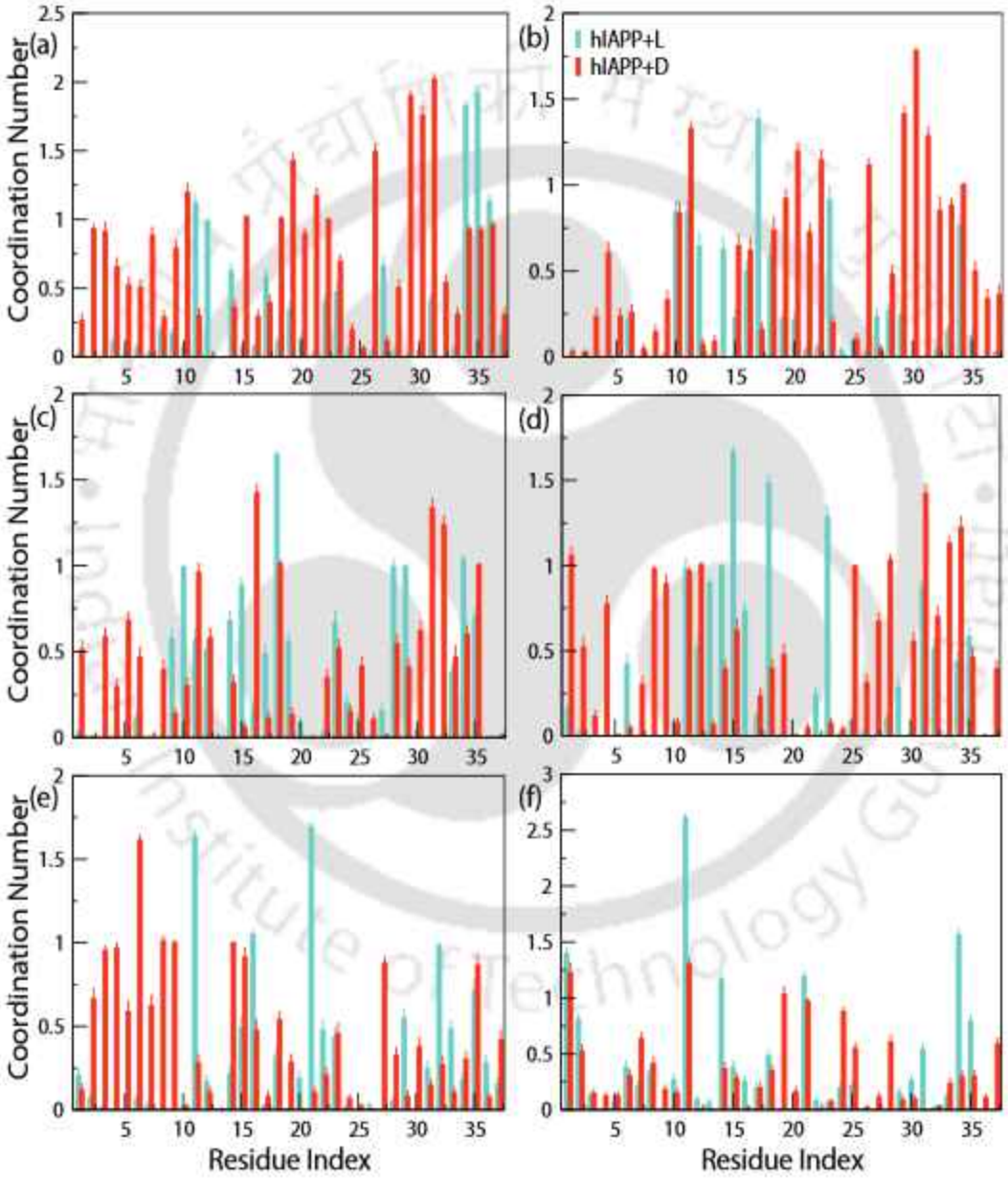

Figure 4.20: *First shell coordination number of (a) Asn, (b) Phe, (c) Gly, (d) Ala, (e) Ile and (f) Leu residues of nl around each residue of full-length hIAPP in different systems.*

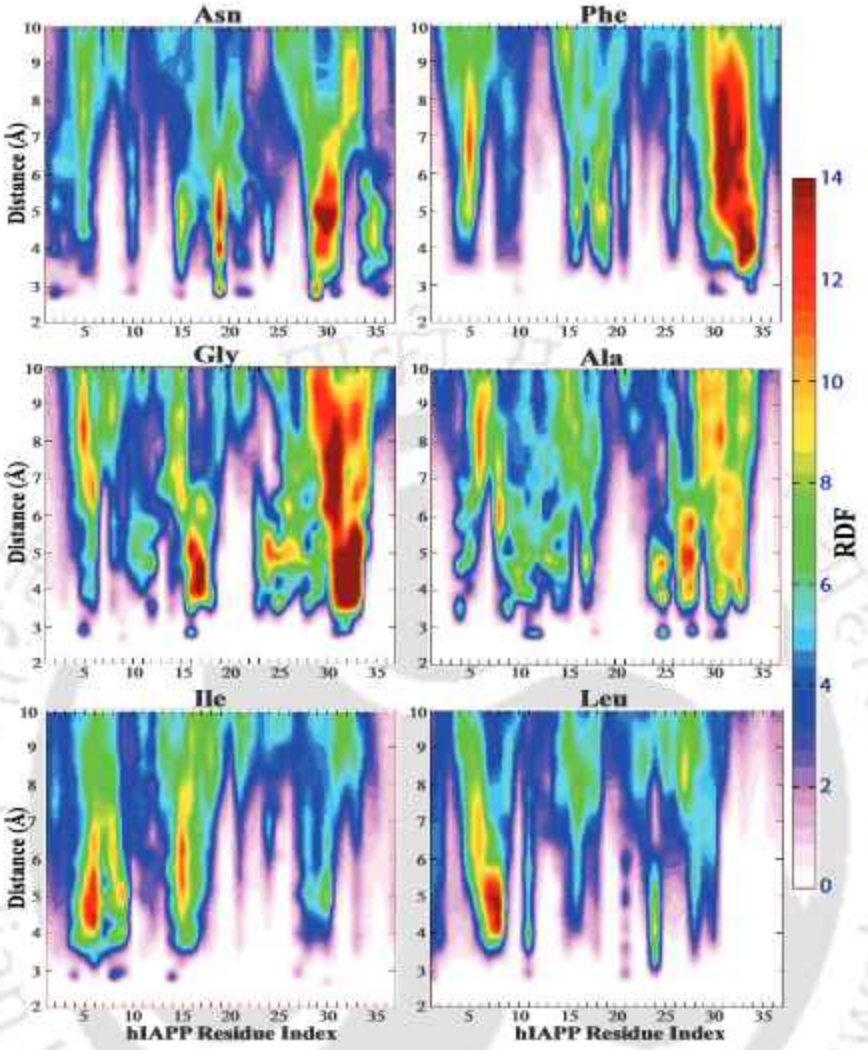

Figure 4.21: *A two dimensional heat map displaying the radial distribution functions (RDF) between centre of mass of the residues of D-nl with that of full-length hIAPP in hIAPP+D system.*

System	hIAPP+D
ΔE_{vdw}	-312.89 ± 0.31
ΔE_{ele}	-926.82 ± 2.64
ΔG_{GB}	1087.88 ± 2.63
ΔG_{NP}	-44.62 ± 0.04
ΔG_{bind}	-196.45 ± 0.31

Table 4.5: *Decomposition of binding energy (kcal/mol) of D-nl with full-length hIAPP for the hIAPP+D system.*

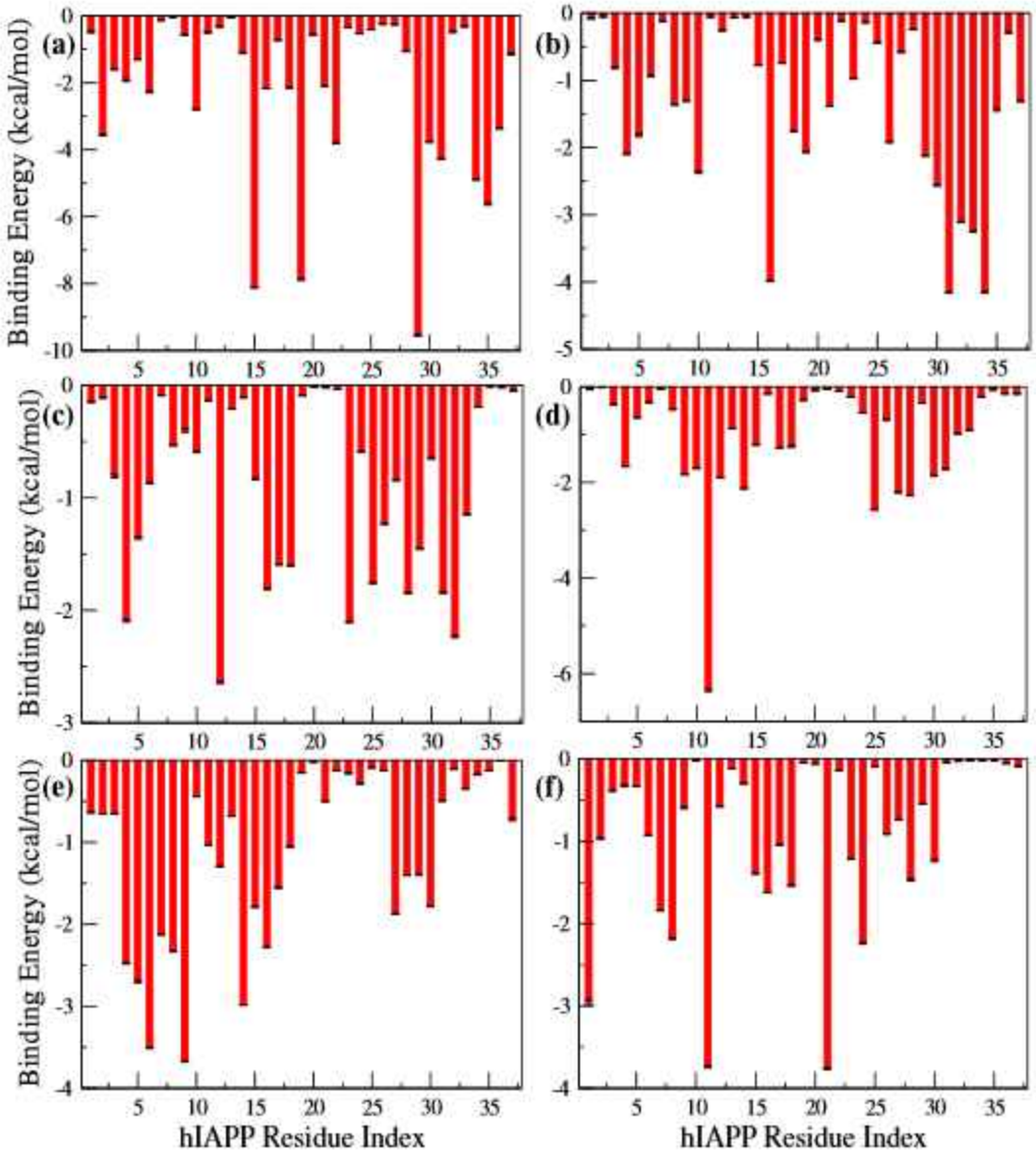

Figure 4.22: *Binding free energy between (a) Asn, (b) Phe, (c) Gly, (d) Ala, (e) Ile and (f) Leu residues of D-nl peptides with each residue of full-length hIAPP in hIAPP+D system.*

Probing into the residue wise contribution to the binding energy values (Fig 4.22), we observe that the results match with that of the previous analyses (D-Asn, D-Phe and D-Gly have higher binding affinity with the C-terminal residues of hIAPP, while D-Ala, D-Ile and D-Leu has more interaction with the N-terminal residues).

The magnitude of the interaction between the L or D-nl peptides and hIAPP is first analyzed by calculating the interaction energy values (Table 4.4). Both the L and

D-nl peptides have substantial interaction energy values with hIAPP, with more favourable interaction energy values for the hIAPP+D system. Since hydrogen bonds between hIAPP and inhibitors play an important role in the inhibition mechanism, we estimate the average hydrogen bond numbers between each residue of hIAPP with L- and D-nl peptides (Figures 4.19c, d and 4.23).

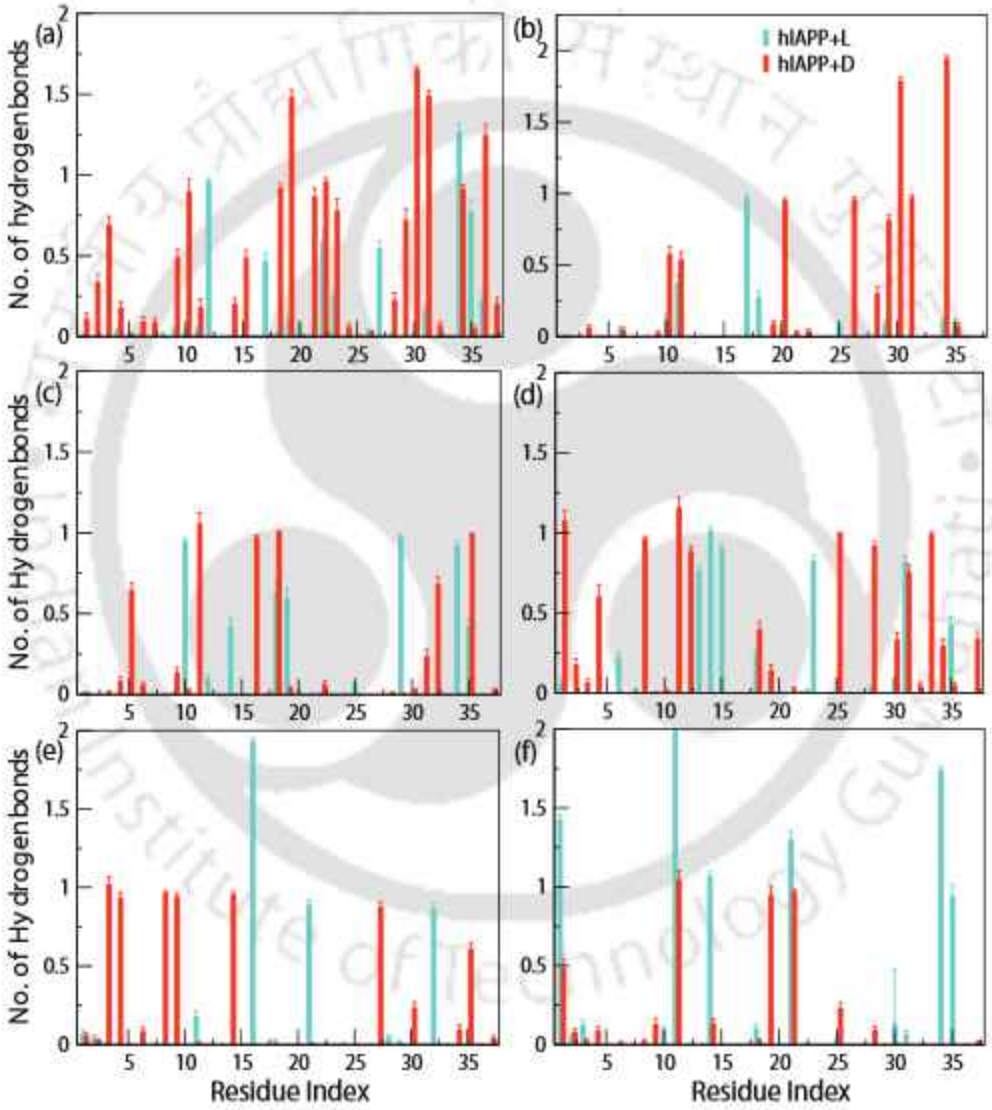

Figure 4.23: *Average hydrogen bond number between (a) Asn, (b) Phe, (c) Gly, (d) Ala, (e) Ile and (f) Leu residues of nl with each residue of full-length hIAPP in different systems.*

The trend of the hydrogen bond number between hIAPP and nl peptides is similar to the trend of first shell coordination number. The polar residue in D-nl peptide, D-Asn, has the

highest number of hydrogen bonds with hIAPP, mostly forming with the polar residues of hIAPP. Fewer hydrogen bonds are formed with the other residues of D-nl peptides due to the absence of polar groups in the side chain of these residues. Among them, D-Gly and D-Ala, utilizing their backbone atoms, form hydrogen bonds with hIAPP, owing to the small size of their side chain atoms. The number of hydrogen bonds between hIAPP and L-nl peptide are much less. Moreover, the hIAPP residues having the highest hydrogen bond number in hIAPP+L system differ from those in the hIAPP+D system, which suggests that the change in the stereochemistry of the nl peptide residues modifies the interaction pattern of nl peptides with hIAPP.

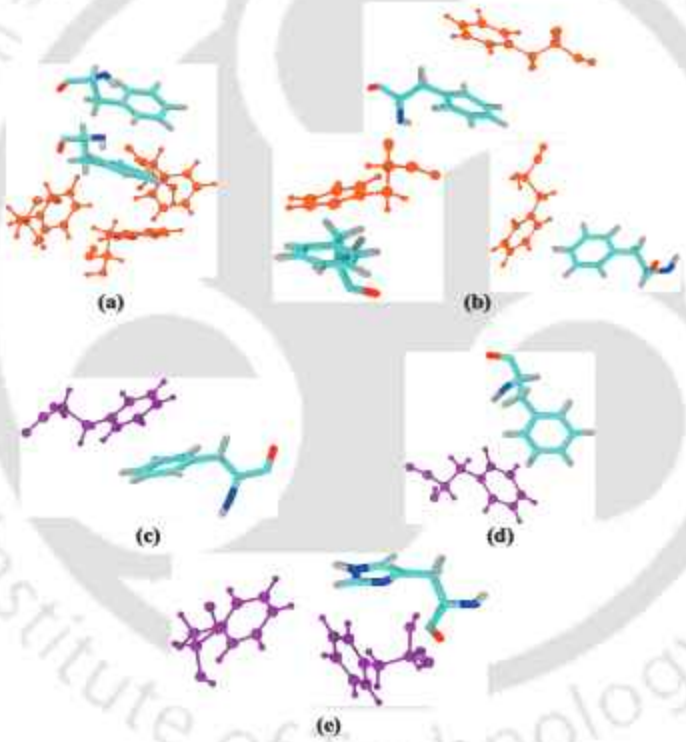

Figure 4.24: *Representative snapshots showing π-π stacking between (a) Phe15 (cyan) and (b) Phe23 (cyan) of hIAPP with L-Phe (orange) and (c) Phe15, (d) Phe23 and (e) His18 (cyan) of hIAPP with D-Phe (purple).*

Another interaction which is important in amyloid formation and also in the peptide-drug design is π-π stacking between the aromatic rings of the aromatic amino acids[27]. Hence, we investigate the presence of possible π-stacking interactions between the aromatic ring of either L-Phe or D-Phe with those of the aromatic residues of hIAPP

(Fig 1.6a). In hIAPP+L system, it is observed that Phe15 of hIAPP is involved in π-π stacking with four L-Phe residues (Fig 4.24a). Similarly, three stacking interactions are observed between Phe23 and L-Phe (Fig 4.24b). However, the probability of stacking between hIAPP and D-Phe is much less. There is only one each of π-π stacking between D-Phe and Phe15 (Fig 4.24c) and Phe23 (Fig 4.24d). Additionally His18 is involved in stacking with three D-Phe residues (Fig 4.24e). Moreover, the orientation of the stacking interaction also changes with the stereochemistry of the nl peptides (Fig 4.25).

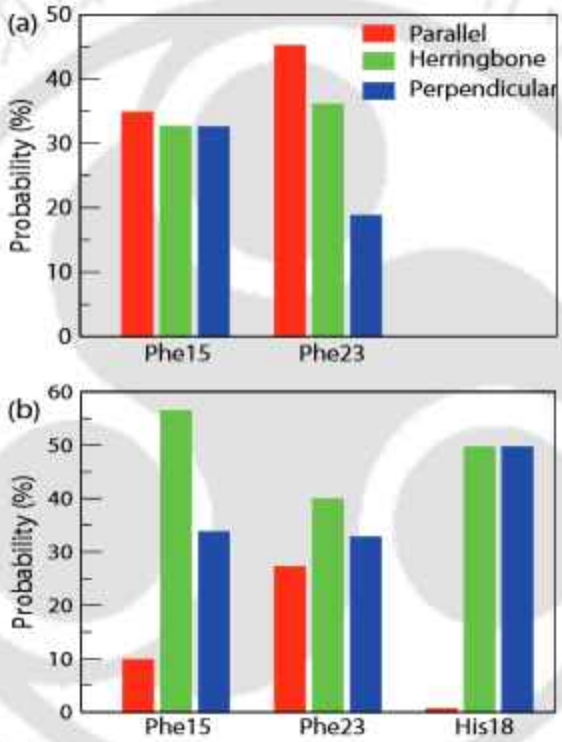

Figure 4.25: *Probability of stacking orientation between aromatic residues of hIAPP and Phe in (a) L-nl peptide and (b) D-nl peptide.*

In case of stacking interaction between Phe15 and Phe of either of the nl peptides, it is observed that the probability of all orientations is almost similar for Phe15–L-Phe stacking. However, D-Phe is mostly involved in herringbone stacking with Phe15, followed by a perpendicular arrangement. Phe23, on the other hand, is involved in parallel stacking with L-Phe and herringbone orientation with D-Phe. Hence, while parallel stacking is most favourable for the L-nl peptides, herringbone stacking orientation predominates in case of D-nl peptides.

The binding mode of the nl peptides with hIAPP can also be visualized by some snapshots, which corroborate with the results obtained from the above analyses. We had mentioned earlier that the L-peptides gather around the aggregated hIAPP structure and stabilizes it (Fig 4.26a). In Fig 4.26b, it is observed that the β-hairpin in the three stranded β-sheet structure of hIAPP in system hIAPP+L is stabilized by strong hydrophobic contacts with L-nl peptide.

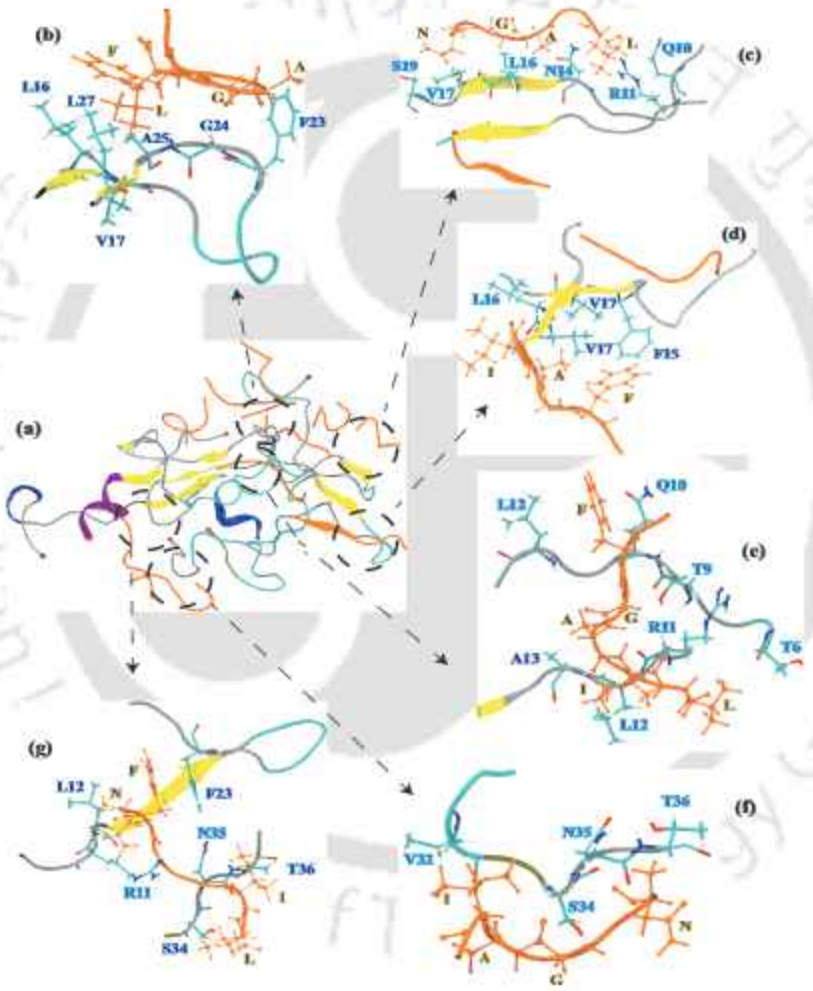

Figure 4.26: *Representative snapshots showing interactions between full-length hIAPP and L-nl peptides. hIAPP is represented in cartoon form, depicting β-sheet in yellow, coil in silver, turn in cyan, α-helix in purple and 3_{10}-helix in blue. The L-nl peptides are depicted in orange. The black dashed circles highlight the interactions of specific L-nl peptides with hIAPP.*

The contacts between Phe23 and Gly24 in the turn of β-hairpin with L-Ala and L-Gly

and also between Leu16, Val17, Ala25, Leu27 and L-Phe and L-Leu enhance the stability of the β-hairpin structure. Moreover, an extended β-sheet structure composed of a β-strand formed by L-nl peptide and two β-strands of hIAPP is observed (Fig 4.26c). The hydrophobic interaction between the side chains of L-Ile and Leu12 and that of L-Ala and two Val17 enhances the stability of this β-sheet structure. Further the aromatic rings of L-Phe and Phe15 are involved in stacking interaction.

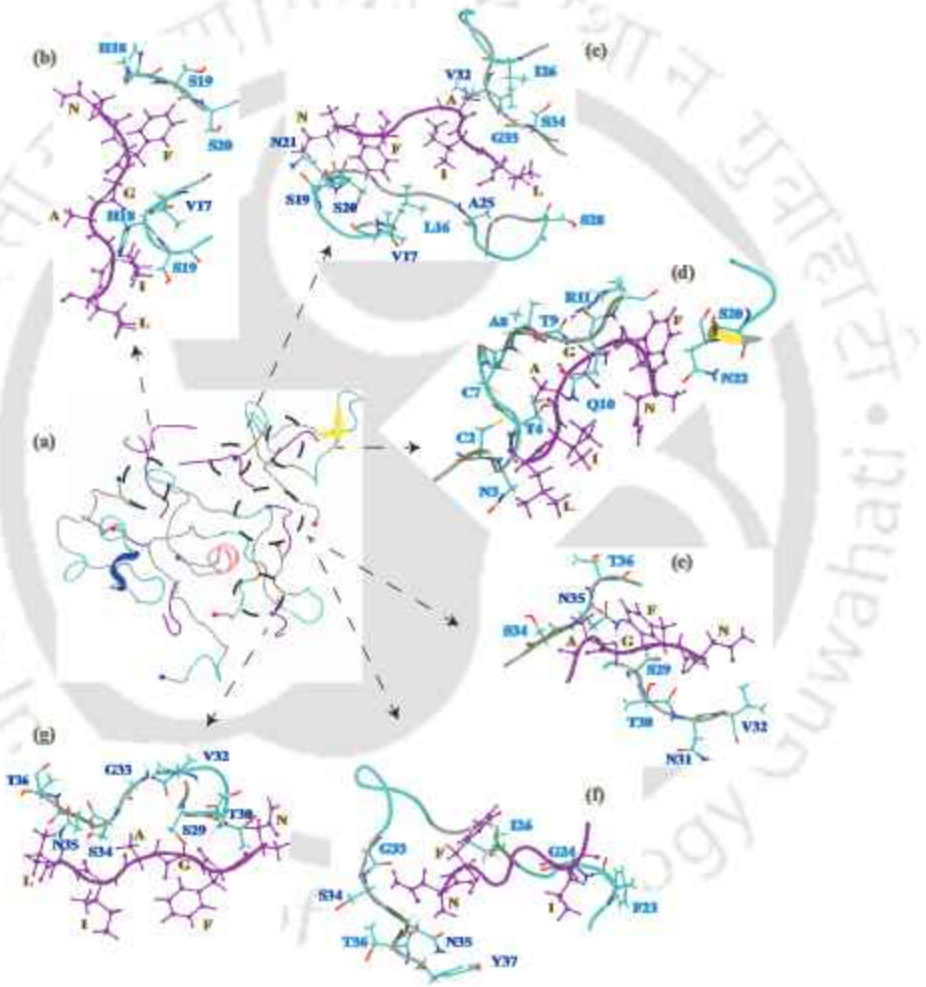

Figure 4.27: *Representative snapshots showing interactions between full-length hIAPP and D-nl peptides. hIAPP is represented in cartoon form, depicting β-sheet in yellow, coil in silver, turn in cyan, α-helix in purple and 3_{10}-helix in blue. The D-nl peptides are depicted in purple. The black dashed circles highlight the interactions of specific D-nl peptides with hIAPP.*

Another L-nl peptide on the other side of the hIAPP β-strands interacts with this β-sheet

structure via hydrophobic contacts as well as by forming hydrogen bonds (L-Asn–Ser19 and L-Leu–Gln10) (Fig 4.26d), adding extra stability to the β-sheet structure. Similar hydrogen bonds and hydrophobic interactions between hIAPP and L-nl peptides are shown in other snapshots (Fig 4.26e-g), which compliments the results obtained earlier. From all the snapshots, we mostly observe that the hIAPP peptides strongly interacts with each other and their aggregation is enhanced by L-nl peptides.

The circumstance is different in the hIAPP+D system. Most of the D-nl peptides are interacting with the C-terminal residues of hIAPP (Fig 4.27a). D-Asn is involved in hydrogen bonding with His18-Ser19 (Fig 4.27b), Ser19-Asn21 (Fig 4.27c), Asn22 (Fig 4.27d), Ser29-Val32 (Fig 4.27e), Gly33-Thr36 (Fig 4.27f) and Ser29-Thr30 (Fig 4.27g). Hydrophobic interaction between the phenyl ring of D-Phe and Ile26 (Fig 4.27f) and the long chain of Arg11 (Fig 4.27d) is also observed. The methyl group in the side chain of D-Ala interacts with Ile26, Val32-Gly33 (Fig 4.27c) and Cys7-Gln10 (Fig 4.27d). Finally D-Ile and D-Leu interacts with Val17-Ser19 (Fig 4.27b), Cys2-Thr4 (Fig 4.27d), Phe23-Gly24 (Fig 4.27f) and Val3-Thr36 (Figs 4.27c and g).

From all the above observations, we can conclude that the favourable interaction of L-nl peptides with Asn14-His18 region of hIAPP enhances the stability of the β-sheet formed by this region in hIAPP. L-nl peptides, not only favour the aggregation of hIAPP, but also stabilize the aggregated β-sheet rich structure. On the other hand, D-nl peptides interrupt the interactions between hIAPP by mostly interact with the C-terminal region of hIAPP.

4.1.3.7 D-nl peptides Destabilize hIAPP Protofibrils

We now focus our attention on how D-nl peptides destabilize pre-formed hIAPP protofibrils. In order to compare the results, we have also analyzed the effect of L-nl peptides on the hIAPP protofibrils. For this, we have carried out independent 1 μs simulations on hIAPP protofibrillar structure obtained by two different methods, NMR and cryo-EM. The snapshots of the protofibrils at the beginning and the end of the simulations are provided (Figures 4.28 and 4.29). The effect in the structural stability of hIAPP protofibrils is first analyzed by the change in the RMSD of Cα atoms of hIAPP, which is calculated using the

initial structures as the reference.

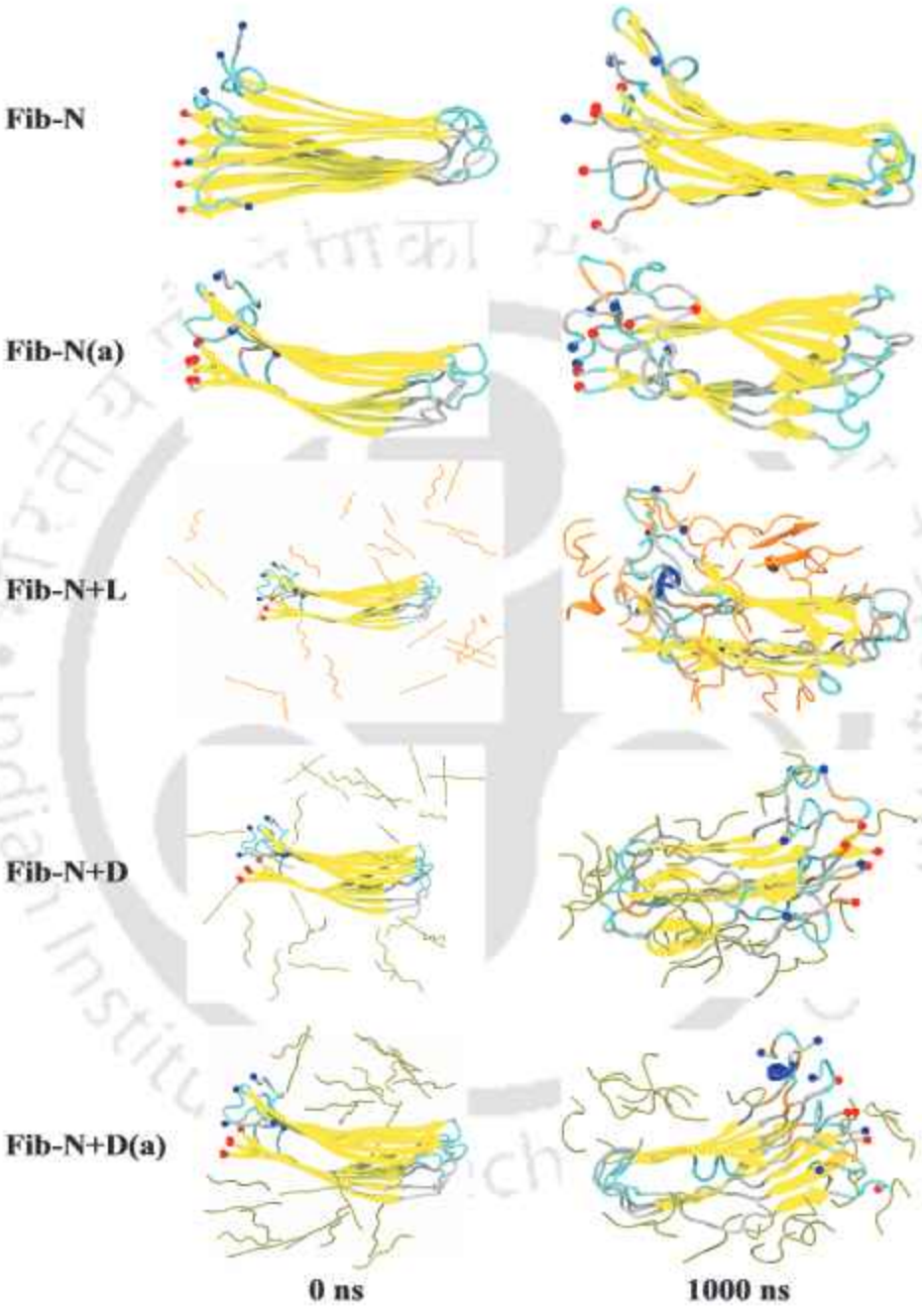

Figure 4.28: *Snapshots of the initial and the final configuration of NMR-derived hIAPP protofibrils in different systems. The protofibrils are represented in cartoon form, depicting β-sheet in yellow, coil in white, bend in cyan and 3_{10}-helix in blue. L-NFGAIL is depicted in orange and D-NFGAIL is depicted in green.*

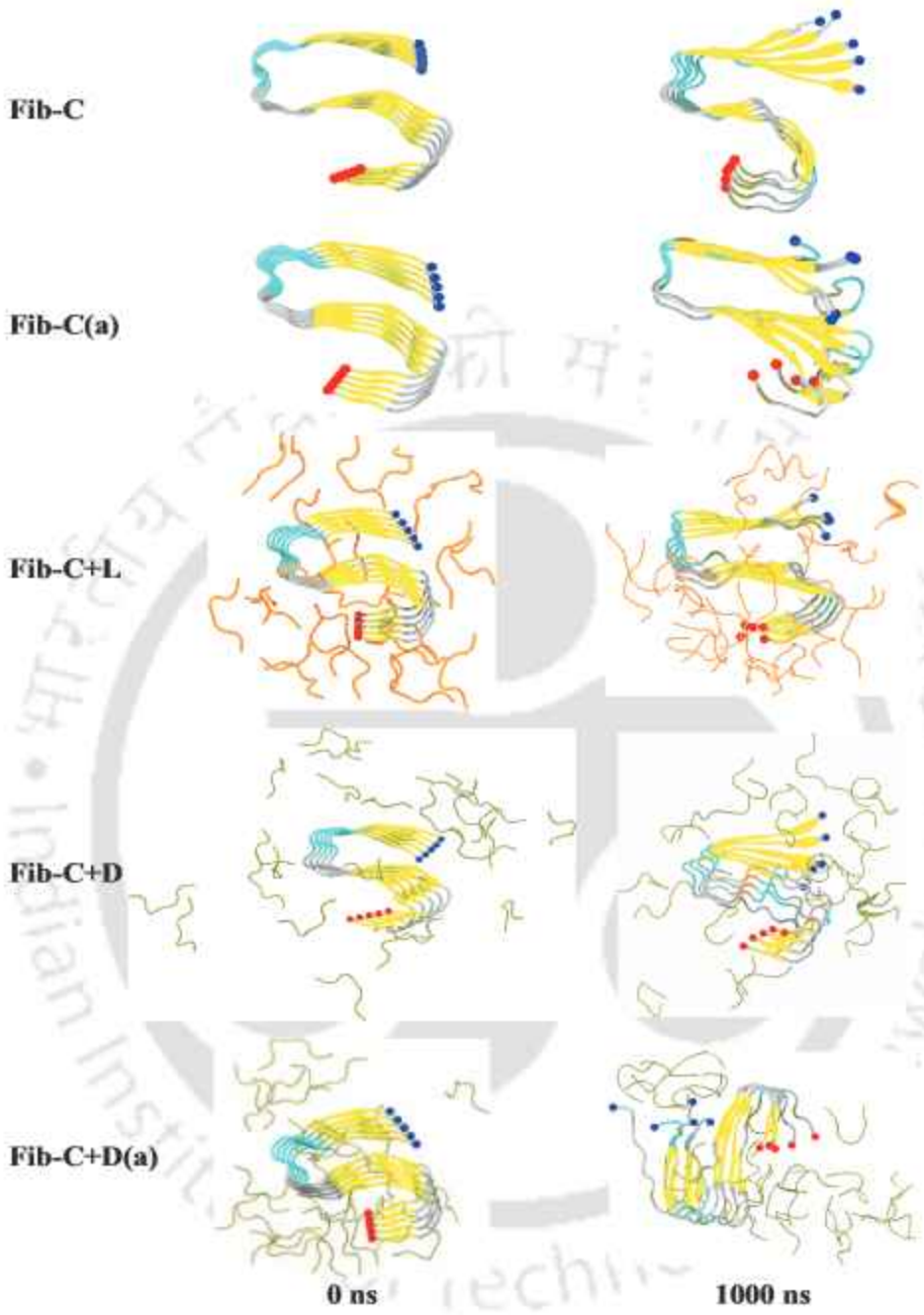

Figure 4.29: *Snapshots of the initial and the final configuration of cryo-EM-derived hIAPP protofibrils in different systems. The protofibrils are represented in cartoon form, depicting β-sheet in yellow, coil in white, bend in cyan and 3_{10}-helix in blue. L-NFGAIL is depicted in orange and D-NFGAIL is depicted in green.*

We observe a slight increase in the RMSD values for the Fib-N systems with the addition

of D-nl peptides (Figures 4.30a and 4.31a).

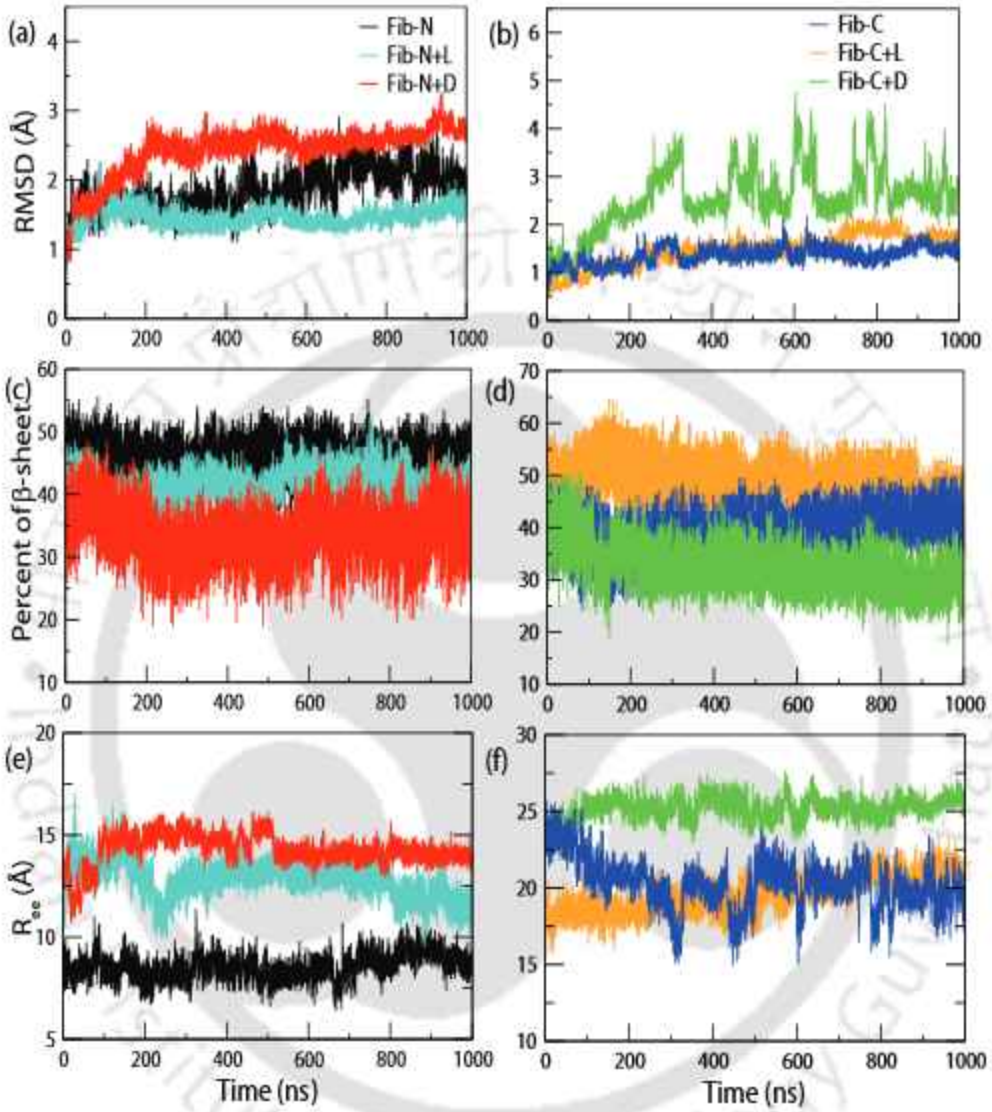

Figure 4.30: *Time evolution of (a,b) RMSD, (c,d) β-sheet and (e,f) R_{ee} of hIAPP protofibrils in different systems.*

However, the deviation is much more pronounced for the cryo-EM structure of hIAPP protofibril (Fig 4.30b and 4.31a). Similarly, in presence of D-nl peptides, the end-to-end distance, i.e., the distance between the terminal ends of each hIAPP chain, (R_{ee}) increases for the protofibrillar systems. This increase in R_{ee} suggests that the two terminals of the hIAPP protofibril move farther from each other, thus destabilizing the β-hairpin network. The S-shaped protofibrillar structure in the Fib-C systems (Fig 4.30f and 4.31c) results

in higher value of R_{ee} compared to the hairpin structure in the Fib-N systems (Fig 4.30e and 4.31c). L-nl peptides, on the contrary, hardly have any destabilization effect on the protofibrils.

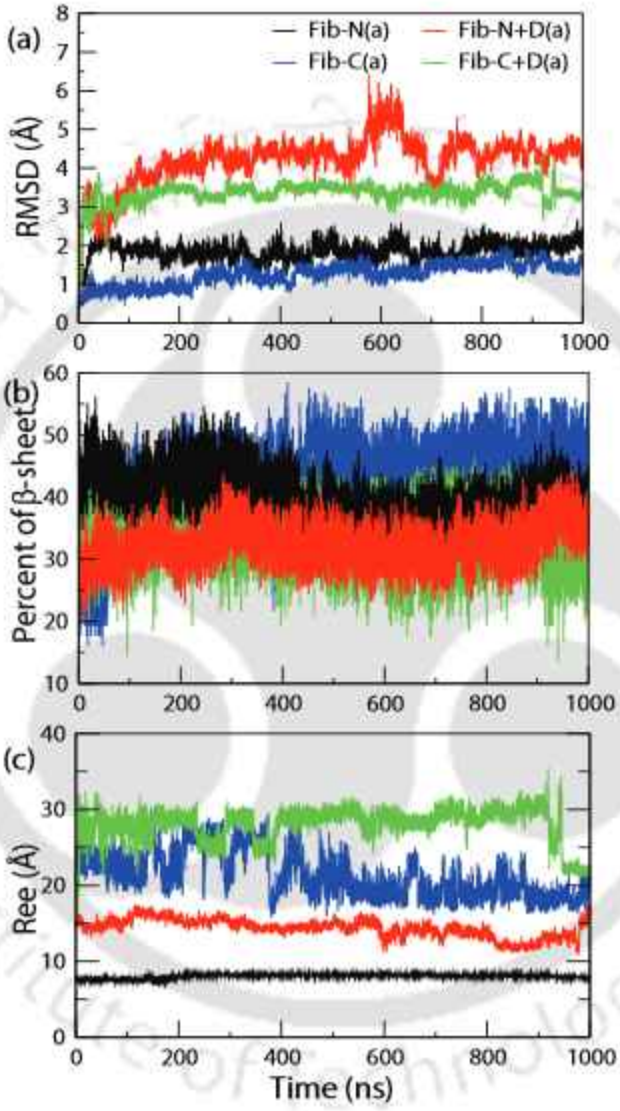

Figure 4.31: *Time evolution of (a) RMSD, (b) β-sheet and (c) R_{ee} of hIAPP fibrils in different systems.*

Increase in RMSD and R_{ee} values for the systems containing D-nl peptides point out the deviation of the ordered fibrillar structure and the destabilization of the β-sheet arrangement. On investigating the change in the β-sheet structure of the protofibrils, we observed a decrease in the β-sheet conformation along the simulation time for the protofibrils in

presence of D-nl peptides, compared to that of L-nl peptides or the pure water systems (Figures 4.30c,d and 4.31b).

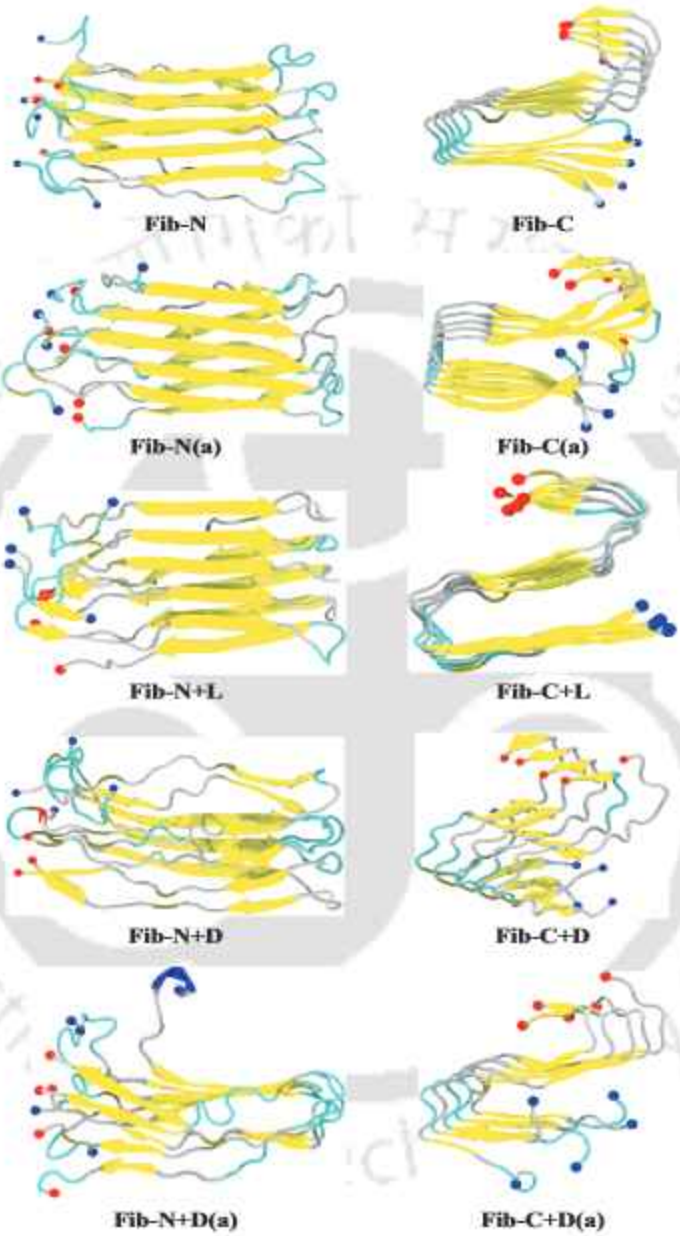

Figure 4.32: *Representative conformations of the most populated structure of hIAPP protofibrils in different systems. The peptides are represented in cartoon form, depicting β-sheet in yellow, coil in silver, turn in cyan, α-helix in purple and 3_{10}-helix in blue. The blue and red balls represent the N and C-terminal ends respectively.*

From the average secondary structure contents (Table 4.2), we also find that not only the β-sheet percentage decreases but also the random coil percentage increases in presence of

D-nl peptides. Since both the hIAPP protofibrils consists of β-sheet rich conformation, a reduction in the β-sheet percentage hints at the instability of the packed fibrils.

The most populated structure, obtained from the cluster analysis, adequately exhibits the change in the hIAPP protofibril conformation in presence of D-nl (Fig 4.32). The coordination number of D-nl peptides around hIAPP protofibrils represent an even distribution of D-nl peptides at the terminal and the turn regions of the protofibrils (Fig 4.33).

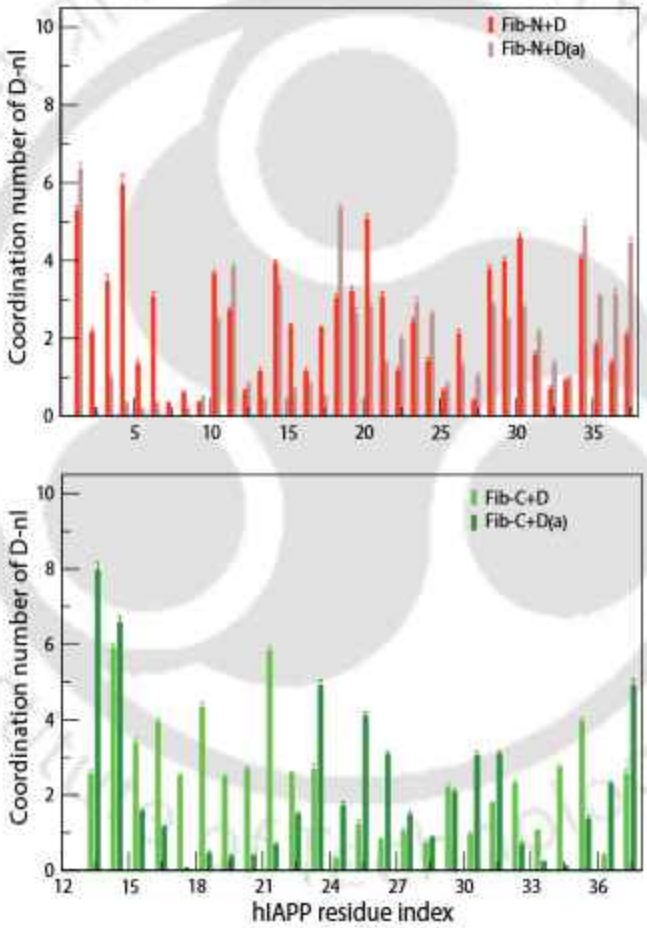

Figure 4.33: *Residue wise coordination number of D-nl around hIAPP protofibrils in different systems.*

A high distribution of D-nl is observed around Ala13-Phe23 region of both the hIAPP protofibrils. The electrostatic and vdW interaction energy between hIAPP peptides becomes unfavourable (Table 4.4) accompanied by a decrease in the average hydrogen bond

values in presence of D-nl peptides (Table 4.3). Considerable values of hydrogen bonds (Table 4.3) and interaction energy (Table 4.4) between hIAPP and D-nl peptide further suggest the binding between hIAPP and the inhibitor peptides.

4.1.4 Discussions

Due to the high specificity and low toxicity of peptide inhibitors, they are a viable choice for inhibitors against hIAPP aggregation. The application of an amyloidogenic core fragment of hIAPP, NFGAIL, as an inhibitor of hIAPP aggregation by changing the chirality of the amino acid residues motivated this study. At first, we analyze how the insertion of D-NFGAIL alters the stability of regular L-NFGAIL aggregates. In our previous study[17], we had observed that this amyloidogenic core of hIAPP aggregated to form a β-barrel like structure. This structure is replaced with alternate D-amino acid strands to produce a hybrid LD structure. On comparing the stability of this hybrid structure with the original aggregate, the barrel structure of the LD hybrid is found to be completely destabilized, due to which the β-sheet conformation almost vanishes. The interaction energy of the peptides becomes less favourable, accompanied by a reduction in the peptide-peptide hydrogen bonds, with the incorporation of D-nl into L-nl peptides.

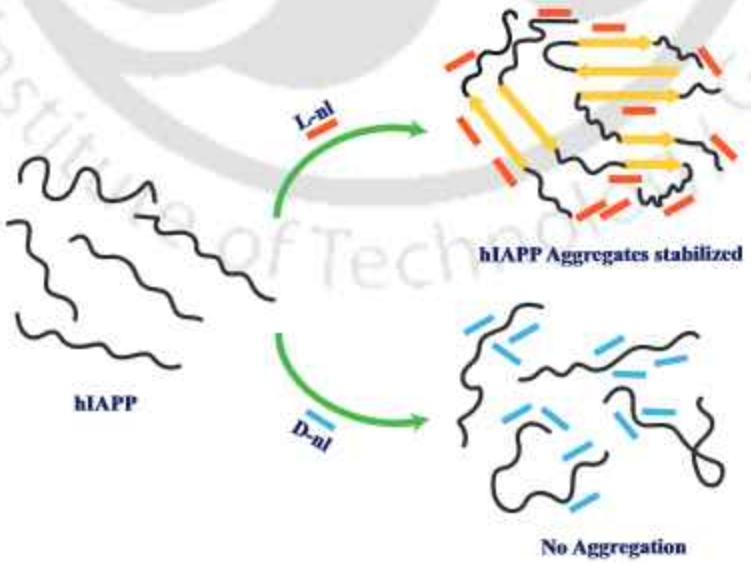

Figure 4.34: *A schematic representation of the effect of L-NFGAIL and D-NFGAIL on the aggregation of hIAPP.*

The inhibitory activity of D-NFGAIL on hIAPP aggregation is then examined on the full length hIAPP. For this, we have also compared the effect of L-NFGAIL on the hIAPP aggregation. The full length hIAPP aggregates to form a three stranded β-sheet conformation in pure water, which is also observed in case of hIAPP dimer[17, 28]. This β-sheet conformation is also prevalent in presence of L-nl peptides, but is absent for the system containing D-nl peptides. Hence, the tendency of hIAPP to form β-sheet rich aggregates in pure water or in the presence of L-nl peptides is discouraged by D-nl peptides and, thus, hIAPP remains in random coil conformation. This leads to enhancement in the Rg and SASA values, which further confirmed that, while the aggregation propensity is hardly affected by L-nl peptides, it is strongly disfavoured by D-nl peptides, resulting in decrease in the interaction between hIAPP. hIAPP preferentially interacts with itself over L-nl peptides, but the formation of β-sheet rich aggregates is stabilized by L-nl. D-nl, on the other hand, interferes with the hIAPP-hIAPP interaction by adhering to hIAPP itself (Fig 4.34). Indetailed analyses reveal that the hydrophobic core residues in L-nl interact with the β-sheet favouring region of hIAPP, thus promoting hIAPP aggregation. The D-nl peptides have higher contact with hIAPP residues, where D-Asn, D-Phe and D-Gly mostly interact with the C-terminal region of hIAPP, and the remaining D-nl residues favour the N-terminal region. Furthermore, the number of hydrogen bonds formed between D-nl and hIAPP exceeds that between L-nl peptides. On the other hand, the number of stacking interactions between L-Phe and Phe residues in hIAPP is greater than with D-Phe. The destabilization of the ordered hIAPP protofibrils comprising of parallel arrangement of β-sheets by D-nl is also analyzed. D-nl partially destabilizes the hIAPP protofibrillar structures obtained from NMR as well as cryo-EM methods, although, the effect is more prominent for the cryo-EM model.

4.1.5 Conclusion

In summary, our study highlights the inhibitory activity of a small peptide, which is derived from hIAPP and consists of all D-amino acid residues (D-NFGAIL), on the aggregation of hIAPP. A series of molecular dynamics simulations validates that D-NFGAIL can effectively refrain randomly packed full-length hIAPP from self-association. After β-sheet is initially formed at a small region of hIAPP, further growth of of hIAPP aggregates is abrogated

by D-NFGAIL. On the other hand, L-NFGAIL strengthens the β-sheet rich aggregates of hIAPP by binding to the β-sheet prone regions of hIAPP. The incorporation of D-NFGAIL further denatures the ordered β-barrel structure, comprising of L-NFGAIL peptides. From umbrella sampling simulations, it is also conjectured that the formation of hIAPP dimer, which is the initial step towards aggregation, is obstructed by D-NFGAIL. The hydrogen bond and hydrophobic (stacking) interactions between hIAPP and NFGAIL peptides are crucial in the binding mechanism. In addition, the presence of D-NFGAIL can also lead to the partial dissolution of pre-formed fibrils of hIAPP. These findings adequately describe the pathway via which the pancreatic β-cell amyloids can be effectively regulated by a small hIAPP derived peptide. The results also highlight the hIAPP residues responsible for aggregation, thereby imparting information about the biochemical targets for mitigating cytotoxic amyloid species. Lastly, this study guides us in designing potent peptide inhibitors to combat Type II diabetes and other amyloid diseases.

4.2 Disparate Effect of Hybrid Peptidomimetics Containing Isomers of Aminobenzoic Acid on hIAPP Aggregation

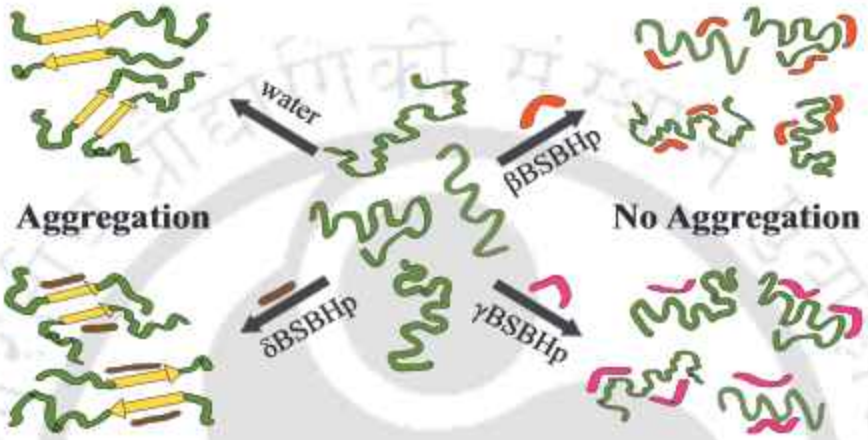

4.2.1 Introduction

The small peptides or peptide mimetics derived either from the hIAPP sequence or by de novo design have proven to be excellent hIAPP inhibitors[29]. Nonetheless, due to the sequence resemblance of small peptide inhibitors derived from hIAPP with the parent peptide, they often self-aggregate at low concentrations to form amyloid-like aggregates, several of which are toxic to the cells[29]. Consequently, various β-breaker elements have been incorporated in the parent sequence, which prevent the misfolding of hIAPP into β-sheet rich structure[29].

However, most of the conformationally restricted elements contain α-amino acids, which makes them proteinogenic, thus unstable against proteolytic degradation. Therefore, Paul et al. have designed a set of conformationally constrained β-sheet breaker hybrid peptidomimetics (BSBHps), which contains β (2-aminobenzoic acid), γ (3-aminobenzoic acid), and δ (4-aminobenzoic acid) aromatic amino acids[30]. The presence of these structurally rigid aromatic amino acids in the hybrid peptides enhances their stability toward proteolytic degradation and hence are promising candidates against amyloid aggregation. The derivatives of 2-aminobenzoic acid have been used as inhibitors of amyloid β aggregation[31] and also transthyretin amyloid fibril[32]. The conformationally constrained aminobenzoic acids (Abz) are inserted into the peptide segment extracted from the amyloidogenic core of hIAPP, $hIAPP_{22-27}$ or NFGAIL.

Here, Ile26 is replaced to give rise to three BSBHps containing one breaker element (single substituted BSBHps) and Gly24 and Ile26 are both simultaneously replaced to design another set of two breaker element containing BSBHps (double substituted BSBHps). The modulation of Gly24 and Ile26 residues in the wild type sequence, NFGAIL, has previously produced peptide inhibitors against hIAPP aggregation[33, 34]. Interestingly, the β and γ-Abz containing peptide analogues efficiently inhibit hIAPP aggregation, whereas the δ BSBHps do not display inhibitory activity. Also, δ BSBHps are itself found to be amyloidogenic in nature, unlike the other two isomeric BSBHps. Furthermore, the double substituted BSBHps are not only superior in their inhibitory capacity, but also are more stable in presence of proteolytic enzymes as compared to single substituted BSBHps. Also, these designed BSBHps disrupted pre-formed amyloids into nontoxic forms and did not af-

fect the cell viability of human embryonic kidney (HEK) cells (up to 1 μM concentration).

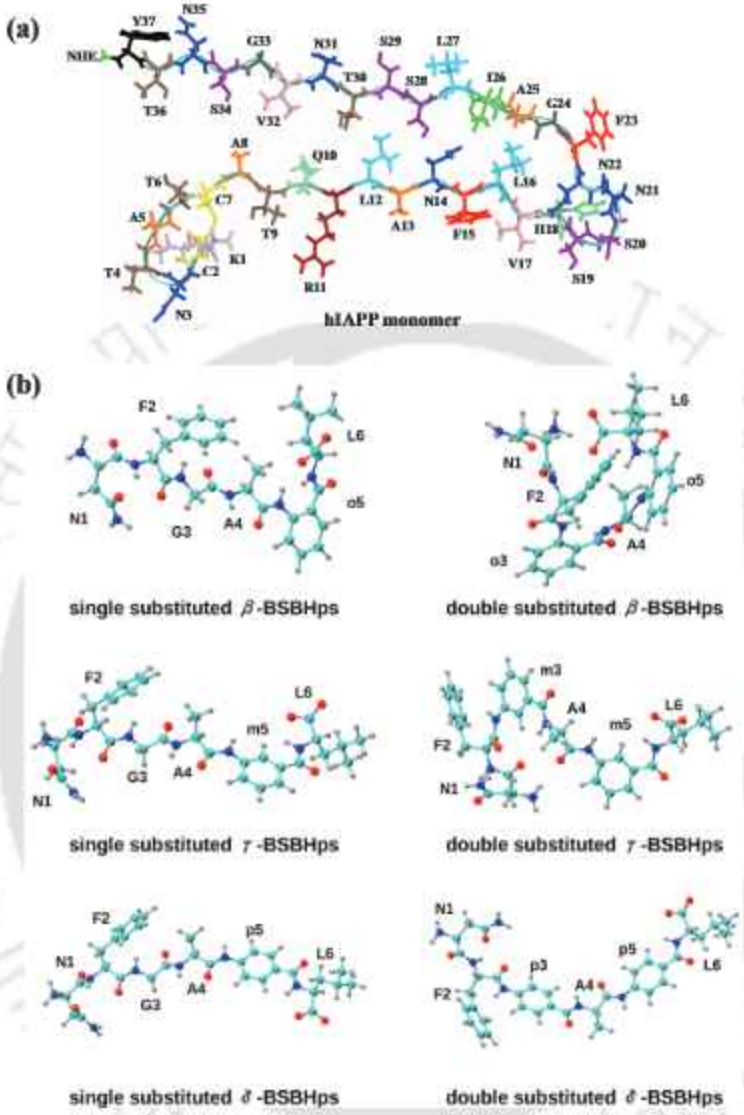

Figure 4.35: *(a) Sequence of hIAPP monomer and (b) Structures of the BSBHps used in the simulations. The N, O, H and C atoms in the BSBHps are depicted in blue, red, silver and cyan respectively. 'o', 'm' and 'p' residues indicate ortho, meta and para-aminobenzoic acid moieties respectively.*

It is intriguing to perceive that the incorporation of three different isomers of the same aromatic amino acid, i.e., aminobenzoic acid, in the BSBHps displays such contrasting influence on hIAPP aggregation. The stereochemistry of amyloid inhibitors often plays a significant role in their anti-amyloid activity. Stereoisomers of polyphenols have displayed

distinct binding modes and differential inhibitory ability towards amyloid aggregation[35, 36]. The utility of these conformationally restricted peptides as potential inhibitors of the amyloid aggregation of hIAPP is a novel approach for the treatment of T2D. Therefore, the dissimilar pathway via which these hybrid peptides interact with hIAPP needs to be determined. Keeping this in mind, we have performed molecular dynamics simulations of hIAPP monomers in presence of different hybrid peptides. Corroborating with the experimental results[30], our simulation results also depict that the aggregation of hIAPP is inhibited by β and γ-BSBHps. The δ BSBHps, on the other hand, facilitate the β-sheet formation of hIAPP and thus assists in its aggregation. This contrast in the effect of the different isomeric hybrid peptides on hIAPP aggregation is due to the variation in the preferential binding conformation of hIAPP.

The methods applied in this study are described in the Simulation Method section. The in-detail explanation of our findings and our deductions are stated in the Results section, and the overall observations is summarized in the Conclusion section.

4.2.2 Simulation method

4.2.2.1 Simulation Setup

The initial coordinates of the hIAPP monomer is extracted from the solid state NMR structure of hIAPP[19] (Fig 4.35a). The small peptide based inhibitors used in our study was constructed by AMBERTools[21] (Fig 4.35b). The isomers of aminobenzoic acid inserted in the peptides was parameterized using pyRED calculations[37] on the R.E.D server[38–41]. Four hIAPP monomers were placed sufficiently apart in a cubic box such that the hIAPP monomers are at least 20 Å apart. Eight BSBHps are added to in the systems at a minimum distance of 10 Å from each of the hIAPP monomers. In the experimental study[30], three hIAPP:BSBHp molar ratios (1:2, 1:5 and 1:10) were used, and the BSBHps showed inhibitory ability towards hIAPP aggregation at all molar ratios, with the effect being most pronounced at the highest concentration of BSBHps (i.e., 1:10). However, in our study, we have used hIAPP:BSBHp ratio of 1:2, which will enable us to properly identify the specific interactions between hIAPP and BSBHps, without the interference of excess BSBHps molecules. As a control, hIAPP was simulated in absence of any BSBHps. Each

system was repeated twice with different initial configuration, in order to overcome the influence of the starting structure. and the details of each of the system are mentioned in Table 4.6. Each of the simulation was conducted for 1000 ns, following simulation protocols mentioned in Chapter 1 (Section 1.5.2). Overall, a total of 14 μs of unbiased molecular dynamics simulation was carried out for this study.

System		N_h	N_β	N_γ	N_δ	N_w	Box length (Å)
hIAPP	**1**	4				10000	68.64
	2	4				10000	68.62
OS	**1**	4	8			15000	85.86
	2	4	8			15000	85.85
MS	**1**	4		8		15000	85.9
	2	4		8		15000	85.88
PS	**1**	4			8	15000	85.93
	2	4			8	15000	85.92
OD	**1**	4	8			15000	85.90
	2	4	8			15000	85.91
MD	**1**	4		8		15000	85.93
	2	4		8		15000	85.88
PD	**1**	4			8	15000	85.9
	2	4			8	15000	85.90
Dimer+OS		2	4			5000	54.81
Dimer+MS		2		4		5000	54.81
Dimer+OD		2	4			5000	54.85
Dimer+MD		2		4		5000	54.84

Table 4.6: *System Details. N_h, N_β, N_γ, N_δ and N_w defines the number of hIAPP monomers, β-BSBHps, γ-BSBHps, δ-BSBHps and water incorporated into the systems. The addition of single and double substituted peptides is indicated by 'S' and 'D' alphabets respectively in the system names.*

4.2.2.2 Simulation Analysis

The simulation analyses were carried out following the protocols discussed in Chapter 1 (Section 1.5.3). The free energy landscapes (FELs) were computed using radius of gyration (R_g) and SASA (and number of contacts between the heavy atoms of the hIAPP residues and the hydrogen bonds formed by hIAPP) as the reaction coordinates, following the equation 1.19. An isovalue of 0.5 was considered for evaluating the spatial distribution

functions of the inhibitor peptides around hIAPP. The first solvation shell coordination number of the BSBHps was determined by the number of the respective BSBHps present within a distance of 5 Å from each residue of hIAPP, considering all the heavy atoms[23], while a non-polar contact between hIAPP and BSBHps was defined by same, considering only the aliphatic carbon atoms[42].

The potentials of mean force (PMFs) of hIAPP dimer formation was calculated via umbrella sampling (US) method[24] to estimate the effect of the BSBHps on hIAPP dimerization. The US simulations were renormalized using Weighted-Histogram Analysis Method (WHAM)[25, 26]. Initially two full-length hIAPP peptides were simulated for 400 ns, in presence of single and double substituted β and γ-BSBHps, following above mentioned protocols for unbiased simulations. The starting structures for the US simulations were extracted from the final trajectory of the above simulations. The distance between the center of masses of the Cα atoms of two hIAPP monomers was applied as the reaction coordinate for the US simulations, which spanned from 3 to 20 Å, with 0.2 Å increment. A pull force of 2.5 kcal mol^{-1} Å^2 was applied and each window was simulated in NPT ensemble at 300 K for 30 ns. Hence, the four systems resulted in additional 11.92 (1.6 of unbiased and 10.32 of biased) μs of simulations. The PMF of hIAPP dimer in pure water was plotted using the results obtained in the previous study (Chapter 4.1)[43].

4.2.3 Results

4.2.3.1 Effect of BSBHps on the conformation of hIAPP

In this study, at first, we have investigated how the structure and the aggregation propensity of hIAPP is regulated by the different hybrid peptidomimetics. Figs 4.36 and 4.37 represent the snapshots of the four hIAPP peptides along the course of the simulation. The initially separated peptides accumulate to form β-sheet rich structure in absence of any BSBHps. In presence of β and γ-BSBHps, hIAPP mostly remains in an unstructured coil conformation. On the other hand, numerous β-sheet conformation is observed for the system containing δ-BSBHps.

Since the conformation of hIAPP undergoes deviation from random coil to β-sheet during its aggregation, to probe the influence of the BSBHps on this conformational space,

we have constructed a 2D free energy landscapes (FELs) that highlight protein ensembles

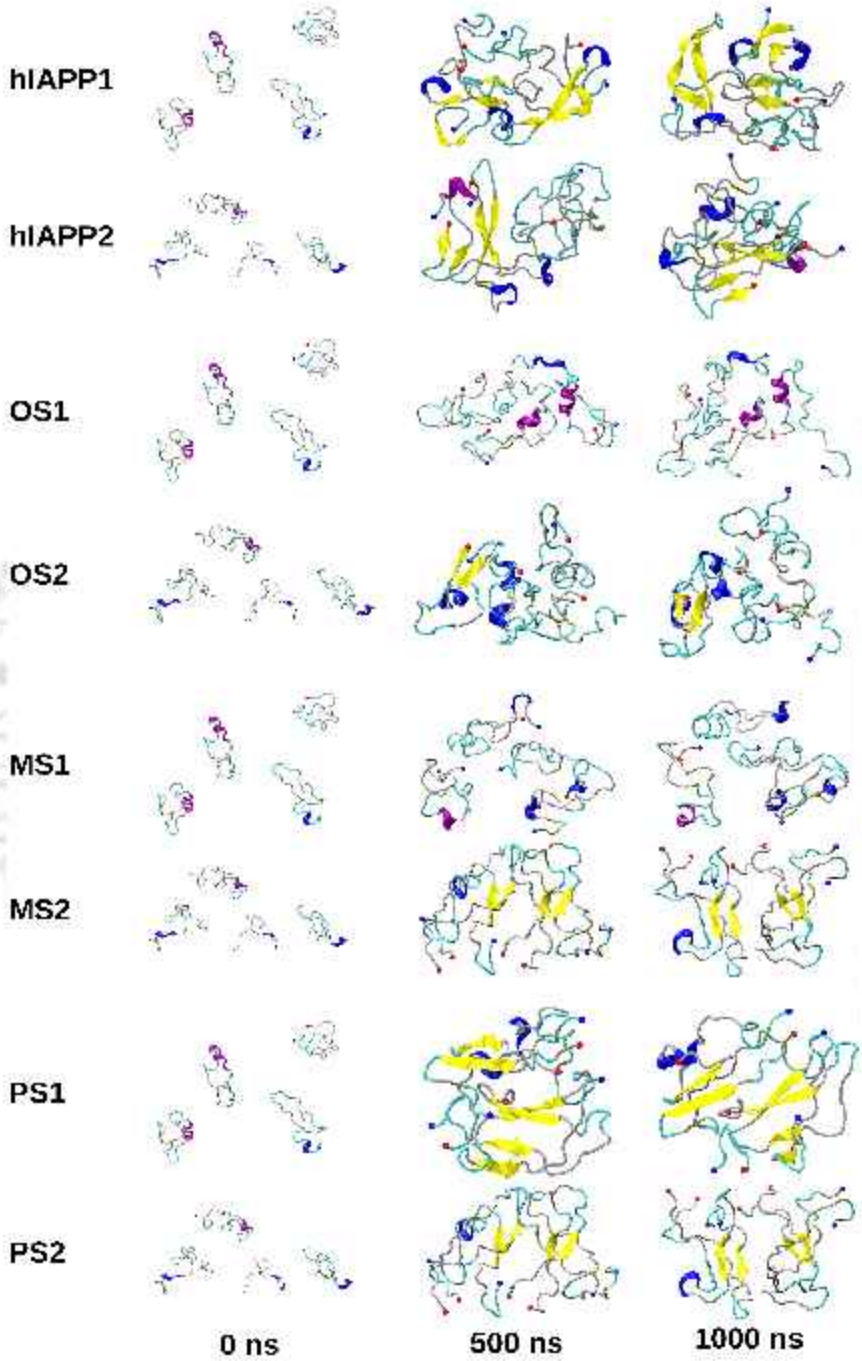

Figure 4.36: *Representative snapshots of hIAPP at different simulation time in pure hIAPP (hIAPP1/hIAPP2) systems and that in presence of single substituted β (OS1/OS2), γ (MS1/MS2) and δ (PS1/PS2) BSBHps. The peptides are represented in cartoon form, depicting β-sheet in yellow, coil in silver, turn in cyan, α-helix in purple and 3_{10}-helix in blue.*

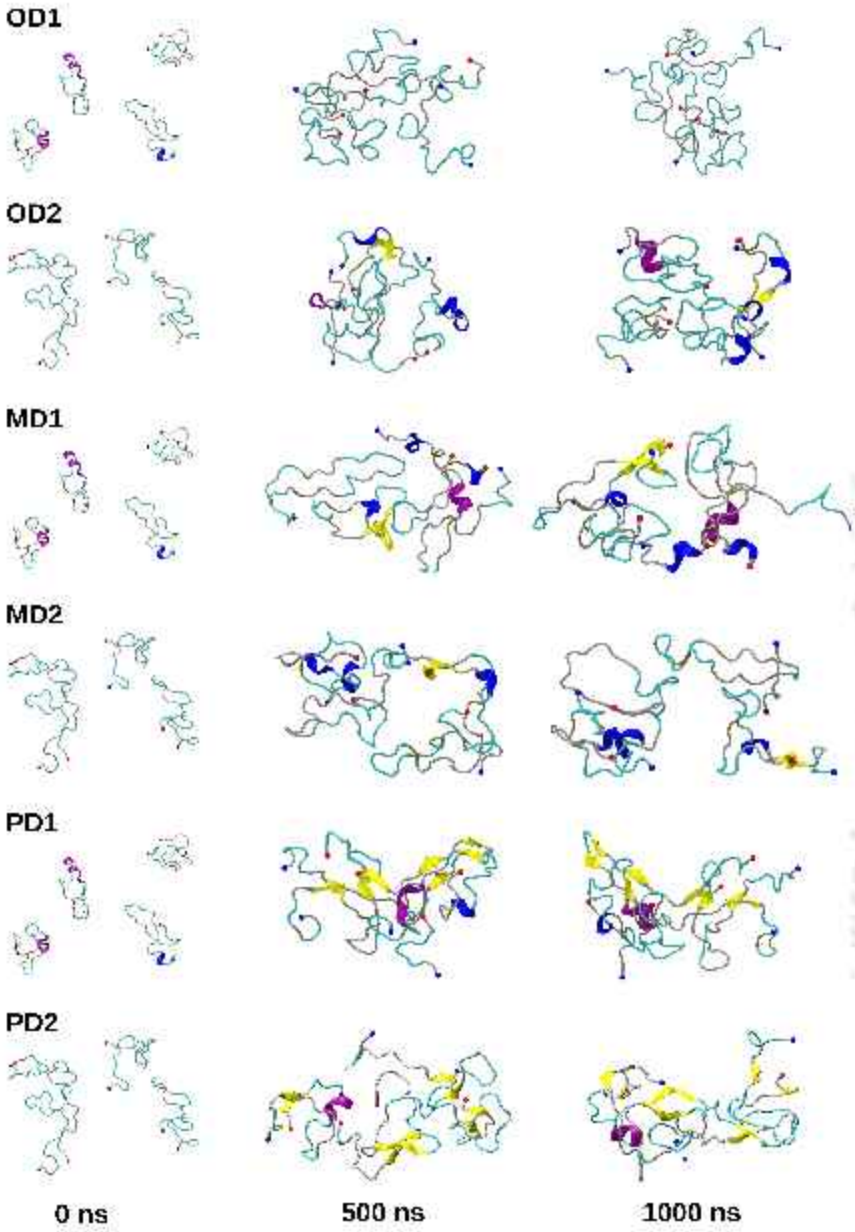

Figure 4.37: *Representative snapshots of hIAPP at different simulation time in systems containing double substituted β (OD1/OD2), γ (MD1/MD2) and δ (PD1/PD2) BSBHps. The peptides are represented in cartoon form, depicting β-sheet in yellow, coil in silver, turn in cyan, α-helix in purple and 3_{10}-helix in blue.*

as a function of radius of gyration (R_g) and solvent accessible surface area (SASA) of the hIAPP peptides. From the FELs (Fig 4.38), we observed that, in case of isolated hIAPP, the

minimum is centered around R_g=10.8 Å and SASA=8200 Å^2. The center of the minimum shifts to much larger values of R_g and SASA for the systems containing single substituted β and γ-BSBHps, indicating the occupancy of extended morphologies. In addition, the energy basins in these systems are broader and are accompanied by other shallower wells. The incorporation of single substituted δ-BSBHps into the systems leads to the appearance of a minimum well with much lower R_g (10.6 Å) and SASA (7000 Å^2) values. The SASA and R_g of hIAPP surrounded by double substituted BSBHps (Table 4.7) follow a similar trend as the above systems.

The presence of loosely packed hIAPP monomers in the β and γ-BSBHps containing systems is evident from their higher R_g values of hIAPP compared to that in the isolated hIAPP and also in presence of δ-BSBHps.

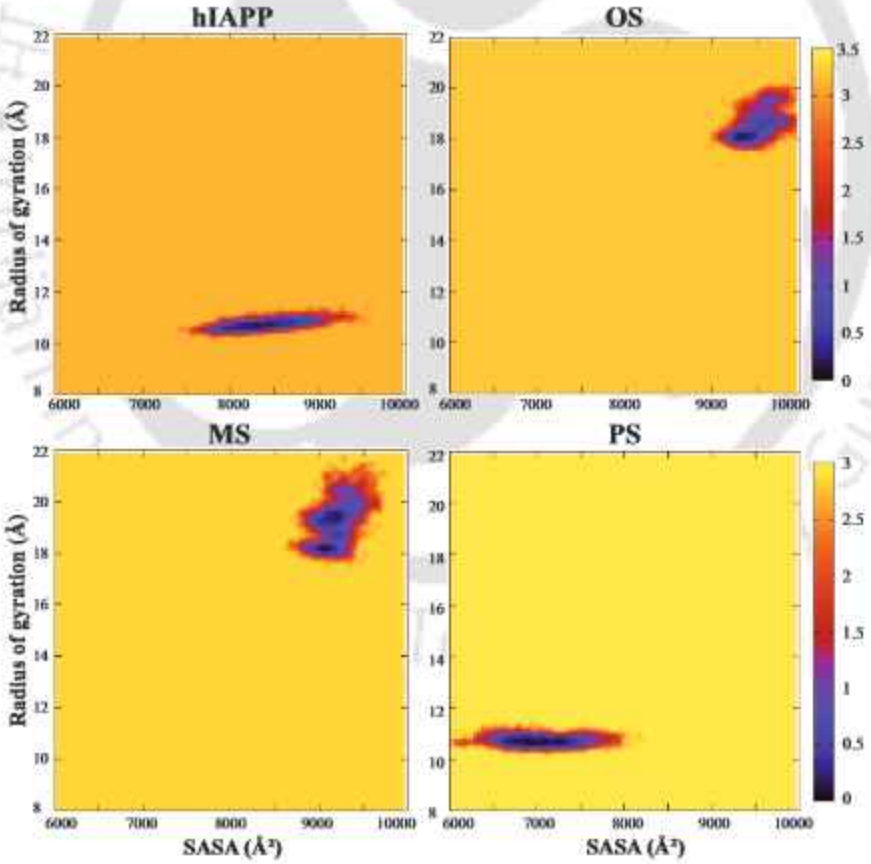

Figure 4.38: *Free energy plot (kcal/mol) as a function of R_g and SASA of hIAPP in pure hIAPP (hIAPP) system and that in presence of single substituted β (OS), γ (MS) and δ (PS) BSBHps. The last 200 ns of simulation of the two replicates is used for analyzing each system.*

System		R_g (Å)	SASA (Å^2)
OD	1	16.7 ± 0.001	9738 ± 2.35
	2	16.9 ± 0.003	9105 ± 1.7
MD	1	18.12 ± 0.005	10160 ± 2.93
	2	19.31 ± 0.01	9692 ± 2.57
PD	1	10.91 ± 0.002	8145 ± 4.36
	2	12.27 ± 0.003	8680 ± 5.65

Table 4.7: *The average radius of gyration (R_g) and SASA of hIAPP in systems containing double substituted β (OD1/OD2), γ (MD1/MD2) and δ (PD1/PD2) BSBHps.*

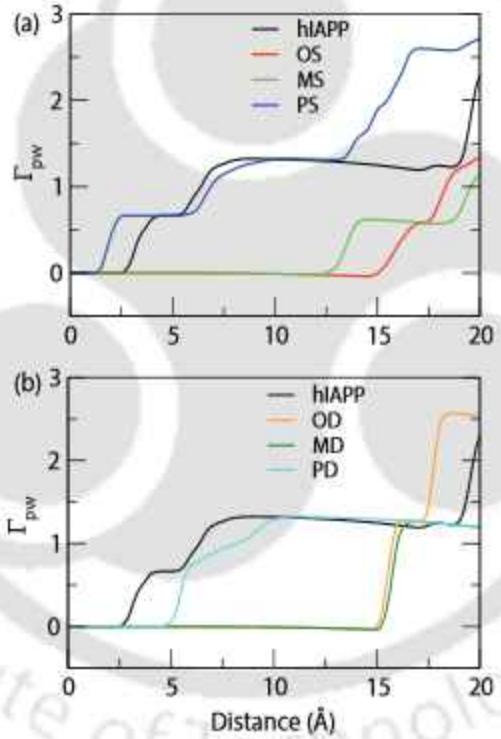

Figure 4.39: *Preferential interaction parameters of hIAPP for hIAPP-hIAPP over hIAPP-water interactions for pure hIAPP (hIAPP) system and that in presence of (a) single substituted β (OS), γ (MS) and δ (PS) and (b) double substituted β (OD), γ (MD) and δ (PD) BSBHps. The last 200 ns of simulation of the two replicates is used for analyzing each system.*

These extended hIAPP conformers demonstrate much less propensity to aggregate, and hence are more exposed to the solvent molecules, resulting in higher SASA values for the systems bearing β and γ-BSBHps. Hence this leads a low negative value (upto ∼12 Å) of

the preferential interaction parameter (Γ_{pw}) in these systems (Fig 4.39). Γ_{pw} explores the preference of hIAPP to interact with itself over the solvent molecules, and from equation 1.18, its positive value indicates that hIAPP favorably interacts with itself rather than the solvent. A positive value of Γ_{pw} is observed after ~2 Å for pure hIAPP and also in presence of δ-BSBHps (Fig 4.39). This suggests that at lower distances, the hIAPP peptides are more solvated in water, leading to less propensity to aggregate in the systems having β and γ-BSBHps.

The secondary structure conformation of amyloid peptides plays a crucial role in their aggregation. Hence we probe into the secondary structure details of hIAPP in presence of the conformationally restricted peptides. The progression of the secondary structures of each residue of hIAPP with time (Figs 4.40 and 4.41) shows that, in pure system,

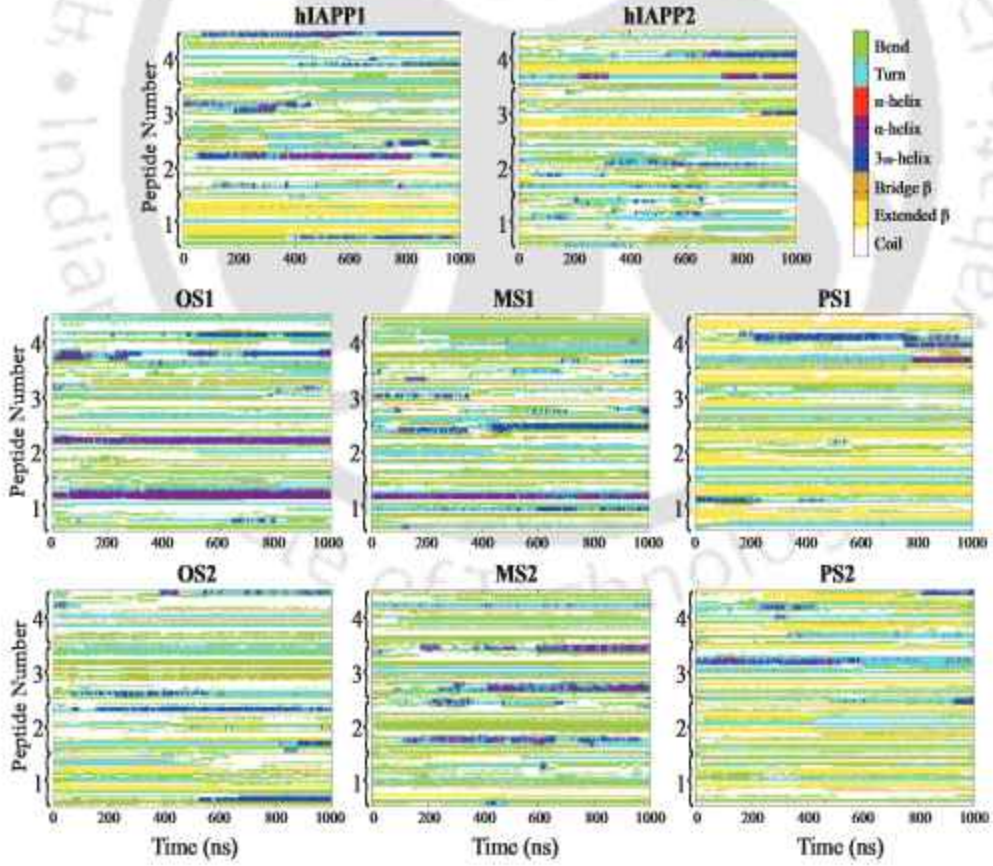

Figure 4.40: *Time evolution of change of secondary structures of each residue of hIAPP in pure hIAPP (hIAPP1/hIAPP2) systems and that in presence of single substituted β (OS1/OS2), γ (MS1/MS2) and δ (PS1/PS2) BSBHps.*

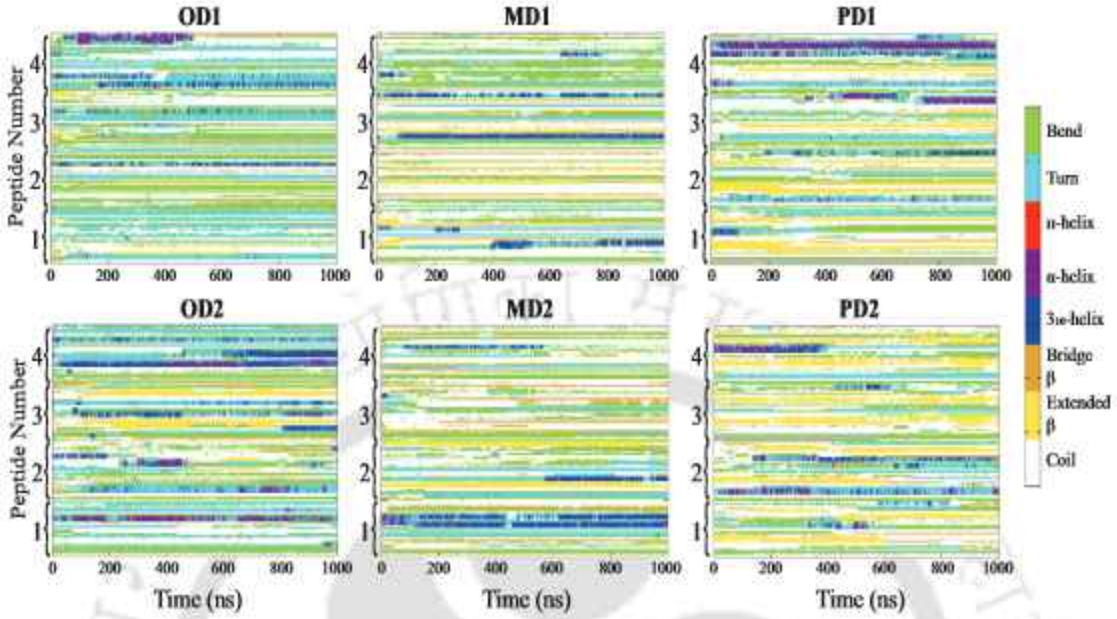

Figure 4.41: *Time evolution of change of secondary structures of each residue of hIAPP in double substituted β (OD1/OD2), γ (MD1/MD2) and δ (PD1/PD2) BSBHps systems.*

System		Extended-β	Bridge-β	3_{10}-helix	α-helix	Coil
hIAPP	1	12.5 ± 0.4	4.8 ± 0.2	6.2 ± 0.3	0.3 ± 0.0	40.5
	2	12.3 ± 0.3	4.3 ± 0.3	4.4 ± 0.3	2.8 ± 0.3	35.1
OS2	1	0.3 ± 0.0	2.6 ± 0.2	4.1 ± 0.2	7.9 ± 0.4	40.2
	2	3.7 ± 0.3	3.6 ± 0.3	6.1 ± 0.3	5.1 ± 0.3	31.4
MS2	1	0.3 ± 0.0	5.7 ± 0.3	5.1 ± 0.2	2.1 ± 0.2	41.1
	2	0.4 ± 0.0	5.8 ± 0.3	2.1 ± 0.1	5.0 ± 0.3	41.0
PS2	1	21.9 ± 0.5	3.8 ± 0.2	1.3 ± 0.1	4.1 ± 0.2	37.0
	2	14.8 ± 0.4	4.1 ± 0.2	2.4 ± 0.1	0.4 ± 0.0	39.4
OD2	1	0.3 ± 0.0	3.2 ± 0.2	3.1 ± 0.2	0.0 ± 0.0	41.3
	2	4.1 ± 0.3	2.8 ± 0.2	10.6 ± 0.3	2.8 ± 0.1	34.0
MD2	1	3.2 ± 0.2	4.9 ± 0.3	5.0 ± 0.3	0.1 ± 0.0	49.7
	2	3.7 ± 0.2	5.8 ± 0.3	4.8 ± 0.3	0.7 ± 0.1	45.6
PD2	1	13.1 ± 0.6	4.1 ± 0.3	2.4 ± 0.3	1.8 ± 0.2	36.7
	2	11.7 ± 0.4	3.9 ± 0.2	3.3 ± 0.2	5.3 ± 0.3	38.0

Table 4.8: *The secondary structure contents of hIAPP in pure hIAPP (hIAPP1/hIAPP2) systems and that in presence of single substituted β (OS1/OS2), γ (MS1/MS2) and δ (PS1/PS2) and double substituted β (OD1/OD2), γ (MD1/MD2) and δ (PD1/PD2) BSBHps.*

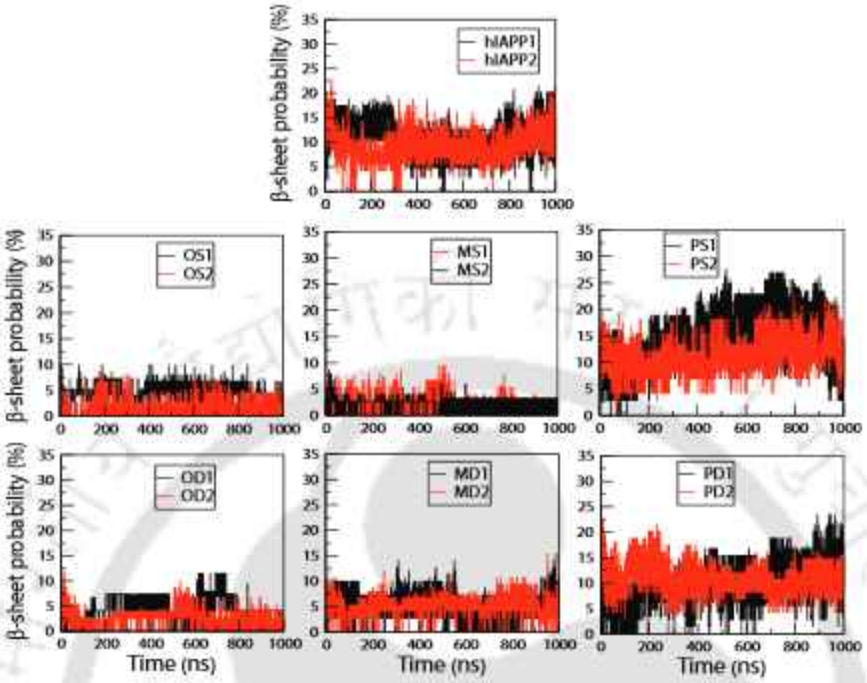

Figure 4.42: *Time evolution of change of β-sheet of hIAPP in pure hIAPP (hIAPP1/hIAPP2) systems and that in presence of single substituted β (OS1/OS2), γ (MS1/MS2) and δ (PS1/PS2) and double substituted β (OD1/OD2), γ (MD1/MD2) and δ (PD1/PD2) BSBHps.*

the hIAPP monomers instantly aggregate to form ordered β-sheet structure (marked in yellow). Similar phenomenon is also observed for the system with δ-BSBHps. However, in presence of β and γ-BSBHps, some unstable β-strands are formed, which eventually dwindles. This corroborates with the CD and FTIR results obtained in the experimental study[30]. The total β-sheet percentage along the simulation time quantify the above discussed evolution of this conformation in all the system (Fig 4.42), which decreases to 0.25 % (β-BSBHp)/ 0.3 % (γ-BSBHp) from 12.49 % (pure hIAPP) (Table 4.8) towards the end of the simulation. With decrease in β-sheet conformation, the hIAPP monomers mostly remain in a disordered, random coil state.

The impact of the BSBHps on the three dimensional conformation of hIAPP is investigated by the cluster analysis. Three of the most populous structure are represented in Fig 4.43a-d (and 4.44a-c). In absence of BSBHps, hIAPP is mostly present in disordered conformation, which corroborates with prior reports[28]. However, more β-sheet

conformation is observed in the pure system compared to the ones with β and γ-BSBHps.

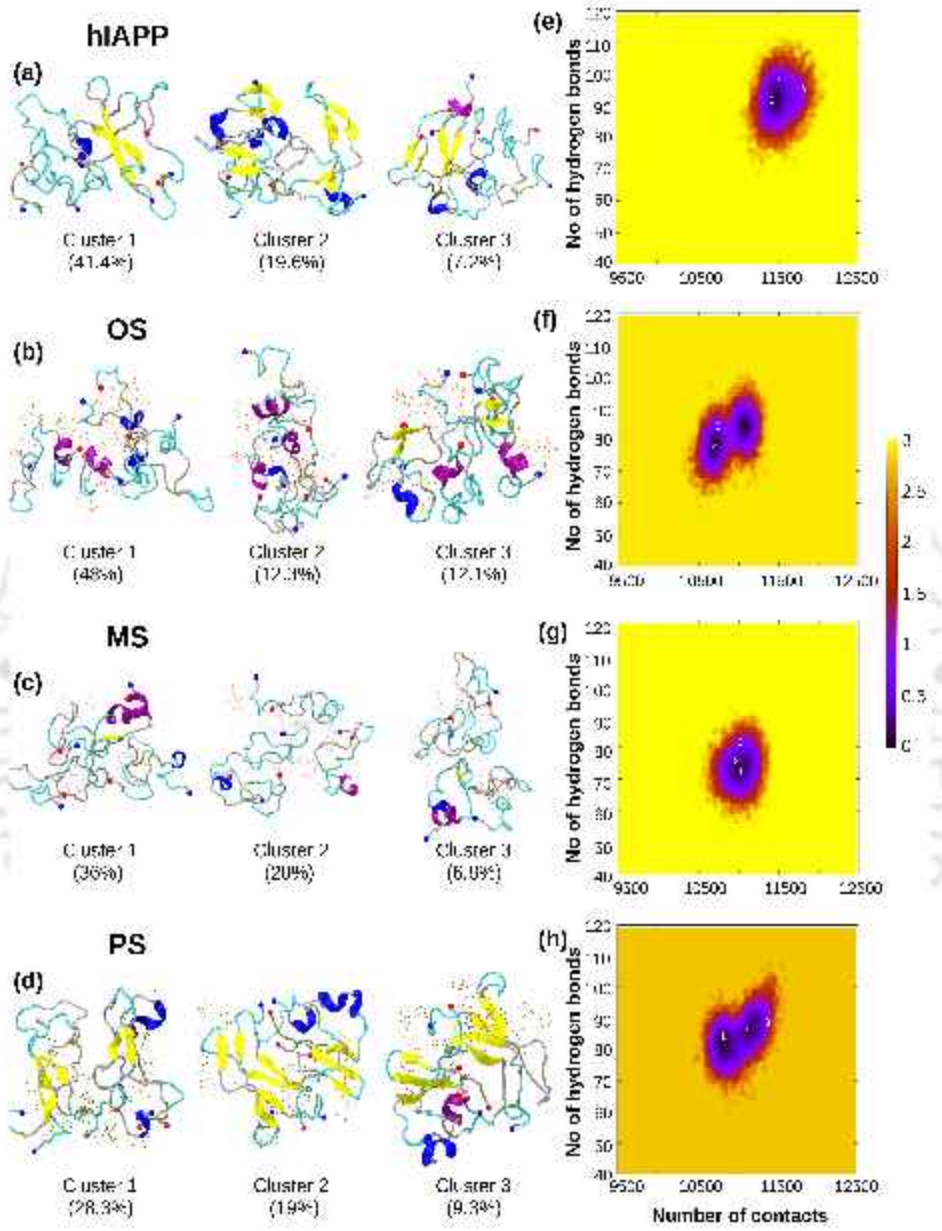

Figure 4.43: *Representative hIAPP structures of three of the most populated clusters (a-d) and the free energy plot (kcal/mol) with respect to the number of contacts and the hydrogen bond formed between hIAPP (e-h) in pure hIAPP system (hIAPP) and in presence of single substituted β (OS), γ (MS) and δ (PS) BSBHps respectively. The distribution of the respective BSBHps are shoum in dots around hIAPP. The last 200 ns of simulation of the two replicates is used for analyzing each system.*

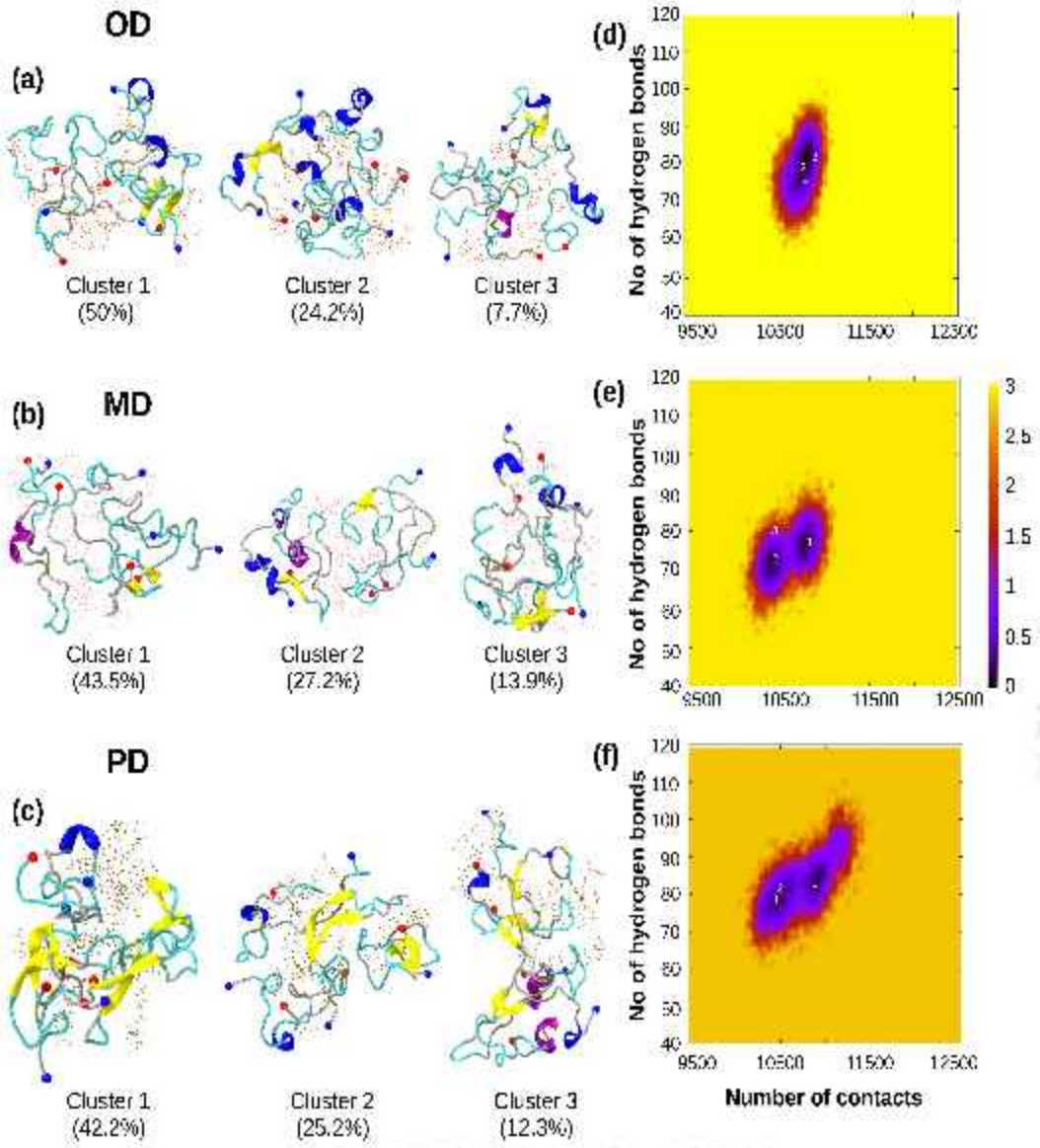

Figure 4.44: *Representative hIAPP structures of three of the most populated clusters (a-c) and the free energy plot (kcal/mol) with respect to the number of contacts and the hydrogen bond formed between hIAPP (d-f) in pure hIAPP system (hIAPP1/hIAPP2) and in presence of double substituted Bβ (OD), γ (MD) and δ (PD) BSBHps. The distribution of the respective BSBHps are shown in dots around hIAPP. The last 200 ns of simulation of the two replicates is used for analyzing each system.*

The β-strands stretch over Ala8-Phe15, Asn21-Ile26 and Ser29-Gly33 residues of hIAPP, consistent with previous simulation reports[42]. In presence of δ-BSBHps, hIAPP at-

tain similar β-sheet rich structure, with mostly parallel β-strands, agreeing with earlier studies[28, 44]. For β and γ-BSBHps bearing systems, hIAPP predominantly exists in random coil conformation with some short β-strands. This complements our results obtained from secondary structure analyses (Fig 4.40, 4.41 and 4.42).

Systems		P-P	P-N
hIAPP	**1**	93.69 ± 0.08	-
	2	91.05 ± 0.08	
OS	**1**	77.99 ± 0.07	24.46 ± 0.04
	2	84.16 ± 0.07	23.56 ± 0.04
MS	**1**	72.81 ± 0.07	20.29 ± 0.04
	2	75.25 ± 0.07	20.45 ± 0.04
PS	**1**	87.21 ± 0.07	24.43 ± 0.06
	2	81.17 ± 0.07	26.06 ± 0.04
OD	**1**	75.48 ± 0.07	26.21 ± 0.04
	2	78.88 ± 0.07	15.88 ± 0.04
MD	**1**	71.74 ± 0.06	30.58 ± 0.05
	2	72.81 ± 0.07	31.1 ± 0.05
PD	**1**	85.91 ± 0.09	23.04 ± 0.04
	2	82.92 ± 0.07	24.06 ± 0.05

Table 4.9: *Average hydrogen bond numbers between hIAPP-hIAPP (P-P) and hIAPP-BSBHp (P-N) interactions in pure hIAPP (hIAPP1/hIAPP2) systems and that in presence of single substituted β (OS1/OS2), γ (MS1/MS2) and δ (PS1/PS2) and double substituted β (OD1/OD2), γ (MD1/MD2) and δ (PD1/PD2) BSBHps.*

In order to examine the effect of the BSBHps on the hIAPP-hIAPP interactions, the number of contacts and hydrogen bond formed between hIAPP are employed to compose a free energy plot (Fig 4.43e-h and 4.44d-f). The center of the energy well of isolated hIAPP appears when the number of contacts and hydrogen bonds are 11646 and 98 respectively. However, in presence of β and γ-BSBHps, it shifts to much lower values of contact and hydrogen bond, reflecting a reduction in interactions between hIAPP (Table 4.9), and hence impeding aggregation. For the systems containing δ-BSBHps, broad energy basins are observed, which extend towards higher values of both collective variables, which stabilize the aggregated oligomers. The average number of hydrogen bonds formed between hIAPP are shown in Table 4.9, which quantifies the change in the aggregation-favoring hIAPP-hIAPP hydrogen bonds. The top three clusters of each system (acquired from cluster

analysis) lie in the energy well of the respective systems. This decrease in the hIAPP interactions is quantified by the non-bonded interaction energy values, which is categorized into electrostatic (ele) and van der Waals (vdW) energies (Table 4.10).

System		P-P		P-N	
		ele	vdw	ele	vdw
hIAPP	1	-4657 ± 0.69	-486.3 ± 0.43		
	2	-4551 ± 0.71	-433.4 ± 0.28		
OS	1	-4300 ± 0.86	-281.5 ± 0.29	-462.1 ± 0.7	-266.7 ± 0.21
	2	-4347 ± 0.64	-313.7 ± 0.27	-593.9 ± 1.03	-223.2 ± 0.24
MS	1	-4271 ± 0.59	-359.7 ± 0.27	-525.4 ± 0.68	-188.5 ± 0.15
	2	-4273 ± 0.94	-336.8 ± 0.28	-562.6 ± 1.04	-169.7 ± 0.23
PS	1	-4465 ± 0.54	-351 ± 0.29	-774.3 ± 1.09	-225.9 ± 0.19
	2	-4401 ± 0.78	-366.9 ± 0.27	-684.2 ± 1.79	-285.6 ± 0.39
OD	1	-4374 ± 0.6	-283.9 ± 0.31	-371.5 ± 0.62	-239.8 ± 0.15
	2	-4313 ± 0.64	-300.4 ± 0.28	-788.4 ± 0.96	-310.7 ± 0.19
MD	1	-4289 ± 0.66	-312.5 ± 0.3	-702.7 ± 0.88	-307.5 ± 0.18
	2	-4300 ± 0.67	-276.7 ± 0.33	-566.9 ± 0.84	-303.8 ± 0.18
PD	1	-4494 ± 0.48	-340 ± 0.24	-421.6 ± 1.05	-291.5 ± 0.17
	2	-4339 ± 0.76	-356.4 ± 0.31	-495.5 ± 0.85	-192.2 ± 0.14

Table 4.10: *Interaction energy (kcal mol^{-1}) of hIAPP-hIAPP (P-P) and hIAPP-BSBHp (P-N) interactions in pure hIAPP (hIAPP1/hIAPP2) systems and that in presence of single substituted β (OS1/OS2), γ (MS1/MS2) and δ (PS1/PS2) and double substituted β (OD1/OD2), γ (MD1/MD2) and δ (PD1/PD2) BSBHps.*

In presence of β and γ-BSBHps, both the energy contributions for the hIAPP-hIAPP interaction is less favorable compared to that for isolated hIAPP and also for the one containing δ-BSBHps systems. Also, the effect is more pronounced for the vdW contribution. The contribution of the BSBHps on the dominant hIAPP interactions is further understood by constructing contact map displaying the distance between the Cα atoms of each pair of hIAPP residues (Figures 4.45 and 4.46). Contacts between Ala8-Val17, Asn21-Ser29 and Val32-Tyr37 stretches are abundant in the pure hIAPP system, depicting the closeness of the hIAPP monomers. β-strands are also predominant in these regions, as observed in the clusters (Fig 4.43a-d and 4.44a-c). Similar interaction interface between hIAPP dimer (Gln10-Leu27) is also reported in a prior study[28]. Also fluorescence titration binding assays report analogous region (Ala8-His18 and Asn22-Ser28) for hIAPP-hIAPP

interaction[45].

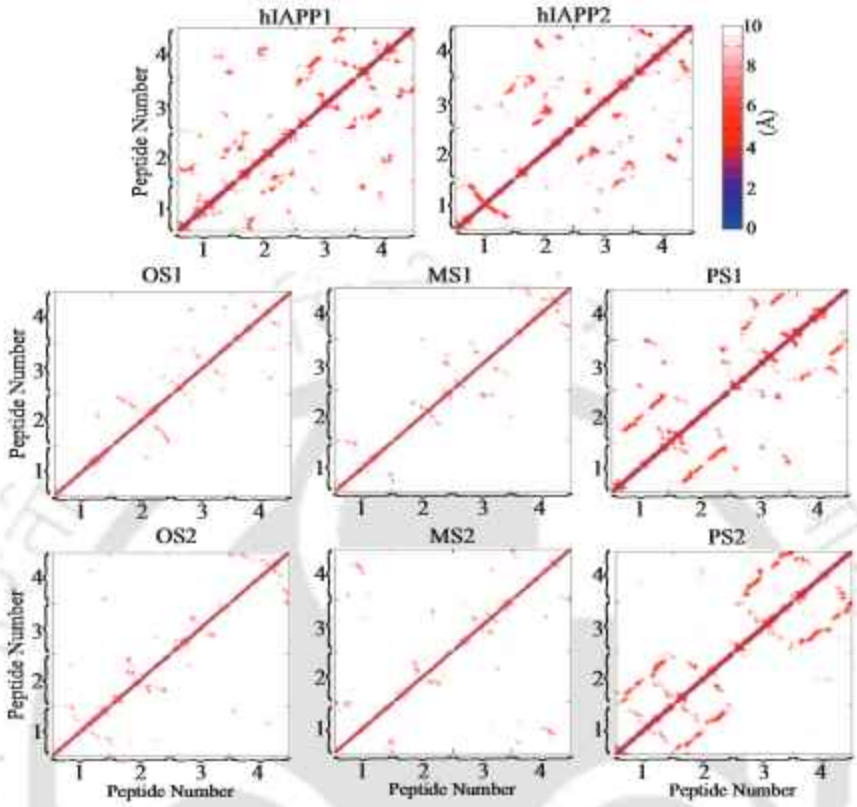

Figure 4.45: *Residue-residue contact map of the backbone atoms of hIAPP in pure hIAPP (hIAPP1/hIAPP2) system and that in presence of single substituted β (OS1/OS2), γ (MS1/MS2) and δ (PS1/PS2) BSBHps.*

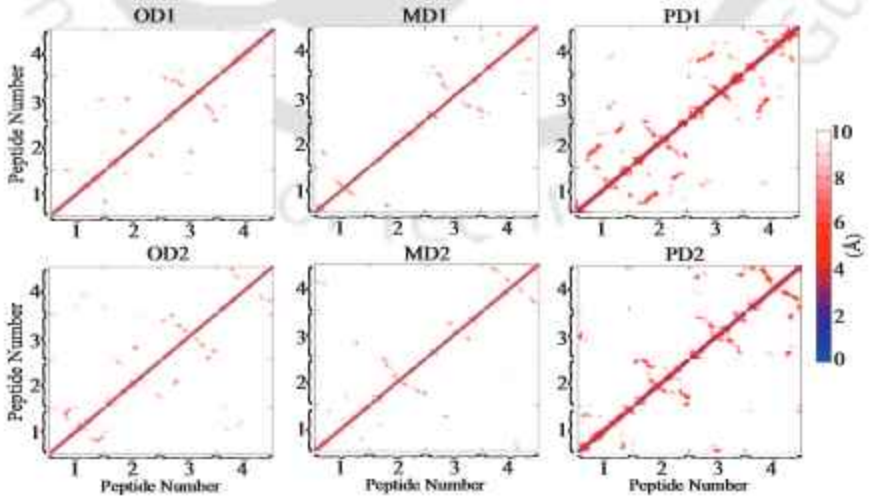

Figure 4.46: *Residue-residue contact map of the backbone atoms of hIAPP in systems containing double substituted β (OD1/OD2), γ (MD1/MD2) and δ (PD1/PD2) BSBHps.*

However, the contacts markedly disappear with the addition of β and γ-BSBHps, suggesting a decrease in the hIAPP-hIAPP interaction.

Hence, it is deduced that interaction between hIAPP is intervened by the β and γ-BSBHps, which promotes hIAPP to remain in a disordered conformation, thus preventing hIAPP aggregation. The δ-BSBHp, on the other hand, enhances the formation of ordered β-sheet rich aggregates, and hence is unable to inhibit the amyloid aggregation, verifying with previous experimental report[30]. In addition, the time evolution of β-sheet percentage (Fig 4.42) ascertains that the convergence of all the systems is achieved in the last 200 ns of the trajectory.

4.2.3.2 Potentials of Mean Force

The effect of the BSBHps on the stability of hIAPP-hIAPP interaction is further investigated by calculating the potential of mean force (PMF) of association between two hIAPP monomers via umbrella sampling simulations. The PMF of two hIAPP monomers in absence and presence of β and γ-BSBHps are shown in Fig 4.47.

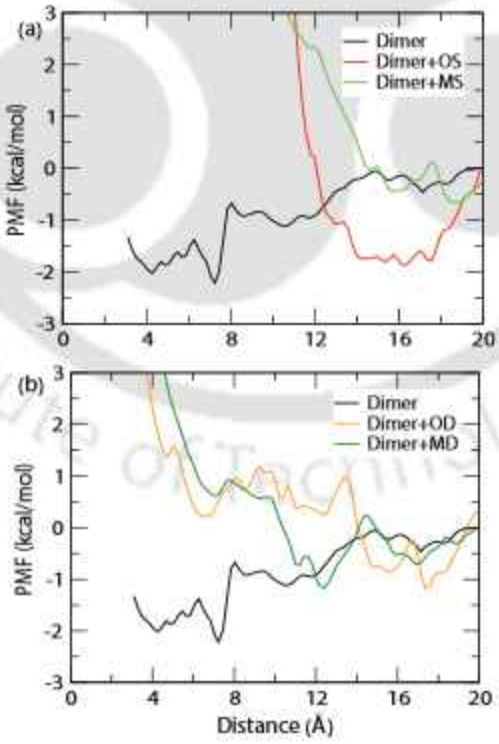

Figure 4.47: *Potential of mean force of two hIAPP monomers in pure hIAPP system (hIAPP) and that in presence of β (Dimer+OS and Dimer+OD) and γ-BSBHps (Dimer+MS and Dimer+MD).*

Since δ-BSBHps possess no inhibitory effect on hIAPP aggregation, PMF for the system in presence of δ-BSBHps is not calculated. The hIAPP dimer is most stable (with minimum free energy), when the distance between the center of mass of the monomer is 7.5 Å. For the system containing single substituted β and γ-BSBHps, the distance at which the free energy minimum occurs shifts beyond 14 Å (Fig 4.47a). The addition of double substituted β and γ-BSBHps also pushes the free energy minimum to around 12 Å distance (Fig 4.47b). Further, the minimum for the pure system not only appears at a lower distance but the well depth is also more favorable than the systems containing BSBHps. Hence the hIAPP dimer formation is stable when the monomers are closer to each other, but the BSBHps drift the hIAPP monomers apart, impairing the dimerization propensity. Since dimerization is the first step towards aggregation, an interruption in this stage hinders further hIAPP aggregation.

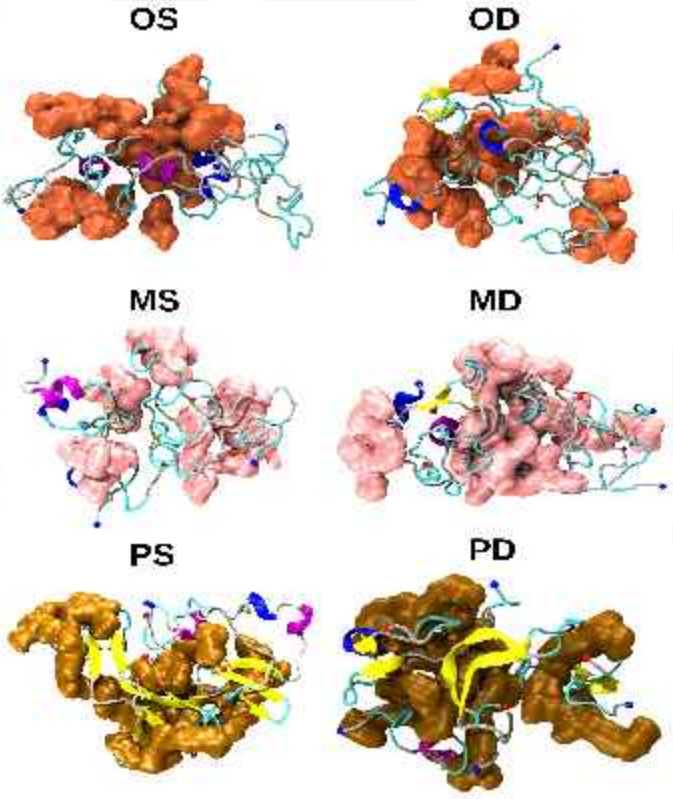

Figure 4.48: *Spatial distribution functions of BSBHps around hIAPP in presence of single substituted β (OS), γ (MS) and δ (PS) and double substituted β (OD), γ (MD) and δ (PD) BSBHps. The peptides are represented in cartoon form, depicting β-sheet in yellow, coil in silver, turn in cyan, α-helix in purple and 3_{10}-helix in blue. The last 200 ns of simulation of the two replicates is used for analyzing each system.*

4.2.3.3 Interaction of BSBHps with hIAPP

In order to rationalize the dissimilarity in the inhibitory ability of the three isomeric BSBHps on hIAPP aggregation, we have conducted an in-depth examination into the interactions between them. The extent of interaction of hIAPP with the hybrid peptides is examined by the non-bonded interaction energy values (Table 4.10).

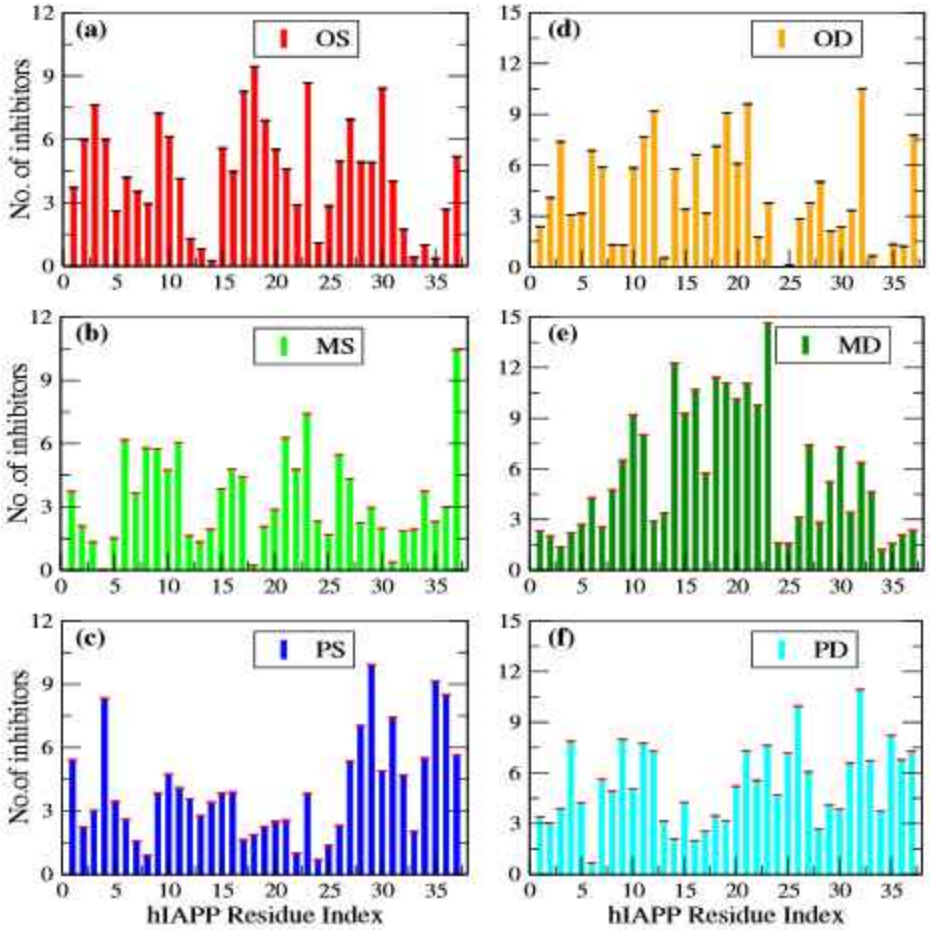

Figure 4.49: *Residue wise coordination number of single substituted (a) β (OS), (b) γ (MS) and (c) δ (PS) and double substituted (d) β (OD), (e) γ (MD) and (f) δ (PD) BSBHps around hIAPP. The last 200 ns of simulation of the two replicates is used for analyzing each system.*

Significant values for the electrostatic as well as the van der Waals energy is observed for all systems. Here again, the electrostatic energy contributes more towards the total energy. The spatial distribution function provides a three-dimensional view of the organization of

the BSBHps around hIAPP monomers at a distance of 5 Å (Fig 4.48).

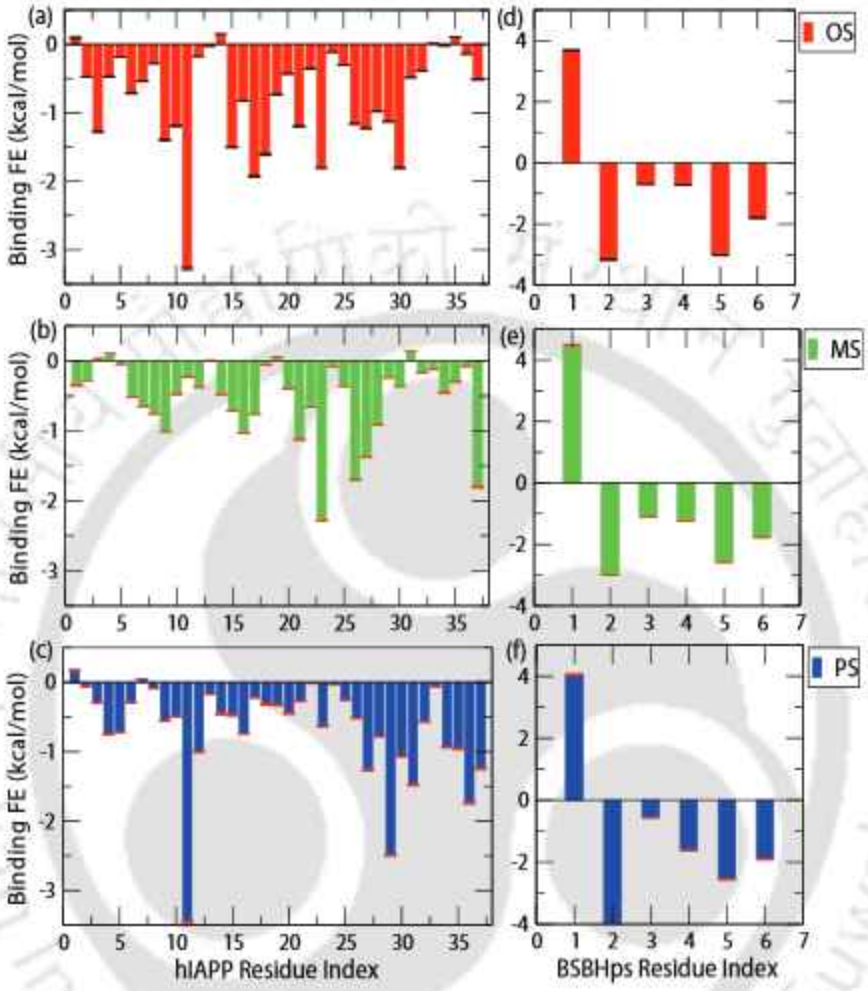

Figure 4.50: *Binding free energy between each residue of (a-c) hIAPP with the respective single substituted β (OS), γ (MS) and δ (PS) BSBHps and (d-f) the corresponding BSBHps with hIAPP. The last 200 ns of simulation of the two replicates is used for analyzing each system.*

To identify the primary binding sites, at first, we have calculated the first shell coordination number of each BSBHps around the hIAPP residues (Fig 4.49). The single substituted β-BSBHps was observed to have maximum coordination number around Phe15-Asn21 residues (Fig 4.49a). In addition, secondary interaction hotspots are also identified in the N-terminal region encompassing Cys2-Arg11 residues and Ile26-Asn31 in the C-terminal stretch. The single substituted γ-BSBHps display abundant interaction with Thr6-Arg11, Phe15-Val17, Asn21-Phe23, Ile26 and Leu27 residues (Fig 4.49b). In presence of single

substituted δ-BSBHps, most frequent contact is perceived in the C-terminal end around Leu27-Tyr37 (Fig 4.49c). The double substituted BSBHps display relatively similar interaction pattern with hIAPP. The β-BSBHps exhibit highest coordination number around Gln10-Asn21 residues, as well as considerable contact with Cys2, Asn3, Thr6, Cys7, Phe23, Leu27, Ser28, Val32 residues (Fig 4.49d). The γ-BSBHps mostly interact with Ala8-Arg11 and Asn14-Phe23 in the N-terminal region, along with some lesser extent of interaction with Ile26-Gly33 residues (Fig 4.49e). The C-terminal region stretching from Ser20 to Leu27 and Asn31-Tyr37 residues of hIAPP display the highest coordination number

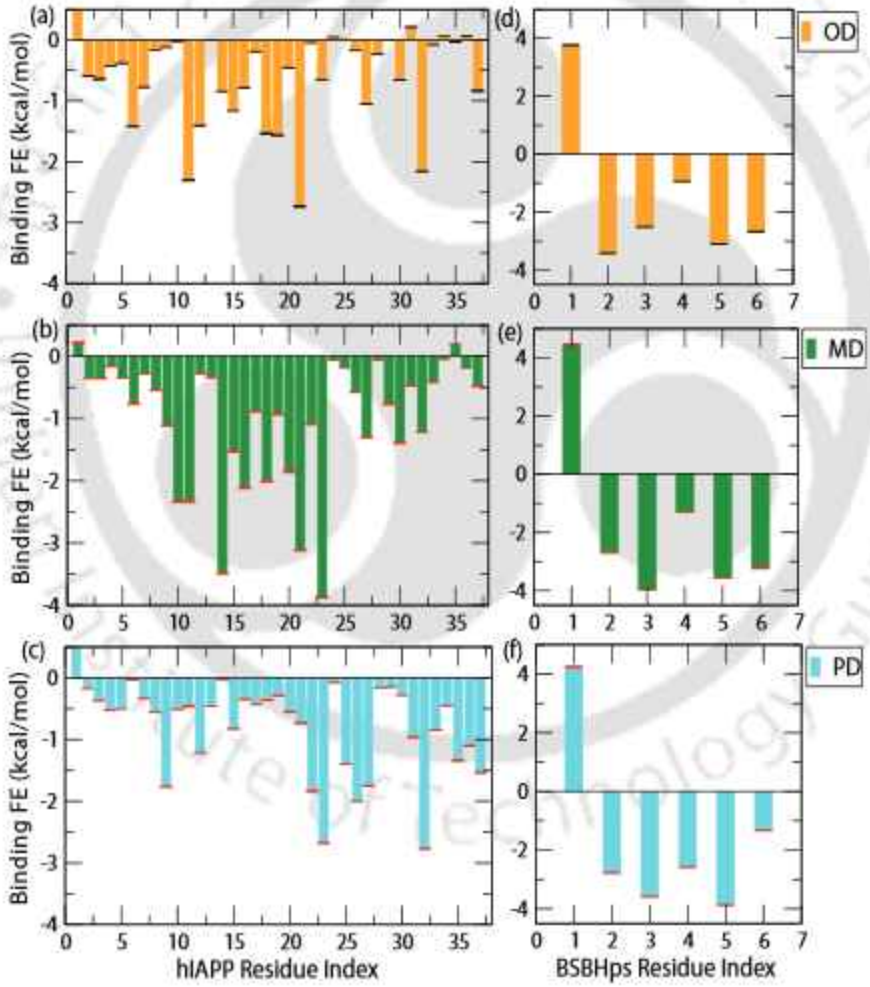

Figure 4.51: *Binding free energy between each residue of (a-c) hIAPP with the respective double substituted β (OD), γ (MD) and δ (PD) BSBHps and (d-f) the corresponding BSBHps with hIAPP. The last 200 ns of simulation of the two replicates is used for analyzing each system.*

with δ-BSBHps (Fig 4.49f). The probable binding sites of the different BSBHps is further investigated by the binding free energy values between the BSBHps and hIAPP. Here we observed that, favorable free energy values are obtained for the binding interaction in all the systems. Also, the residue-based binding free energy data (Figs 4.50a-c and 4.51a-c) is comparable to that of the first shell coordination number (Fig 4.49).

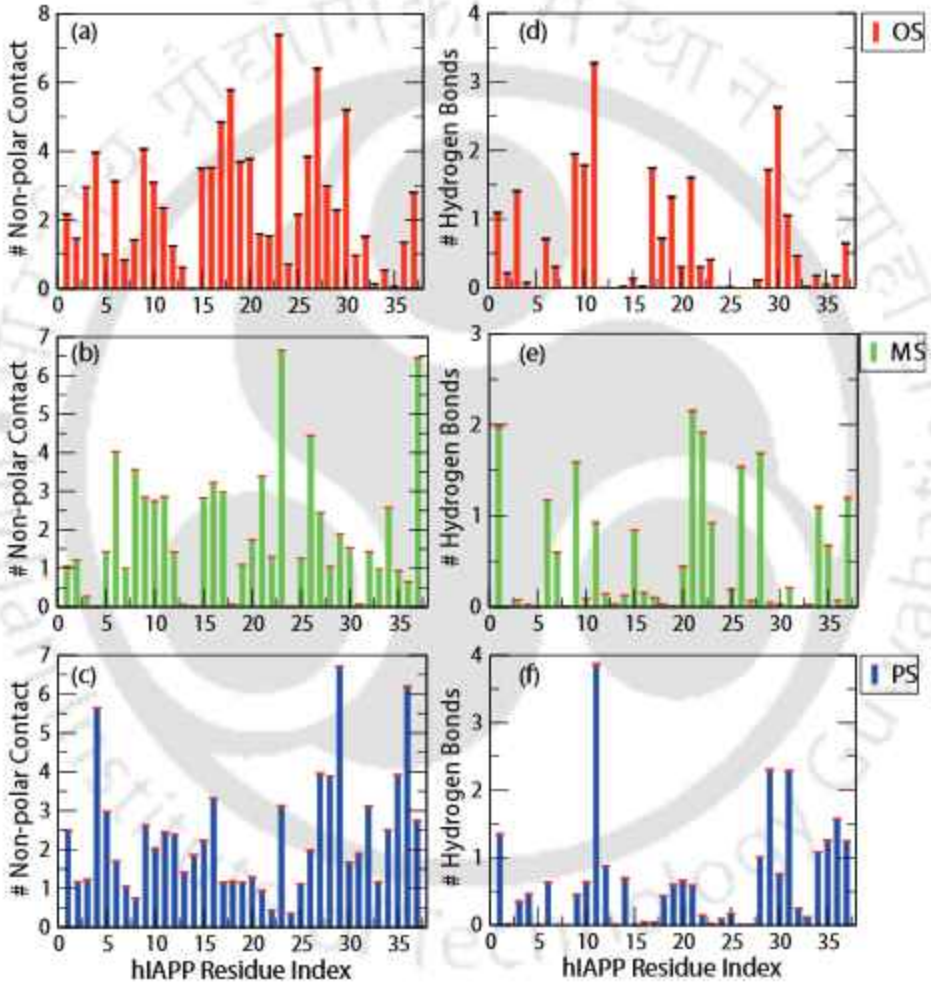

Figure 4.52: *Average (a-c) non-polar contact and (d-f) hydrogen bond number between single substituted β (OS), γ (MS) and δ (PS) BSBHps and each residue of hIAPP. The last 200 ns of simulation of the two replicates is used for analyzing each system.*

The primary factors which drive the interaction of amyloid peptides with their inhibitors are hydrophobic interactions and hydrogen bonding between them. To account for this, we have calculated the number of non-polar contacts and hydrogen bonds formed

between the hIAPP residues and the different BSBHps (Figs 4.52 and 4.53). Maximum non-polar contact is observed with the following hIAPP residues in the respective systems:

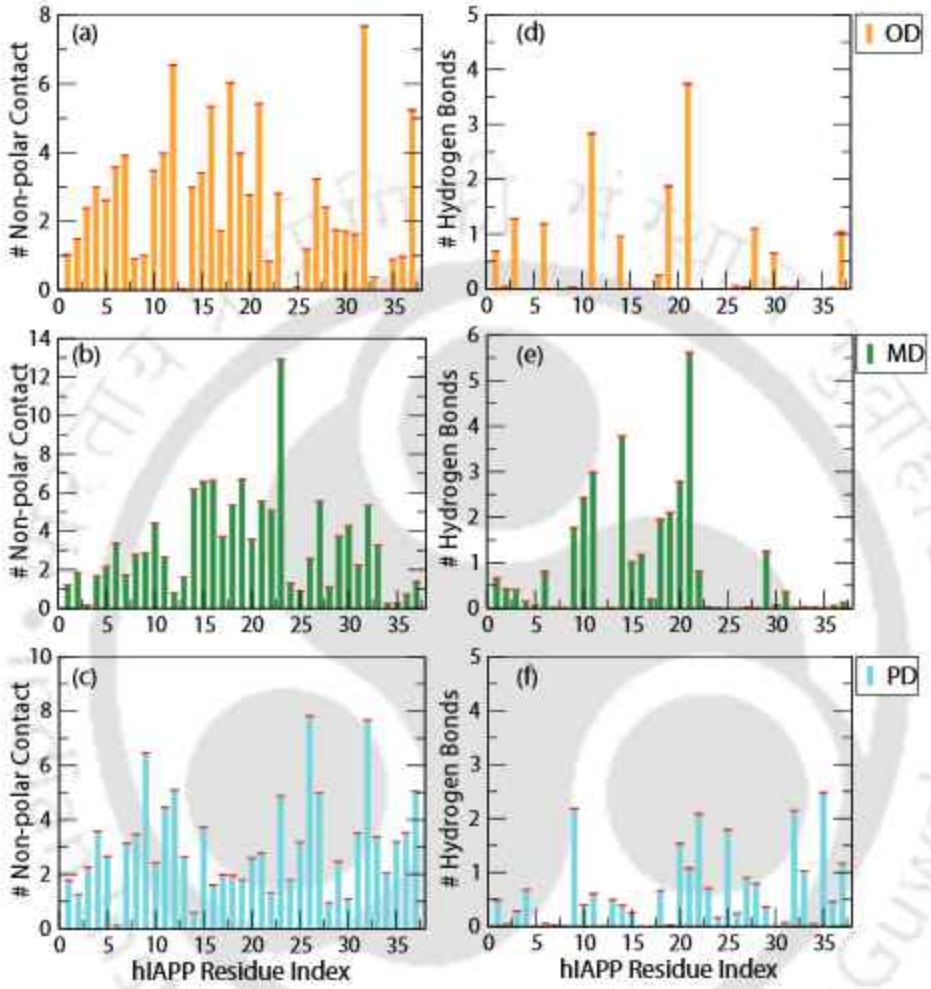

Figure 4.53: *Average (a-c) non-polar contact and (d-f) hydrogen bond number between double substituted β (OD), γ (MD) and δ (PD) BSBHps and each residue of hIAPP. The last 200 ns of simulation of the two replicates is used for analyzing each system.*

Asn3, Thr4, Thr6, Thr9, Gln10, Phe15-Ser20, Phe23, ILe26-Ser28, Thr30 in single substituted β-BSBHps system (Fig 4.52a), Thr6, Ala8-Arg11, Phe15-Val17, Asn21, Phe23, ILe26 and Tyr37 in single substituted γ-BSBHps system (Fig 4.52b), Thr4, Ala5, Leu16, Phe23, Leu27-Ser29, Val32 and Asn35-Tyr37 in single substituted δ-BSBHps system (Fig 4.52c), Thr4, Thr6, Cys7, Gln10-Leu12, Asn14-Leu16, His18-Asn21, Phe23, Leu27, Gly33, Tyr37 in double substituted β-BSBHps system (Fig 4.53a), Thr6, Ala8-Arg11, Asn14-Phe23, Leu27, Ser29, Thr30, Val32, Gly33 in double substituted γ-BSBHps system (Fig

4.53b), and Thr4, Cys7-Thr9, Arg11, Leu12, Phe15, Phe23, Ala25-Leu27, Asn31-Gly33 and Asn35-Tyr37 in double substituted δ-BSBHps system (Fig 4.53c).

The average number of hydrogen bonds formed by each BSBHps with hIAPP is shown in Table 4.9. A detailed look into the residue wise hydrogen bond of hIAPP with the BSBHps reveals that Lys1, Asn3, Thr9-Arg11, Val17, Ser19, Asn21 and Ser29-Asn31 in single substituted β-BSBHps system (Fig 4.52d), Lys1, Thr6, Thr9, Arg11, Asn21-Phe23, ILe26, Ser28, Ser34, Tyr37 in single substituted γ-BSBHps system (Fig 4.52e), Lys1, Arg11, Ser28-Asn31, Ser34-Tyr37 in single substituted δ-BSBHps system (Fig 4.52f),

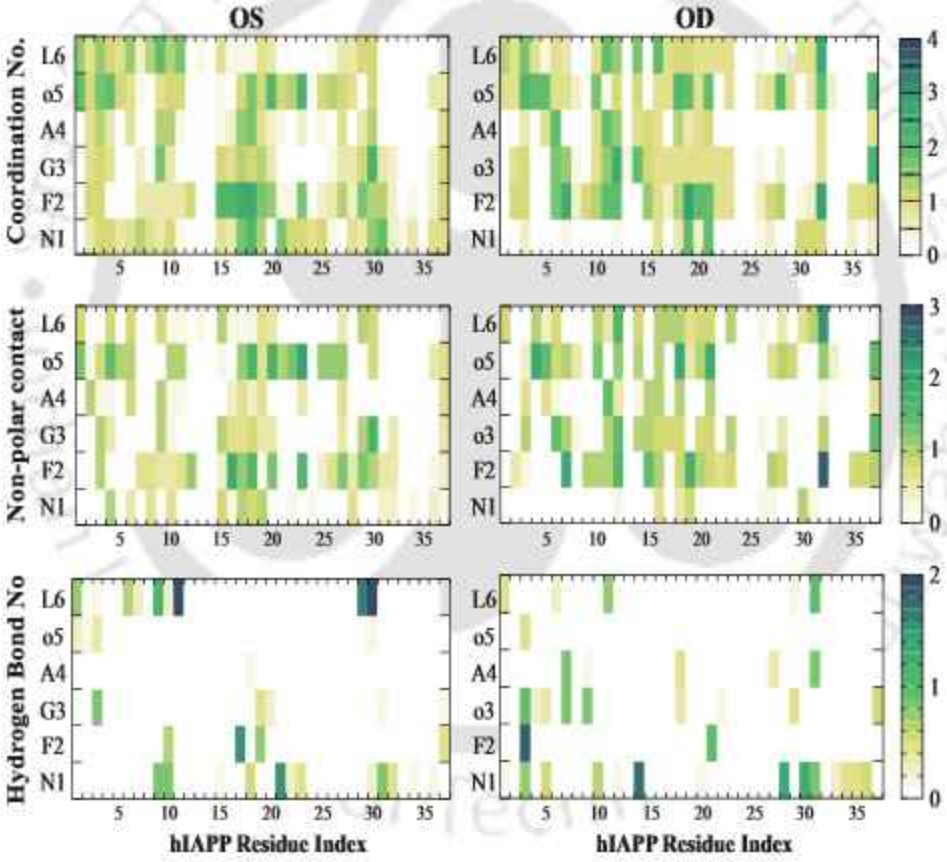

Figure 4.54: *Coordination number, non-polar contact and hydrogen bond number between each residue of hIAPP and that of BSBHps for the single (OS) and double (OD) substituted β-BSBHps containing systems. The last 200 ns of simulation of the two replicates is used for analyzing each system.*

Asn3, Thr6, Arg11, Asn14, Asn31, Ser19, Asn21, Ser28, Tyr37 in double substituted β-BSBHps system (Fig 4.53d), Thr9-Arg11, Asn14-Leu16, His18-Asn22, Ser29 in double sub-

stituted γ-BSBHps system (Fig 4.53e) and Thr9, Ser20-Asn22, Ala25, Val32, Gly33, Asn35 Tyr37 in double substituted δ-BSBHps system (Fig 4.53f) forms the highest number of hydrogen bonds with the corresponding BSBHps.

For a more detailed inspection, the interaction between each residue of hIAPP with that of the various BSBHps have also been investigated. The residues of hIAPP and BSBHps are represented by the three and one letter codes of amino acids respectively. Also, ortho, meta and para-Abz is indicated by 'o', 'm' and 'p' letters. Considering the system containing single substituted β-BSBHps (Fig 4.54), F2 and o5 of single substituted BSBHp have the most frequent contact with the hIAPP residues followed by L6 and N1. N1 and F2 in the N-terminal end of the BSBHps mostly interact with the Phe15-Asn21 of hIAPP, while o5 and L6 have more association to the N-terminal end of hIAPP.

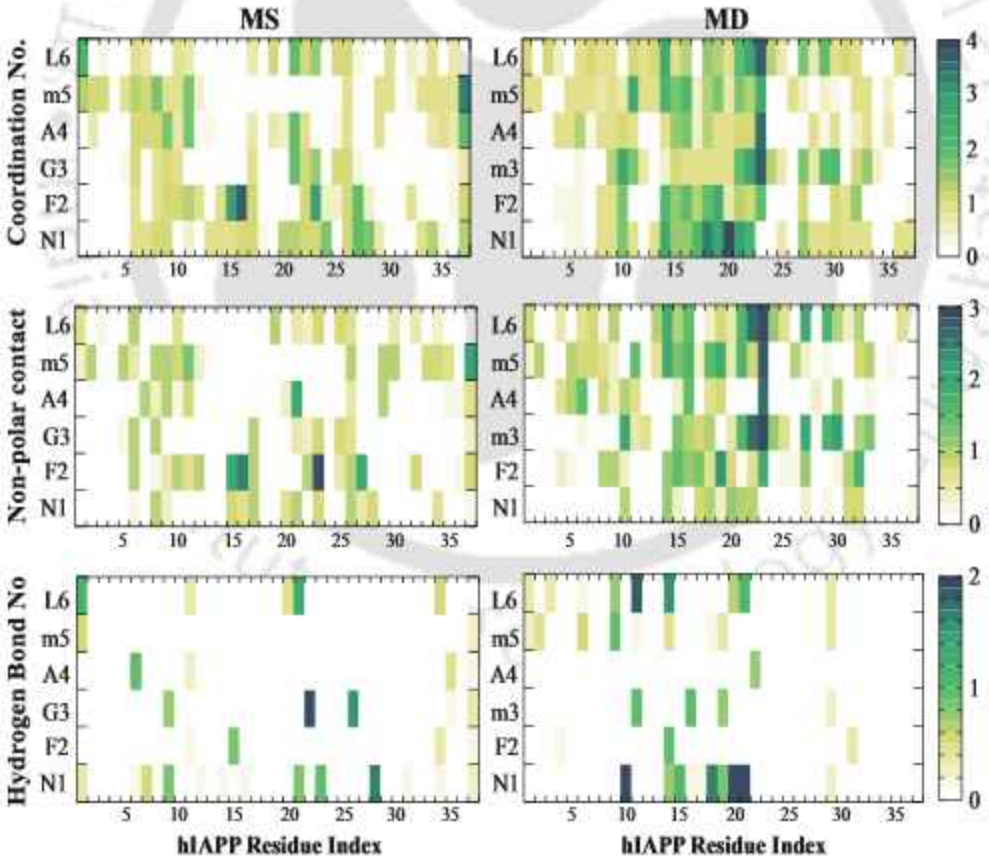

Figure 4.55: *Coordination number, non-polar contact and hydrogen bond number between each residue of hIAPP and that of BSBHps for the single (MS) and double (MD) substituted γ-BSBHps containing systems. The last 200 ns of simulation of the two replicates is used for analyzing each system.*

Now, in presence of double substituted β-BSBHps (Fig 4.54), also F2 and o5 mostly dominate the interaction between the BSBHps and the N-terminal stretch of hIAPP. In addition, the other hydrophobic residues in the BSBHps, such as o3, A4 and L6 also display significant contact.

The interaction propensity of γ-BSBHps with hIAPP is dispersed in the N-terminal region of hIAPP, with comparatively higher around Ala8-Arg11, Phe15, Leu16, Ser20-Gly24 (Fig 4.55). Among the residues of BSBHps, here also, the aromatic F2 display most frequent contact, while N1, A4, o5, L6 also possess abundant contacts. The contact frequency of the double substituted BSBHps is more pronounced than the single substituted peptides (Fig 4.55). The terminal residues of the BSBHp, N1, F2, m5, L6 have the highest contact propensity followed by remaining inner core residues with Asn14-Phe23 of hIAPP.

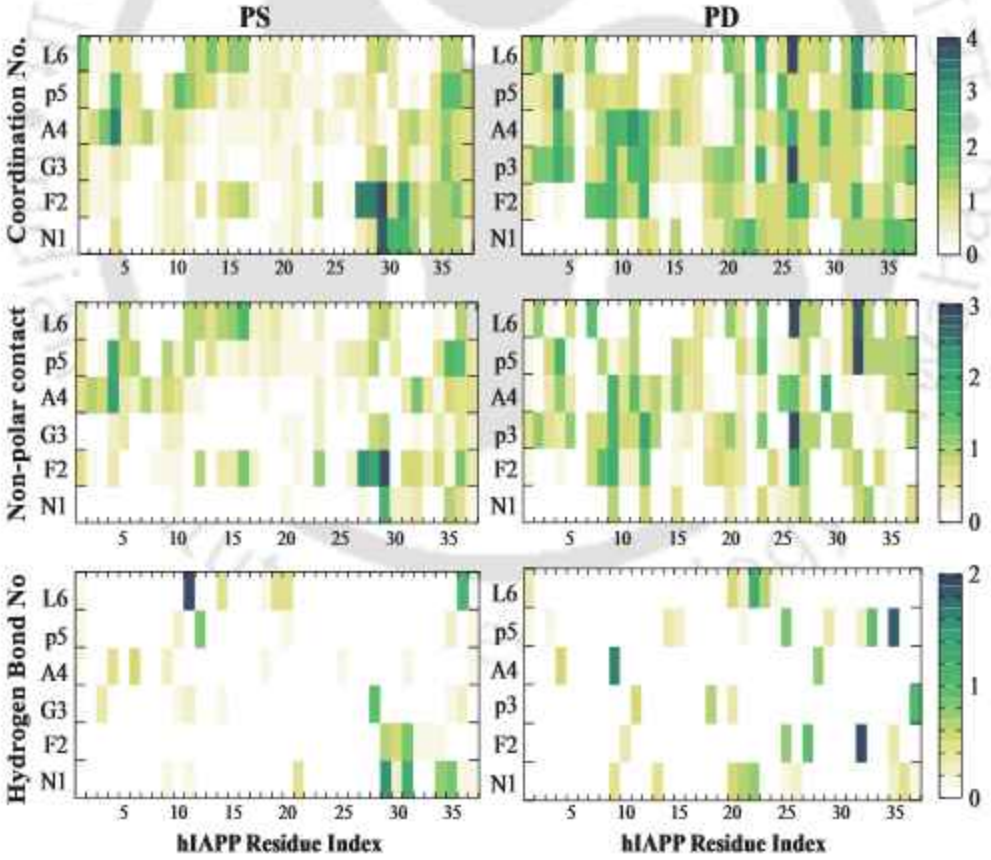

Figure 4.56: *Coordination number, non-polar contact and hydrogen bond number between each residue of hIAPP and that of BSBHps for the single (PS) and double (PD) substituted δ-BSBHps containing systems. The last 200 ns of simulation of the two replicates is used for analyzing each system.*

The δ-BSBHps, on the other hand, binds to hIAPP in a considerably different fashion. The single substituted δ-BSBHp favorably interacts with the C-terminal of hIAPP, via mostly N1, F2 and L6 residues (Fig 4.56). The hIAPP-BSBHps interaction is dominated by F2, p3, A4 and p5 residues of double substituted δ-BSBHp (Fig 4.56), which preferentially interact with the amyloid prone region of hIAPP, Ser19-Ser29. Further a secondary interaction hotspot also exist in the N-terminal region of hIAPP. All these interactions are guided by hydrophobic interactions and hydrogen bonding which are also analyzed in detail (Figs 4.54, 4.55 and 4.56).

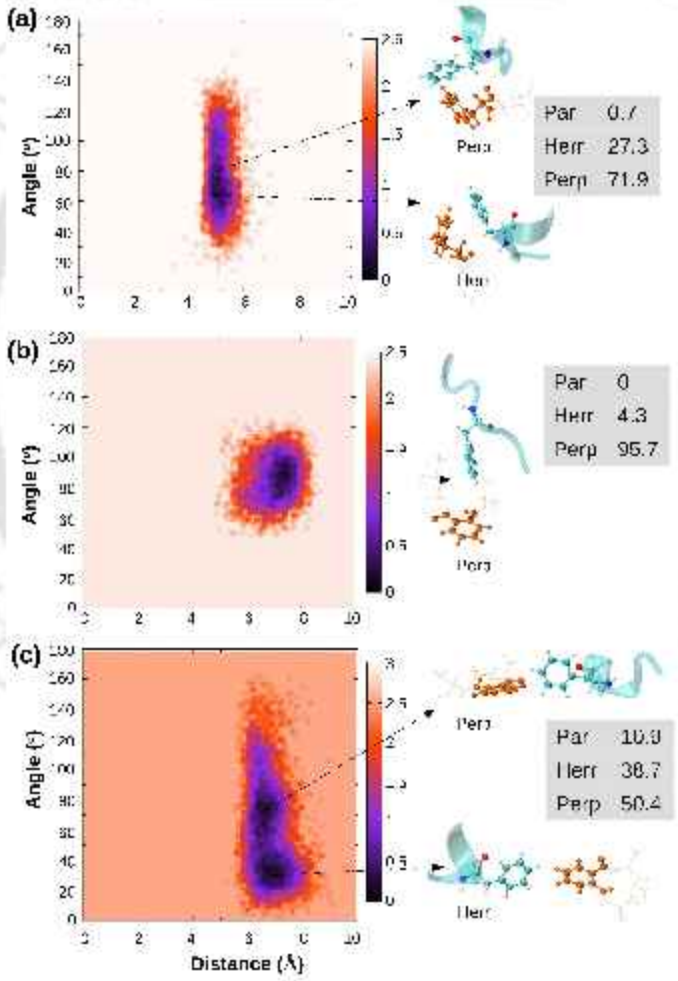

Figure 4.57: *Stacking orientation of (a) Phe23 (hIAPP)-F2 (BSBHp), (b) Phe15 (hIAPP)-o5 (BSBHp) and (c) Phe23 (hIAPP)-o5 (BSBHp) in presence of single substituted β-BSBHps. The hIAPP and the β-BSBHp residues are depicted in cyan and orange respectively. The probabilities of the parallel (Par), herringbone (Herr) and the perpendicular (Perp) are also provided. The last 200 ns of simulation of the two replicates is used for analyzing each system.*

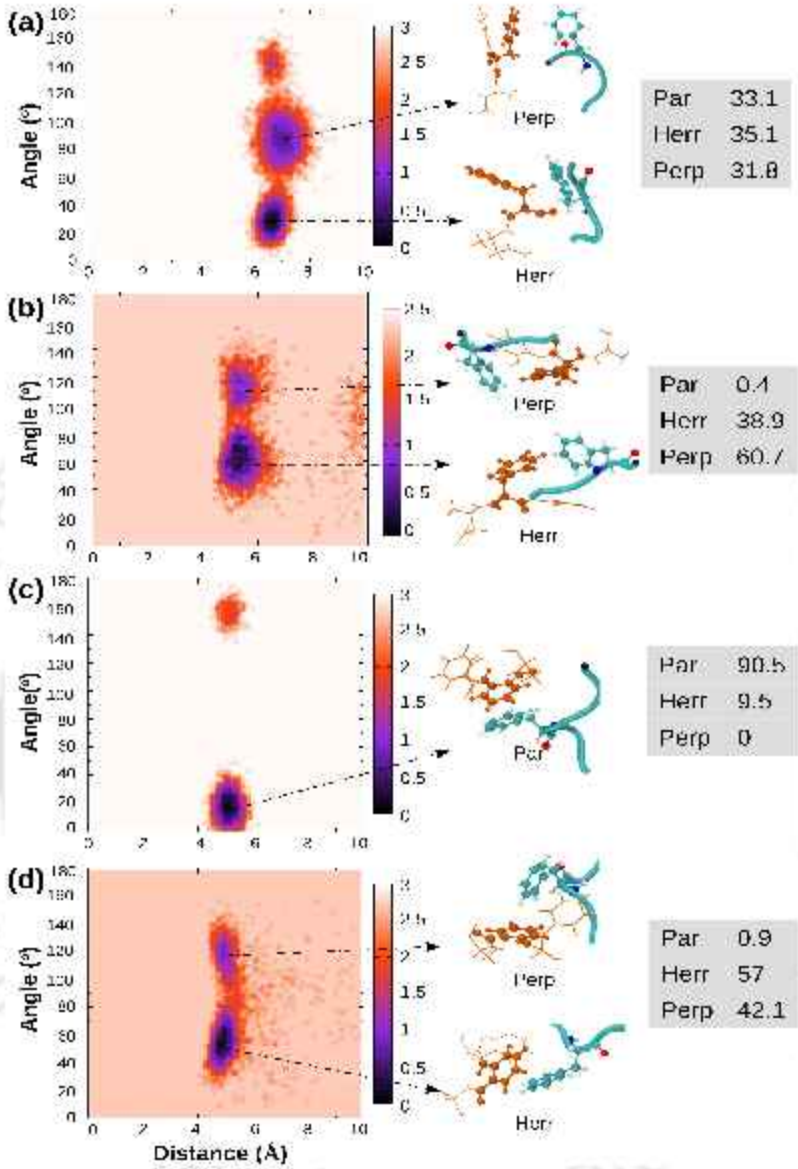

Figure 4.58: *Stacking orientation of (a) Phe15 (hIAPP)-F2 (BSBHp), (b) Phe23 (hIAPP)-F2 (BSBHp), (c) Phe15 (hIAPP)-o3 (BSBHp) and (d) Phe23 (hIAPP)-o3 (BSBHp) in presence of double substituted β-BSBHps. The hIAPP and the β-BSBHp residues are depicted in cyan and orange respectively. The probabilities of the parallel (Par), herringbone (Herr) and the perpendicular (Perp) are also provided. The last 200 ns of simulation of the two replicates is used for analyzing each system.*

The aromatic amino acid residues in all the different BSBHps, i.e., F2 and Abz moieties has the most favorable binding energy with hIAPP, closely followed by L6 residue (Figs

4.50d-f and 4.51d-f).

The interaction between Phe23 residues aids in the oligomerization of hIAPP and, hence, contact between this residue and inhibitors is crucial for β-sheet reduction[46]. Therefore, the aromatic stacking pattern between the aromatic ring of F2 and that of the aminobenzoic acid (Abz) residues in the BSBHps with that of Phe15 and Phe23 residues of hIAPP is further investigated (Fig 1.6a). In Fig 4.57, we observe that perpendicular π-π stacking is most dominant in all stacking pairs for the system containing single substituted β-BSBHps. On the other hand, all three types of arrangement is observed in the double substituted β-BSBHps system (Fig 4.58). F2 of single substituted γ-BSBHp is favorable to parallel stacking with both Phe15 and Phe23 of hIAPP (Fig 4.59). In presence of double substituted γ-BSBHps also, all the different stacking arrangement are perceived (Fig 4.60). Further, among all the other systems, stacking probability is highest in this system. The herringbone and perpendicular stacking is most favorable in single (Fig 4.61) and double (Fig 4.62) substituted δ-BSBHps systems respectively.

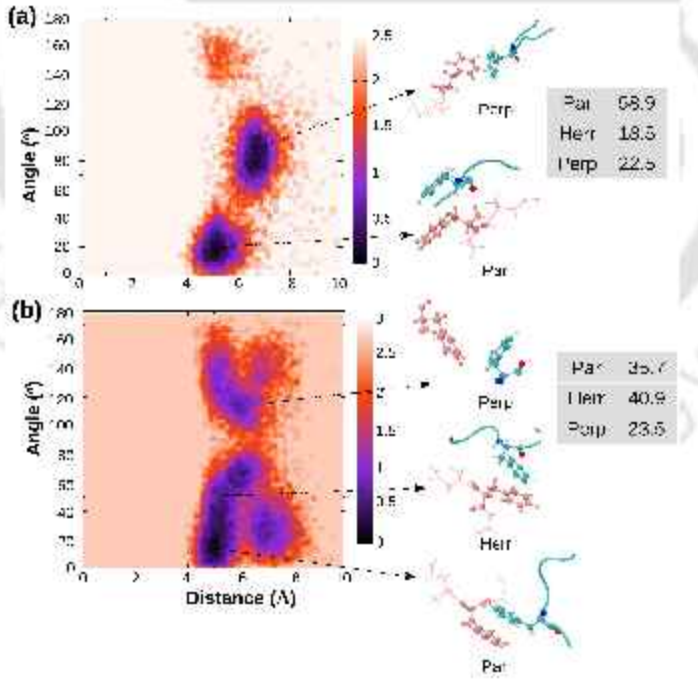

Figure 4.59: *Stacking orientation of (a) Phe15 (hIAPP)-F2 (BSBHp) and (b) Phe23 (hIAPP)-F2 (BSBHp) in presence of single substituted γ-BSBHps. The hIAPP and the γ-BSBHp residues are depicted in cyan and pink respectively. The probabilities of the parallel (Par), herringbone (Herr) and the perpendicular (Perp) are also provided. The last 200 ns of simulation of the two replicates is used for analyzing each system.*

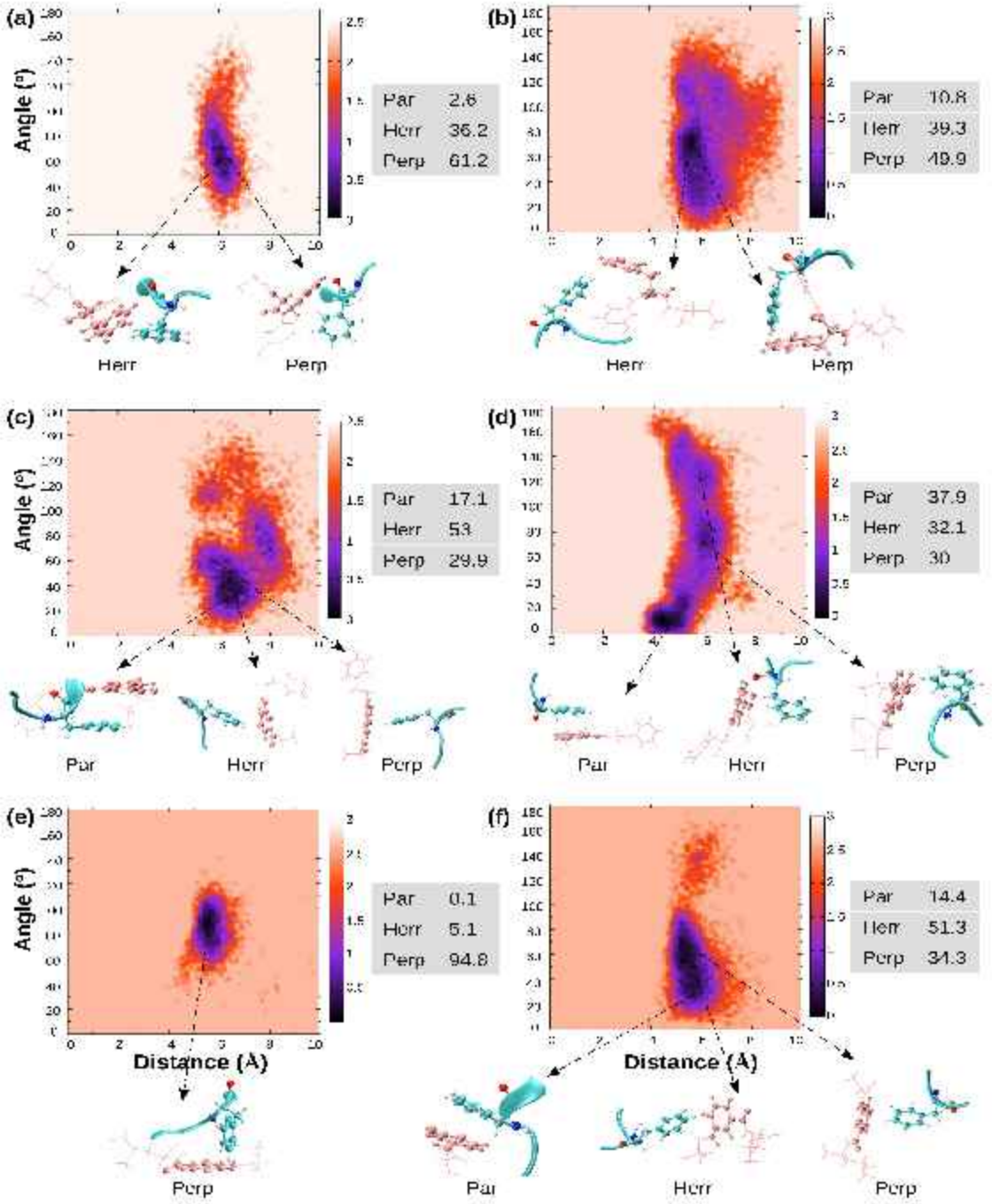

Figure 4.60: *Stacking orientation of (a) Phe15 (hIAPP)-F2 (BSBHp), (b) Phe23 (hIAPP)-F2 (BSBHp), (c) Phe15 (hIAPP)-m3 (BSBHp), (d) Phe23 (hIAPP)-m3 (BSBHp), (e) Phe15 (hIAPP)-m5 (BSBHp) and (d) Phe23 (hIAPP)-m5 (BSBHp) in presence of double substituted γ-BSBHps. The hIAPP and the γ-BSBHp residues are depicted in cyan and pink respectively. The probabilities of the parallel (Par), herringbone (Herr) and the perpendicular (Perp) are also provided. The last 200 ns of simulation of the two replicates is used for analyzing each system.*

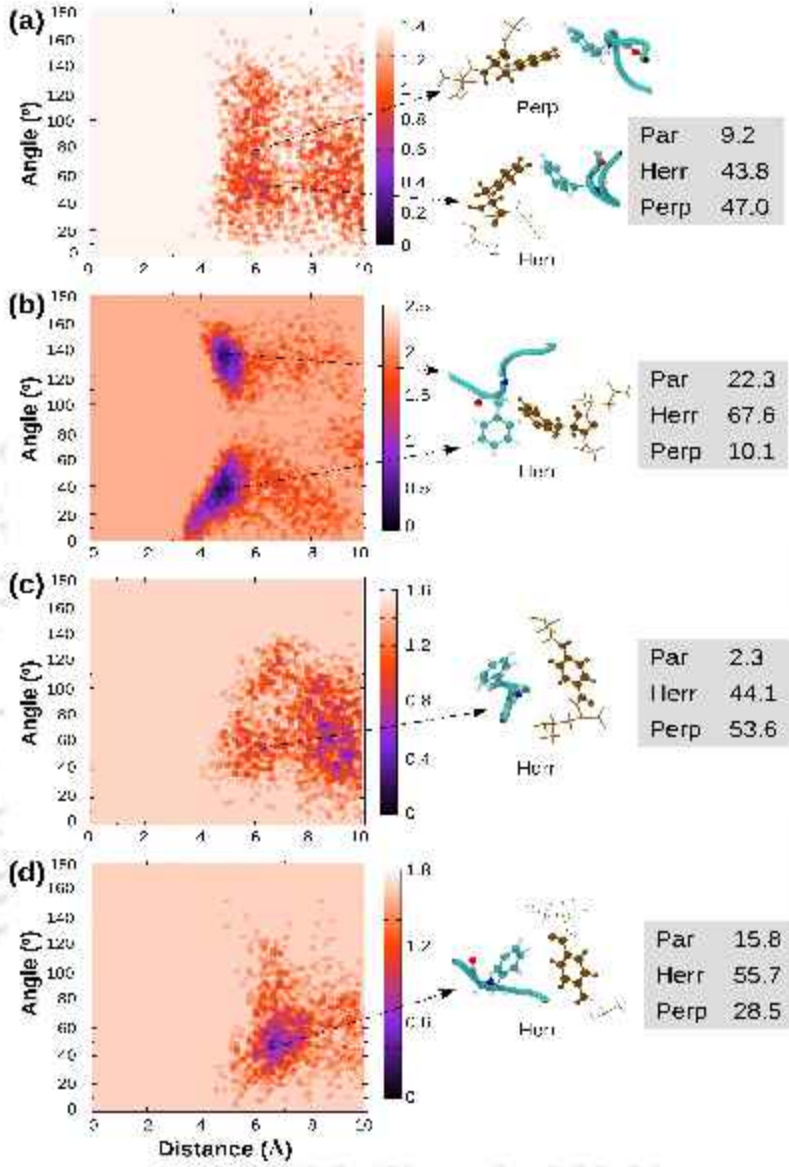

Figure 4.61: *Stacking orientation of (a) Phe15 (hIAPP)-F2 (BSBHp), (b) Phe23 (hIAPP)-F2 (BSBHp), (c) Phe15 (hIAPP)-p5 (BSBHp) and (d) Phe23 (hIAPP)-p5 (BSBHp) in presence of single substituted δ-BSBHps. The hIAPP and the δ-BSBHp residues are depicted in cyan and ochre respectively. The probabilities of the parallel (Par), herringbone (Herr) and the perpendicular (Perp) are also provided. The last 200 ns of simulation of the two replicates is used for analyzing each system.*

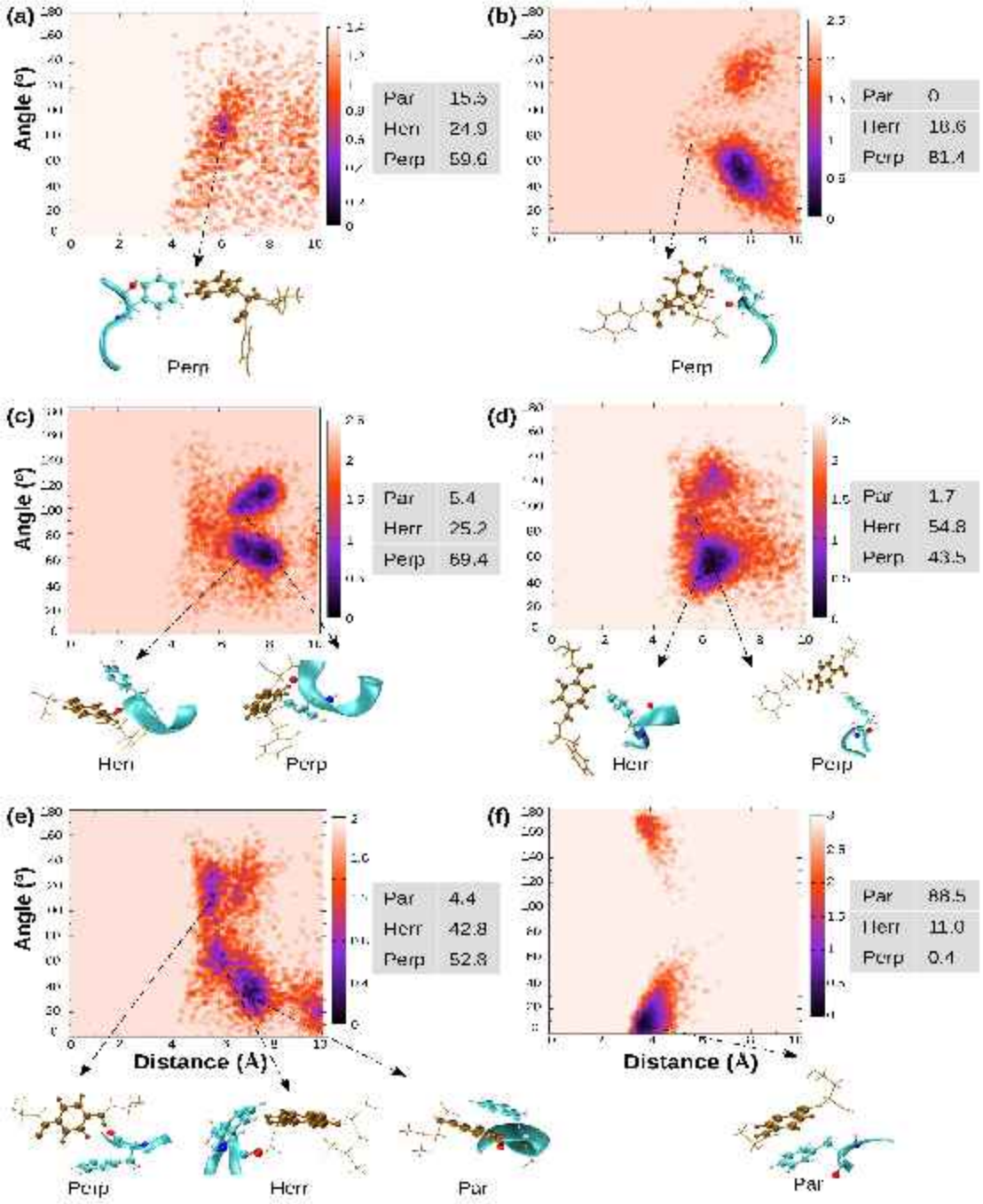

Figure 4.62: *Stacking orientation of (a) Phe15 (hIAPP)-F2 (BSBHp), (b) Phe23 (hIAPP)-F2 (BSBHp), (c) Phe15 (hIAPP)-p3 (BSBHp), (d) Phe23 (hIAPP)-p3 (BSBHp), (e) Phe15 (hIAPP)-p5 (BSBHp) and (d) Phe23 (hIAPP)-p5 (BSBHp) in presence of double substituted δ-BSBHps. The hIAPP and the δ-BSBHp residues are depicted in cyan and ochre respectively. The probabilities of the parallel (Par), herringbone (Herr) and the perpendicular (Perp) are also provided. The last 200 ns of simulation of the two replicates is used for analyzing each system.*

Due to the disordered structure of the β and γ-BSBHps, a variety of stacking arrangement is perceived in those systems. However, the planar arrangement of the δ-BSBHps favor specific orientation of π-π stacking. In addition, apart from the double substituted γ-BSBHps system, stacking between all possible aromatic pairs of BSBHps and hIAPP is only observed for the systems containing δ-BSBHps (which enhance hIAPP aggregation).

4.2.3.4 Interaction Mechanism of BSBHps with hIAPP

Assembling the results in the above section, we propose a mechanism via which the contrasting effect of the different BSBHps can be explained. The hIAPP monomer mostly remains in a random coil, disordered structure. However, the monomers aggregate to form an ordered, straight chain β-sheet conformation, which is favored by δ-BSBHps, but not by β and γ-BSBHps. The amine and carboxylic groups in ortho-aminobenzoic acid form an angle of 60°, hence the short hybrid peptides containing this moiety occupy a disordered conformation. The single substituted BSBHps attain a bend structure, while the double substituted peptides are present in a random, S-shaped structure (Fig 4.35b). These disordered, bend hybrid peptides easily bind to the disordered morphology of hIAPP, impeding their transition into ordered β-sheet structure (Figs 4.63 and 4.64). Hence, the interaction between the hIAPP monomers is interrupted by the binding of BSBHps to them. Similar phenomenon is observed for the systems containing γ-BSBHps, which guides the inhibitory action of these BSBHps on hIAPP aggregation (Figs 4.35b, 4.63 and 4.64). Now, in case of δ-BSBHps, the situation is vastly different. Here, due to the presence of 180° angle between the amino and carboxylic groups in para-aminobenzoic acid, the BSBHps can adapt into straight chain arrangement (Fig 4.35b). Hence these BSBHps can easily interact with the planar β-sheet arrangement of hIAPP, thus promoting hIAPP aggregation (Figs 4.63 and 4.64). The conformational difference of the isomeric BSBHps is validated by their R_g values (Table 4.11), where it is observed that the R_g of β and γ-BSBHps are much lower than that of the δ-BSBHps, validating the bend, compact structure of the former peptidomimetics, and an extended conformation for the latter (resulting in higher R_g). Experiments report that this planar conformation of δ-BSBHps also gives rise to β-sheet formation among themselves, which is not observed for β and γ-BSBHps, due to a kink in their peptide

backbone[30].

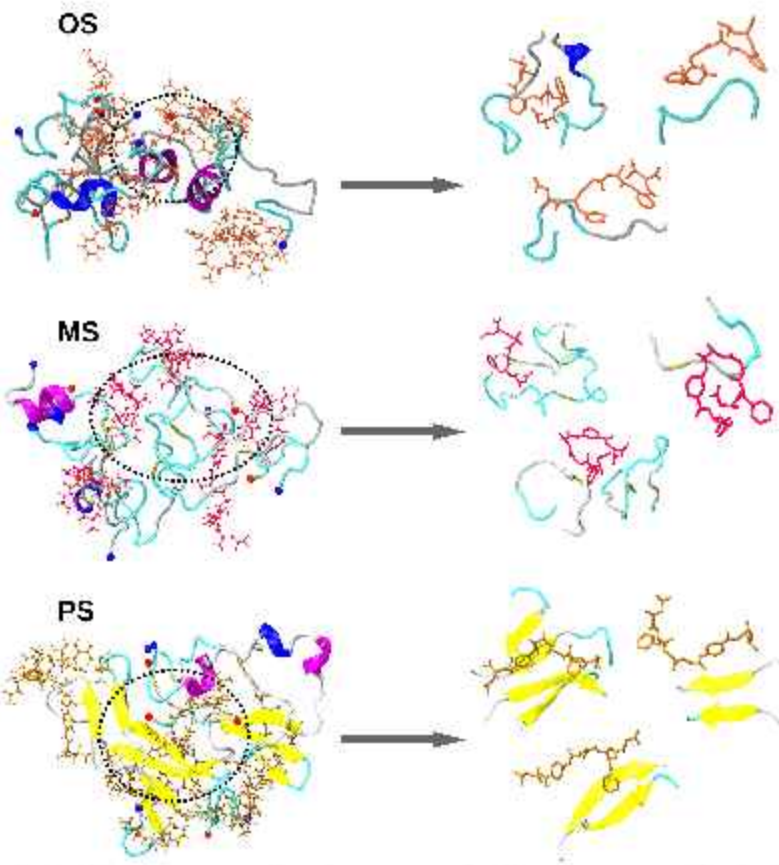

Figure 4.63: *Representative snapshots showing interactions between single β (OS), γ (MS) and δ (PS) substituted BSBHps and hIAPP. hIAPP is represented in cartoon form, depicting β-sheet in yellow, coil in silver, turn in cyan, α-helix in purple and 3_{10}-helix in blue. The β, γ and δ-BSBHps are depicted in orange, pink and ochre respectively. The β and γ-BSBHps attain a bend conformation and bind to disordered hIAPP conformation. The planar arrangement of δ-BSBHps interact with the planar β-sheet of hIAPP. The images on the right side of the arrow provide a closer look into the image on the left. The last 200 ns of simulation of the two replicates is used for analyzing each system.*

In addition, from the coordination number, hydrophobic contacts and hydrogen bond analyses, it can be concluded that the β and γ-BSBHps favorably interact with the N-terminal stretch of hIAPP, while δ-BSBHps prefer to bind with the C-terminal region. The double substituted δ-BSBHp specifically interacts with the amyloidogenic region of hIAPP, Ser20-Ser29, which substantiates the concept that the δ-BSBHps preferably attaches itself to the β-sheet prone region of hIAPP. This is further verified by the residue wise secondary

structure details of hIAPP monomers. In Fig 4.65a, it is observed that the residues Thr9-Leu16 in the N-terminal region and Asn22-Val32 in C-terminal region have the highest β-sheet percentage for the isolated hIAPP system. Similar β-sheet propensity is also noted for the δ-BSBHps containing systems (Fig 4.65b and c), verifying that the δ-BSBHps interact with β-sheet region of hIAPP, thus stabilizing it. The β-sheet percentage of hIAPP in presence of β and γ-BSBHps is negligible, conforming with the results from secondary structure analyses.

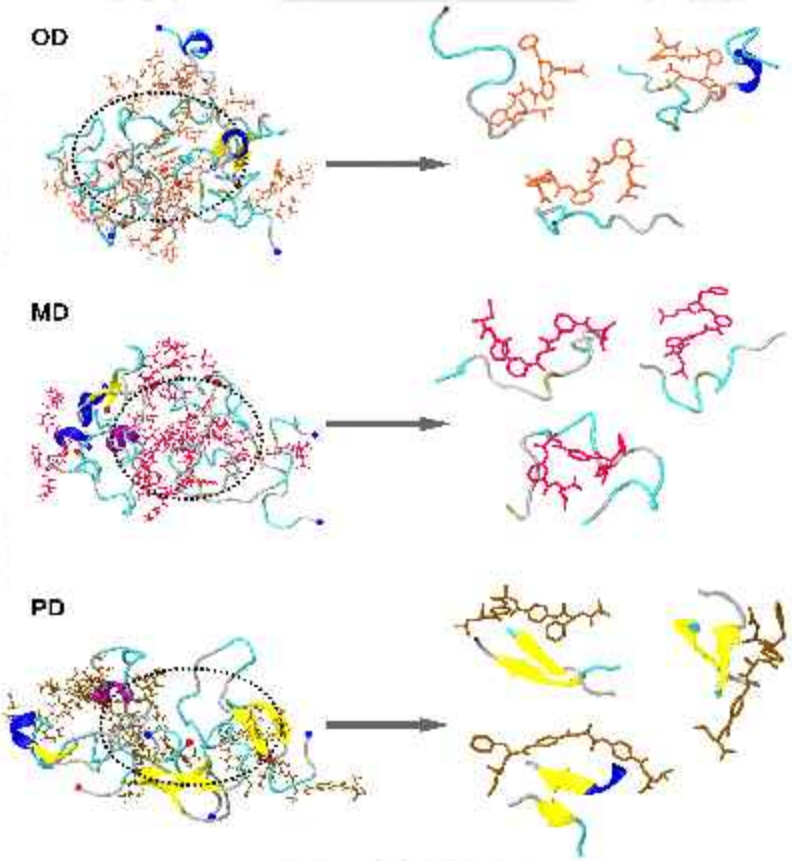

Figure 4.64: *Representative snapshots showing interactions between double substituted β (OD), γ (MD) and δ (PD) BSBHps and hIAPP. hIAPP is represented in cartoon form, depicting β-sheet in yellow, coil in silver, turn in cyan, α-helix in purple and 3_{10}-helix in blue. The β, γ and δ-BSBHps are depicted in orange, pink and ochre respectively. The β and γ-BSBHps attain a bend conformation and bind to disordered hIAPP conformation. The planar arrangement of δ-BSBHps interact with the planar β-sheet of hIAPP. The images on the right side of the arrow provide a closer look into the image on the left. The last 200 ns of simulation of the two replicates is used for analyzing each system.*

System	R_g (Å)
OS	4.48 ± 0.56
MS	4.77 ± 0.15
PS	5.91 ± 0.64
OD	4.58 ± 0.34
MD	5.59 ± 0.09
PD	7.87 ± 0.39

Table 4.11: *Radius of gyration (R_g) of β (OS/OD), γ (MS/MD) and δ BSBHps (PS/PD). The last 200 ns of simulation of the two replicates is used for analyzing each system.*

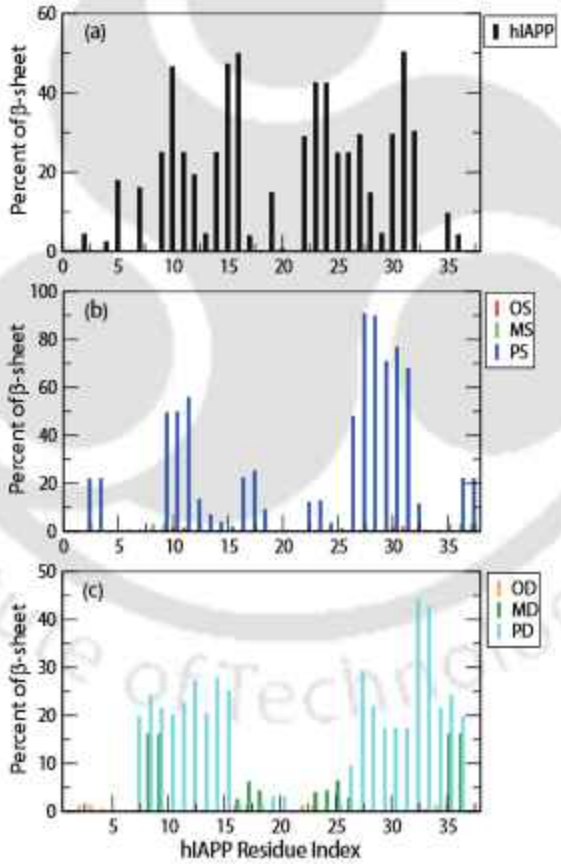

Figure 4.65: *Residue wise β-sheet percentage of hIAPP in (a) pure water (hIAPP) and in presence of (b) single substituted β (OS), γ (MS) and δ (PS) and (c) double substituted β (OD), γ (MD) and δ (PD) BSBHps. The last 200 ns of simulation of the two replicates is used for analyzing each system.*

4.2.4 Limitations

Since intrinsically disordered peptides lack well-defined three-dimensional structures, applying the appropriate force field is essential. Even though, the use of AMBER14SB has been validated to study amyloid peptides, this force field overestimate the CD-derived helical content in the peptide conformation[47]. In our study, the β-sheet percentage for hIAPP in absence of any inhibitors is 12.49%, which matches with the results (12.39%) of a previous simulation study carried out using CHARMM36[48] (another popular force field used for studying IDPs). However, due to the overestimation of helical content by AMBER, the helix percentage in our study (6.47%) is slightly higher than the one reported in the above study (0%)[48]. Also the effect of ions on the aggregation of hIAPP is not considered in this study. In addition, the experimental study on which our work is based on, have reported three hIAPP:BSBHps molar ratios (1:2, 1:5 and 1:10) at which the BSBHps affect hIAPP aggregation. We have considered only 1:2 molar ratios of hIAPP:BSBHps in our work so that we can effectively identify the detailed interactions between hIAPP and BSBHps residues, without the interference of extra BSBHps. However, the presence of higher concentrations of BSBHps might have an influence on their binding with hIAPP. Finally, the sampling deficiency in simulating disordered peptides is omnipresent and affect the structure and dynamics of the aggregation process. We have tried to address this problem by repeating each simulation with different initial configuration, such that various aggregation pathway can be accessed. Nevertheless this issue can be overcome by performing multiple long simulations, which is computationally very expensive and also time consuming and hence, difficult to tackle.

4.2.5 Conclusion

This work focuses on the inhibitory ability of a class of β-sheet breaker hybrid peptidomimetics (BSBHps) on the aggregation of hIAPP. The BSBHps consists of a small peptide sequence derived from the amyloidogenic core of hIAPP ($N_{22}FGAIL_{27}$) with three different isomers of aminobenzoic acid (Abz), i.e., β, γ and δ-Abz, inserted into them. In our molecular dynamics simulations, we observed that the β-sheet rich structure, which is formed by hIAPP in pure water, is absent in presence of β and γ-Abz containing BSBHps. The δ-BSBHps, on the other hand, favor the hIAPP-hIAPP interactions and stabilize ag-

gregated structure of hIAPP. Hence the β and γ-BSBHps can effectively act as inhibitors of hIAPP aggregation, unlike δ-BSBHps, which closely corroborate with the experimental results[30]. The disparity in the inhibitory ability of the β and γ-BSBHps with that of the δ-BSBHps is attributed to the variation in the angle formed by the amino and carboxyl groups in Abz moiety. This causes a significant difference in the orientation of the BSBHps, and, hence, the individual BSBHps prefer to align themselves to distinct conformations of hIAPP and display variational effect on hIAPP aggregation. The β and γ-BSBHps interacts with the disordered hIAPP structures, while δ-BSBHps preferably binds to the amyloid prone region of hIAPP and interacts with its β-sheet conformation. Also, the BSBHps with two breaker elements (Abz) display greater interaction with hIAPP than the BSBHps with one Abz group. This further validates the reports asserting that the former BSBHps are more efficient in their inhibitory ability against hIAPP aggregation[30]. The hydrogen bonding, hydrophobic and stacking interactions drive the binding of BSBHps to hIAPP. The interactions between the aromatic moieties of BSBHps and hIAPP play a pivotal role in their binding. The planar structure of δ-BSBHps offers a specific type stacking arrangement with Abz/Phe of BSBHps and Phe residues of hIAPP, which stabilize β-sheet of hIAPP. However, the β and γ-BSBHps are more receptive to different types of arrangement (parallel, perpendicular and herringbone), due to their bend backbone, further signifying their disordered binding alignment. Hence the conformation attained by BSBHps guides the pathway of their interaction with hIAPP, and thus their inhibitory ability. The use of conformationally restricted peptides for the inhibition of hIAPP aggregation has produced excellent results[49, 50], which led to the clinical trials of some of these peptides as drug candidates against T2D[51]. In addition, the non-proteinogenic nature of Abz adds to the stability of BSBHps, in presence of proteolytic enzymes[30]. Hence, our study provides key information which might be helpful in the drug design with better pharmacodynamic and pharmakinetic profile against type II diabetes and other amyloidoses.

References

[1] Tang, Y.; Zhang, D.; Zhang, Y.; Liu, Y.; Gong, X.; Chang, Y.; Ren, B.; Zheng, J. Introduction and Fundamentals of Human Islet Amyloid Polypeptide Inhibitors. *ACS Appl. Bio Mater.* **2020**, *3*, 8286–8308.

[2] Chalifour, R. J.; McLaughlin, R. W.; Lavoie, L.; Morissette, C.; Tremblay, N.; Boulé, M.; Sarazin, P.; Stéa, D.; Lacombe, D.; Tremblay, P. et al. Stereoselective Interactions of Peptide Inhibitors with the β-Amyloid Peptide. *J. Biol. Chem.* **2003**, *278*, 34874–34881.

[3] Warso, M. A.; Richards, J. M.; Mehta, D.; Christov, K.; Schaeffer, C.; Bressler, L. R.; Yamada, T.; Majumdar, D.; Kennedy, S. A.; Beattie, C. W. et al. A first-in-class, first-in-human, phase I trial of p28, a non-HDM2-mediated peptide inhibitor of p53 ubiquitination in patients with advanced solid tumours. *Br. J. Cancer* **2013**, *108*, 1061–1070.

[4] Huggins, K. N. L.; Bisaglia, M.; Bubacco, L.; Tatarek-Nossol, M.; Kapurniotu, A.; Andersen, N. H. Designed Hairpin Peptides Interfere with Amyloidogenesis Pathways: Fibril Formation and Cytotoxicity Inhibition, Interception of the Preamyloid State. *Biochemistry* **2011**, *50*, 8202–8212.

[5] Maris, N. L.; Shea, D.; Bleem, A.; Bryers, J. D.; Daggett, V. Chemical and Physical Variability in Structural Isomers of an l/d α-Sheet Peptide Designed To Inhibit Amyloidogenesis. *Biochemistry* **2017**, *57*, 507–510.

[6] Kellock, J.; Hopping, G.; Caughey, B.; Daggett, V. Peptides Composed of Alternating L- and D-Amino Acids Inhibit Amyloidogenesis in Three Distinct Amyloid Systems Independent of Sequence. *J. Mol. Biol.* **2016**, *428*, 2317–2328.

[7] Wiesehan, K.; Buder, K.; Linke, R. P.; Patt, S.; Stoldt, M.; Unger, E.; Schmitt, B.; Bucci, E.; Willbold, D. Selection of D-Amino-Acid Peptides That Bind to Alzheimer's Disease Amyloid Peptide Aβ142 by Mirror Image Phage Display. *ChemBioChem* **2003**, *4*, 748–753.

[8] van Groen, T.; Wiesehan, K.; Funke, S.; Kadish, I.; Nagel-Steger, L.; Willbold, D. Reduction of Alzheimer's Disease Amyloid Plaque Load in Transgenic Mice by D3, a D-Enantiomeric Peptide Identified by Mirror Image Phage Display. *ChemMedChem* **2008**, *3*, 1848–1852.

[9] Funke, S. A.; van Groen, T.; Kadish, I.; Bartnik, D.; Nagel-Steger, L.; Brener, O.; Sehl, T.; Batra-Safferling, R.; Moriscot, C.; Schoehn, G. et al. Oral Treatment with the d-Enantiomeric Peptide D3 Improves the Pathology and Behavior of Alzheimer's Disease Transgenic Mice. *ACS Chem. Neurosci.* **2010**, *1*, 639–648.

[10] Xi, W.; Hansmann, U. H. E. The effect of retro-inverse D-amino acid Aβ-peptides on Aβ-fibril formation. *J. Chem. Phys.* **2019**, *150*, 095101.

[11] Pandey, P.; Nguyen, N.; Hansmann, U. H. d-Retro Inverso Amylin and the Stability of Amylin Fibrils. *J. Chem. Theory Comput.* **2020**, *16*, 5358–5368.

[12] Tenidis, K.; Waldner, M.; Bernhagen, J.; Fischle, W.; Bergmann, M.; Weber, M.; Merkle, M. L.; Voelter, W.; Brunner, H.; Kapurniotu, A. Identification of a Penta- and Hexapeptide of Islet Amyloid Polypeptide (IAPP) with Amyloidogenic and Cytotoxic Properties. *J. Mol. Biol.* **2000**, *295*, 1055–1071.

[13] Melquiond, A.; Gelly, J. C.; Mousseau, N.; Derreumaux, P. Probing Amyloid Fibril Formation of the NFGAIL peptide by Computer Simulations. *J. Chem. Phys* **2007**, *126*, 065101.

[14] Mo, Y.; Lu, Y.; Wei, G.; Derreumaux, P. Structural Diversity of the Soluble Trimers of the Human Amylin(20–29) Peptide revealed by Molecular Dynamics Simulations. *J. Chem. Phys* **2009**, *130*, 125101.

[15] Wang, L.; Lei, L.; Li, Y.; Wang, L.; Li, F. A hIAPP-derived all-d-amino-acid inhibits hIAPP fibrillation efficiently at membrane surface by targeting α-helical oligomeric intermediates. *FEBS Lett.* **2014**, *588*, 884–891.

[16] Soriaga, A. B.; Sangwan, S.; Macdonald, R.; Sawaya, M. R.; Eisenberg, D. Crystal Structures of IAPP Amyloidogenic Segments Reveal a Novel Packing Motif of Out-of-Register Beta Sheets. *J. Phys. Chem. B* **2016**, *120*, 5810–5816.

[17] Roy, R.; Paul, S. Potential of ATP toward Prevention of hIAPP Oligomerization and Destabilization of hIAPP Protofibrils: An In Silico Perspective. *J. Phys. Chem. B* **2021**, *125*, 3510–3526.

[18] Giri, R. S.; Pal, S.; Roy, S.; Dolai, G.; Manne, S. R.; Paul, S.; Mandal, B. Nanostructures from protected L/L and D/L amino acid containing dipeptides. *Pept. Sci.* **2020**, *113*.

[19] Luca, S.; Yau, W. M.; Leapman, R.; Tycko, R. Peptide Conformation and Supramolecular Organization in Amylin Fibrils: Constraints from Solid-State NMR. *Biochemistry* **2007**, *46*, 13505–13522.

[20] Nielsen, J.; Bjerring, M.; Jeppesen, M.; Pedersen, R.; Pedersen, J.; Hein, K.; Vosegaard, T.; Skrydstrup, T.; Otzen, D.; Nielsen, N. Unique Identification of Supramolecular Structures in Amyloid Fibrils by Solid-State NMR Spectroscopy. *Angew. Chem. Int. Ed.* **2009**, *48*, 2118–2121.

[21] Case, D. A. et al. *AMBER 2018.* University of California, San Francisco, 2018.

[22] Röder, C.; Kupreichyk, T.; Gremer, L.; Schäfer, L. U.; Pothula, K. R.; Ravelli, R. B. G.; Willbold, D.; Hoyer, W.; Schröder, G. F. Cryo-EM structure of islet amyloid polypeptide fibrils reveals similarities with amyloid-β fibrils. *Nat. Struct. Mol. Biol.* **2020**, *27*, 660–667.

[23] Pal, S.; Roy, R.; Paul, S. Potential of a Natural Deep Eutectic Solvent, Glyceline, in the Thermal Stability of the Trp-Cage Mini-protein. *J. Phys. Chem. B* **2020**, *124*, 7598–7610.

[24] Torrie, G.; Valleau, J. Nonphysical Sampling Distributions in Monte Carlo Free-Energy Estimation: Umbrella sampling. *J. Comput. Phys.* **1977**, *23*, 187–199.

[25] Kumar, S.; Rosenberg, J. M.; Bouzida, D.; Swendsen, R. H.; Kollman, P. A. The Weighted Histogram Analysis Method for Free-Energy Calculations on Biomolecules. I. The method. *J. Comput. Chem* **1992**, *13*, 1011–1021.

[26] Grossfield, A. WHAM: The Weighted Histogram Analysis Method, version 2.0.10.2, `http://membrane.urmc.rochester.edu/wordpress/?page_id=126` (accessed on July 27, 2021).

[27] Tu, L. H.; Raleigh, D. P. Role of Aromatic Interactions in Amyloid Formation by Islet Amyloid Polypeptide. *Biochemistry* **2013**, *52*, 333–342.

[28] Mo, Y.; Lei, J.; Sun, Y.; Zhang, Q.; Wei, G. Conformational Ensemble of hIAPP Dimer: Insight into the Molecular Mechanism by Which a Green Tea Extract Inhibits hIAPP Aggregation. *Sci. Rep.* **2016**, *6*, 33076.

[29] Saini, R. K.; Goyal, D.; Goyal, B. Targeting Human Islet Amyloid Polypeptide Aggregation and Toxicity in Type 2 Diabetes: An Overview of Peptide-Based Inhibitors. *Chem. Res. in Toxicol.* **2020**, *33*, 2719–2738.

[30] Paul, A.; Kalita, S.; Kalita, S.; Sukumar, P.; Mandal, B. Disaggregation of Amylin Aggregate by Novel Conformationally Restricted Aminobenzoic Acid containing α/β and α/γ Hybrid Peptidomimetics. *Sci. Rep.* **2017**, *7*, 40095.

[31] Simons, L. J.; Caprathe, B. W.; Callahan, M.; Graham, J. M.; Kimura, T.; Lai, Y.; LeVine, H.; Lipinski, W.; Sakkab, A. T.; Tasaki, Y., et al. The synthesis and structure–activity relationship of substituted N-phenyl anthranilic acid analogs as amyloid aggregation inhibitors. *Bioorganic Med. Chem. Lett.* **2009**, *19*, 654–657.

[32] Oza, V. B.; Petrassi, H.; Purkey, H. E.; Kelly, J. W. Synthesis and evaluation of anthranilic acid-based transthyretin amyloid fibril inhibitors. *Bioorganic Med. Chem. Lett.* **1999**, *9*, 1–6.

[33] Kapurniotu, A.; Schmauder, A.; Tenidis, K. Structure-Based Design and Study of Non-Amyloidogenic, Double N-methylated IAPP Amyloid Core Sequences as Inhibitors of IAPP Amyloid Formation and Cytotoxicity. *J. Mol. Biol.* **2002**, *315*, 339–350.

[34] Zhou, S.; Wang, Q.; Ren, M.; Zhang, A.; Liu, H.; Yao, X. Molecular Dynamics Simulation on the Inhibition Mechanism of Peptide-Based Inhibitor of Islet Amyloid

Polypeptide (IAPP) to Islet Amyloid Polypeptide ($IAPP_{22-28}$) Oligomers. *Chem. Biol. Drug. Des.* **2017**, *90*, 31–39.

[35] García-Viñuales, S.; Ilie, I. M.; Santoro, A. M.; Romanucci, V.; Zarrelli, A.; Fabio, G. D.; Caflisch, A.; Milardi, D. Silybins inhibit human IAPP amyloid growth and toxicity through stereospecific interactions. *Biochim. Biophys. Acta - Proteins Proteom.* **2022**, *1870*, 140772.

[36] Zhan, C.; Lao, Z.; Tang, Y.; Qiao, Q.; Wei, G. Natural stereoisomeric flavonoids exhibit different disruptive effects and the mechanism of action on $A\beta_{42}$ protofibril. *Chem. Commun.* **2021**, *57*, 4267–4270.

[37] Wang, F.; Becker, J. P.; Cieplak, P.; Dupradeau, F.-Y. R.E.D. Python: Object oriented programming for Amber force fields, Université de Picardie - Jules Verne, Sanford Burnham Prebys Medical Discovery Institute. **2013**.

[38] Dupradeau, F.-Y.; Pigache, A.; Zaffran, T.; Savineau, C.; Lelong, R.; Grivel, N.; Lelong, D.; Rosanski, W.; Cieplak, P. The R.E.D. tools: advances in RESP and ESP charge derivation and force field library building. *Phys. Chem. Chem. Phys.* **2010**, *12*, 7821–7839.

[39] Vanquelef, E.; Simon, S.; Marquant, G.; Garcia, E.; Klimerak, G.; Delepine, J. C.; Cieplak, P.; Dupradeau, F.-Y. R.E.D. Server: a web service for deriving RESP and ESP charges and building force field libraries for new molecules and molecular fragments. *Nucleic Acids Res.* **2011**, *39*, W511–W517.

[40] Frisch, M. J. et al. Gaussian˜09 Revision A.02. 2016; Gaussian Inc. Wallingford CT.

[41] Bayly, C. I.; Cieplak, P.; Cornell, W.; Kollman, P. A. A Well-Behaved Electrostatic Potential Based Method Using Charge Restraints for Deriving Atomic Charges: the RESP Model. *J. Phys. Chem.* **1993**, *97*, 10269–10280.

[42] Lao, Z.; Chen, Y.; Tang, Y.; Wei, G.; Molecular Dynamics Simulations Reveal the Inhibitory Mechanism of Dopamine Against Human Islet Amyloid Polypeptide (hIAPP) Aggregation and its Destabilization Effect on hIAPP Protofibrils. *ACS Chem. Neurosci.* **2019**, *10*, 4151–4159.

[43] Roy, R.; Paul, S. hIAPP-Amyloid-Core Derived d-Peptide Prevents hIAPP Aggregation and Destabilizes Its Protofibrils. *J. Phys. Chem. B* **2022**, *126*, 822–839.

[44] Buchanan, L. E.; Maj, M.; Dunkelberger, E. B.; Cheng, P.-N.; Nowick, J. S.; Zanni, M. T. Structural Polymorphs Suggest Competing Pathways for the Formation of Amyloid Fibrils That Diverge from a Common Intermediate Species. *Biochemistry* **2018**, *57*, 6470–6478.

[45] Dupuis, N. F.; Wu, C.; Shea, J.-E.; Bowers, M. T. Human Islet Amyloid Polypeptide Monomers Form Ordered β-hairpins: A Possible Direct Amyloidogenic Precursor. *J. Am. Chem. Soc.* **2009**, *131*, 18283–18292.

[46] King, K. M.; Bevan, D. R.; Brown, A. M. Molecular Dynamics Simulations Indicate Aromaticity as a Key Factor in the Inhibition of IAPP(20–29) Aggregation. *ACS Chem. Neurosci.* **2022**, *13*, 1615–1626.

[47] Man, V. H.; Nguyen, P. H.; Derreumaux, P. High-Resolution Structures of the Amyloid-β 1-42 Dimers from the Comparison of Four Atomistic Force Fields. *J. Phys. Chem. B* **2017**, *121*, 5977–5987.

[48] Paul, S.; Paul, S. Molecular Dynamics Simulation Study on the Inhibitory Effects of Choline-O-Sulfate on hIAPP Protofibrilation. *J. Comput. Chem.* **2019**, *40*, 1957–1968.

[49] Gilead, S.; Gazit, E. Inhibition of Amyloid Fibril Formation by Peptide Analogues Modified with α-Aminoisobutyric Acid. *Angew. Chem.* **2004**, *43*, 4041–4044.

[50] Mishra, A.; Misra, A.; Sri Vaishnavi, T.; Thota, C.; Gupta, M.; Ramakumar, S.; Chauhan, V. S. Conformationally Restricted Short Peptides Inhibit Human Islet Amyloid Polypeptide (hIAPP) Fibrillization. *Chem. Commun.* **2013**, *49*, 2688–2690.

[51] Wang, H.; Ridgway, Z.; Cao, P.; Ruzsicska, B.; Raleigh, D. P. Analysis of the Ability of Pramlintide To Inhibit Amyloid Formation by Human Islet Amyloid Polypeptide Reveals a Balance between Optimal Recognition and Reduced Amyloidogenicity. *Biochemistry* **2015**, *54*, 6704–6711.

Chapter 5

Inhibition of hIAPP Aggregation by Boron Nitride Nanomaterials

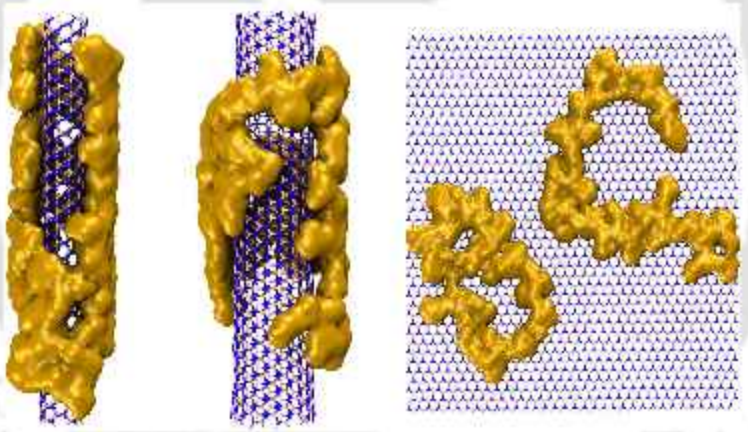

"Nanotechnology in medicine is going to have a major impact on the survival of the human race."

— Bernard Marcus

Overview

Nanoparticles, particularly carbon nanoparticles, have gathered significant interest in the field of anti-aggregation research. However, due to their cytotoxicity, the exploration of biocompatible nanoparticles has become a new frontier in the quest for drugs against human amyloid diseases. The application of non-cytotoxic and biocompatible boron nitride (BN) nanoparticles against amyloid aggregation has been probed to tackle this issue. BN nanoparticles have displayed inhibitory activity against the aggregation of Aβ and α-syn peptides. In this work, the effect of BN nanoparticles on the dimerization of hIAPP, which is associated with the pathogenesis of type 2 diabetes, is studied. BN nanoparticles prevent the misfolding of hIAPP into β-sheet rich aggregates. On varying the curvature, the nanoparticles display variation in the interaction preference with hIAPP. Interestingly, as the hydrophobicity of the nanoparticles increase from (5,5) BN nanotube to BN nanosheet, the interaction propensity shifts from N-terminal to the amyloid prone C-terminal of hIAPP. The hydrophobic and aromatic stacking interactions play a contributing factor towards the binding between hIAPP and BN. Due to this, the flat surface of the nanosheet shows better interaction potential towards hIAPP, compared to the nanotubes. Further, the nanoparticles can also disassemble preformed hIAPP fibrils and the effect is more pronounced for (5,5) nanotube and the nanosheet. This study provides an insight into the inhibitory mechanism of hIAPP aggregation by boron nitride nanoparticles and also an understanding of the significance of the curvature of nanoparticles in their interaction with amyloid peptides, which is valuable for the design of anti-amyloid drugs.

5.1 Introduction

Due to the ease of blood-brain barrier penetration, application of surface-functionalized ligands, and body clearance, utilization of nanoparticles in anti-aggregation research has received great attention in recent years[1]. The nanoparticles have a large surface-to-volume ratio, which enables them to provide strong adsorption sites to trap amyloid peptides, both in vitro and in vivo, thus controlling self-aggregation possibility[2]. The efficiency of these inhibitors depends on the shape, size, surface charge and ligands, and lattice facets of the nanoparticles[1].

Although much effort has been devoted to the application of carbon nanoparticles in the field of amyloid aggregation, the cytotoxicity of these nanomaterials, along with their effect on cell damage, swelling of endoplasmic reticulum and nervous system toxicity proves to be a disadvantage[3]. In this respect, boron nitride nanotube (BNNT), which is structurally similar and isoelectronic to CNT, serves as a superior alternative. The higher Young's modulus, thermal conductivity, and chemical stability of BNNTs makes it superior to CNTs[4, 5]. BNNTs also have a wide band gap, regardless of its chirality and are resistance to oxidation. More importantly, they are nontoxic and biocompatible to living cells and possess antibacterial properties[6], due to their chemical inertness and structural stability over CNTs. These characteristics make BNNTs ideal candidates for therapeutic and diagnostic applications[7, 8] and superior to CNTs. BNNTs have also been used to deliver anticancer drugs in brain[8] and also DNA oligomers[9]. Recently, the application of boron nitride (BN) nanoparticles in the inhibition of aggregation of amyloid peptides has also been explored[10–12]. Sorout et al discovered that (3,3)BNNT stabilizes helical Aβ trimers and inhibits their conformational transition to β-sheet rich aggregates, thus preventing Aβ self-assembly[10]. Furthermore, they have also observed that, with variation in curvature of BN nanoparticles, structural changes of Aβ and its interactions with the nanoparticle differs[11]. Although all BN nanoparticles interrupt the transition of helical Aβ monomer to a β-sheet, the pathway followed in this process varies[11]. The helical structure of Aβ monomer is stabilized in presence of (3,3)BNNT i.e., BN with highest curvature, (as seen in the previous study[10]), while, in presence of BN nanosheet (BNNS), which has zero curvature, it forms random coil conformations[11]. The destabilization effect of BNNT and BNNS on amyloid aggregation of α-synuclein, which is associated with PD,

is also reported[12]. Here, BNNS demonstrates better inhibitory potential against α-syn aggregation than BNNT[12]. These studies suggest that the curvature of nanoparticles influences peptide-nanoparticle interactions[13, 14]. In addition, the polar nature of the B–N bonds results in variation of interaction between BN nanoparticles and amino acids of different polarities[15]. Hence, an understanding in this regard is crucial for the application of nanoparticles in anti-amyloid drug research.

The application of nanoparticles in the modulation of protein aggregation and also in the biomedical field have received significant attention in the recent years. In addition, as the research of multi-target amyloid drugs (drugs which can simultaneously target multiple amyloid peptides) is encouraged, many candidates have been identified which can prevent the aggregation of both hIAPP and Aβ[16–23]. Keeping these in mind, the quest to employ non-toxic and biocompatible nanomaterials for the inhibition of hIAPP aggregation led us to speculate the effect of BN nanoparticles on the peptide self-assembly. Using molecular dynamics simulations, we have investigated hIAPP dimerization in presence of BN nanoparticles with three different chiralities, i.e., (5,5)BNNT, (10,10)BNNT and BNNS. Like in Aβ[10, 11], the conformational transition of hIAPP to β-sheet oligomers is prevented by BN nanoparticles. The nanoparticles exhibit differential interaction preference with hIAPP, which varies with its curvature and surface area. This variation gives rise to change in the hydrophobicity of these nanoparticles, which plays a crucial role in the interaction preference. Further, BN nanoparticles also display the ability to destabilize preformed hIAPP fibrils and the effect is more pronounced for (5,5)BNNT and BNNS.

The rest of the chapter contains the details of the methods used for conducting and analyzing the simulations in the Simulation Method section, which is followed by the discussion of the results in Results section, and Discussions and Conclusions section, finally, provides a summary of this study.

5.2 Simulation method

5.2.1 Simulation Setup

In this work, we have investigated the inhibitory potential of BN nanoparticles on the dimerization of hIAPP. For this, we have considered two hIAPP monomers and examined

its aggregation behavior in presence of three BN nanoparticles with varying chiralities, i.e., (5,5)BNNT, (10,10)BNNT and BNNS. The perimeter vector of the nanotubes is calculated from the its chiral indices (n,m), which can be further used to determine its diameter[24]. The structure of hIAPP (Fig 5.1a and b) was taken from the solid state NMR structure[25].

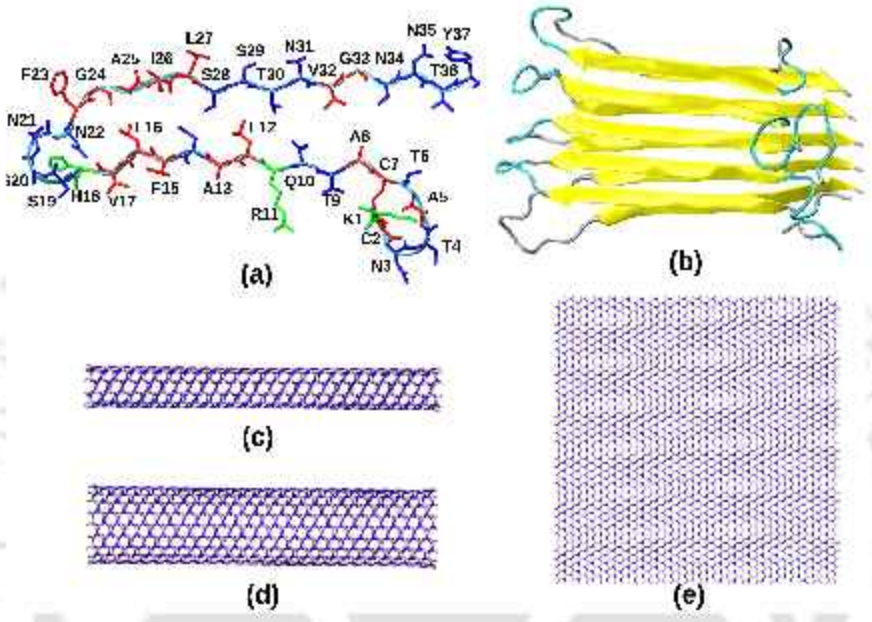

Figure 5.1: *Structures of (a) hIAPP monomer, (b) hIAPP protofibril, (c) (5,5)BNNT, (d) (10,10) BNNT and (e) BNNS. The polar, non-polar and basic residues in hIAPP monomer are represented in blue, red and green respectively. B and N atoms in BN nanoparticles are in pink and blue colors.*

The hIAPP chain extracted from the protofibril is simulated at a high temperature of 500 K and cooled gradually to obtain the structure which was used as the initial structure for further simulations. The open-ended boron nitride nanotubes (BNNTs) were modelled with chiralities (5,5) and (10,10), each of which had a length of 62.6 Å, while the square boron nitride nanosheet (BNNS) were of 82×82 $Å^2$ dimension (Fig 5.1c-e). The BN nanoparticles were positioned such that they were at least 10 Å away from the hIAPP monomers, which were randomly dispersed sufficiently apart from each other. In the isolated dimer system, only two hIAPP monomers were considered. Multiple independent simulations were carried out for the systems to negate the dependence of the simulation results on the initial configurations. Each of the systems containing BN was repeated thrice, such that, in each replica, the position of the hIAPP monomers was altered with respect to the nanoparticles.

The control system was simulated twice starting with different initial configuration.

System		N_{hIAPP}	N_{BN}	N_{water}
Dimer	MD1	2	1	15000
	MD2	2	1	15000
Dimer+BNT5	MD1	2	1	15000
	MD2	2	1	15000
	MD3	2	1	15000
Dimer+BNT10	MD1	2	1	15000
	MD2	2	1	15000
	MD3	2	1	15000
Dimer+BNS	MD1	2	1	30000
	MD2	2	1	30000
	MD3	2	1	30000
Fib	MD1	5	1	15000
	MD2	5	1	15000
Fib+BNT5	MD1	5	1	15000
	MD2	5	1	15000
Fib+BNT10	MD1	5	1	15000
	MD2	5	1	15000
Fib+BNS	MD1	5	1	30000
	MD2	5	1	30000

Table 5.1: *System Details. N_{hIAPP}, N_{BN}, and N_{water} define the number of hIAPP monomers, BN nanoparticles and water incorporated into the systems.*

Bond Length (Å)			
B-N	1.446		
Non-bonding Parameters			
Atom	**ϵ (kJ/mol))**	**$R_{min}/2$ (Å)**	**Partial Charge**
B	0.3971	1.937	+0.4
N	0.606	1.888	-0.4
H	0.0683	1.578	0

Table 5.2: *Parameters of boron nitride parameters.*

The effect of BN nanoparticles on the stabilization of preformed hIAPP protofibrils was also studied. Similar simulation protocols were followed for the protofibril systems. The nanoparticle was placed at a distance of 10 Å on either side of the U-shaped model of the

protofibril, producing two initial structures, which were simulated individually. The entire system was placed in an octahedral box. The minimum distance between the solute and water box wall was 10 ÅThe details of the simulation systems are presented in Table 5.1. The parameters for boron nitride were obtained using previous studies[4, 5, 26, 27] and are provided in Table 5.2.

The molecular dynamics simulations were carried out in AMBER20 package[28], following simulation protocols mentioned in Chapter 1 (Section 1.5.2). In all the simulations, B and N atoms were harmonically constrained with 100 kcal mol^{-1} $Å^{-2}$ force constant[26]. Altogether, 19 μs of simulation was carried out for this study.

5.2.2 Simulation Analysis

The simulation analyses were carried out following the protocols discussed in Chapter 1 (Section 1.5.3). For most of the analyses, the results were averaged over the replicas for each system. An isovalue of 0.5 was considered for evaluating the spatial distribution functions of hIAPP around BN nanoparticles[29]. A contact between hIAPP and BN was taken into account if any heavy atom of hIAPP was with a distance of 4 Å from BN surface[10]. To represent π-π stacking, the free energy landscape (FEL) was plotted with the distance between the center of mass of each ring (r) and the angle formed by the normals of these rings (θ), using the equation 1.19 (Fig 1.6a).[30] The distance between the centre of mass of NH_3^+ group of Arg11 and BN nanoparticles was applied to examine the presence of NH-π stacking (Fig 1.6b)[17]. The contact surface area (CSA) was defined as half of the difference between SASA of the hIAPP protofibril-BN and the sum SASAs of hIAPP protofibril and BN calculated separately[23, 27].

5.3 Results

5.3.1 Effect of BN Nanoparticles on the Conformation of hIAPP dimer

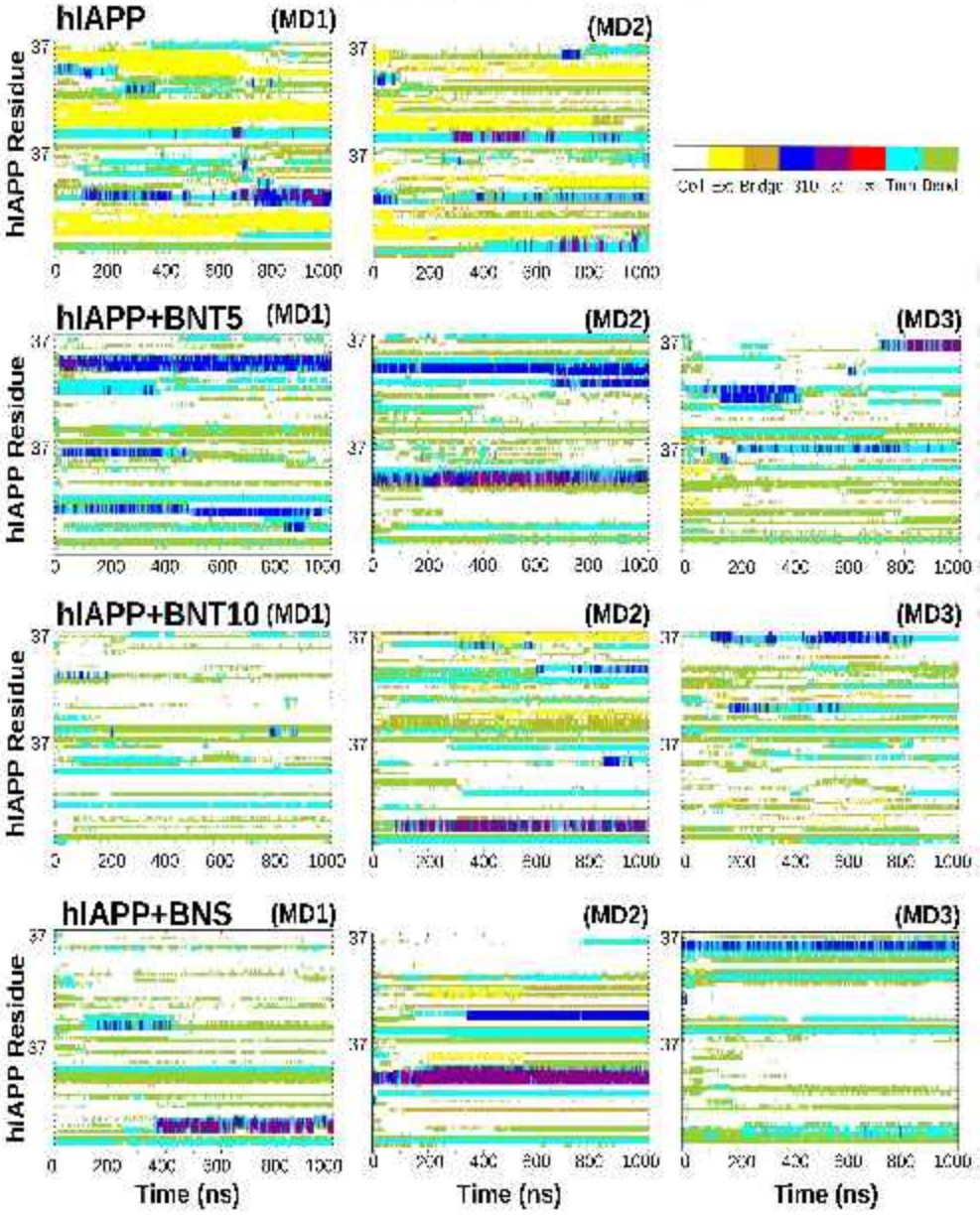

Figure 5.2: *Time evolution of change of secondary structures of each residue of hIAPP dimer.*

The aggregation of amyloid peptides is primarily accompanied by a transition in the secondary structure conformation of the peptides. Previous reports suggest that hIAPP monomers misfold to form β-sheet rich oligomers[31]. To probe into this matter, we begin our study by investigating the progression of secondary structures of hIAPP with time (Fig 5.2). In absence of any nanomaterials, the formation of β-sheet structure is detected at the onset of the simulation. The generation of the β-sheet between two hIAPP monomers are observed in the snapshots (Figures 5.3 and 5.4). This β-sheet conformation encloses Gln10-Leu16 and Ala25-Ser30 in the N- and C-terminal regions

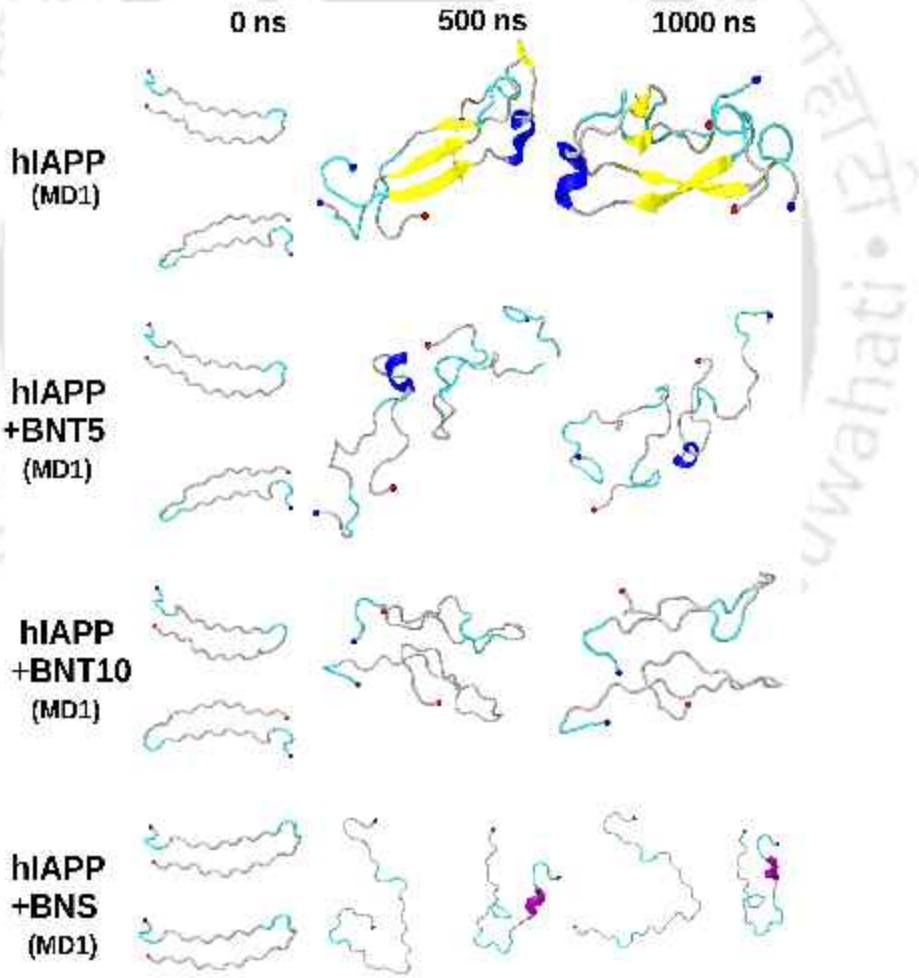

Figure 5.3: *Snapshots of hIAPP dimer at 500 ns time interval. The monomers are represented in cartoon form, depicting β-sheet in yellow, coil in white, bend in cyan and 3_{10}-helix in blue. The blue and red balls at the end of the peptides chains indicate the N- and C-terminal respectively.*

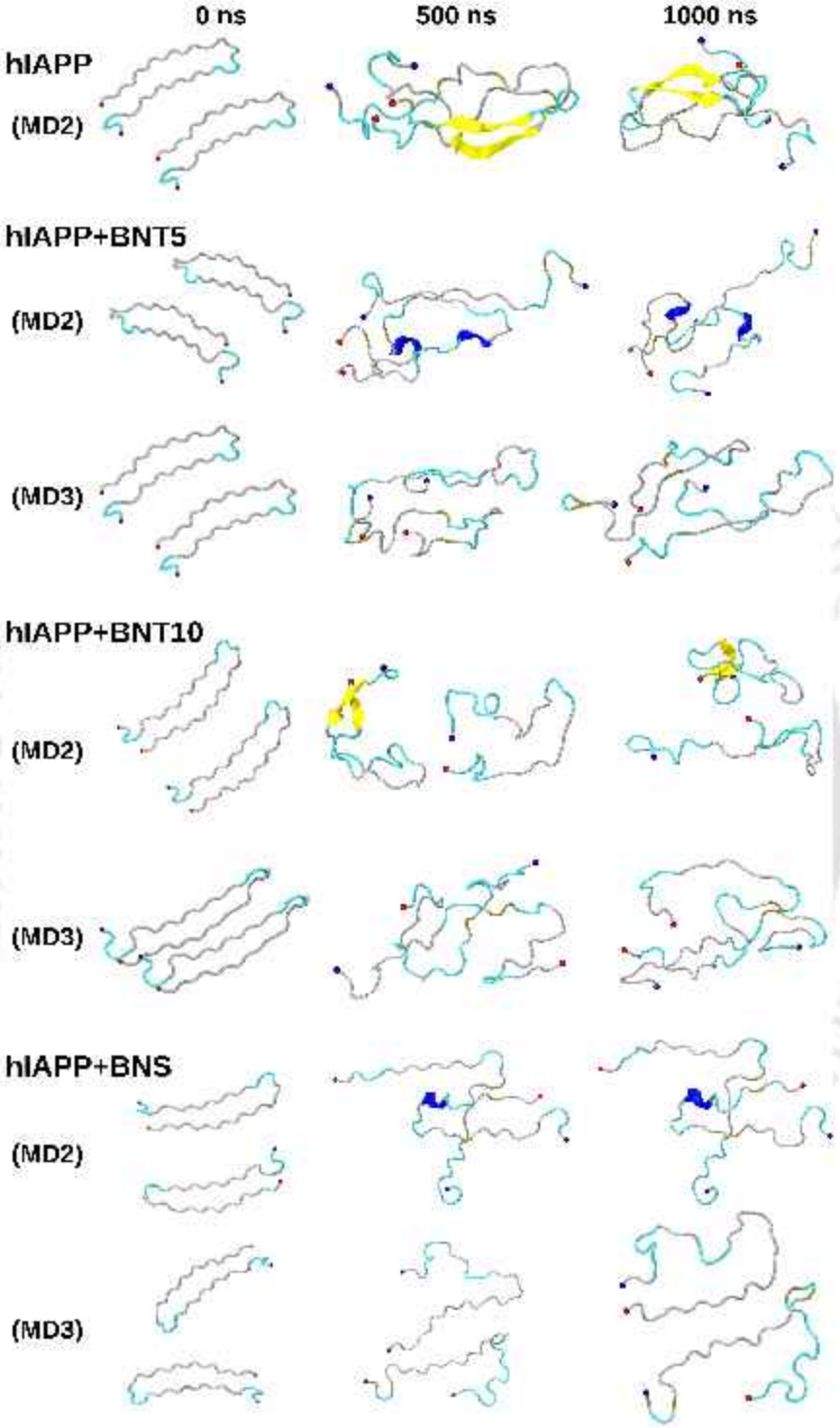

Figure 5.4: *Snapshots of hIAPP dimer at 500 ns time interval. The monomers are represented in cartoon form, depicting β-sheet in yellow, coil in white, bend in cyan and 3_{10}-helix in blue. The blue and red balls at the end of the peptides chains indicate the N- and C-terminal respectively.*

respectively (Figures 5.5b and 5.2). β-sheet at N-terminal region is observed to be less stable towards the simulation end than that at C-terminal, which comprises the amyloidogenic core of hIAPP[16, 31, 32] (Fig 5.2).

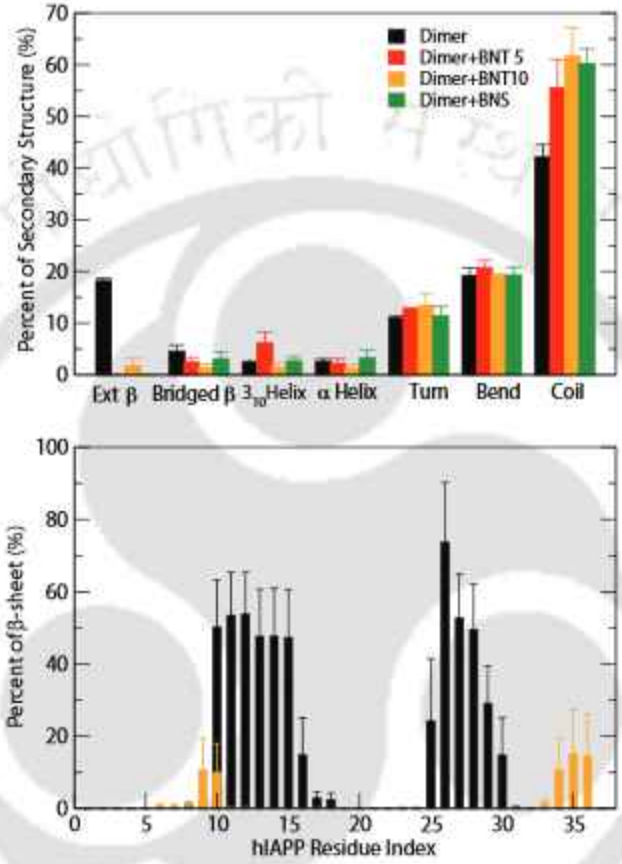

Figure 5.5: *(a) The different secondary structure contents and (b) Residue wise β-sheet percentage of hIAPP dimer.*

Addition of BN nanoparticles leads to β-sheet conformation to be almost inconspicuous (although some β-sheets are observed in one simulation run of hIAPP with (10,10)BNNT). On quantifying this change in secondary structure components (Fig 5.5a), it is noted that β-sheet percentage of hIAPP decreases from 18.2% (in isolated system) to 0.01/1.76/0.0 % in presence of (5,5)BNNT/(10,10)BNNT/BNNS. This decrease is accompanied by an increase in the disordered coil formation. Besides helix percentage is higher in the systems containing (5,5)BNNT, compared to that of the other nanoparticles, where coil structures is mostly perceived. The hIAPP monomers, therefore, depict extended coil conformation,

alongwith some helices in the snapshots of the systems containing BN nanoparticles (Figures 5.3 and 5.4). Hence, the formation of β-sheet structures in hIAPP is prevented by BN nanoparticles, which promote hIAPP to attain helical and disordered coil conformers.

The modulation of the aggregation of hIAPP by BN nanoparticles is further monitored by the solvent accessible surface area (SASA) of hIAPP peptides (Table 5.3). In absence of nanoparticles, SASA of hIAPP is 4591 Å^2. The incorporation of BN nanoparticles shifts the SASA to much higher values. In presence of (5,5)BNNT, SASA appears at 6113 Å^2, while for the systems containing (10,10)BNNT and BNNS, further higher SASA values are observed. In presence of nanoparticles, the peptides have a low propensity to aggregate, and hence hIAPP monomers attain extended conformation. This enhances solvent exposure of the peptide chains, resulting in higher SASA of hIAPP. Further, the helical conformers in the systems containing (5,5)BNNT lead to lower SASA of peptides, compared to other nanoparticles.

System	SASA (Å^2)	Hydrogen Bonds
Dimer	4591 ± 166	41.66 ± 2.1
Dimer+BNT5	6113 ± 77	12.55 ± 0.3
Dimer+BNT10	6162 ± 207	12.61 ± 1.8
Dimer+BNS	6181 ± 196	11.36 ± 0.9

Table 5.3: *SASA and hydrogen bond number of hIAPP dimer.*

Representative snapshots of the most probable conformation are obtained by performing cluster analysis using all trajectories and the conformation of the four most populated clusters (covering more than 60% of the conformation) are shown in Fig 5.6. Isolated hIAPP dimer clusters exhibits an assortment of disordered structures, containing significant β-sheet and helical conformers (Fig 5.6a and 5.2). β-strands cover Thr9-Val17 and Gly24-Ser29 regions, which is almost in accordance with our secondary structures analyses (Fig 5.5b). These β-sheet regions closely resemble with prior reports[16, 32]. hIAPP dimer, adsorbed on the nanoparticle surface, are predominantly disordered. Some short helical structures are noticed on (5,5)BNNT (Fig 5.6b) and BNNS (Fig 5.6d), while one cluster depicts β-sheet structure on (10,10)BNNT (Fig 5.6c). The large surface area of BNNS enables hIAPP monomers to attain an extended conformation. Hence, with decrease in

curvature of BN nanoparticles (from (5,5)BNNT to BNNS), the peptide chains are more prone to procure disordered extended conformation, which results in higher SASA values and hence lower aggregation propensity.

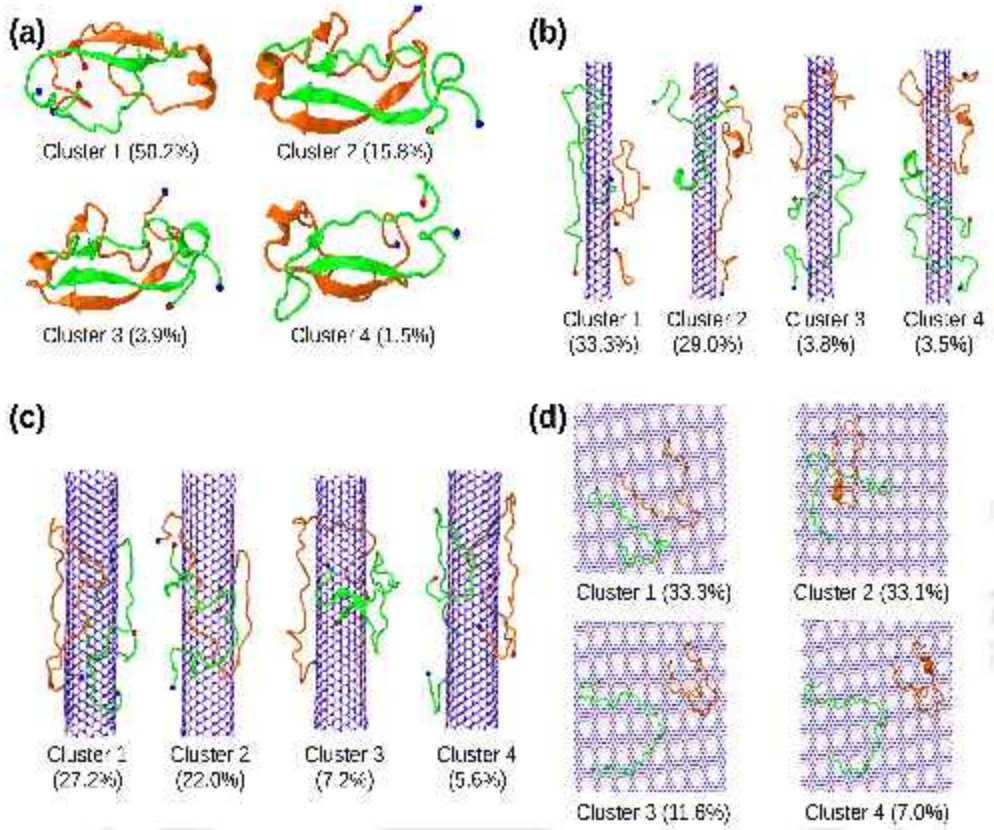

Figure 5.6: *Representative conformation of the four most populated clusters in (a) Dimer, (b) Dimer+BNT5, (c) Dimer+BNT10 and (d) Dimer+BNS systems. The two chains of hIAPP are represented by green and orange colors and the blue and red balls at the end of the chains indicate the N- and C-terminal respectively.*

A deeper understanding into the effect of nanoparticles on the dominant interactions between hIAPP is gained through Cα-Cα contact map, which depicts the distance between Cα atoms of each residue pair (Fig 5.7). Distinctive interaction patterns are observed in the isolated hIAPP dimer, which is also corroborated by the strength of hydrogen bonds formed between the hIAPP monomers (Table 5.3). Residues Ala5-Val17 and Ala25-Gly33 are in close contact, indicating strong hydrogen bonding and hydrophobic interactions between them. These interaction prone regions are in accordance with those

having high β-sheet probability (Fig 5.5b), and is endorsed by previous studies[18, 19, 31].

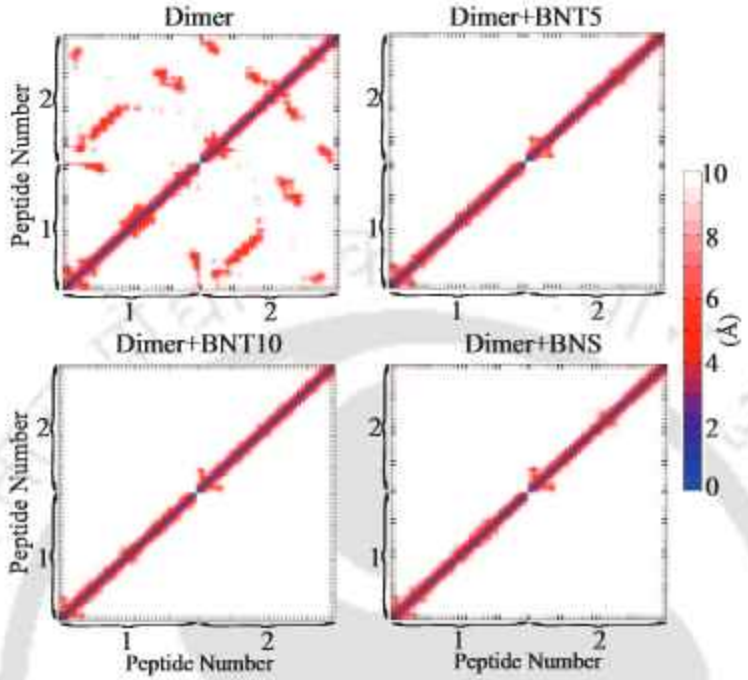

Figure 5.7: *Residue-residue contact map of the Cα atoms of hIAPP dimer. The color bar designates the distance between Cα atoms.*

System	hIAPP—hIAPP		hIAPP—BNT	
	Ele	vdW	Ele	vdW
Dimer	-9347.1 ± 38.5	-753.8 ± 51.5		
Dimer+BNT5	-8836.6 ± 41.8	-91.9 ± 27.2	-24.3 ± 2.5	-1264.1 ± 4.6
Dimer+BNT10	-2076.3 ± 17.9	-59.2 ± 8.6	-30.7 ± 3.8	-1621 ± 133.5
Dimer+BNS	-8563.3 ± 48.9	-17.1 ± 7.4	126.4 ± 59.8	-2229.2 ± 108.8
Fibril	-20476.5 ± 61.9	-2702.0 ± 9.6		
Fibril+BNT5	-22346.7 ± 115.1	-1297.5 ± 68.6	-23.8 ± 0.4	-1273.6 ± 43.5
Fibril+BNT10	-22480.6 ± 127.2	-1228 ± 0.8	-29.1 ± 1.3	-1760 ± 53.5
Fibril+BNS	-21380.2 ± 2.9	-852.7 ± 6.3	-1004.8 ± 334.3	-3605.1 ± 302.9

Table 5.4: *Non-bonded interaction energy (kJ mol^{-1}) of hIAPP-hIAPP and hIAPP-BN nanoparticle interactions.*

On addition of BN nanoparticles, these patterns disappear, indicating interruption in hIAPP-hIAPP interactions, which is also deduced from the decrease in the hydrogen bond

numbers (Table 5.3). A closer look into the non-bonded interaction energy between hIAPP depicts that BN nanoparticles modifies van der Waals as well as electrostatic energy towards more unfavorable values, compared to that of the isolated system (Table 5.4). However, a greater effect on the alteration is observed on the van der Waals energy. Hence the inter-peptide interactions, which stabilize its aggregation, are inhibited by BN nanoparticles and the hydrophobic interactions between hIAPP are more affected by it.

5.3.2 Interactions between hIAPP and BN nanoparticles

The impact of BN nanoparticles towards the aggregation behavior of hIAPP is attributed to the adsorption of peptides over the nanoparticle surface. A three dimensional probabilistic distribution of hIAPP around the nanoparticles is provided by its spatial distribution function plots. From Fig 5.8a, it is observed that, hIAPP is distributed along the surface of (5,5)BNNT, parallel to the nanotube axis. Due to increase in the radial surface of (10,10)BNNT, hIAPP is adsorbed more around the axis perpendicular to the nanotube (Fig 5.8b). The flat surface of BNNS assists hIAPP to attain extended conformation, leading to a spread-out distribution (Fig 5.8c). This varying distribution of hIAPP is ascribed to the difference in curvature of nanoparticles, which causes differential binding preference of hIAPP.

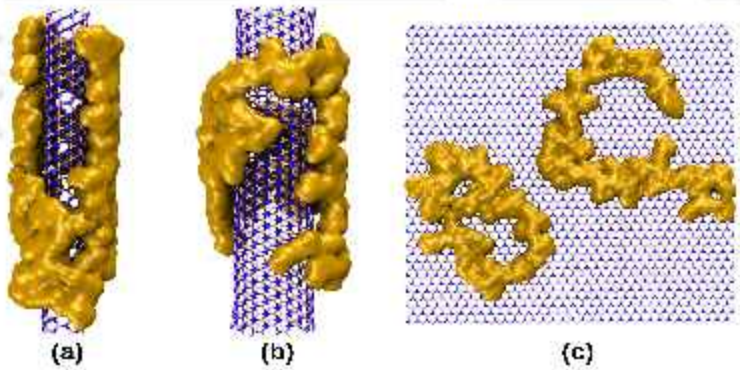

Figure 5.8: *Spatial distribution functions of hIAPP over the surface of (a) (5,5)BNNT, (b) (10,10)BNNT and (c) BNNS.*

In order to explore the binding site of hIAPP, contact number between each hIAPP residue and the nanoparticles is calculated (Fig 5.9a-c). With (5,5)BNNT, higher contact propensity is noticed by Gln10-His18, along with Asn21-Phe23 residues, i.e., the propensity is

mostly confined to N-terminal (Fig 5.9a). The residues Gln10-Arg11, Asn14-Leu27, depict substantial contacts with (10,10)BNNT (Fig 5.9b). On the other hand, the contact propensity of hIAPP around BNNS is considerable in the N-terminal residues (Gln10-Arg11, Phe15) and is more significant around Asn21-Val32 residues in C-terminal (Fig 5.9c).

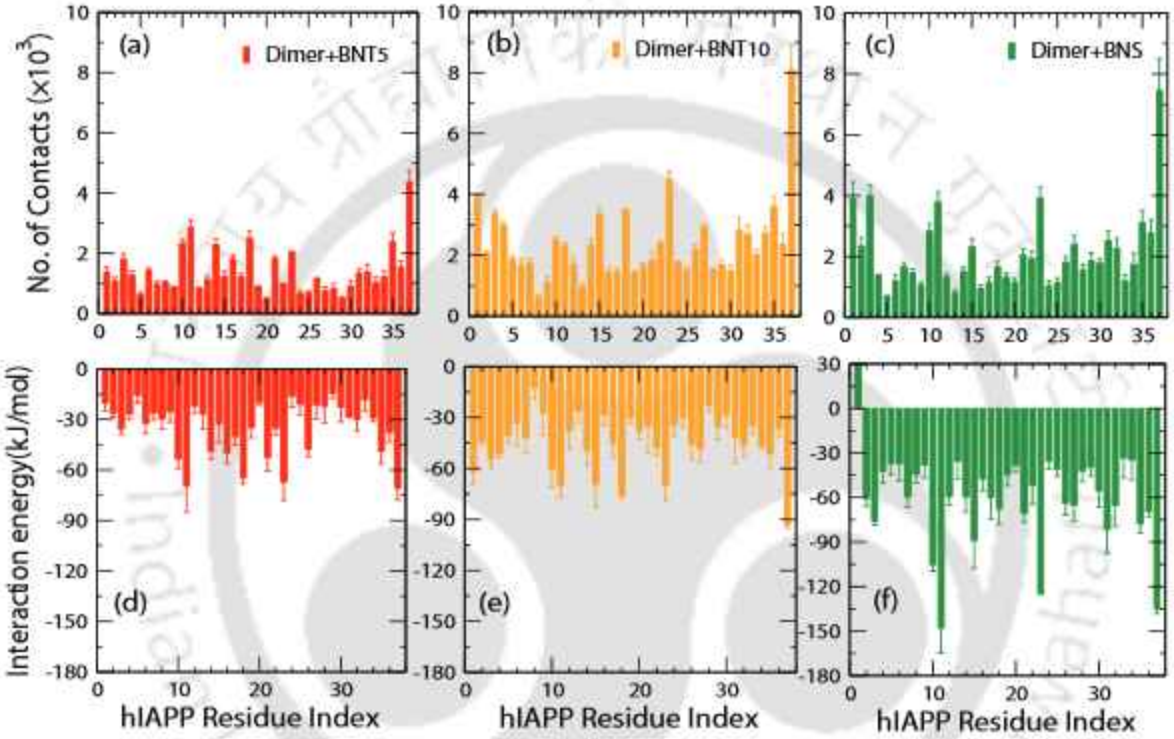

Figure 5.9: *Residue wise (a-c) contact number and (d-f) interaction energy between hIAPP and BN nanoparticles.*

The residue wise interaction energy pattern of hIAPP with nanoparticles corroborate with the above results (Fig 5.9d-f). It is observed that Gln10-Phe23 and Gln10-Leu27 have favorable interactions with (5,5)BNNT and (10,10)BNNT respectively. BNNS interacts with Gln10-Arg11, Phe15 and Asn21-Val32 residues. Overall, the interaction strength of hIAPP with BN nanoparticles increases with decrease in the curvature of nanoparticles, from (5,5)BNNT to BNNS. In addition, (5,5)BNNT displays higher interaction propensity towards N-terminal of hIAPP, while BNNS towards C-terminal region. Comparing these results with that of residue wise β-sheet percentage of hIAPP, it is evident that (5,5)BNNT targets the high propensity β-sheet region in N-terminal, while BNNS does the same for

C-terminal.

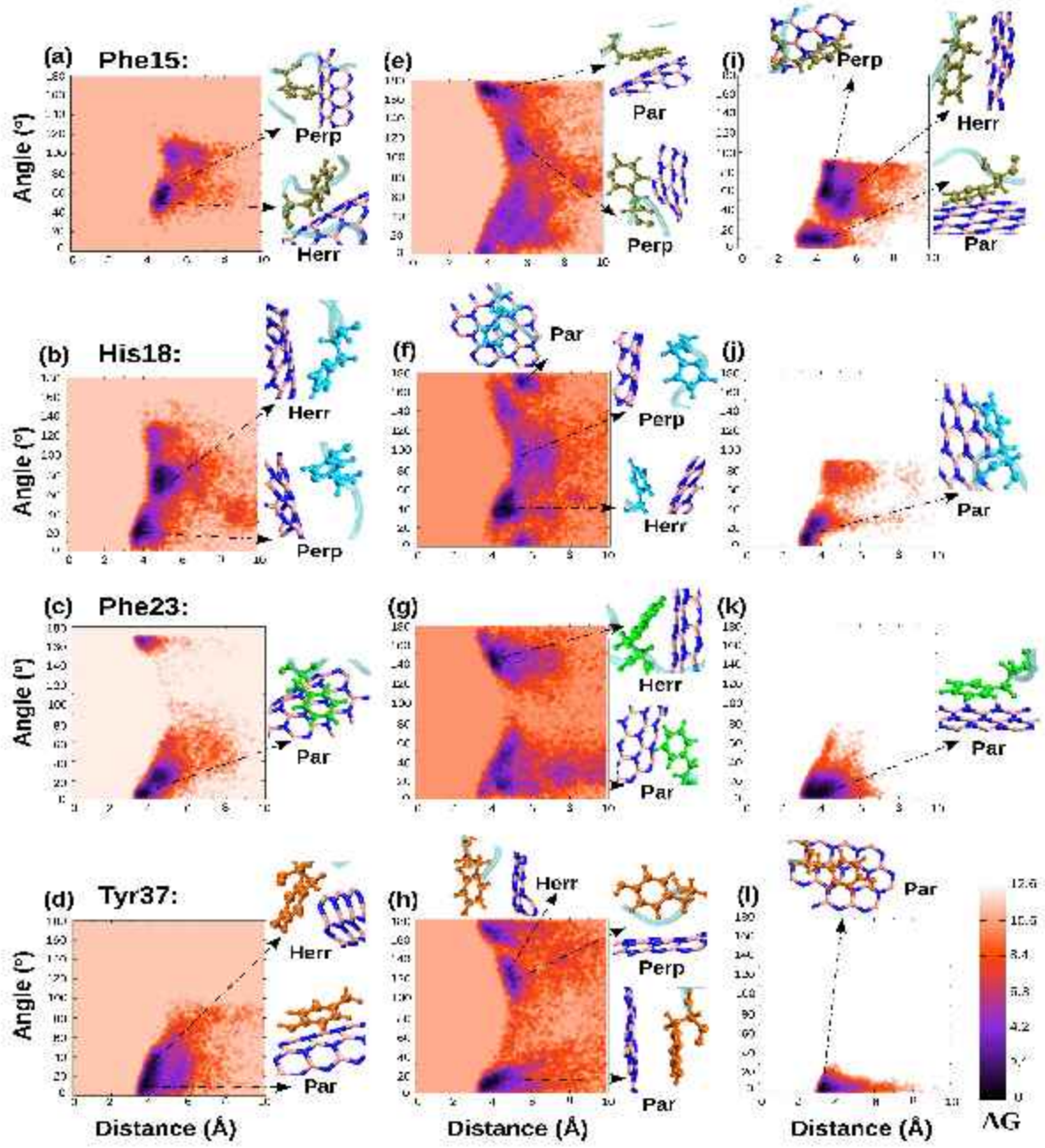

Figure 5.10: *Stacking orientation of the aromatic residues Phe15 (tan), His18 (blue), Phe23 (green) and Tyr37 (orange) with (a-d)(5,5)BNNT, (e-h) (10,10)BNNT and (i-l) BNNS. The free energy landscape (ΔG in kJ/mol) is plotted with respect to COM distance of the aromatic rings and the angle between them and the stacking conformations corresponding to the minima states are presented.*

The interaction site of (10,10)BNNT resembles with the other two nanoparticles. The hydrophobic nature of BNNS enables it to preferentially interact with the more hydrophobic C-terminal. Due to lower extent of hydrophobicity in (5,5)BNNT, it interacts better with N-terminal region. Further, significant interaction between positively charged Arg11/His18 residues and BNNTs are observed, owing to their hydrophilicity. BNNS, on the other hand, displays notable contacts with residues which can participate in π stacking interactions.

Aromatic stacking interaction is necessary for the binding of hIAPP with amyloid drugs, as it destabilizes the aggregation-prone stacking among the aromatic residues of hIAPP itself[33]. The aromatic residues Phe15, His18, Phe23 and Tyr37 are involved in π-π stacking interactions with BN nanoparticles (Fig 5.10). Phe23 and Tyr37 in C-terminal display greater stacking probability with BNNS than Phe15 and His18 in N-terminal and the reverse is true for the systems containing BNNTs, validating the aforementioned interaction preference of BN nanoparticles (Fig 5.11).

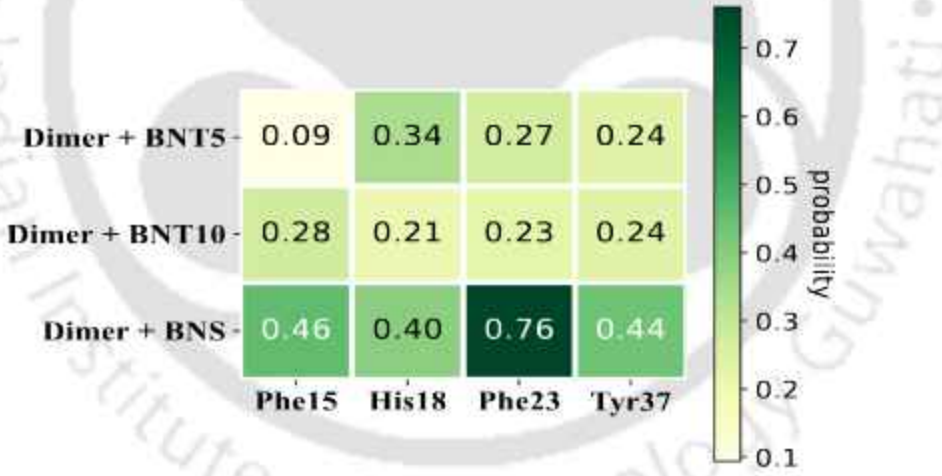

Figure 5.11: *Probability of stacking between the different aromatic residues of hIAPP and BN nanoparticles.*

Further, the planar surface of BNNS facilitates parallel stacking arrangement with all the residues, except Phe15 (where herringbone and perpendicular is also observed) (Fig 5.12c). In case of (5,5)BNNT, parallel stacking predominates, but the other orientations are also observed (Fig 5.12a). However, all different stacking probabilities are observed with (10,10)BNNT (Fig 5.12b). Since parallel alignment is most favorable among aromatic

stacking in proteins, and it is dominant in the systems containing BNNS, stacking interactions between hIAPP and BNNS can be stipulated to be most favorable. In addition, narrow energy basins are observed for parallel stacking between aromatic residues and BNNS (Fig 5.10i-l), which appear at lower distance and angle values, compared to that of the nanotubes (Fig 5.10a-h). This further substantiates that the flat surface of BNNS results in stronger stacking interactions with hIAPP, rather than the curved nanotubes (where energy basins are much broader, especially for (10,10)BNNT).

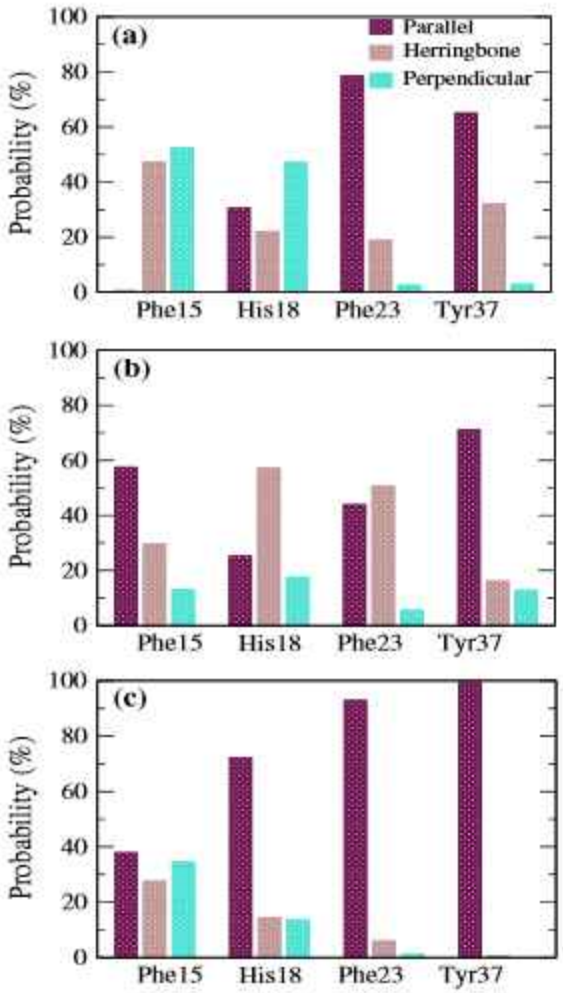

Figure 5.12: *Probability of the orientation of stacking between the different aromatic residues of hIAPP and (a) (5,5)BNNT, (b) (10,10)BNNT and (c) BNNS.*

Furthermore, the contact number and interaction energy analyses depict strong interactions with Arg11, which can advocate the presence of NH-π stacking between NH_3^+ group of Arg11 and the hexagonal rings of BN nanoparticles (Fig 5.13). Here also, higher probability occurring at lower distance depicts that the extent of NH-π interactions is much greater with BNNS.

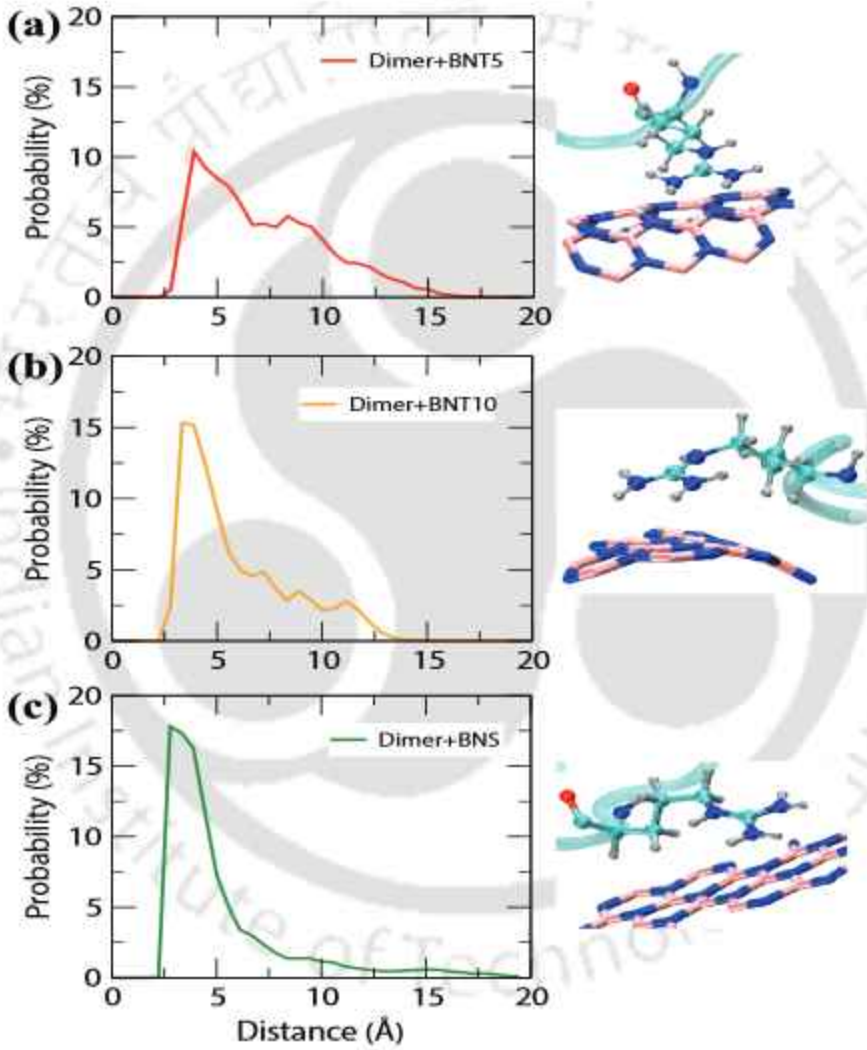

Figure 5.13: *Probability distribution of the centroid distance between NH_3^+ group of Arg11 and (a) (5,5)BNNT, (b) (10,10)BNNT and (c) BNNS, alongwith the corresponding snapshots. This figure represents NH-π stacking between Arg11 and BN nanoparticles.*

Thus, the aggregation of hIAPP is prevented by BN nanoparticles, which interact with the peptides mostly via hydrophobic and stacking interactions. Also, the binding site

between hIAPP and the nanoparticles differs with the change in curvature and surface area of BN nanoparticles. Among the three, BNNS exhibits maximum interaction propensity with hIAPP.

5.3.3 Destabilization of hIAPP Protofibrils by BN nanoparticles

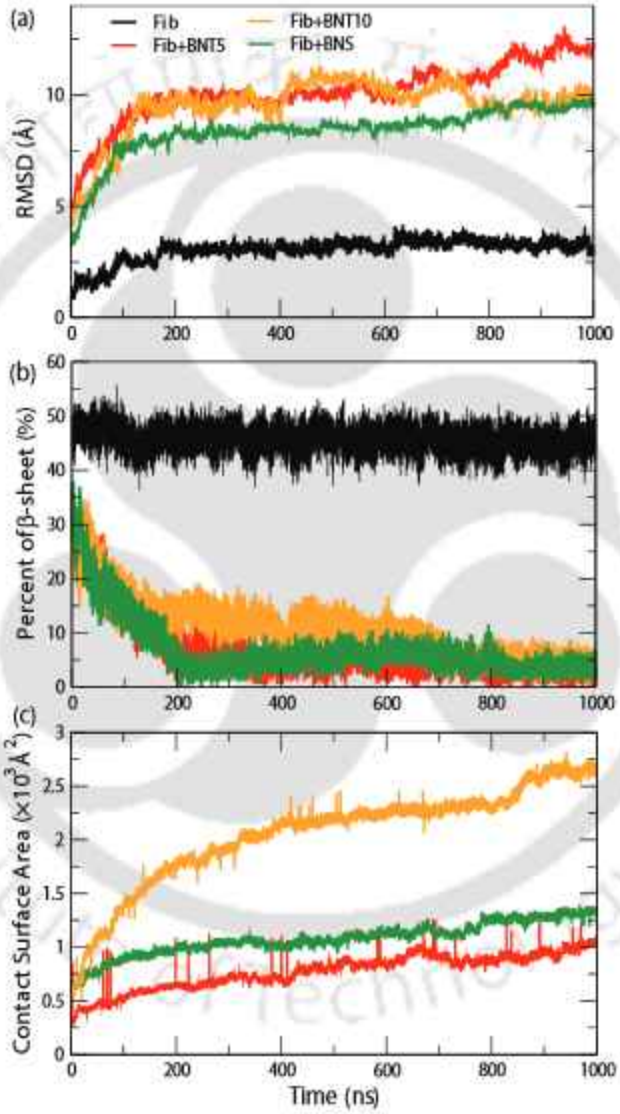

Figure 5.14: *Time evolution of (a) RMSD, (b) β-sheet of hIAPP protofibril and (c) Contact surface area between BN and hIAPP protofibril. The blue and red balls at the end of the peptides chains indicate the N- and C-terminal respectively.*

In this section, the inhibitory ability of BN nanoparticles on amyloid aggregation of hIAPP is further determined by their capacity to destabilize preformed fibrils. In this regard,

the stabilization of hIAPP protofibrils in absence and presence of BN nanoparticles is investigated. The RMSD of hIAPP protofibrils considering backbone atoms is calculated using the initial structure as reference (Fig 5.14a). RMSD of hIAPP protofibrils in presence of nanoparticles extends from 8 to 12 Å, which is much higher than that of the isolated system. The protofibrils adsorbed on BNNS depicted lower RMSD than those on the nanotubes. Further, β-sheet percentage of hIAPP protofibrils adsorbed on nanoparticles decreases steadily in first 200 ns of simulation and approaches a value of 5% (Fig 5.14b). This is a significant drop from β-sheet percentage of the isolated system (45%), maintained throughout the simulation time (Fig 5.15).

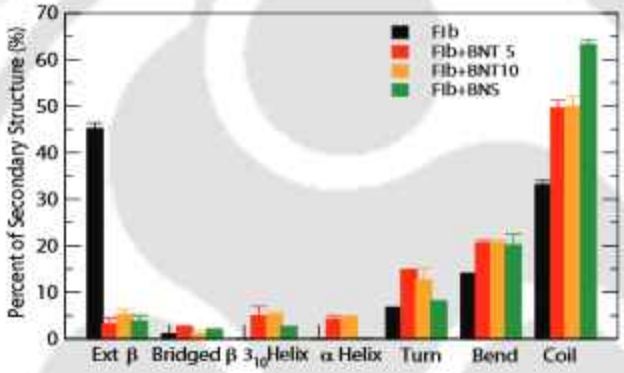

Figure 5.15: *The different secondary structure contents of hIAPP protofibril.*

The increase in RMSD signifies the deviation of ordered protofibrillar structure and destabilization of β-hairpin chains, indicated by the decrease in β-sheet probability. This destabilization effect is most pronounced by (5,5)BNNT, followed by BNNS. The snapshots of the protofibrils provide a clear picture of the observations stated above (Figures 5.16 and 5.17). The ordered hairpin structure of the protofibril becomes dispersed, in presence of nanosheet and the β-strands mostly transition into random coils, leading to an considerable increase in the random coil conformation (Fig 5.15).

The adsorption of hIAPP protofibrils on BN nanoparticles is ascertained by their contact surface area (CSA) (Fig 5.14c). CSA of hIAPP-nanoparticle increases along the simulation time, implying stronger interaction between the protofibrils and nanoparticles. CSA of hIAPP with nanoparticle follows the order: (5,5)BNNT < (10,10)BNNT < BNNS, as the surface area of nanoparticles increases in that order. This increase in the interactions is observed in the non-bonded interaction energy values (Table 5.4). Here again, van

der Waals contribution dominates over electrostatic energy. This leads to weakening of hIAPP-hIAPP interactions, where the effect on vdW energy is much more pronounced than electrostatic energy. Hence, much like hIAPP dimer, hydrophobicity of nanoparticles plays a crucial role on the adsorption of hIAPP protofibrils.

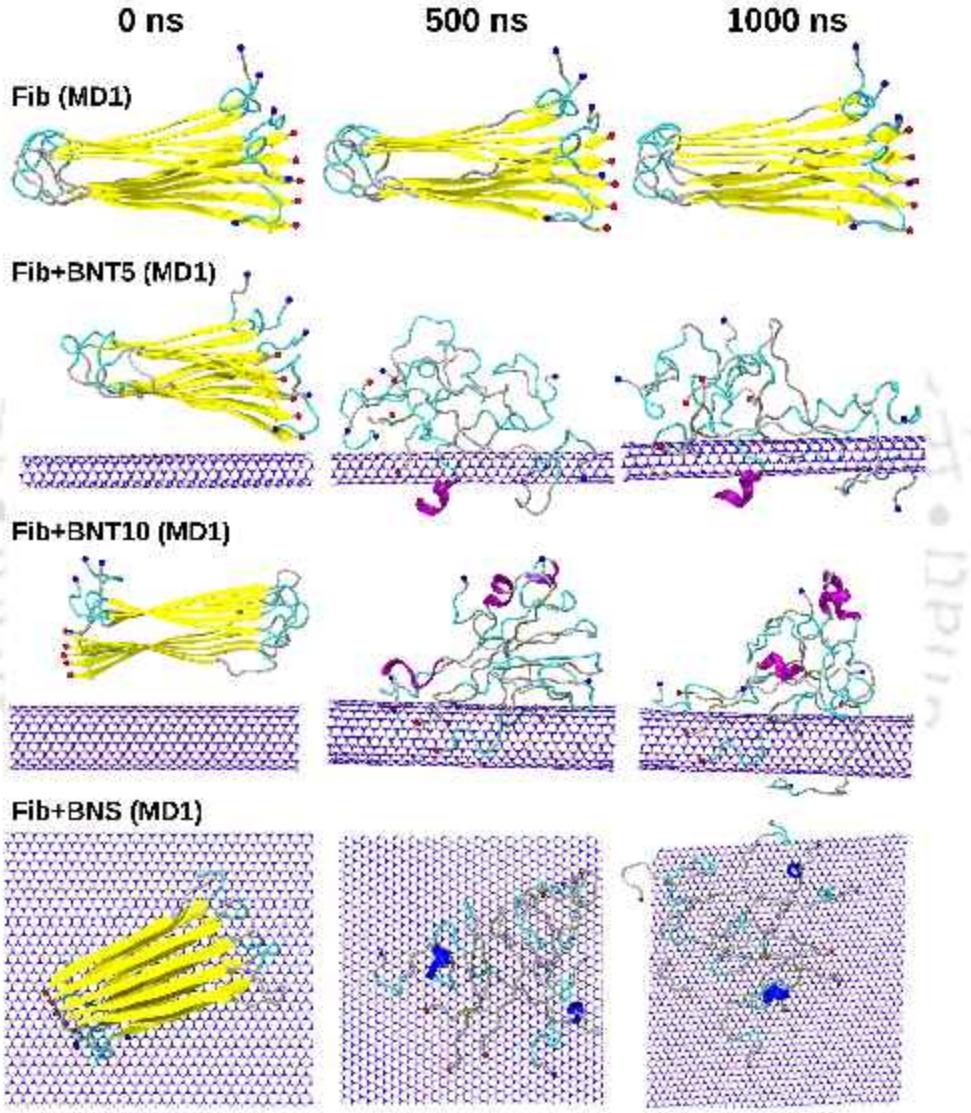

Figure 5.16: *Snapshots of hIAPP protofibrils at 500 ns time interval. The protofibrils are represented in cartoon form, depicting β-sheet in yellow, coil in white, bend in cyan and 3_{10}-helix in blue. The blue and red balls at the end of the peptides chains indicate the N- and C-terminal respectively.*

In order to identify the specific residues which are fundamental for protofibril-

nanoparticle interactions, the protofibrillar regions which undergo most fluctuation on adsorption is determined by root mean square fluctuation (RMSF) (Fig 5.18). The last two hIAPP chains of the protofibrils display most fluctuation in all systems containing nanoparticles. The protofibrils in presence of (10,10)BNNT display least fluctuation.

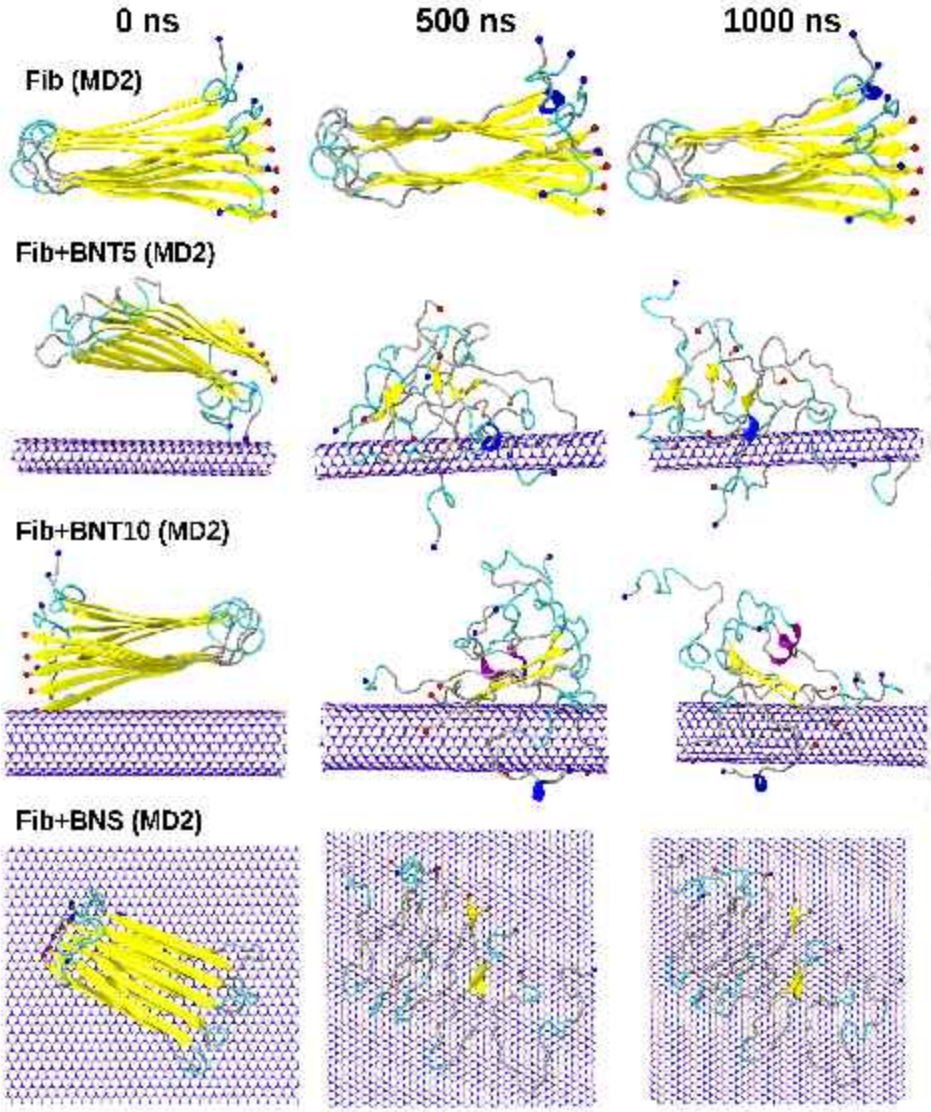

Figure 5.17: *Snapshots of hIAPP protofibrils at 500 ns time interval. The protofibrils are represented in cartoon form, depicting β-sheet in yellow, coil in white, bend in cyan and 3_{10}-helix in blue.*

There is greater fluctuation among the N-terminal residues, especially the first 20-24 residues in most chains. Besides, the moderation of β-sheet in N-terminal (Ala8-Ser20)

is much more conspicuous than that in C-terminal (Ala25-Thr36) by BN nanoparticles (Fig 5.19(a-c)). This suggests preferable interaction of nanoparticles with the N-terminal of protofibrils, which is further manifested by the contact number between protofibrillar residues and the nanoparticles (Fig 5.19(d-f)).

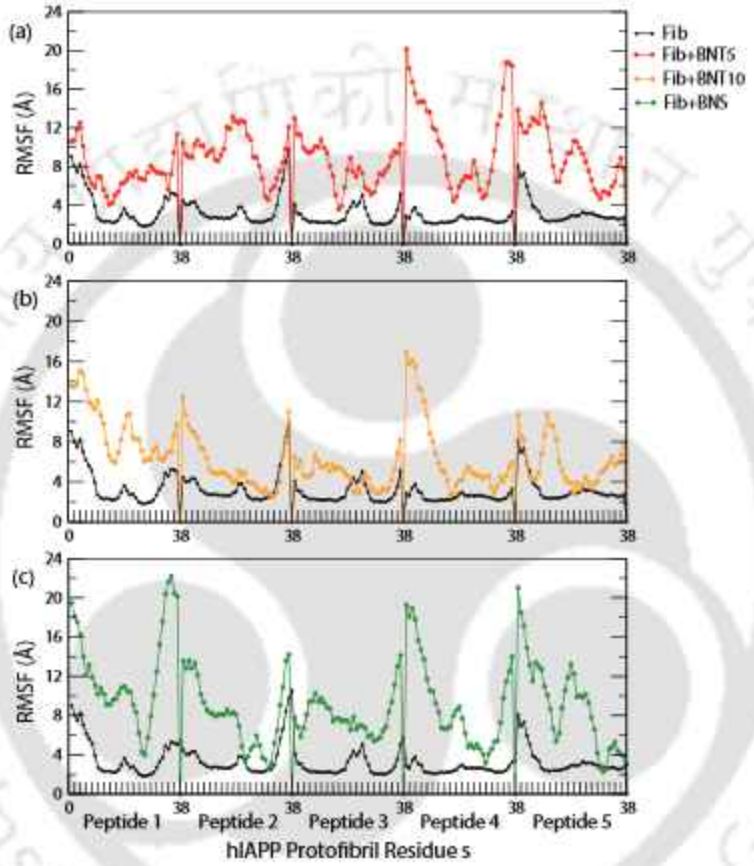

Figure 5.18: *Root mean square fluctuation (RMSF) of each residue in hIAPP protofibrils in isolated system and in presence of (a) (5,5)BNNT, (b) (10,10)BNNT and (c) BNNS.*

Consequently, hIAPP residues which have lowest contact with BN project highest β-sheet percentage, further signifying that adsorption of hIAPP over nanoparticles disintegrates β-sheets. (5,5)BNNT depicts greater contacts with Gln10-His18 residues, while BNNS displays considerable interaction with C-terminal (Ile26-Val32), in addition to N-terminal (Thr6-Arg11 and Asn14-Phe23) region. This interaction pattern relates to that perceived for hIAPP dimer. The least contact is observed with (10,10)BNNT. Hence, in conclusion, hIAPP protofibrils are destabilized by BN nanoparticles, which interacts with N-terminal region of the protofibrils. Further, (5,5)BNNT and BNNS display greater desta-

bilization capacity than (10,10)BNNT towards hIAPP protofibrils.

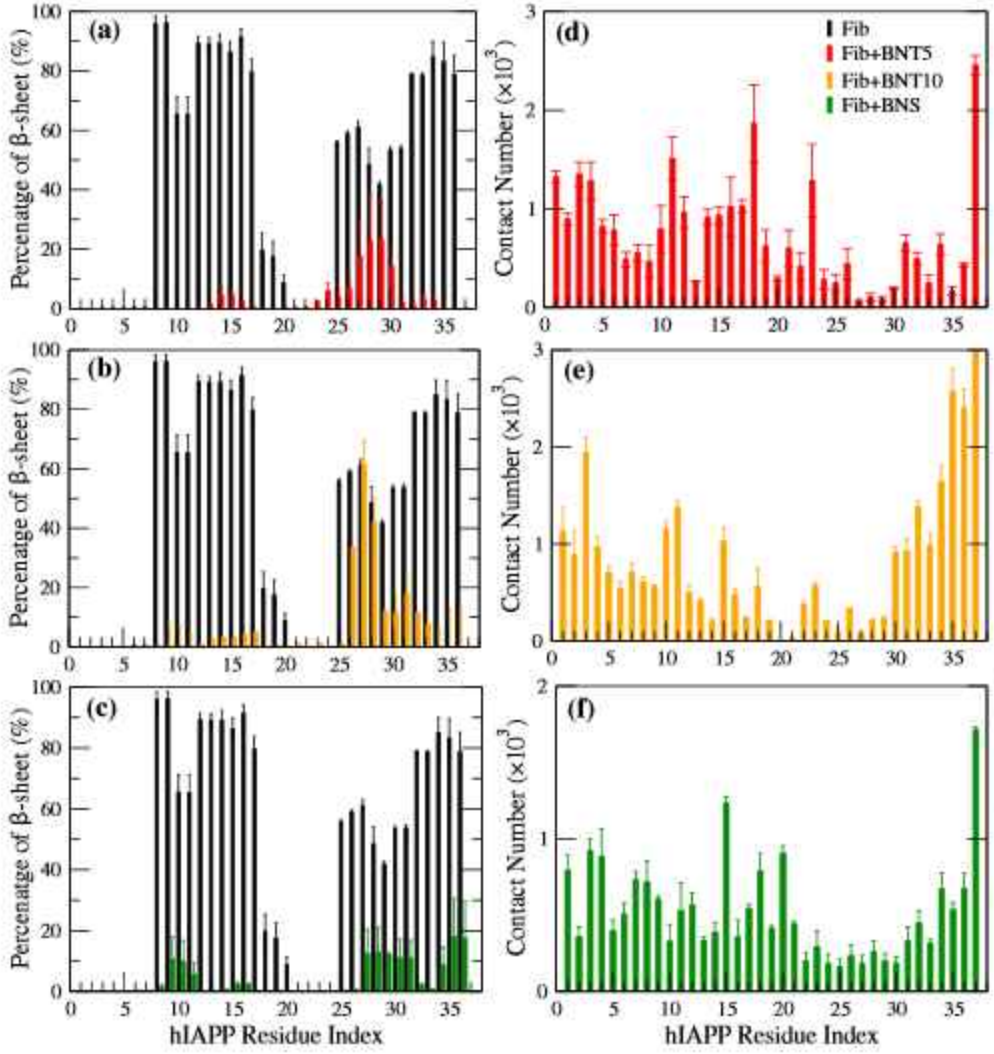

Figure 5.19: *Residue wise (a-c) β-sheet percentage and (d-f) contact number of hIAPP protofibrils with BN nanoparticles.*

5.3.4 Discussion and Conclusions

This study outlines the impact of boron nitride nanoparticles on the aggregation of hIAPP. Since the application of nanoparticles in the field of amyloidosis is fast growing, the prospect of this biocompatible candidate in the control of T2D is of particular interest. In this work, we have evaluated the dimerization of hIAPP in presence of three BN nanoparticles of different curvature, i.e., (5,5) and (10,10) BN nanotube and BN nanosheet. Via all-atom

molecular dynamics simulations, we observed that, in isolated system, hIAPP monomers aggregate to form β-sheet rich conformers, encompassing Thr9-Val17 and Ala25-Asn30 segments. With the addition of BN nanoparticles, these monomers attain disordered, coiled structures, in conjunction with helices. (5,5)BNNT induces helix conformation in hIAPP more than the other nanoparticles, while disordered, extended monomers are formed on BNNS surface. Similar secondary structure propensity is also observed for Aβ monomer adsorbed on BN nanoparticles, where higher curvature of the nanoparticles stabilized helical structures, while BNNS induces the formation of random coils[11]. The extended monomers result in higher SASA and lower inter-peptide contacts and hydrogen bonding, compared to the isolated system. van der Waals contribution towards inter-peptide interactions becomes more unfavorable in presence of BN nanoparticles than electrostatic interactions, as the former dominates over the latter in hIAPP-nanoparticle interactions. Hence, hydrophobic interactions play a dominant role in the adsorption of hIAPP over the nanoparticles. With variation in curvature of BN nanoparticles, their binding preference toward hIAPP differ. (5,5)BNNT preferentially interacts with Gln10-Phe23 region, (10,10)BNNT interacts with Asn14-Leu27, and BNNS with Asn21-Val32. This is justified by the change in the hydrophobicity of nanoparticles. With increase in curvature of BN nanoparticles from BNNS to (5,5)BNNT, the hydrophobicity decreases, and the interaction preference shifts from hydrophobic C-terminal to the N-terminal region. The adsorption of hIAPP over BNNS is more favorable compared to that of (5,5)BNNT, and BNNS also preferentially interacts with amyloidogenic C-terminal of hIAPP. The planar surface of BNNS leads to superior stacking orientation with hIAPP, making it most favorable as an inhibitor of hIAPP dimerization. The better performance of BNNS over BNNT is also detected in their inhibition towards α-syn aggregation[12]. These BN nanoparticles also display the potential to destabilize ordered protofibrillar structure of hIAPP by interacting with N-terminal side of protofibrils. The destabilization effect is more pronounced for (5,5)BNNT and BNNS. In summary, we can conclude that BN nanoparticles can inhibit aggregation of hIAPP and destabilize preformed fibrils. However, extensive experimental studies are required to further validate our findings and determine the potential of BN nanoparticles in the anti-amyloid drug research. The curvature of nanoparticles is crucial in its inhibitory potential, which is proven in our results and, hence, is pivotal for their use in anti-amyloid drug research.

References

[1] Tang, Y.; Zhang, D.; Zhang, Y.; Liu, Y.; Gong, X.; Chang, Y.; Ren, B.; Zheng, J. Introduction and Fundamentals of Human Islet Amyloid Polypeptide Inhibitors. *ACS Applied Bio Materials* **2020**, *3*, 8286–8308.

[2] Liu, Z.; Robinson, J. T.; Sun, X.; Dai, H. PEGylated Nanographene Oxide for Delivery of Water-Insoluble Cancer Drugs. *J. Am. Chem. Soc.* **2008**, *130*, 10876–10877.

[3] Zhou, R.; Gao, H. Cytotoxicity of Graphene: Recent Advances and Future Perspective. *Wiley Interdiscip. Rev. Nanomed. Nanobiotechnol.* **2014**, *6*, 452–474.

[4] Won, C. Y.; Aluru, N. R. Structure and Dynamics of Water Confined in a Boron Nitride Nanotube. *J. Phys. Chem. C* **2008**, *112*, 1812–1818.

[5] Won, C. Y.; Aluru, N. R. Water Permeation through a Subnanometer Boron Nitride Nanotube. *J. Am. Chem. Soc.* **2007**, *129*, 2748–2749.

[6] Merlo, A.; Mokkapati, V. R. S. S.; Pandit, S.; Mijakovic, I. Boron Nitride Nanomaterials: Biocompatibility and Bio-applications. *Biomater. Sci.* **2018**, *6*, 2298–2311.

[7] Ciofani, G.; Raffa, V.; Menciassi, A.; Cuschieri, A. Boron Nitride Nanotubes: An Innovative Tool for Nanomedicine. *Nano Today* **2009**, *4*, 8–10.

[8] Xu, H.; Wang, Q.; Fan, G.; Chu, X. Theoretical Study of Boron Nitride Nanotubes as Drug Delivery Dehicles of Some Anticancer Drugs. *Theor. Chem. Acc.* **2018**, *137*, 104.

[9] Chen, X.; Wu, P.; Rousseas, M.; Okawa, D.; Gartner, Z.; Zettl, A.; Bertozzi, C. R. Boron Nitride Nanotubes Are Noncytotoxic and Can Be Functionalized for Interaction with Proteins and Cells. *Journal of the American Chemical Society* **2009**, *131*, 890–891, PMID: 19119844.

[10] Sorout, N.; Chandra, A. Effects of Boron Nitride Nanotube on the Secondary Structure of Aβ(1–42) Trimer: Possible Inhibitory Effect on Amyloid Formation. *J. Phys. Chem. B* **2020**, *124*, 1928–1940.

[11] Sorout, N.; Chandra, A. Interactions of the Aβ(1–42) Peptide with Boron Nitride Nanoparticles of Varying Curvature in an Aqueous Medium: Different Pathways to Inhibit β-Sheet Formation. *J. Phys. Chem. B* **2021**, *125*, 11159–11178.

[12] Smida, K.; Albedah, M.; Rashid, R. F.; Al-Qawasmi, A.-R. Molecular Dynamics Method for Targeting α-synuclein Aggregation Induced Parkinson's Disease Using Boron Nitride Nanostructures. *Eng. Anal. Bound. Elem.* **2023**, *146*, 89–95.

[13] Zhang, N.; Yeo, J.; Lim, Y.; Guan, P.; Zeng, K.; Hu, X.; Cheng, Y. Tuning the Structure of Monomeric Amyloid Beta Peptide by the Curvature of Carbon Nanotubes. *Carbon* **2019**, *153*, 717–724.

[14] John, T.; Adler, J.; Elsner, C.; Petzold, J.; Krueger, M.; Martin, L. L.; Huster, D.; Risselada, H. J.; Abel, B. Mechanistic Insights into the Size-dependent Effects of Nanoparticles on Inhibiting and Accelerating Amyloid Fibril Formation. *J. Colloid Interface Sci.* **2022**, *622*, 804–818.

[15] Mukhopadhyay, S.; Scheicher, R. H.; Pandey, R.; Karna, S. P. Sensitivity of Boron Nitride Nanotubes toward Biomolecules of Different Polarities. *J. Phys. Chem. Lett.* **2011**, *2*, 2442–2447.

[16] Mo, Y.; Lei, J.; Sun, Y.; Zhang, Q.; Wei, G. Conformational Ensemble of hIAPP Dimer: Insight into the Molecular Mechanism by which a Green Tea Extract inhibits hIAPP Aggregation. *Sci. Rep.* **2016**, *6*, 33076.

[17] Roy, R.; Paul, S. Theoretical Investigation of the Inhibitory Mechanism of Norepinephrine on hIAPP Amyloid Aggregation and the Destabilization of Protofibrils. *J. Phys. Chem. B* **2020**, *124*, 10913–10929.

[18] Mo, Y.; Brahmachari, S.; Lei, J.; Gilead, S.; Tang, Y.; Gazit, E.; Wei, G. The Inhibitory Effect of Hydroxylated Carbon Nanotubes on the Aggregation of Human Islet Amyloid Polypeptide Revealed by a Combined Computational and Experimental Study. *ACS Chem. Neurosci.* **2018**, *9*, 2741–2752.

[19] Bai, C.; Lin, D.; Mo, Y.; Lei, J.; Sun, Y.; Xie, L.; Yang, X.; Wei, G. Influence of

Fullerenol on hIAPP Aggregation: Amyloid Inhibition and Mechanistic Aspects. *Phys. Chem. Chem. Phys.* **2019**, *21*, 4022–4031.

[20] Roy, R.; Paul, S. Illustrating the Effect of Small Molecules Derived from Natural Resources on Amyloid Peptides. *J. Phys. Chem. B* **2023**, *127*, 600–615.

[21] Liu, F.; Wang, W.; Sang, J.; Jia, L.; Lu, F. Hydroxylated Single-Walled Carbon Nanotubes Inhibit Aβ_{42} Fibrillogenesis, Disaggregate Mature Fibrils, and Protect against Aβ_{42}-Induced Cytotoxicity. *ACS Chem. Neurosci.* **2019**, *10*, 588–598.

[22] Bednarikova, Z.; Huy, P. D. Q.; Mocanu, M.-M.; Fedunova, D.; Li, M. S.; Gazova, Z. Fullerenol $C_{60}(OH)_{16}$ Prevents Amyloid Fibrillization of Aβ_{40}– In Vitro and In Silico Approach. *Phys. Chem. Chem. Phys.* **2016**, *18*, 18855–18867.

[23] Xie, L.; Luo, Y.; Lin, D.; Xi, W.; Yang, X.; Wei, G. The Molecular Mechanism of Fullerene-Inhibited Aggregation of Alzheimer's β-Amyloid Peptide Fragment. *Nanoscale* **2014**, *6*, 9752–9762.

[24] Qin, L.-C. Determination of the chiral indices (n,m) of carbon nanotubes by electron diffraction. *Phys. Chem. Chem. Phys.* **2007**, *9*, 31–48.

[25] Luca, S.; Yau, W. M.; Leapman, R.; Tycko, R. Peptide Conformation and Supramolecular Organization in Amylin Fibrils: Constraints from Solid-State NMR. *Biochemistry* **2007**, *46*, 13505–13522.

[26] Mukhopadhyay, T. K.; Datta, A. Deciphering the Role of Solvents in the Liquid Phase Exfoliation of Hexagonal Boron Nitride: A Molecular Dynamics Simulation Study. *J. Phys. Chem. C* **2017**, *121*, 811–822.

[27] Mukhopadhyay, T. K.; Datta, A. Screening Two Dimensional Materials for the Transportation and Delivery of Diverse Genetic Materials. *Nanoscale* **2020**, *12*, 703–719.

[28] Case, D. A. Belfon, K. Ben-Shalom, I. Y. Brozell, S. R. Cerutti, D. S. Cheatham, III, T. E. Cruzeiro, V. W. D. Darden, T. A. Duke, R. E. Giambasu, G. et al. *AMBER 2020.* University of California, San Francisco, 2020.

[29] Moral, R.; Paul, S. Influence of Salt and Temperature on the Self-Assembly of Cyclic Peptides in Water: A Molecular Dynamics Study. *Phys. Chem. Chem. Phys.* **2023**, *25*, 5406–5422.

[30] Pal, S.; Roy, R.; Paul, S. Deciphering the Role of ATP on PHF6 Aggregation. *J. Phys. Chem. B* **2022**, *126*, 4761–4775.

[31] Dupuis, N. F.; Wu, C.; Shea, J.-E.; Bowers, M. T. The Amyloid Formation Mechanism in Human IAPP: Dimers Have β-Strand Monomer–Monomer Interfaces. *J. Am. Chem. Soc.* **2011**, *133*, 7240–7243.

[32] Lao, Z.; Chen, Y.; Tang, Y.; Wei, G. Molecular Dynamics Simulations Reveal the Inhibitory Mechanism of Dopamine against Human Islet Amyloid Polypeptide (hIAPP) Aggregation and Its Destabilization Effect on hIAPP Protofibrils. *ACS Chem. Neurosci.* **2019**, *10*, 4151–4159.

[33] King, K. M.; Bevan, D. R.; Brown, A. M. Molecular Dynamics Simulations Indicate Aromaticity as a Key Factor in the Inhibition of IAPP(20–29) Aggregation. *ACS Chem. Neurosci.* **2022**, *13*, 1615–1626.

Chapter 6

Summary and Our View on hIAPP Aggregation and its Inhibition

"One never notices what has been done; one can only see what remains to be done."

– Marie Curie

The aggregation of human islet amyloid polypeptide (hIAPP) is connected to the pathogenesis of Type II Diabetes, a metabolic disorder affecting nearly 460 million individuals globally, with projections of a further rise in the near future. Functioning as a neuroendocrine hormone, hIAPP is co-secreted alongside insulin from the β-cells of the islet of Langerhans in the pancreas. In order to counteract the advancement of this disease, a possible therapeutic avenue is to curb the misfolding and aggregation of hIAPP. Within this thesis, we embark on a comprehensive exploration on the intricate journey of hIAPP aggregation, coupled with the myriad classes of compounds harboring the potential to impede this process.

In order to devise therapeutic strategies targeting the aggregation of hIAPP, the intermediates encompassing the early oligomerization process has to be investigated. Therefore, we begin our study with the the aggregation pathway of $hIAPP_{20-29}$ dimer, which consists of the amyloid prone residues of the full-length hIAPP sequence. Via Markov State Modeling, the different metastable states of $hIAPP_{20-29}$ dimer is discovered, where the most populated state is featured by an anti-parallel β-sheet, consisting of $F^{23}GAILS^{28}$ residues. Investigation of the transition pathway from a relatively disordered state to this extended-β conformation reveals a number of pathways, most of which entails a transient α-helical intermediate. In addition, turn conformers are also prominent prior to the formation of β-sheets. Since the β-sheet configuration is considered to be the amyloidogenic precursor, this study provides information on the process leading to the amyloid formation of hIAPP.

Furthermore, the inhibitory potency of an assortment of compounds on the aggregation of hIAPP is studied. Three such categories of inhibitors are explored, starting from small molecules, to peptides and then nanomaterials. Among the small molecules, the effect of norepinephrine, which is a common neurotransmitter, on the amyloidogenesis of hIAPP is investigated. Norepinephrine preferentially interacts with the C-terminal amyloid prone region of hIAPP to interrupt its self-assembly. Also, the tendency of ATP, which is recognized as the energy source for biochemical processes, to prevent the oligomerization of hIAPP is discerned. Both norepinephrine and ATP, not only prevent the aggregation of hIAPP, but also disassemble previously formed aggregates. These molecules are bioavailable and possess aromatic moieties, as well as hydrophilic groups, and hence can interact effectively with the hydrophobic and hydrophilic amino acid residues and interrupt the

interactions among hIAPP monomers. However, the contribution of the adenosine moiety of ATP towards hIAPP-ATP interactions dominates over the triphosphate chain, which indicates that the hydrophobic interactions are preferred.

To study the role of peptides and peptidomimetics in shaping the aggregation narrative, a peptide fragment is extracted from the amyloid core region of hIAPP, consisting of $N^{22}FGAIL^{27}$ sequence. The residues in this hIAPP fragment are replaced with their stereochemical D-isomer, and is used to prohibit the self-assembly of full-length hIAPP. While L-NFGAIL (which consists of L-amino acids) stabilizes the β-sheet-rich aggregates of full-length hIAPP, the inhibitor, D-NFGAIL, promotes the random coil conformation of hIAPP and interrupts hIAPP-hIAPP interaction. In another study, a conformationally restricted element, aminobenzoic acid (Abz) is incorporated into the NFGAIL fragment, by replacing I26 and/or G24 residues. Here, three different isomers of aminobenzoic acid, i.e., (β, γ, δ) are used. While β- and γ-Abz containing peptidomimetics successfully prevent the self-assembly of hIAPP, δ-Abz peptidomimetics promote it, highlighting the contrasting behaviour of the isomers. The difference in the angle between the amino and carboxyl groups in the isomers of the Abz moiety results in the diversity of the binding affinity of the peptidomimetics with hIAPP, and consequently their inhibitory efficacy.

Finally, the alliance between boron nitride nanomaterials and hIAPP aggregation is also explored. These biocompatible nanomaterials not only inhibit the dimerization of hIAPP, but also disaggregate pre-formed fibrils. The curvature of the nanomaterials is observed to have an impact on their interaction site with hIAPP. As the hydrophobicity of the nanomaterials vary with their curvature, their binding affinity shifts from the amyloidogenic C-terminal to the N-terminal region of hIAPP. These studies enlighten us about the diversity of the molecular structures that can modulate the aggregation of hIAPP and the effect of these structures on the activity of the inhibitors. In addition, the impact of stereochemistry of the amino acid residues or modified organic moieties on the inhibitory potential of peptides or peptidomimetics is also conveyed. Finally, the significance of the curvature of nanomaterials in their interaction with amyloid peptides is also implied. In unity, this thesis stands as an ardent exploration, deciphering the aggregation pathway of hIAPP and unveiling a constellation of agents poised to intervene. The information regarding the structure and activity of the various inhibitors provides a holistic comprehension of the crucial molecular scaffolds and properties required to design drugs for combatting

T2D's relentless advance.

Clinical trials in search of drugs targeting T2D are ongoing. However, developing new drugs, which pass through the clinical trials are both cost- and time-consuming. Due to the disordered nature of IDPs, high resolution characterization of protein-protein and protein-inhibitor interactions are limited experimentally. This issue is tackled by MD simulation studies. Our thesis, thus, attempts to provide information on the interactions in-between hIAPP that stabilize its amyloid aggregation and also the interactions with the diverse inhibitors, which disfavours this self-assembly, which will assist in the drug design against T2D. However, advanced experimental studies are necessary to translate these results into clinical outcomes.

List of Figures

List of Tables

Publications

1. Pal, S.; Roy, R.; Paul, S. Potential of a Natural Deep Eutectic Solvent, Glyceline, in the Thermal Stability of the Trp-Cage Mini-protein. *J. Phys. Chem. B* **2020**, *124*, 7598–7610.

2. Roy, R.; Paul, S. Theoretical Investigation of the Inhibitory Mechanism of Norepinephrine on hIAPP Amyloid Aggregation and the Destabilization of Protofibrils. *J. Phys. Chem. B* **2020**, *124*, 10913–10929.

3. Roy, R.; Paul, S. Potential of ATP towards Prevention of hIAPP Oligomerization and Destabilization of hIAPP Protofibrils: An In Silico Perspective. *J. Phys. Chem. B* **2021**, *125*, 3510–3526.

4. Roy, R.; Paul, S. hIAPP-Amyloid-Core Derived D-Peptide Prevents hIAPP Aggregation and Destabilizes Its Protofibrils. *J. Phys. Chem. B* **2021**, *125*, 3510–3526.

5. Pal, S.; Roy, R.; Paul, S. Deciphering the Role of ATP on PHF6 Aggregation". *J. Phys. Chem. B* **2022**, *126*, 4761–4775.

6. Roy, R.; Paul, S. Disparate Effect of Hybrid Peptidomimetics Containing Isomers of Aminobenzoic Acid on hIAPP Aggregation. *J. Phys. Chem. B* **2022**, *126*, 10427–10444.

7. Roy, R.; Paul, S. Illustrating the Role of Small Molecules Derived from Natural Resources on Amyloid Peptides. *J. Phys. Chem. B* **2023**, *127*, 600–615.

8. Roy, R.; Paul, S. Exploring the Curvature-Dependence of Boron Nitride Nanoparticles on the Inhibition of hIAPP Aggregation *J. Phys. Chem. B* **2023**, *127*, 7558–7570.

9. Roy, R.; Paul, S. Disclosing the Conformational Transition of $hIAPP_{20-29}$ Dimers via Markov State Modeling *Manuscript under Preparation.*

Conferences and Workshops

1. Presented a poster in the conference 'Frontiers in Chemical Sciences' (FICS-2018) held at Guwahati, IIT Guwahati.

2. Presented a poster in the conference 'Theoretical Chemistry Symposium' (TCS-2019) held at Pilani, BITS-PILANI.

3. Presented a poster in the conference 'Research Conclave' (RC-2019) held at Guwahati, IIT Guwahati.

4. Presented Flash Presentation in the conference 'Statistical Mechanics in Chemistry and Biology' (SMCB-2021) held online.

5. Presented a poster in the conference 'Theoretical Chemistry Symposium' (TCS-2021).

6. Presented a poster in the conference 'Research & Industrial Conclave' (RC-2022) held at Guwahati, IIT Guwahati.

7. Presented a poster in the '28^{th} CRSI National Symposium in Chemistry' (CRSI NSC-28) held at Guwahati, IIT Guwahati.

8. Presented a poster in the conference 'North-Eastern Research Conclave' (NERC-2022) held at Guwahati, IIT Guwahati.

9. Participated in 'Free Energy Calculations for Chemical and Biological Systems' (FECCBS-2019) held at Kanpur, IIT Kanpur.

10. Participated in 'Tools and Techniques to Perform Molecular Modelling and Computer-Aided Drug Design' (MMTT-2021) held online by NIPER Guwahati.

11. Participated in 'Machine Learning for Chemistry and Drug Design' organized online by IIIT Hyderabad.

12. Participated in 'Introduction to Machine Learning with Python' organized in Guwahati, IIT Guwahati.